

学位論文

Production of Omega Mesons
in Au+Au collisions at $\sqrt{s_{NN}} = 200$ GeV

大内田 美沙紀

目次

1. 主論文

Production of Omega Mesons in Au+Au collisions at $\sqrt{s_{NN}} = 200$ GeV

(核子対あたり重心系衝突エネルギー200GeV金+金衝突における
オメガ中間子生成測定)

大内田 美沙紀

2. 公表論文

(1) Production of ω mesons in p + p, d + Au, Cu + Cu, and Au + Au collisions at
 $\sqrt{s_{NN}} = 200$ GeV

A. Adler *et al.* (PHENIX Collaboration)

..... Physical Review C 84, 044902 (2011).

3. 参考論文

(1) Transverse momentum dependence of η meson suppression in Au+Au
collisions at $\sqrt{s_{NN}} = 200$ GeV

A. Adler *et al.* (PHENIX Collaboration)

..... Physical Review C 82, 011902 (2010).

(2) Suppression Pattern of Neutral Pions at High Transverse Momentum in
Au+Au Collisions at $\sqrt{s_{NN}} = 200$ GeV and Constraints on Medium

A. Adler *et al.* (PHENIX Collaboration)

..... Physical Review Letter 101, 232301 (2008).

主論文

Production of Omega Mesons
in Au+Au collisions at $\sqrt{s_{NN}} = 200$ GeV

Misaki Ouchida

Graduate School of Science, Hiroshima University
Higashi-Hiroshima, 739-8526, JAPAN

August 2012

Abstract

The measurement of hadrons produced in relativistic heavy-ion collisions is a well established tool in the study of the hot and dense matter created by the collisions. The PHENIX experiment at the Relativistic Heavy Ion Collider (RHIC) has carried out systematic measurements of hadrons in $p+p$, $d+Au$, $Cu+Cu$, and $Au+Au$ collisions. Solid baseline results of π^0 and η measurements in $p+p$, $d+Au$ and a comparison study of the invariant yield measurement in heavy-ion collisions suggested that the particle production is effected by jet quenching which is considered to be an effect of the matter created by the heavy-ion collisions.

We measure ω mesons via the hadronic decay mode ($\pi^0\gamma$) in $Au+Au$ collisions at C.M.S. collision energy per nucleon pairs of 200 GeV taken at the PHENIX experiment. The ω meson comprises light valence quarks similar to the π^0 and η , but has a larger mass and a spin (1), thus make it an additional probe to a systematic study to understand mechanisms of parton energy loss and hadron production in the collisions. The most challenging part of this analysis is to tackle huge combinatorial background when reconstructing particles from γ s in the high multiple collisions. We carry out the simulation in advance to calculate an acceptance and to check a multiplicity dependence expected in $Au+Au$ collisions, then optimize the signal selection where S/B is improved. Furthermore, event mixing method is executed to extract mainly uncorrelated background. Finally, the ω invariant yield as a function of transverse momentum is successfully made in different degrees of collision overlaps in $Au+Au$ collisions.

The results show that ω production has a suppression pattern at high transverse momentum, similar to that of π^0 and η in central and mid-central collisions, but no suppression is observed in peripheral collisions. The ω/π ratio has no indication that the ratios depend on transverse momentum. The nuclear modification factors R_{AA} are consistent in $Cu+Cu$ and $Au+Au$ collisions at similar numbers of participant nucleons, which supports the scenario that the energy loss takes place at the parton level in the hot and dense medium formed in the collisions.

Contents

1	Introduction	1
1.1	Quark-Gluon Plasma and Relativistic Heavy Ion Collisions	1
1.2	Space Time Evolution	3
1.3	Hard Scattering and Jet Quenching	6
1.3.1	The Nuclear Modification Factor	8
1.3.2	Parton Energy Loss	8
1.3.3	Cold Nuclear Matter Effects	10
1.3.4	Current Results	11
1.4	The ω Meson	17
1.4.1	Property	17
1.4.2	Baseline Results	18
1.4.3	Results from Other Experiments	25
1.4.4	Aim of the Thesis	27
2	Experimental Setup	28
2.1	The RHIC	28
2.2	The PHENIX Detector	30
2.2.1	The Inner Detectors	34
2.2.2	The Muon Arm Detectors	36
2.2.3	The Central Arm Detectors	36
2.2.4	The Electro Magnetic Calorimeter	40
2.2.5	The Hadron Blind Detector	45
2.3	Computing	46
3	Analysis	49
3.1	Overview	49
3.2	Event and Signal Selection	49

3.2.1	Trigger	50
3.2.2	Photon Identification	54
3.2.3	Distribution of π^0 Invariant Mass	57
3.2.4	Optimized Cuts for Reconstructing ω	58
3.3	Simulation	60
3.3.1	Event Generator	60
3.3.2	Detector Simulation	61
3.3.3	Multiplicity Dependence	64
3.4	Background Consideration	67
3.4.1	Combinatorial Background	67
3.4.2	K_s^0 Contribution	69
3.4.3	Other Components	70
3.4.4	Cocktail Simulation Study	70
3.4.5	Cut Optimization	72
3.5	Yield Extraction	75
3.5.1	Reconstruction of the ω	75
3.5.2	Event Mixing	76
3.5.3	BG Trial Method (Run4)	78
3.5.4	Fitting Method (Run7)	79
3.6	Invariant Mass Spectra	80
3.6.1	Run 4	80
3.6.2	Run 7	87
3.7	Calculation of Invariant Yield	92
3.7.1	Bin Shift Correction	92
3.8	Systematic uncertainties	93
3.8.1	Peak Extraction Uncertainties	93
3.8.2	Other Errors for Background Scaling (Run4)	94
3.8.3	Uncertainties of Bin Shift Correction	95
3.8.4	EMC Uncertainties	95
3.8.5	Acceptance Correction	95
3.8.6	Conversion Correction Uncertainty	95
3.8.7	Branching Ratio Uncertainties	96
3.8.8	N_{part} and N_{coll} Uncertainty	96
3.8.9	Summary	96
4	Results and Discussion	98
4.1	Invariant Yields	98
4.2	The ω/π Ratio	101

4.3 The Nuclear Modification Factor	104
5 Summary and Conclusion	108
A Kinematics	112
B Data Table	115

List of Figures

1.1	A schematic QCD phase diagram. The grey band indicates the phase transition from hadronic matter to the Quark-Gluon Plasma. Arrows indicate expected nuclear reactions of each relativistic heavy ion collisions (see text).	2
1.2	Schematic view of nucleus-nucleus collisions. b indicates the impact parameter. In this case, red shadowed area contains participants.	3
1.3	Space time evolution of a nucleus-nucleus collisions. Horizontal axis indicates coordinate space and vertical axis indicates time (increasing to the bottom). The graphic is from [1].	5
1.4	Diagram for the hadron production in the hadron reaction of $a + b \rightarrow c + d$	6
1.5	Left: The cross section for h^\pm at mid-rapidity as a function of p_T for several values of \sqrt{s} in $p + p$ collisions [2]. Right: The PHENIX measurement of π^0 in $p + p$ collisions at $\sqrt{s}= 200$ GeV [3].	7
1.6	Top: Nuclear modification factor R_{dA} for $(h^+ + h^-)/2$ in minimum bias d + Au compared to R_{AA} in the 10% most central Au + Au collisions. Bottom: Comparison of R_{dA} for $(h^+ + h^-)/2$ and the average of the π^0 measurements in d + Au [4].	12
1.7	Nuclear modification factor R_{AA} for π^0 (open squares, points shifted for clarity) [5] and η (solid circles) [6] in MB Au + Au collisions. Error bars include statistical and p_T -uncorrelated systematic errors, bands show p_T -correlated systematic errors. The pairs of bands at $R_{AA}=1$ are the absolute normalization error for $p + p$ (larger, dark) and Au + Au (lighter) for π^0 (left) and η (right).	13

1.8	Top: R_{AA} vs. p_T for ϕ , π^0 , η , $(K^+ + K^-)$ and $(p + \bar{p})$ in central Au + Au collisions. Middle: R_{AA} vs. p_T for ϕ and π^0 in 10%-20% mid-central Au + Au collisions. Bottom: R_{AA} vs. p_T for ϕ and $p + \bar{p}$ in 60%-92% and for π^0 in 80%-92% peripheral Au + Au collisions. The uncertainty in the determination of $\langle N_{coll} \rangle$ is shown as a box on the left.	14
1.9	Integrated nuclear modification factor (R_{AA}) for π^0 as a function of collision centrality expressed in terms of N_{part} . The last two points correspond to overlapping centrality bins, 0-10% and 0-5%. The dashed lines show the fit to a function (see text).	16
1.10	Fractional energy loss S_{loss} versus centrality given by N_{part} . The lines are fits of the form $\propto N_{part}^{2/3}$ for each p_T range.	16
1.11	(Color online) Invariant transverse momentum spectra of ω production in $p + p$ and d + Au collisions at $\sqrt{s}=200$ GeV [7]. The dashed lines represent fits to $p + p$ results by a Tsallis distribution [8] scaled by the corresponding number of binary collisions for d + Au.	20
1.12	Measured ω/π ratio as a function of p_T in $p + p$ collisions at $\sqrt{s}=200$ GeV [7]. The dashed line shows a fit of constant value to data points at $p_T > 2$ GeV/c (Fit result: $0.81 \pm 0.02(\text{stat}) \pm 0.09(\text{sys})$). The box around the dashed line is overall error of the fitting. The solid line is the PYTHIA prediction [9] for $p + p$ at $\sqrt{s}=200$ GeV. Previously published results [10] and other lower energy experiments: the E706 experiment at $\sqrt{s_{\pi N}} = 31$ GeV [11] and the ISR experiment at $\sqrt{s} = 62$ GeV [12] are shown as a comparison.	21
1.13	ω/π ratio versus transverse momentum in d + Au (0-88%) for $\omega \rightarrow e^+e^-$, $\pi^0\pi^+\pi^-$ and $\pi^0\gamma$ [7]. The dashed lines and boxes are a fit of constant value to data points at $p_T > 2$ GeV/c in $p + p$ (Fit result: $0.81 \pm 0.02(\text{stat}) \pm 0.09(\text{sys})$).	23
1.14	Nuclear modification factor, R_{dAu} , measured for ω in 0-88, 0-20, and 60-88% in d + Au collisions at $\sqrt{s}=200$ GeV [7]. The box at the right edge of the constant fit line shows the uncertainty of the fit. The previously published data of ω [10] and π^0 [13] shown for comparison.	24

1.15	Left plot: $\pi^0\gamma$ invariant mass for the Nb data (solid histogram) and LH ₂ data (dashed histogram) after background subtraction[14]. Right plot: Mean value of the $\pi^0\gamma$ invariant mass as a function of the ω momentum at an estimated average density of $0.6\rho_0$ for the Nb data (circles) and the LH ₂ (crosses) along with a fit.	25
1.16	ω signal for the Nb target from reanalysis results (solid points) in comparison to the ω line shape measurement on a LH ₂ target (dashed curve) and simulation (solid curve) assuming a mass shift by -16% at normal nuclear matter density.	26
2.1	The RHIC complex.	29
2.2	RHIC Beam Interaction Points.	30
2.3	The PHENIX Detector configuration (2004).	32
2.4	The PHENIX Detector configuration (2007).	33
2.5	The position of BBC. The BBCs are placed 144 cm from the center of the interaction diamond and surround the beam pipe. Assume the arrival times of leading charged particles from beam collisions to each BBC south and north as T_S and T_N . So then the vertex position is $(T_S - T_N)/2 \times c$	34
2.6	PHENIX central magnet field lines.	38
2.7	Interior view of PbSc module.	40
2.8	Exploded view of a PbGl supermodule(SM).	41
2.9	Cross-sectional and front view of cluster schematics.	44
2.10	χ^2 distribution for showers induced by 2 GeV/ c electrons and pions in the PbSc calorimeter [15].	45
2.11	Design of the HBD [16]. Left: 3D view of the HBD final design. Right: an exploded view of one HBD vessel showing the main elements.	46
2.12	Schematic diagram of the PHENIX On-Line system.	47
3.1	The Integrated Luminosity vs Weeks into the Run in Run4 [17]. The black line is the recorded minimum bias and the blue line is the recorded with Muon active.	50
3.2	The Integrated Luminosity vs Weeks into the Run in Run7 [18]. The total Integrated luminosity (blue filled region) is 813 μb^{-1} corresponds to 5.12 Billion minimum bias events, which is about 3.4 times bigger than Run4 integrated luminosity. . .	51

3.3	The schematic view of nuclear collisions. The left is the most peripheral and the right is the most central collision. The more the collisions is central, the more BBC collects the participants of the collisions and the less ZDC collects the spectators. . . .	52
3.4	The correlation plot of the energy deposit in the ZDC and the charge deposit in the BBC.	52
3.5	Example of cut region of the BBC charge sum. Charge sum was divided at 1% step segmentation.	53
3.6	Excluded modules in the EMCal. Maps on the left side are in the west arm and maps on the right side are in the east arm. Lower two maps on the right side are PbGl and the others are PbSc.	55
3.7	The distributions of energy (left) and a Time-Of-Flight (right). A plateau seen in the energy distribution is generated by Minimum Ionizing Particles.	56
3.8	Example of invariant mass reconstructed from 2 photons. . . .	57
3.9	Position of π^0 peak as a function of $\pi^0 p_T$	59
3.10	Width of π^0 mass as a function of $\pi^0 p_T$	59
3.11	The p_T spectra of generated ω mesons in the simulation. . . .	61
3.12	Demonstration of simulated 100 ω mesons' tracks (red lines denote electron and positron, blue dotted lines denote photons and green dotted lines denote muons). EMCal, PC1/PC2/PC3, and DC are drawn (see the Chapter 2).	62
3.13	Invariant mass spectrum of the single ω event for all p_T	63
3.14	The effect of multiplicity on the Cluster Algorithm.	64
3.15	Invariant mass spectrum of simulated ω embedding to the real data.	65
3.16	Invariant mass spectrum reconstructed by the true clusters. A peak around 0.1-0.2 (GeV/ c^2) is due to the cluster splitting causing the measured energy lower than true energy.	66
3.17	Typical geometrical acceptance (geo) and total reconstruction efficiencies for the $\omega \rightarrow \pi^0 \gamma$. The total efficiencies include the embedding efficiency and analysis cuts: solid lines are for 60-92% centrality, dotted lines are for 20-60% centrality and dot-dashed lines are for 0-20% centrality in Au + Au.	66
3.18	Conceivable combinations during 3γ reconstruction. Suppose γ_1 and γ_2 are the π^0 candidate (selected as π^0 mass) that we reconstruct first.	67

3.19	A schematic of Event mixing. Oval shapes indicate γ clusters and color differences (red or blue) indicate different collision events.	68
3.20	Invariant mass spectra shape of two different event mixing	68
3.21	A schematic of K_s^0 reconstruction	69
3.22	Reconstructed 3 gammas requiring K_s^0 mass range	69
3.23	p_T spectra of generated particles used for cocktail simulation.	70
3.24	Example output of reconstructed invariant mass of cocktail simulation in minimum bias at $2.5 < p_T < 3.5$ GeV/c. Black points are real data and red points are simulation output.	71
3.25	Schematic view of cut optimization method. We calculate S/\sqrt{B} where the single ω simulation is used for a numerator and real data is used for a denominator.	72
3.26	Flow chart of the cut optimization (see the text).	73
3.27	Absolute S/\sqrt{B} using the optimized cuts for MinBias, 0-20% and 60-92% centrality.	74
3.28	A schematic of Event mixing. Oval shapes indicate γ clusters and color differences (red or blue) indicate different collision events.	76
3.29	Invariant mass spectra of π^0	77
3.30	(a) Foreground and scaled background histograms in one of the p_T bins in Au + Au. (b) Foreground histogram after subtraction of scaled background.	78
3.31	(a) Foreground and scaled background histograms in one of the p_T bins in Au + Au. (b) Foreground histogram after subtraction of scaled background.	79
3.32	Invariant Mass Spectra (0-20% cent, $p_T=6.0$, $p_T=7.0$ and $p_T=8.0-10.0$ GeV/c). Left Side: Black points denote Foreground, Green points denote BG1, Red points denote BG2, Blue points denote BG3 and Magenta points denote BG1+BG2+BG3. Red solid lines denote SG (mean and width are fixed value extracted by the embedding simulation).	81
3.33	Invariant Mass Spectra (20-60% cent, $p_T=5.0$, $p_T=6.0$ and $p_T=7.0$ GeV/c).	82

3.34	Invariant Mass Spectra (20-60% cent, $p_T=8.0$, $p_T=9.0$ and $p_T=10.0$ GeV/ c). Left Side: Black points denote Foreground, Green points denote BG1, Red points denote BG2, Blue points denote BG3 and Magenta points denote BG1+BG2+BG3. Red solid lines denote SG (mean and width are fixed value extracted by the embedding simulation).	83
3.35	Invariant Mass Spectra (60-92% cent, $p_T=3.0$, $p_T=4.0$, $p_T=5.0$ and $p_T=6.0-10.0$ GeV/ c).	84
3.36	Invariant Mass Spectra (0-92% cent, $p_T=6.0$, $p_T=7.0$, $p_T=8.0$ GeV/ c). Left Side: Black points denote Foreground, Green points denote BG1, Red points denote BG2, Blue points denote BG3 and Magenta points denote BG1+BG2+BG3. Red solid lines denote SG (mean and width are fixed value extracted by the embedding simulation).	85
3.37	Invariant Mass Spectra (0-92% cent, $p_T=9.0$ and $p_T=10.0$ GeV/ c). Left Side: Black points denote Foreground, Green points denote BG1, Red points denote BG2, Blue points denote BG3 and Magenta points denote BG1+BG2+BG3. Red solid lines denote SG (mean and width are fixed value extracted by the embedding simulation).	86
3.38	Invariant mass spectra at 0-92% centrality.	88
3.39	Invariant mass spectra at 0-20% centrality.	89
3.40	Invariant mass spectra at 20-60% centrality.	90
3.41	Invariant mass spectra at 60-92% centrality.	91
3.42	Examples of fits used for evaluation of raw yield extraction systematic uncertainties.	93
3.43	Systematic uncertainties for peak extraction in four centrality bins. The values were extracted by constant fitting (solid red line).	94
4.1	Invariant transverse momentum spectra of the ω in Au + Au from the $\omega \rightarrow \pi^0\gamma$ decay channel for three centrality bins and minimum bias. The dashed lines are the $p + p$ results scaled by the corresponding number of binary collisions: N_{coll} values used for the scaling were shown in Section 3.8.	99

4.2	Invariant transverse momentum spectra of the ω production in (a) Cu + Cu and (b) Au + Au collisions from the $\omega \rightarrow \pi^0\gamma$ decay channel for three centrality bins and minimum bias (this work). The dashed lines are the $p + p$ results scaled by the corresponding number of binary collisions: N_{coll} values used for the scaling were shown in Section 3.8. The (a) Cu + Cu data were recorded in 2005 and the (b) Au + Au data were recorded in 2004 (Year 4) and 2007 (Year 7).	100
4.3	The ω/π ratio versus transverse momentum in Au + Au (0-92, 0-20, 60-92%) for the $\omega \rightarrow \pi^0\gamma$. The dashed lines and boxes are fitted of constant values and overall errors in minimum bias (fit results: $0.83 \pm 0.09(\text{stat}) \pm 0.06(\text{sys})$).	102
4.4	The ω/π ratio versus transverse momentum in Cu + Cu (0-94%) for the $\omega \rightarrow \pi^0\gamma$ and in Au+Au (0-92%) for the $\omega \rightarrow \pi^0\gamma$. The dashed lines and boxes are a fit of constant value to data points at $p_T > 2$ GeV/c in $p+p$ [7] (fit result: $0.81 \pm 0.02(\text{stat}) \pm 0.09(\text{sys})$).	103
4.5	Constant fitting values of the ω/π at $p_T > 2$ GeV/c as a function of centrality (N_{part}): $0.75 \pm 0.01(\text{stat}) \pm 0.08(\text{sys})$ in d + Au, $0.71 \pm 0.07(\text{stat}) \pm 0.07(\text{sys})$ in MB Cu + Cu ($0.64 \pm 0.10(\text{stat}) \pm 0.08(\text{sys})$ in 0-20% and $1.32 \pm 0.24(\text{stat}) \pm 0.29(\text{sys})$ in 60-94%), and $0.83 \pm 0.09(\text{stat}) \pm 0.06(\text{sys})$ in MB Au + Au ($1.34 \pm 0.23(\text{stat}) \pm 0.1(\text{sys})$ in 0-20% and $1.51 \pm 0.21(\text{stat}) \pm 0.37(\text{sys})$ in 60-92%). Error bars are combined statistical and systematic values. The dashed line shows a fit of constant value to this plot (0.79 ± 0.04).	103
4.6	R_{AA} of the ω in Au + Au for the $\omega \rightarrow \pi^0\gamma$ decay channel for three centrality bins and minimum bias. The uncertainty in the determination of $p + p$ scaling is shown as a box on the left in each plot.	104
4.7	R_{AA} of the ω in Cu + Cu (left) and Au + Au (right) from $\omega \rightarrow \pi^0\gamma$ decay channel for three centrality bins and minimum bias. The uncertainty in the determination of $p + p$ scaling is shown as a box on the left in each plot. Rhombuses in each plot are R_{AA} of the π^0 in Cu + Cu [19] and Au + Au [5] shown as a comparison.	106

4.8	R_{AA} for the ω meson integrated over the range $p_T > 7$ GeV/ c as a function of the number participating nucleons (N_{part}). Results for π^0 's and η 's R_{AA} are shown for comparison. Squares correspond to $\pi^0 \rightarrow \gamma\gamma$ where $p_T(\pi^0) > 7$ GeV/ c [5], triangles correspond to $\eta \rightarrow \gamma\gamma$ where $p_T(\eta) > 7$ GeV/ c [6] and other points (closed circle, opened circle and opened triangle) correspond to our results. The dashed line shows fitted fractional energy loss function, $R_{AA} = (1 - S_0 N_{part}^a)^{n-2}$	107
5.1	The PHENIX collaboration (taken on May 2008).	111
A.1	Coordinates of the PHENIX experiment.	113

List of Tables

1.1	The status of ω meson [20]	17
1.2	Summary of the analyzed data samples and ω meson decay channels taken in the PHENIX.	19
2.1	The parameters of energy used by the Cluster Algorithm [21] .	43
3.1	The kinematical cut table.	60
3.2	The number of participating collisions ($\langle N_{\text{part}} \rangle$) and the number of binary nucleon-nucleon collisions ($\langle N_{\text{coll}} \rangle$).	96
3.3	Summary of assigned systematic errors in Au + Au analysis. .	97
B.1	The invariant yield of the $\omega \rightarrow \pi^0 \gamma$ in Au + Au (Run4).	116
B.2	The invariant yield of the $\omega \rightarrow \pi^0 \gamma$ in Au + Au (Run7).	116
B.3	The ω/π results for the $\omega \rightarrow \pi^0 \gamma$ in Au+Au in 0-20% , 60-92% and minimum bias in Run4.	117
B.4	The ω/π results for the $\omega \rightarrow \pi^0 \gamma$ in Au+Au in 0-20% , 60-92% and minimum bias in Run7.	117
B.5	R_{AA} of the $\omega \rightarrow \pi^0 \gamma$ in Au + Au (Run4).	118
B.6	R_{AA} of the $\omega \rightarrow \pi^0 \gamma$ in Au + Au (Run7).	118

Chapter 1

Introduction

Nuclear matter is constructed by the most fundamental particles, quarks and leptons. Quarks themselves can not be “liberated” due to gluons that holds together quarks by the strong force. The goal of the relativistic heavy ion physics is to explore the matter where quarks and gluons can be “liberated” by creating hot and dense conditions.

In the former part of this chapter, we will introduce the theoretical backgrounds and current experimental results of hadron production in the relativistic heavy ion collisions. In the latter part, we will focus on the ω meson by showing it’s property and the current results of the baseline measurements.

1.1 Quark-Gluon Plasma and Relativistic Heavy Ion Collisions

The state of the nuclear matter is described by the Quantum Chromodynamics (QCD), a theory of the strong interaction. The QCD exhibits a property called the asymptotic freedom [22] in which the coupling strength of gluons decreases with increasing energy and momentum. As nuclear matter is heated and compressed, hadrons occupy more and more in the available space. Eventually they start to overlap and the initially confined quarks and gluons begin to ‘percolate’ between the hadrons thus being ‘liberated’. This state of matter, the hot and dense fireball made of ‘liberated’ quarks and gluons is commonly called as the Quark-Gluon Plasma (QGP) – first proposed by Bjorken [23] in 1982.

This simple picture has originally provided the basis for models of the

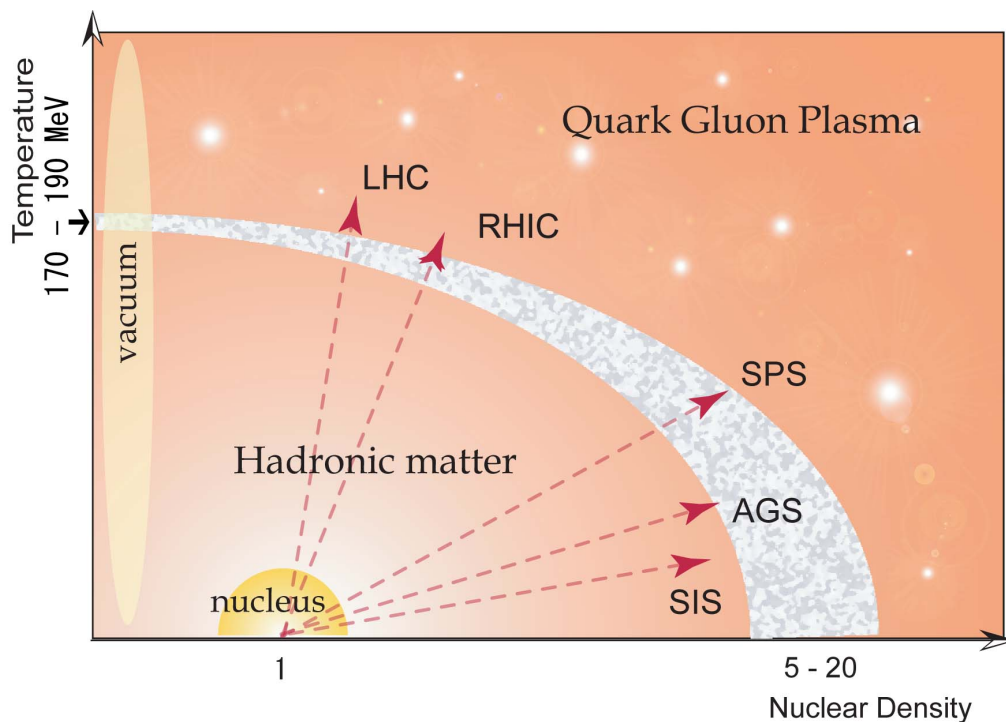


Figure 1.1: A schematic QCD phase diagram. The grey band indicates the phase transition from hadronic matter to the Quark-Gluon Plasma. Arrows indicate expected nuclear reactions of each relativistic heavy ion collisions (see text).

quark-hadron transition and has been essentially confirmed by numerical QCD lattice calculations at finite temperature [24]. The QCD phase diagram is shown in the Figure 1.1. Although the phase boundary between the hadron matter and the QGP is not well known, lattice calculations gave an estimation of the critical temperature T_c and the baryon density needed for the QGP creation. From there we can estimate that T_c is about up to 170 MeV and the density is approximately from 5 to 20 times of the normal nuclear matter. However, the systematic error of the lattice result is not known since it is unattainable using the re-weighting method [24] to consider the volume $V \rightarrow \infty$ when calculating the nuclear density going to 0.

Many experiments have been exploring QCD phase transitions via varying the beam energy. Both temperature and nuclear density vary as a func-

tion of the center-of-mass energy ($\sqrt{s_{NN}}$) [25]. The Heavy Ion Synchrotron (SIS) ($\sqrt{s} \simeq 2A$ GeV) at GSI in Darmstadt, the Alternating Gradient Synchrotron (AGS) ($\sqrt{s} \simeq 5A$ GeV) at Brookhaven National Laboratory (BNL) in New York and the Super Proton Synchrotron (SPS) ($\sqrt{s} \simeq 20A$ GeV) at CERN in Geneva began in mid 80's. The Relativistic Heavy Ion Collider (RHIC) ($\sqrt{s} = 200A$ GeV) at BNL has been ongoing since 2000 and the Large Hadron Collider (LHC) ($\sim \sqrt{s} \sim 5.5A$ TeV) at CERN starts operating from 2008. According to the model predictions [26], RHIC and SPS energies are indeed lying on the phase boundary and the results of RHIC provided evidences of the formation of Quark-Gluon Plasma [27, 28, 29, 30]. AGS is below the boundary line, however, it is not excluded that the fireball in the initial state appears in the deconfined phase since the initial energy density expected at AGS is of the order of $1 \text{ GeV}/\text{fm}^3$ which is larger than the critical energy density along the boundary.

1.2 Space Time Evolution

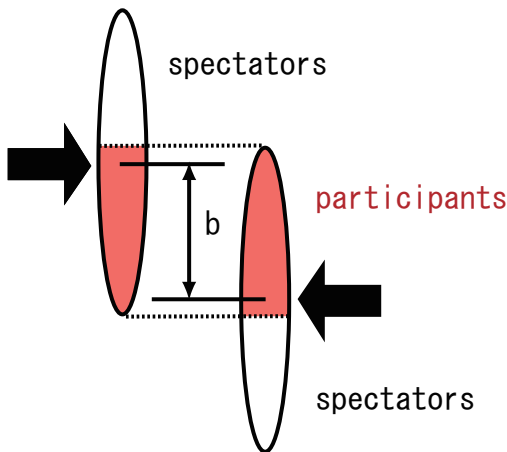


Figure 1.2: Schematic view of nucleus-nucleus collisions. b indicates the impact parameter. In this case, red shadowed area contains participants.

In relativistic heavy-ion collisions, the Lorentz-contracted nuclei interact in the region of geometrical overlap which is determined by the impact parameter b as shown in Figure 1.2. The interacting nucleons are called “participants”, while the nucleons outside the geometrical overlap are called “spectators” which are basically unaffected by the collisions. The geometric parameters of nucleus-nucleus collisions, such as number of participants $\langle N_{part} \rangle$, number of collisions $\langle N_{coll} \rangle$, nuclear overlapping function T_{AA} and impact parameter $\langle b \rangle$, are estimated by the Glauber model [31] which is based on Monte Carlo simulation.

The space-time evolution of two colliding nuclei is illustrated in Figure

1.3. In Bjorken's picture, quarks become point-like, observable objects at very short distance in high energy. The two nuclei head-on when they are traveling at nearly the speed of light. After the first initial interactions between the nucleons the reaction area contains highly excited matter, far from thermal equilibrium (pre-equilibrium state). The pressure created in the initial stage of the collisions results in an expansion of the system formed. As it expands, the temperature drops, eventually crossing the critical temperature and hadronization occurs wherein the partons get bound within hadrons. After thermalization of the system, provided that the temperature and energy density is sufficient, it is possible that Quark-Gluon Plasma is formed: the critical temperature of the phase transition lies within the range of 170-190 MeV (most calculations on lattice also indicate the existence of Quark-Gluon Plasma at > 160 MeV [32]). Then due to the rapid expansion into the surrounding vacuum, the system cools and the quarks recombine into hadrons. This mixed phase would exist only if the transition is of first order. Inelastic collisions between the newly formed hadrons continue to occur until the system cools to the chemical freeze-out point ($T \sim 100$ MeV). Finally, elastic collisions between the hadrons cease at the thermal freeze-out point. At this point, the momentum distributions of all particles are frozen.

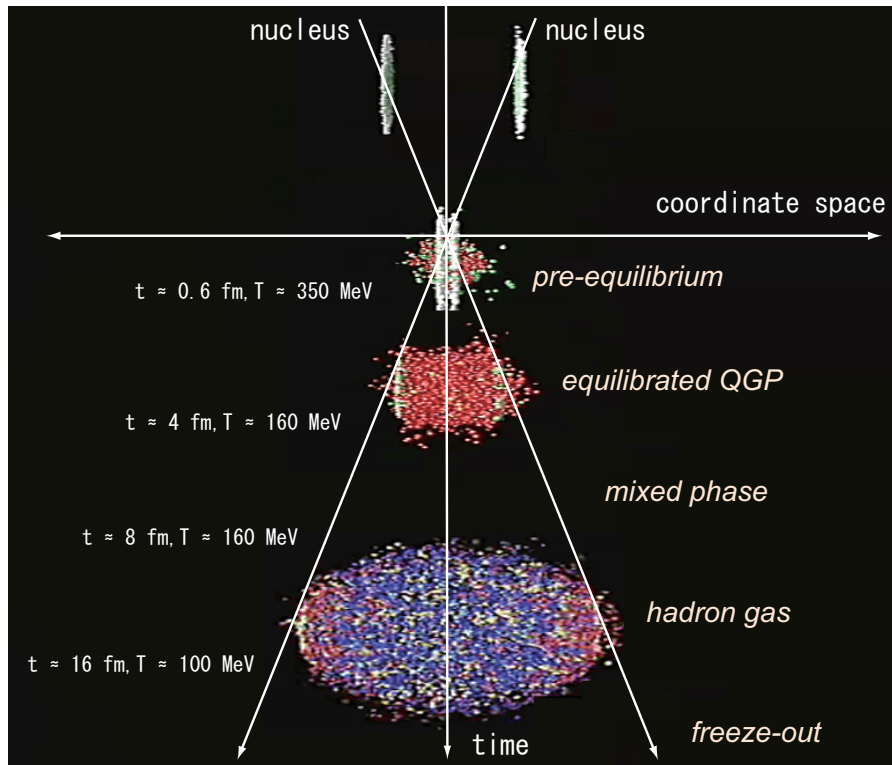


Figure 1.3: Space time evolution of a nucleus-nucleus collisions. Horizontal axis indicates coordinate space and vertical axis indicates time (increasing to the bottom). The graphic is from [1].

1.3 Hard Scattering and Jet Quenching

The particle production in high energy hadron collisions can be treated as a combination of perturbative (hard and semi-hard) parton production and non-perturbative (soft) particle production.

In hadron or heavy-ion collisions, the hard scattering is occurred in the earliest stage of the collision. The Figure 1.4 represents a schematic view of parton reactions of $a + b \rightarrow c + d$.

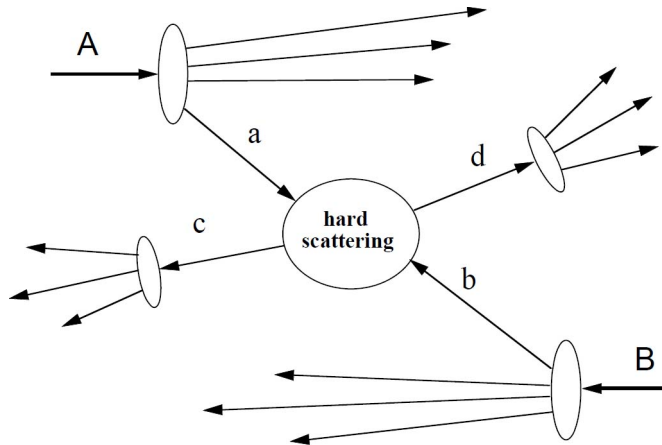


Figure 1.4: Diagram for the hadron production in the hadron reaction of $a + b \rightarrow c + d$.

A parton with smaller transverse momentum than the scale is considered as a part of initial or final hadron structure. The cross section of the hadron production of Figure 1.4 is expressed as following:

$$\sigma^{AB \rightarrow hX} = \sum_{abcd} \int dx_a dx_b dz_c \cdot f_{a/A}(x_a, \mu_F) \cdot f_{b/B}(x_b, \mu_F) \quad (1.1)$$

$$\times \sigma(ab \rightarrow cd) \times D_{h/cd}(z_{cd}, \mu_F) ,$$

where μ_F is the factorization scale, $f_{a/A}(x_a, \mu_F)$ is parton distribution function (PDF) of a parton in the hadron A , $f_{b/B}(x_b, \mu_F)$ is PDF b parton in the hadron B , $D_{h/cd}(z_{cd}, \mu_F)$ is fragmentation function (FF) from c or d parton to the hadron, x and z are the momentum fraction of the initial and final

parton in the initial and final hadron, respectively. $\sigma(ab \rightarrow cd)$ represents the cross section from two partons.

Hard scattering in $p + p$ collisions was discovered at the CERN-ISR in 1972, at $\sqrt{s} = 23.5\text{-}62.4$ GeV. Figure 1.5 (left) is the cross section for h^\pm showing that the exponential behavior at low p_T breaks to a power-law tail which varies systematically with the \sqrt{s} values. Figure 1.5 (right) shows the relative composition of the “hard” and “soft” components of the p_T spectrum in $p+p$ collisions at $\sqrt{s} = 200$ GeV: The soft particle production is dominant for $p_T \leq 1.5$ GeV/ c while hard scattering predominates for $p_T \geq 2.0$ GeV/ c

The inclusive measurements of single or pairs of hadrons at the CERN-ISR were used to establish that high transverse momentum particle in $p + p$ collisions are produced from states with two roughly back-to-back jets which are the results of scattering of constituents of the nucleons. This techniques have been used extensively and further developed at RHIC since they are the only practical method to study hard-scattering and jet phenomena in $A+A$ central collisions due to the large multiplicity [33].

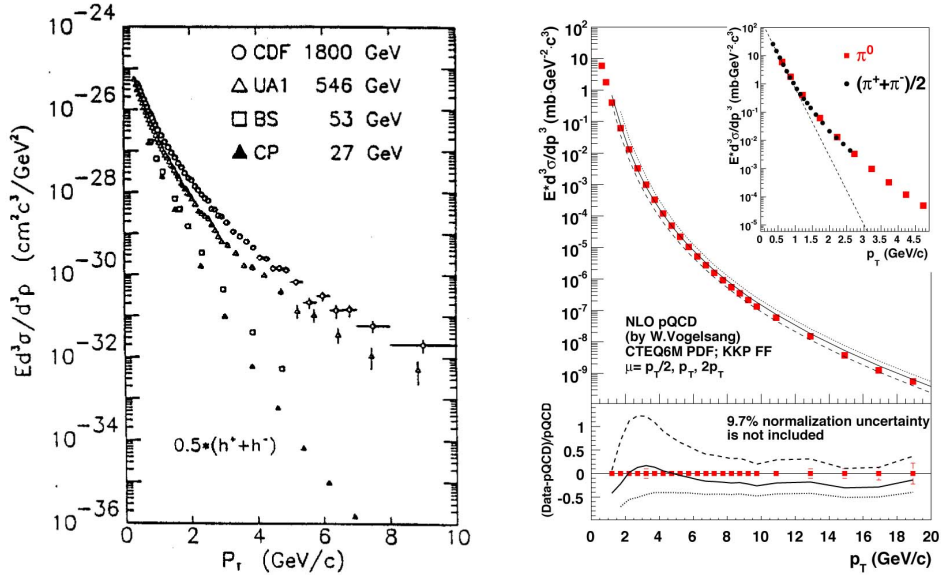


Figure 1.5: Left: The cross section for h^\pm at mid-rapidity as a function of p_T for several values of \sqrt{s} in $p + p$ collisions [2]. Right: The PHENIX measurement of π^0 in $p + p$ collisions at $\sqrt{s} = 200$ GeV [3].

1.3.1 The Nuclear Modification Factor

Considering the multiplicity of partons, the cross section in tow nuclei $A+B$ collisions can be connected to the $p + p$ cross section by a scaling factor, binary nucleon-nucleon collisions (N_{coll}) in the reaction. If there are medium-induced effects in the reaction, it may cause a divergence of the scaling.

Medium-induced effects on high- p_T particle production can be quantified with the nuclear modification factor:

$$R_{AB}(p_T) = \frac{d^2 N_{AB}/dydp_T}{(\langle N_{coll} \rangle / \sigma_{pp}^{inel}) \times d^2 \sigma_{pp}/dydp_T}, \quad (1.2)$$

where $d^2 N_{AB}/dydp_T$ is the differential yield per event in nucleus-nucleus collisions, $\langle N_{coll} \rangle$ is the number of binary nucleon-nucleon collisions averaged over the impact parameter range of the corresponding centrality bin calculated by Glauber Monte-Carlo simulation [31], and σ_{pp}^{inel} and $d^2 \sigma_{pp}/dydp_T$ are the total and differential cross sections for inelastic $p + p$ collisions, respectively. In the absence of medium-induced effects, the yield of high- p_T particle is expected to scale with $\langle N_{coll} \rangle$, resulting in $R_{AB}=1$ at high- p_T . Therefore, evaluating R_{AB} value is a critical probe to see the medium effect.

From the next subsection, we introduce some theoretical prediction which are explaining medium effects leading to a modification of the particle production compared to nucleon-nucleon reactions.

1.3.2 Parton Energy Loss

The possible cause that lead $R_{AA} < 1$ is parton energy loss or jet quenching due to the presence of a hot and dense medium. When a parton transverses a colored medium, it loses energy predominantly by radiating soft gluons, similar to electromagnetic Bremsstrahlung of an electron passing through matter. The theoretical treatment of the energy loss is complicated by the fact that one has to consider destructive interference effects of the emitted gluons if the formation time of the gluon is larger compared to its mean free path in the medium. This quantum interference can produce an energy loss $\delta E/\delta x$ that grows faster than linearly with the path length L of the parton in the medium. Here, we introduce two theoretical calculations of the parton energy loss in the medium using the multiple soft scattering (“BDMPS-Z”) and the single hard scattering (“GLV”) approximation.

The BDMPS-Z Model

Gluon emission off highly virtual hard partons is an essential component in the standard description of parton fragmentation in elementary process. The Baisier-Dokshitzer-Mueller-Peigné-Schiff-Zakharov “BDMPS-Z” model [34] is the multiple soft scattering approximation, which is obtained from a probabilistic iteration of the medium-modified elementary splitting processes ($q \rightarrow qg$ and $g \rightarrow gg$). The average parton energy loss is calculated as:

$$\langle \Delta E \rangle_{R \rightarrow \infty} = \lim_{R \rightarrow \infty} \int_0^\infty d\omega \omega \frac{dI}{d\omega} = \frac{\alpha_s C_R}{2} \omega_c, \quad (1.3)$$

where R is the density parameter, ω is the gluon energy distribution, α_s is the strong coupling constant, and C_R is the QCD coupling factor between the parton and the gluon in the medium. For a hard parton traversing a finite path length L in the medium, the scale of the radiated energy distribution is defined as $\omega_c = 1/2 \hat{q}L$, where \hat{q} is the so-called transport coefficient of the medium. Therefor, the parton energy loss can be translated to have the L^2 -dependence.

The Parton Quenching Model (PQM) [35, 36] is a Monte Carlo model based on the BDMPS-Z framework including final-state gluon radiation. It combines the pQCD BDMPS-Z for the probabilistic calculation of parton energy loss in extended partonic matter of given size and density with a realistic description of the collision overlap geometry in a static medium.

The GLV Model

The model by Gyulassy, Levai, and Vitev (GLV) [37, 38] approaches to the medium-induced non-Abelian energy loss. As for the BDMPS-Z model, the energy loss is calculated to have the L^2 -dependence, as $\Delta E \propto \mu^2 L^2 / \lambda$ by assuming thick “plasmas”: $\bar{n} = L/\lambda > 1$ (\bar{n} is calculated to be ~ 4 at RHIC energies).

To understand the dependence of jet quenching on the heavy ion species and centrality, the effective atomic mass number, A_{eff} , or the number of participants, N_{part} , are substituted for L ($L \propto A_{eff}^{1/3} \propto N_{part}^{1/3}$) to see a dependence of the characteristic plasma parameters. The fractional energy loss scales approximately as, $\epsilon = \Delta E/E \propto A_{eff}^{2/3} \propto N_{part}^{2/3}$. If a parton loses this momentum fraction ϵ during its propagation in the medium to escape with momentum $p_{T_c}^{quench}$, immediately after the hard collision $pT_c = p_{T_c}^{quench}/(1-\epsilon)$. Then the nuclear modification factor can be derived as,

$$\begin{aligned}
R_{AA} &= \frac{\sigma_{pp}^{in}}{N_{AAcol}} \frac{dN_{AA}^h/dyd^2p_T}{d\sigma^h/dyd^2p_T}(exp.) \approx \frac{d\sigma_{quench}^h/dyd^2p_T}{d\sigma^h/dyd^2p_T}(th.) \\
&= (1 - \epsilon_{eff})^{n-2} = \left(1 - \frac{k}{n-2} N_{part}^{2/3}\right)^{n-2},
\end{aligned}$$

where $k/(n-2)$ is the proportionality coefficient in which depends on the microscopic properties of the medium. Thus, the logarithm of nuclear suppression is predicted to have simple power law dependence on the system size.

1.3.3 Cold Nuclear Matter Effects

Other effects on the particle production that are not due to the presence of a hot and dense medium include modifications of the initial state, as well as effects of cold nuclear matter that a jet might have to go through, or multiple soft scatterings of a parton before the final hard scattering process.

Cronin Effect

Since the early 1970's, it has been observed that the cross section of particles produced in $p + A$ collisions does not simply scale with the number of target nucleons when compared to the particle production in $p + p$ collisions [39, 40, 41]. If the A -dependence of the invariant cross section, I , of particle i in $p + A$ is parameterized as :

$$I_i(p_T, A) = I_i(p_T, 1) \cdot A^{\alpha(p_T)}, \quad (1.4)$$

where α is a parameter for the exponent in the parameterization of the $p + A$ cross section for a given p_T . It has been observed that α_i is greater than unity above some p_T above $\sim 1-1.5$ GeV/ c [42]. Therefore, an enhancement of particle production in $p + A$ collisions, compared to the expectation from $p + p$ collisions was observed. This enhancement is traditionally explained as multiple soft scattering of the incoming partons while passing through the nucleus which leads to a broadening of their transverse momentum distribution [43]. This effect is usually called, *Cronin effect*.

Nuclear Shadowing

In addition to Cronin effect, known initial state effects also include so called *nuclear shadowing*. It was discovered in 1982 that Bjorken x -, Q^2 - dependence structure function $F_2(x, Q^2)$ per nucleon in ion differs significantly from that of a free nucleon [44]. Dynamical models of nuclear shadowing [45] observed that shadowing effects defined as below ratio:

$$R(x, Q^2; A) = \frac{F_2^A(x, Q^2)}{F_2^D(x, Q^2)}, \quad (1.5)$$

where $F_2^D(x, Q^2)$ is the nuclear structure function of deuteron, increases with energy ($1/x$) and decrease with Q^2 , which is consistent with data.

The nuclear modification factor rises faster with p_T in d + Au than in peripheral Au + Au, despite the comparable number of binary collisions. As Au + Au involves a second Au nucleus, shadowing effects can be expected to be large, reducing the observed Cronin effect [42].

From the next section, we will show the current results of the hadron productions measured in the PHENIX, then introduce the ω mesons which is a probe for this work.

1.3.4 Current Results

In d + Au at RHIC, the cross-section for high- p_T particle production in d + Au collisions is observed showing that the cross-section is enhanced compared to $p + p$ [4, 46, 47, 48]. The top panel of Figure 1.6 shows R_{dA} for inclusive charged particles $(h^+ + h^-)/2$ measured in the PHENIX compared with R_{AA} observed in central Au + Au collisions, while the lower panel compares $(h^+ + h^-)/2$ with π^0 [4]. The data clearly indicate that there is no suppression of high- p_T particles in d + Au collisions, but indicate an enhancement in inclusive charged particle production at $p_T > 2$ GeV/ c . This enhancement is generally referred to the Cronin effect, the multiple scattering in the cold-nuclear medium of the partons. The smaller enhancement of the π^0 than for inclusive charged particles at $p_T = 2-4$ GeV/ c may be due to different constituent between the π^0 and the charged particles: the charged spectrum includes baryons and anti-baryons [39].

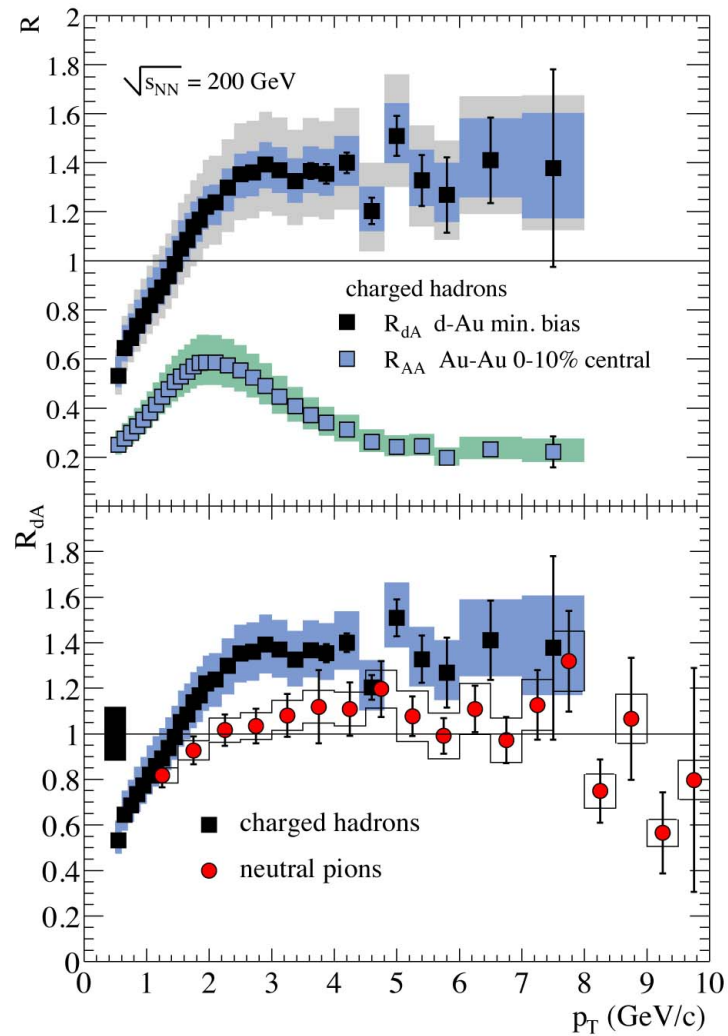


Figure 1.6: Top: Nuclear modification factor R_{dA} for $(h^+ + h^-)/2$ in minimum bias d + Au compared to R_{AA} in the 10% most central Au + Au collisions. Bottom: Comparison of R_{dA} for $(h^+ + h^-)/2$ and the average of the π^0 measurements in d + Au [4].

The yield measurements of π^0 , η and ϕ mesons in the heavy-ion collisions taken in the PHENIX were presented in [5, 6, 49]. Figure 1.7 shows the nuclear modification factor R_{AA} for π^0 and η in minimum bias Au + Au

collisions. The π^0 results show that the yield is suppressed by factor of ~ 5 at 5 GeV/ c compared to the binary scaled $p + p$ reference and the suppression prevails with little or no change up to 20 GeV/ c . The η results are consistent both in magnitude and trend versus p_T and centrality. Figure 1.8 shows a comparison of the R_{AA} with ϕ results. The ϕ meson having heavier mass and strangeness mesons exhibits a different suppression pattern than that of π^0 and η at intermediate p_T range (2-5 GeV/ c), but the difference gradually disappears with decreasing centrality and increasing p_T .

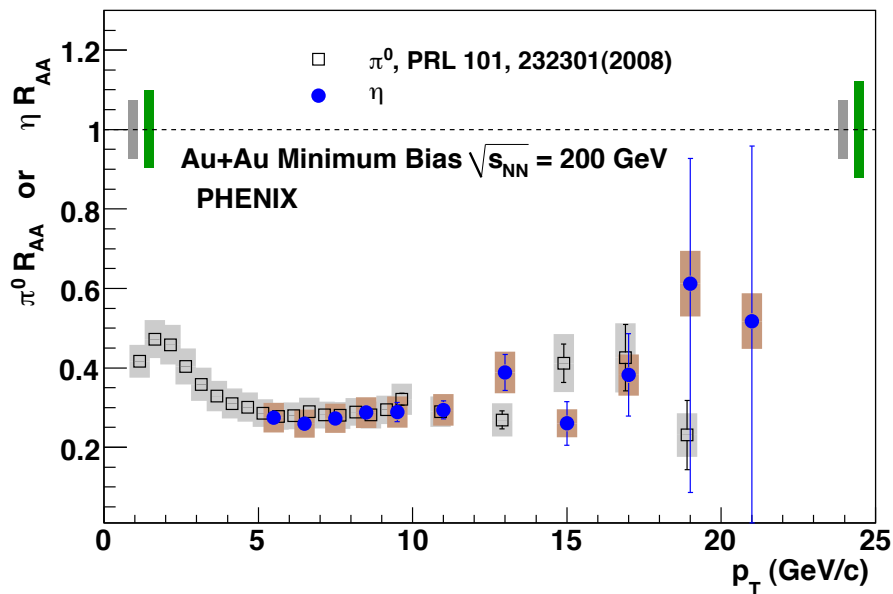


Figure 1.7: Nuclear modification factor R_{AA} for π^0 (open squares, points shifted for clarity) [5] and η (solid circles) [6] in MB Au + Au collisions. Error bars include statistical and p_T -uncorrelated systematic errors, bands show p_T -correlated systematic errors. The pairs of bands at $R_{AA}=1$ are the absolute normalization error for $p + p$ (larger, dark) and Au + Au (lighter) for π^0 (left) and η (right).

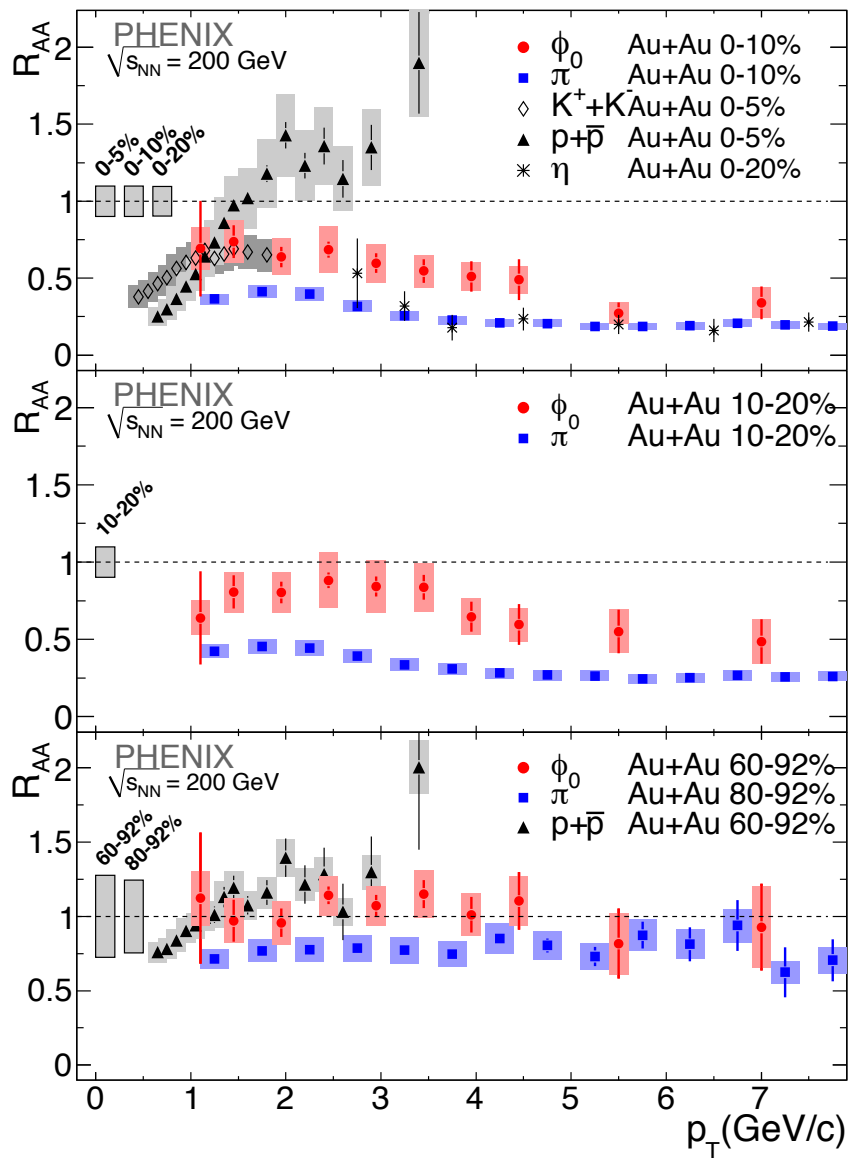


Figure 1.8: Top: R_{AA} vs. p_T for ϕ , π^0 , η , (K^+K^-) and $(p+\bar{p})$ in central Au+Au collisions. Middle: R_{AA} vs. p_T for ϕ and π^0 in 10%-20% mid-central Au+Au collisions. Bottom: R_{AA} vs. p_T for ϕ and $p+\bar{p}$ in 60%-92% and for π^0 in 80%-92% peripheral Au+Au collisions. The uncertainty in the determination of $\langle N_{coll} \rangle$ is shown as a box on the left.

The similarity between the suppression patterns of different mesons at high p_T favors the production of these mesons via jet fragmentation outside the hot and dense medium created in the collisions. The ϕ R_{AA} showing smaller amount of suppression than that of the π^0 and the η in the intermediate p_T range (2-5 GeV/ c) suggests that the excess is linked to the number of constituent quarks rather than the hadron mass because the baryon (protons and anti-protons) excess observed in central Au + Au collisions at intermediate p_T is not observed for the ϕ meson despite the similar mass of the proton and the ϕ .

To see the centrality dependence, Figure 1.9 is plotted to show the integrated nuclear modification factor ($p_T > 5$ GeV/ c , and $p_T > 10$ GeV/ c) for π^0 s as a functions of centrality, with the last two points indicating overlapping 0-10% and 0-5% bins. In both cases the suppression increases monotonically with N_{part} without any signs of saturation, suggesting that larger colliding systems should exhibit even more suppression. The common power-law behavior ($\propto p_T^n$) in $p + p$ and Au + Au allows the suppression to be re-interpreted as a fractional energy loss $S_{loss} = 1 - R_{AA}^{1/(n-2)}$ where n is the power-law exponent, and the previous results found that $S_{loss} \propto N_{part}^a$ [50]. The fractional energy loss S_{loss} as a function of centrality expressed as N_{part} is shown in Figure 1.10, for two different p_T ranges, $3 < p_T < 5$ GeV/ c and $5 < p_T < 7$ GeV/ c . There appears to be a small decrease of S_{loss} with increasing p_T , but the main observation from Figure 1.10 is that S_{loss} increases approximately like $N_{part}^{2/3}$. The fitting to Figure 1.9 with a function $R_{AA} = (1 - S_0 N_{part}^a)^{n-2}$ gives $a = 0.58 \pm 0.07$ for $N_{part} > 20$ for $p_T > 5$ GeV/ c , and $a = 0.56 \pm 0.10$ for $p_T > 10$ GeV/ c [5]. The GLV and PQM models predict that $a \sim 2/3$, which is consistent with the data. The fitted values for S_0 are $(8.3 \pm 3.3) \times 10^{-3}$ and $(9.2 \pm 4.9) \times 10^{-3}$ for $p_T > 5$ GeV/ c and $p_T > 10$ GeV/ c , respectively, shown in Figure 1.9. Note that in this interpretation a constant S_{loss} (independent of p_T) implies that the energy loss increases with p_T .

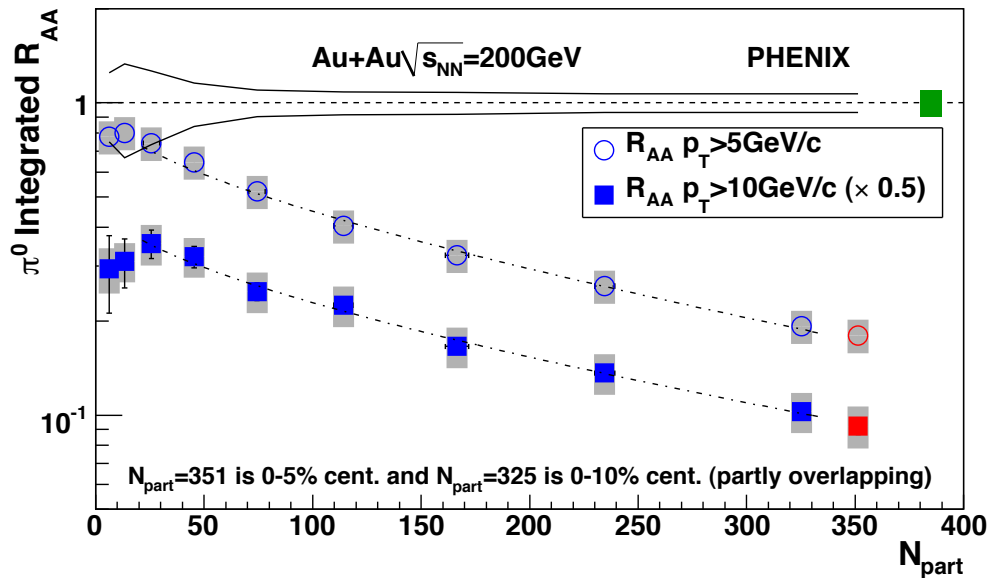


Figure 1.9: Integrated nuclear modification factor (R_{AA}) for π^0 as a function of collision centrality expressed in terms of N_{part} . The last two points correspond to overlapping centrality bins, 0-10% and 0-5%. The dashed lines show the fit to a function (see text).

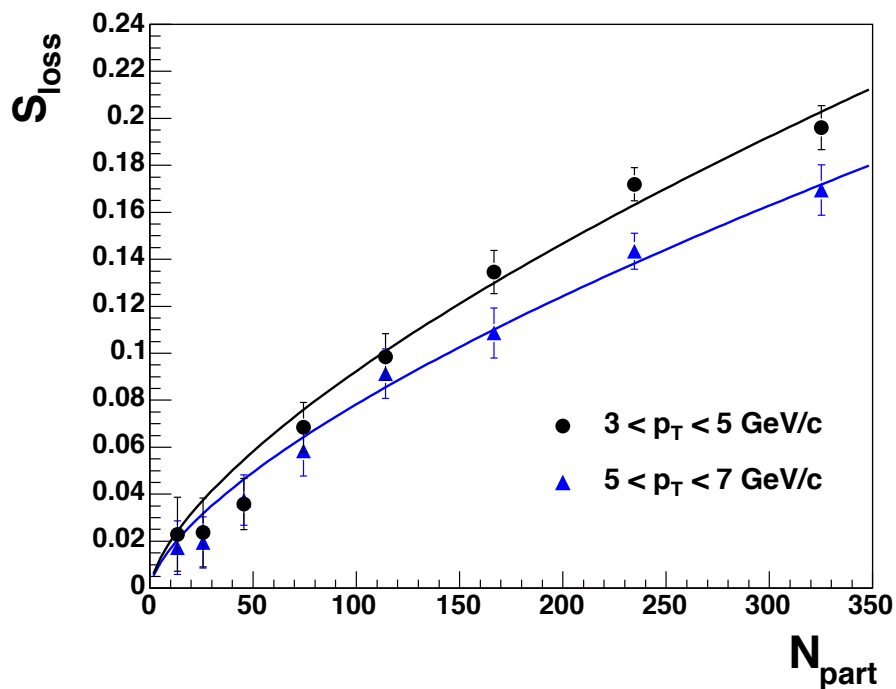


Figure 1.10: Fractional energy loss S_{loss} versus centrality given by N_{part} . The lines are fits of the form $\propto N_{part}^{2/3}$ for each p_T range.

1.4 The ω Meson

The ω meson consists of light valence quarks similar to π^0 and η , but has a larger mass (782 MeV) and a spin (1). These differences make the ω measurement an additional probe to a systematic study to understand mechanisms of parton energy loss and hadron production in the collisions. The production of particle ratio (ω/π) and the nuclear modification factors (R_{AA}) expect to add information to the parton energy loss models by measuring their p_T dependence.

1.4.1 Property

The ω meson has relatively short life time (23 fm/c) which makes the high possibility of decaying in the medium. The Table 1.1 shows the status of the ω meson.

ω (782) meson	
Mass	$m = 782.65 \pm 0.12\text{MeV}$
Full width	$\Gamma = 8.49 \pm 0.08\text{MeV}$
Decay modes	$\pi^+\pi^-\pi^0$ (BR: $89.1 \pm 0.7\%$)
	$\pi^0\gamma$ (BR: $8.90 \pm 0.27 - 0.23\%$)
	\vdots
	e^+e^- (BR: $7.18 \pm 0.12 \times 10^{-5}$)
	\vdots

Table 1.1: The status of ω meson [20]

Many theories and simulation studies [51][52][53] pointed out that a promising approach to investigate in-medium modifications of the ω meson is to study the radiative decay mode ($\omega \rightarrow \pi^0\gamma$). We chose this decay mode being blessed with following essential advantages.

- clean way to investigate the properties (due to its electromagnetic coupling to the nucleons, the reaction probability of the photon is almost the same for all nucleons inside the nucleus)
- large branching ratio (about 3 orders of magnitude larger than e^+e^-)

- no ρ -contribution (since the $\rho \rightarrow \pi^0\gamma$ branching ratio (BR) is only 7×10^{-4} and therefore suppressed by 2 orders of magnitude relative to the ω BR into this channel)

The disadvantage of this decay mode is a possible π^0 -rescattering within the nuclear medium, which would distort the deduced ω invariant mass distribution. However, the distorted events are predicted to accumulate at ~ 500 MeV/ c^2 which is far below the nominal ω invariant mass. This leads to a small contributions of only about 3% in the mass range of interest, $0.6 \text{ GeV}/c^2 < M_{\pi^0\gamma} < 0.8 \text{ GeV}/c^2$ [51].

1.4.2 Baseline Results

Baseline measurements of the ω have been performed for $p+p$ via the leptonic channel [54, 7], and for the $p+p$ and d+Au via the hadronic channel [10, 55, 7]. The first publication of ω/π^0 ratio was found to be independent of transverse momentum and equal to $0.85 \pm 0.05(\text{stat}) \pm 0.09(\text{sys})$ in $p+p$ and $0.94 \pm 0.08(\text{stat}) \pm 0.12(\text{sys})$ in d + Au for $p_T > 2 \text{ GeV}/c$ [10]. The new values of ω/π^0 ratio in the recent publication show that $0.81 \pm 0.02(\text{stat}) \pm 0.09(\text{sys})$ in $p+p$ and $0.75 \pm 0.01(\text{stat}) \pm 0.08(\text{sys})$ in d + Au for $p_T > 2 \text{ GeV}/c$ [7], which are consistent within errors.

The ω measurements in the PHENIX collected in 2003-2008 are summarized in Table 1.2. The data were taken using a minimum bias trigger (MB) and the EMCal-RICH-Trigger (ERT): the ERT trigger was used for $p+p$, d+Au, and Cu+Cu data taking, which required the event to satisfy the MB trigger conditions and that there be at least one high- p_T electron or photon candidate to enhance the statistics at high p_T . The 2003 d + Au data were published in [10] and included here for comparison. The 2005 $p+p$ data were published in [54] and are used as the baseline of R_{AA} in d+Au, Cu+Cu and Au+Au. The recent published data of 2005 Cu+Cu and 2008 d+Au are also added in this work to show a comparison. Two Au + Au data samples were taken in 2004 and 2007, denoted as “Year 4” and “Year 7” respectively in the results. More information of the Au + Au data samples will be described in the Chapter 3.

Figure 1.11 presents the invariant transverse momentum spectra measured for the ω in $p+p$ and d + Au at $\sqrt{s}=200 \text{ GeV}$ [7]. Production of ω was measured in the two hadronic $\omega \rightarrow \pi^0\gamma$, $\omega \rightarrow \pi^0\pi^+\pi^-$ and the leptonic $\omega \rightarrow e^+e^-$ decay channel. Previously published results are shown with open

Table 1.2: Summary of the analyzed data samples and ω meson decay channels taken in the PHENIX.

Dataset	Sampled events	$\int Ldt$	Decay channel	Reference
2003 d + Au	5.5 B	2.74 nb ⁻¹	$\omega \rightarrow \pi^+\pi^-\pi^0$	[10]
			$\omega \rightarrow \pi^0\gamma$	[10]
2004 Au + Au	1.5 B	241 μb^{-1}	$\omega \rightarrow \pi^0\gamma$	this work
2005 $p + p$	85 B	3.78 pb ⁻¹	$\omega \rightarrow e^+e^-$	[54]
			$\omega \rightarrow \pi^+\pi^-\pi^0$	[54]
			$\omega \rightarrow \pi^0\gamma$	[54]
2005 Cu + Cu	8.6 B	3.06 pb ⁻¹	$\omega \rightarrow \pi^0\gamma$	[7]
			$\omega \rightarrow \pi^0\gamma$	[7]
2007 Au + Au	5.1 B	813 μb^{-1}	$\omega \rightarrow \pi^0\gamma$	this work
2008 d + Au	115 B	80 nb ⁻¹	$\omega \rightarrow e^+e^-$	[7]
			$\omega \rightarrow \pi^+\pi^-\pi^0$	[7]
			$\omega \rightarrow \pi^0\gamma$	[7]

markers [10]. A higher statistics data set in 2008 data allowed an increase in the number of centrality classes, extend p_T reach of measurements in the hadronic decay channels and measure ω production in the leptonic channel at low and intermediate p_T . Results for different decay channels and data samples agree within uncertainties in the overlap region. The dashed curves in Figure 1.11 are fixed on $p + p$ results at $p_T > 2$ GeV/ c using a Tsallis distribution [8] and then scaled by the number of binary nucleon-nucleon collisions (N_{coll}) estimated using Glauber Monte-Carlo simulation [31] for d + Au results. The Tsallis distribution including both of exponential and power law described the spectra over the wide p_T range obtained by both of the di-electron decay channel and the hadronic decay channels. As shown in Figure 1.11, Tsallis shows a good fit with ω spectra. The various spectra: $(\pi^+ + \pi^-)/2$, π^0 , $(K^+ + K^-)/2$, K_s^0 , η , ϕ and J/Ψ in $p + p$ collisions at $\sqrt{s} = 200$ GeV are also measured in the PHENIX [55, 56, 57, 58] and showed that Tsallis distribution had a good agreement [54, 59]. If the spectra of all measured mesons are normalized to π^0 at $p_T = 6$ GeV/ c , all spectra expressed pure power law function in $5.0 < p_T < 20$ GeV/ c [59], which is

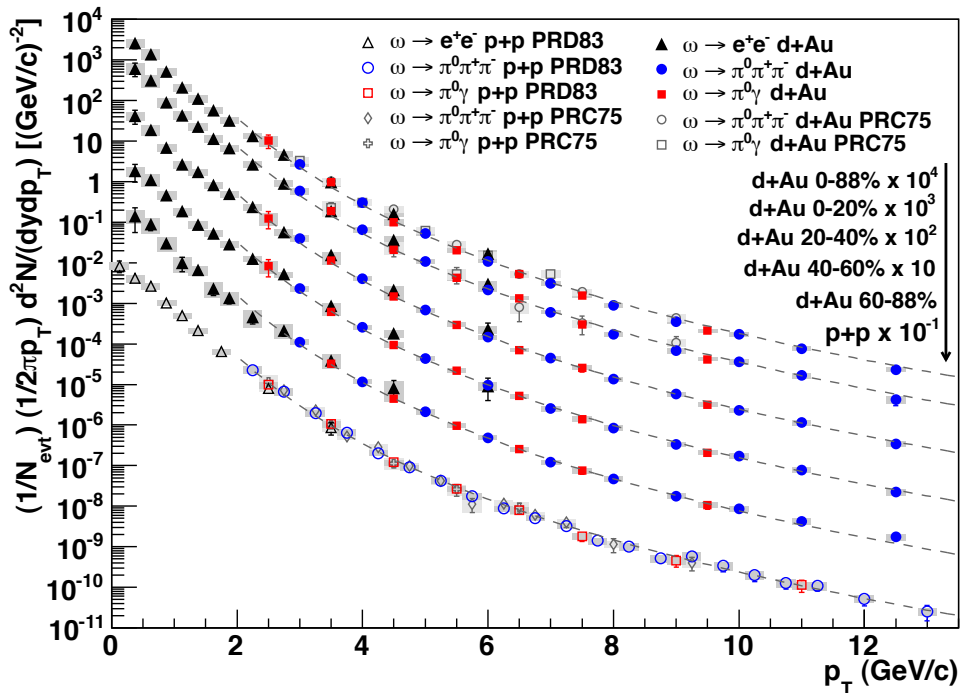


Figure 1.11: (Color online) Invariant transverse momentum spectra of ω production in $p + p$ and $d + Au$ collisions at $\sqrt{s}=200$ GeV [7]. The dashed lines represent fits to $p + p$ results by a Tsallis distribution [8] scaled by the corresponding number of binary collisions for $d + Au$.

consistent with pQCD picture: according to pQCD calculation, the power law behavior represented at high p_T region.

Measurement of ω production can be used to study the relative production of vector and pseudoscalar mesons consisting of the same valence quarks, i.e. ω/π ratio as a function of transverse momentum. In calculating the ω/π ratio the same methodology from [42, 5, 19] for the π^+/π^- and π^0 was used. The charged pion results, $(\pi^+ + \pi^-)/2$, were used to extend neutral pion measurements at the lower limit of the p_T domain from 1 to 0.2 GeV/c. To produce the average pion spectrum in $p + p$ [42] and $d + Au$ collisions [13], simultaneously fit $(\pi^+ + \pi^-)/2$ and π^0 spectra [60] with the modified

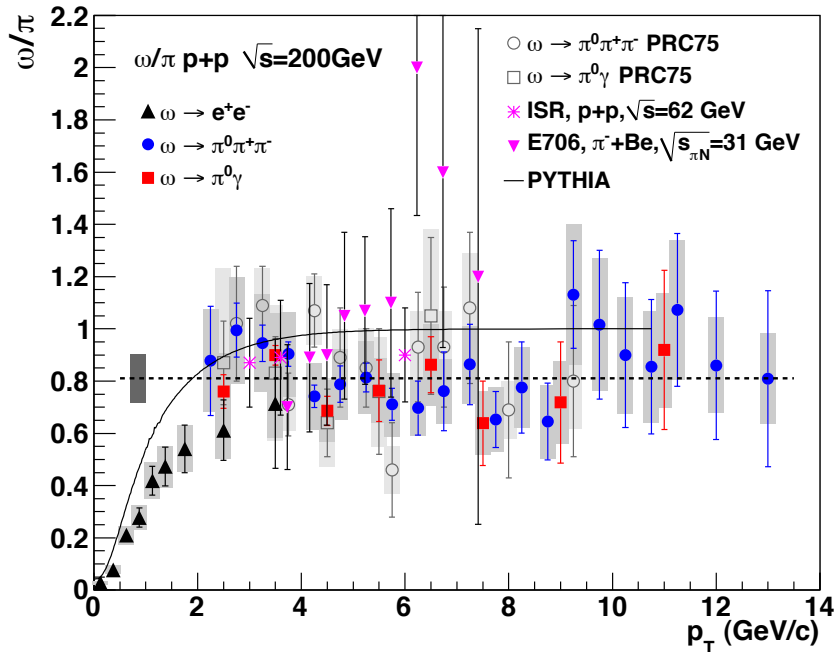


Figure 1.12: Measured ω/π ratio as a function of p_T in $p + p$ collisions at $\sqrt{s}=200$ GeV [7]. The dashed line shows a fit of constant value to data points at $p_T > 2$ GeV/c (Fit result: $0.81 \pm 0.02(\text{stat}) \pm 0.09(\text{sys})$). The box around the dashed line is overall error of the fitting. The solid line is the PYTHIA prediction [9] for $p + p$ at $\sqrt{s}=200$ GeV. Previously published results [10] and other lower energy experiments: the E706 experiment at $\sqrt{s_{\pi N}} = 31$ GeV [11] and the ISR experiment at $\sqrt{s} = 62$ GeV [12] are shown as a comparison.

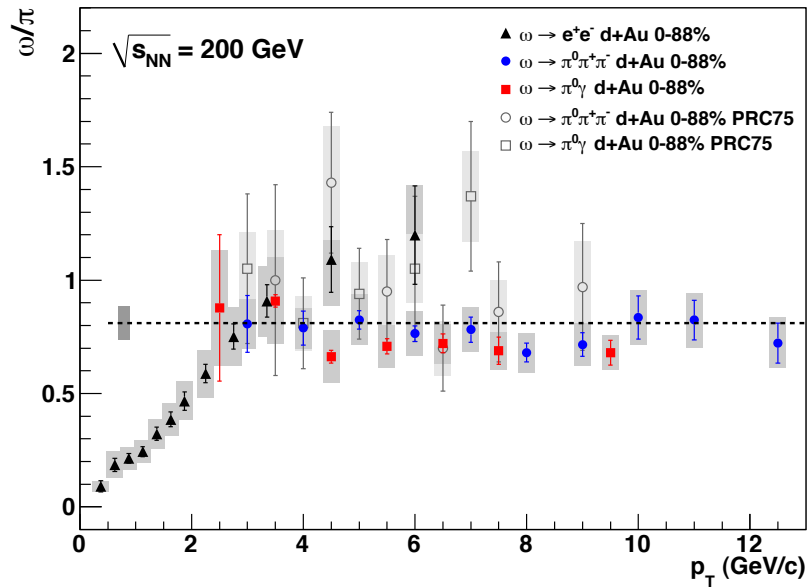
Hagedorn function [61] (Hagedorn function is the the QCD inspired formula which is widely used for fitting elsewhere [62, 63]). Inclusion of the charged pion spectrum in the fit has a small effect in the 1-2 GeV/c overlap region, and is smaller than 5%, compared to the fit result with neutral pions alone. The resulting fitted pion distributions are used to calculate ω/π ratios for $p + p$ and $d + \text{Au}$. Uncertainties for the fit values are evaluated by taking into account statistical and systematic uncertainties of the experimental points as described in [54, 64]. Figure 1.12 presents the ω/π ratio measured in $p + p$ collisions at $\sqrt{s}=200$ GeV as a function of transverse momentum [7].

Open markers show our previous measurements of the ω/π ratio [10]. One can see good agreement between previous results and this measurement. For completeness we also present similar measurements performed in lower energy experiments: $\pi + \text{Be}$ at $\sqrt{s_{NN}} = 31$ GeV (E706 [11]), $p + p$ at $\sqrt{s}=62$ GeV (ISR [12]). Please note that the branching ratio for the $\omega \rightarrow \pi^0\gamma$ decay was set equal to $(8.8\pm 0.5)\%$ that is 6% different from the latest PDG value of $(8.28\pm 0.28)\%$. Within measurement uncertainties the ω/π ratio in hadronic interactions is energy independent at high p_T .

A linear fit to the ratio at $p_T > 2$ GeV/ c gives a value of the linear coefficient consistent with zero within less than one standard deviation (-0.013 ± 0.009 (stat) ± 0.014 (sys)) indicating no significant p_T dependence of the ratio at $p_T > 2$ GeV/ c . A fit to a constant gives a value of the ratio equal to 0.81 ± 0.02 (stat) ± 0.09 (sys) consistent with our previous measurement of 0.85 ± 0.05 (stat) ± 0.09 (sys) [10]. The PYTHIA prediction of the ω/π ratio shown in Figure 1.12 with a solid line above the measured ratio.

The ω/π ratios measured in minimum bias d+Au collisions at $\sqrt{s_{NN}}=200$ GeV are presented in Figure 1.13 [7]. As in the case of $p + p$ collisions there is no indication that the ratios depend on transverse momentum for $p_T > 2$ GeV/ c . Fits to a constant for $p_T > 2$ GeV/ c give the following values of the ω/π ratio: 0.75 ± 0.01 (stat) ± 0.08 (sys) in d + Au collisions. Within the uncertainties the ω/π ratios measured in different collision systems for $p_T > 2$ GeV/ c are in agreement. This agrees with previous measurements in d+Au [10] within the uncertainties. The ratios in various collision systems assume similar suppression factors and p_T dependences within the uncertainties for the ω and π production in nucleus-nucleus collisions at high p_T .

Figure 1.14 presents R_{dAu} measured for ω in minimum bias, most central and peripheral d + Au collisions at $\sqrt{s_{NN}}=200$ GeV [7]. Good agreement is observed between different decay modes, between new and previously published PHENIX ω results [10] shown with open markers. For comparison we also present π^0 results published in [13] in the figure. In peripheral collisions the measured values of R_{dAu} are consistent with unity over the whole p_T range of measurements. In most central collisions a moderate Cronin-like enhancement is observed in a range of p_T from 2 GeV/ c to 6 GeV/ c and suppression of ω production at $p_T > 8$ GeV/ c . A similar enhancement at 2-6 GeV/ c was previously observed for neutral and charged pions [42, 13] and ϕ mesons [49]. Suppression of ω production at higher p_T is in agreement with π^0 results [13]. Similarity of the observed effects for the mesons with very different masses suggests that the collective nuclear effects occur at partonic



level [65, 66, 39].

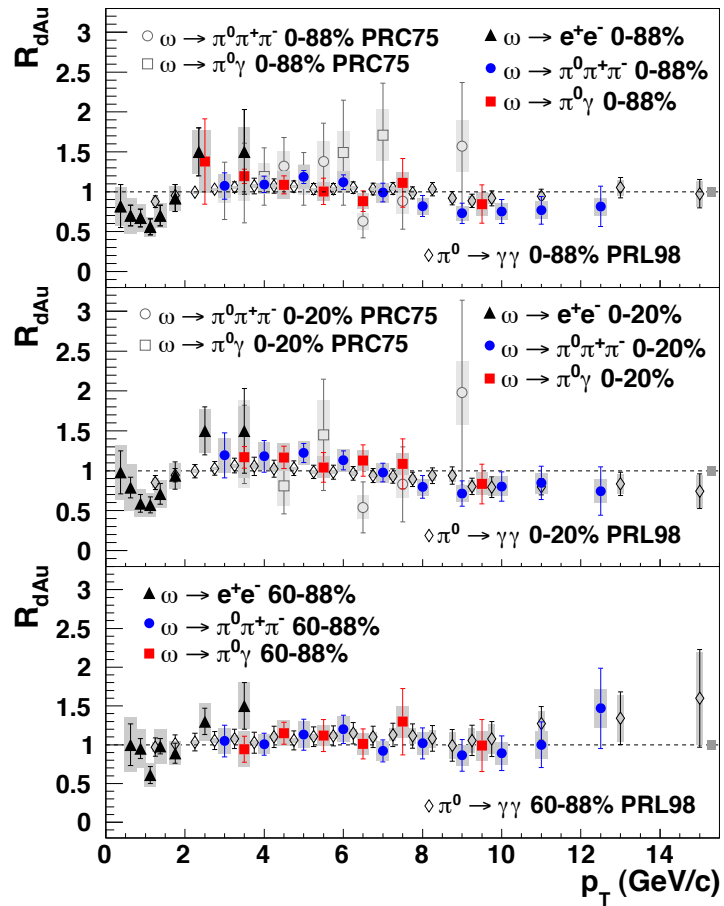


Figure 1.14: Nuclear modification factor, R_{dAu} , measured for ω in 0-88, 0-20, and 60-88% in d + Au collisions at $\sqrt{s}=200$ GeV [7]. The box at the right edge of the constant fit line shows the uncertainty of the fit. The previously published data of ω [10] and π^0 [13] shown for comparison.

1.4.3 Results from Other Experiments

Many ω meson measurements have been proceeded in past. The major was to perform for the in-medium modification study at low p_T physics by using dielectron decay mode ($\omega \rightarrow e^+e^-$) [67, 68, 69, 70]. The $\pi^0\gamma$ decay mode was used in the TAPS experiment as introduced follows.

CBELSA/TAPS Experiment

The photo-production of ω mesons on nuclei has been investigated in the Crystal Barrel/TAPS experiment at the ELSA tagged photon facility in Bonn [14]. Results obtained for Nb are compared to a reference measurement on a LH₂ target. While for recoiling, long-lived mesons (π^0, η and η'), which decay outside of the nucleus, a difference in the line shape for the two data samples is not observed. They find a significant enhancement towards lower masses for ω mesons produced on the Nb target (see the right plot in the Figure 1.15). For momenta less than 500 MeV/c an in-medium ω meson mass of $M_{medium} = [772_{-4}^{+4}(stat)_{35}^{+35}(sys)]$ MeV/c² has been deduced at an estimated average nuclear density of $0.6\rho_0$.

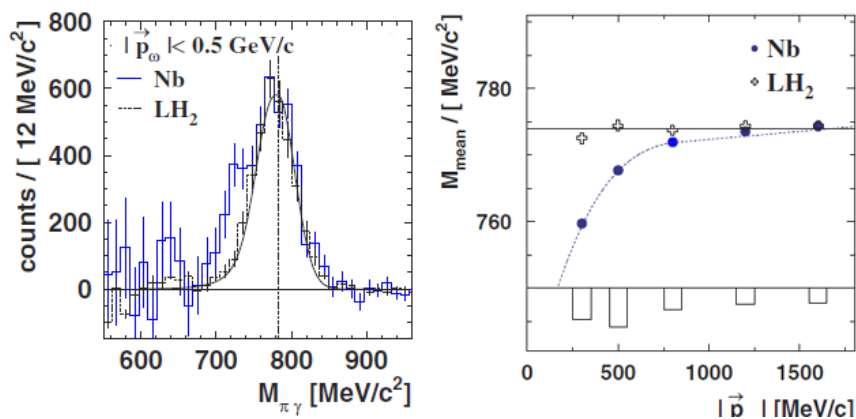


Figure 1.15: Left plot: $\pi^0\gamma$ invariant mass for the Nb data (solid histogram) and LH₂ data (dashed histogram) after background subtraction[14]. Right plot: Mean value of the $\pi^0\gamma$ invariant mass as a function of the ω momentum at an estimated average density of $0.6\rho_0$ for the Nb data (circles) and the LH₂ (crosses) along with a fit.

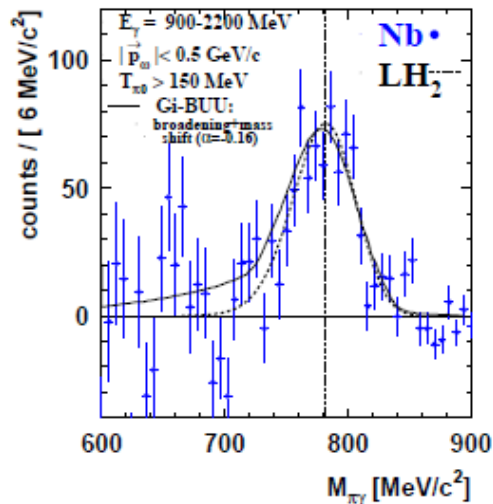


Figure 1.16: ω signal for the Nb target from reanalysis results (solid points) in comparison to the ω line shape measurement on a LH_2 target (dashed curve) and simulation (solid curve) assuming a mass shift by -16% at normal nuclear matter density.

After the first results publication [14], re-analysis was initiated since the extracted ω line shape was found to be sensitive to the background subtraction. The strong broadening of the ω meson in the nuclear medium due to inelastic processes - as determined in a transparency ratio measurement - suppresses contributions to the observed ω signal from the interior of the nucleus. The branching ratio for in-medium decays into the channel of interest is drastically reduced. Thereby, the sensitivity is shifted to the nuclear surface, making the line shape analysis less sensitive to a direct observation of in-medium modifications. Data with much higher statistics will be needed to gain further insight.

1.4.4 Aim of the Thesis

The aim of this thesis is to investigate the suppression pattern of the ω production expected in central Au + Au. If the suppression pattern of the ω is similar to those of π^0 and η , then we can conclude that the energy loss takes place before those particles are formed – at the parton level. However, if the suppression pattern of the ω differs to those of the other mesons, then the energy loss takes place after those particles are formed – at the hadron level. This decision is crucial for the evidence of the hot and dense medium formed in the collisions, i.e. the Quark-Gluon Plasma (QGP), since the former scenario would happen in the QGP but the latter scenario would happen not only in the QGP but also in the hadron gas.

The outline for the thesis is as follows: Chapter 2 gives a brief description of the experimental detector: Chapter 3 contains details of the analysis methods and techniques: in Chapter 4 we present and discuss the results: Finally, Chapter 5 provides the summary and conclusion of this work.

Chapter 2

Experimental Setup

We measured the nuclear collisions via the Pioneering High Energy Nuclear Interactions eXperiment (PHENIX) at the Relativistic Heavy Ion Collider (RHIC) at Brookhaven National Laboratory (BNL). The RHIC is a world-class scientific research facility that began operation in 2000, following 10 years of development and construction [1].

2.1 The RHIC

The process of accelerating an ion involves several accelerators that make up the RHIC complex. The Figure 2.1 shows the RHIC complex.

The ion beam starts its journey in the Tandem Van de Graaff. It consists of two electrostatic accelerators which is capable of producing voltage up to 15 million volts, sending them on their way towards the Booster. From the Tandem, the bunches of ions enter the Tandem-to-Booster beam-line, which carries them through a vacuum via a magnetic field to the Booster. At this point, they are traveling at about 5% the speed of light. Then the ions are provided with more energy at the Booster Accelerator with electromagnetic waves and they reach a speed of 37% that of light. As they whirl around the Alternating Gradient Synchrotron (AGS) and are accelerated as in the Booster, the ions get even more energy – until they are traveling at 99.7% the speed of light. When the ion beam is traveling at top speed in the AGS, it is taken down another beam line called the AGS-To-RHIC (ATR) transfer line. Once they reach the end of the ATR transfer line, the ions are divided into 2 bunches, traveling either clockwise or counterclockwise in the so-called *blue*

and *yellow* lines. From here on, the counter-rotating beams are accelerated, as in the Booster and AGS, and then circulate in RHIC.

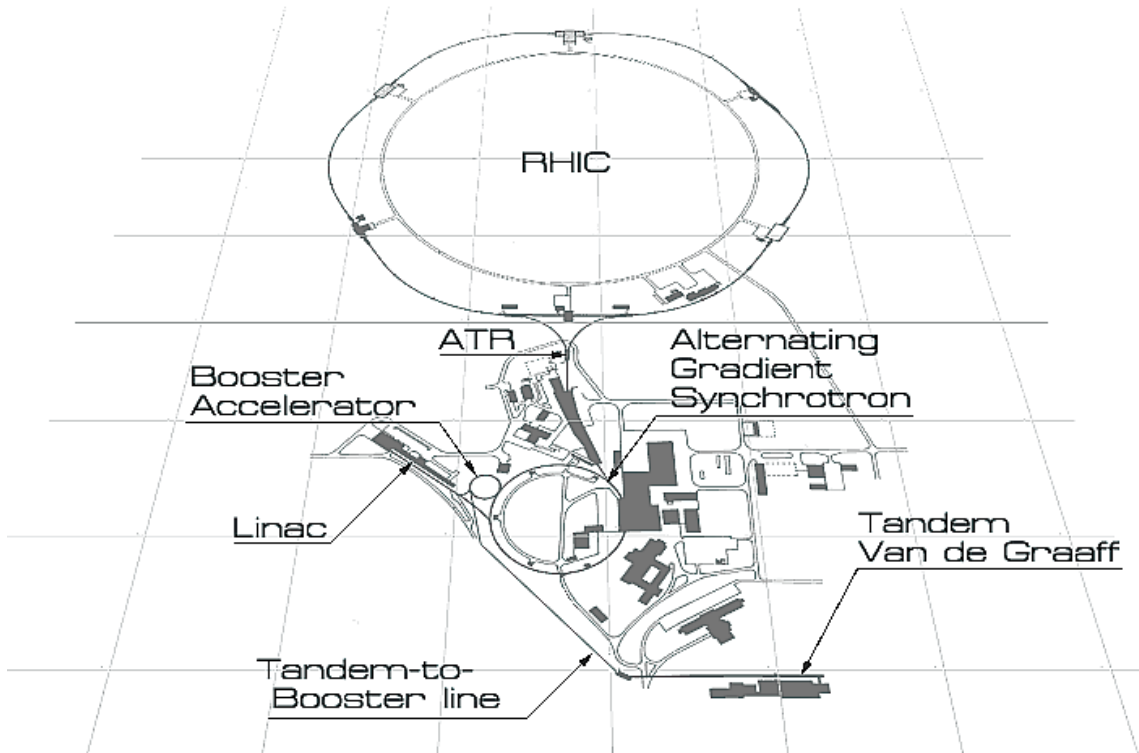


Figure 2.1: The RHIC complex.

The RHIC ring has a circumference of 3.8 km with the maximum bunch of 120 and the designed luminosity is $2 \times 10^{26} \text{cm}^{-2} \text{s}^{-2}$ for Au ion. The ring has six intersection points where its two rings of accelerating magnets cross, allowing the particle beams to collide. The Figure 2.2 shows its interaction points. If RHIC's ring is thought of a clock face, the four current experiments are at 6 o'clock (STAR [71]), 8 o'clock (PHENIX [72]), 10 o'clock (PHOBOS [73]) and 2 o'clock (BRAHMS [74]). There are two additional intersection points at 12 and 4 o'clock where future experiments may be placed.

The PHENIX is the largest of the four experiments where our analysis data is taken. The PHENIX is designed specifically to measure direct probes of the collisions such as electrons, muons, and photons by its multi purpose

detectors. In the subsequent sections we describe the PHENIX detector and its various detector components.

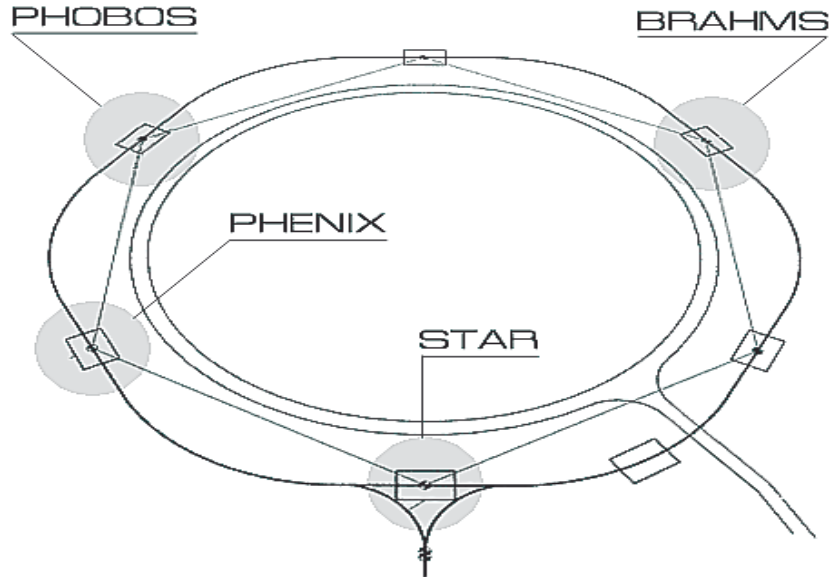


Figure 2.2: RHIC Beam Interaction Points.

2.2 The PHENIX Detector

The PHENIX experiment [72] is designed specifically to measure electromagnetic probes such as electrons, muons, and photons.

The detectors of the PHENIX can be grouped into three categories; inner detectors [75] closed to the beam pipe, two central arms [76] with pseudo-rapidity coverage of ± 0.35 , each covering 90 degrees in azimuthal and pseudo-rapidity coverage of $+(1.2-2.2)$ for the south muon arm and $-(1.2-2.4)$ for the north muon arm. The central arms are used to measure the ω mesons at mid-rapidity.

Two beams coming from the beam pipe will be made to collide at the center of the detector. Then inner detectors measure the start time, vertex and multiplicity of the interactions. Central arms are capable of measuring a variety of particles including pions, protons, kaons, deuterons, electron and

photons while muon arms focus on the measurement of muon particles. Those detectors are described in subsequent sections.

Beam view and side view of the PHENIX detector configurations are shown in Figure 2.3 for Run4 and in Figure 2.4 for Run7. Some detectors in inner part and a part of central arms were installed for Run7 which are described in the last section.

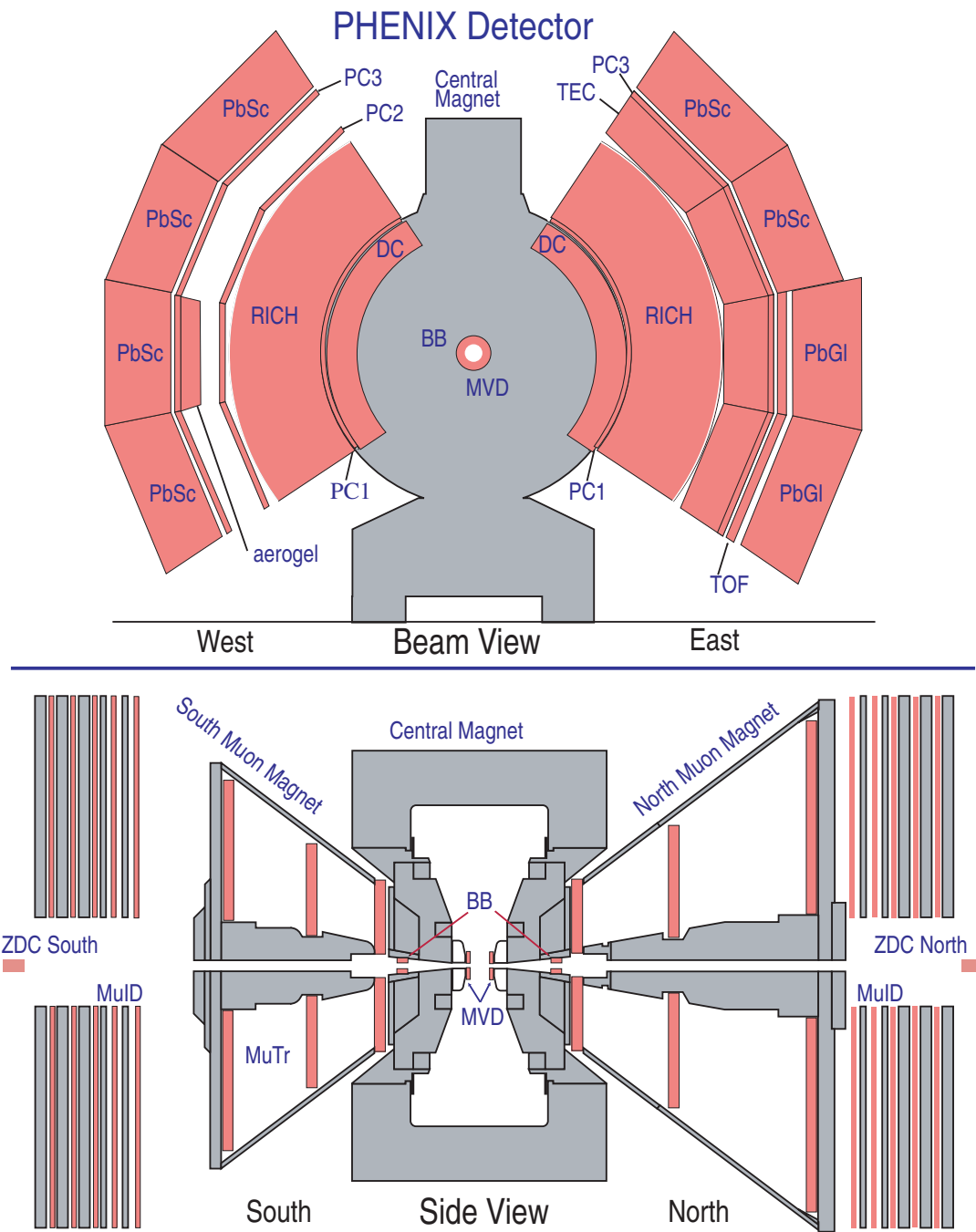


Figure 2.3: The PHENIX Detector configuration (2004).

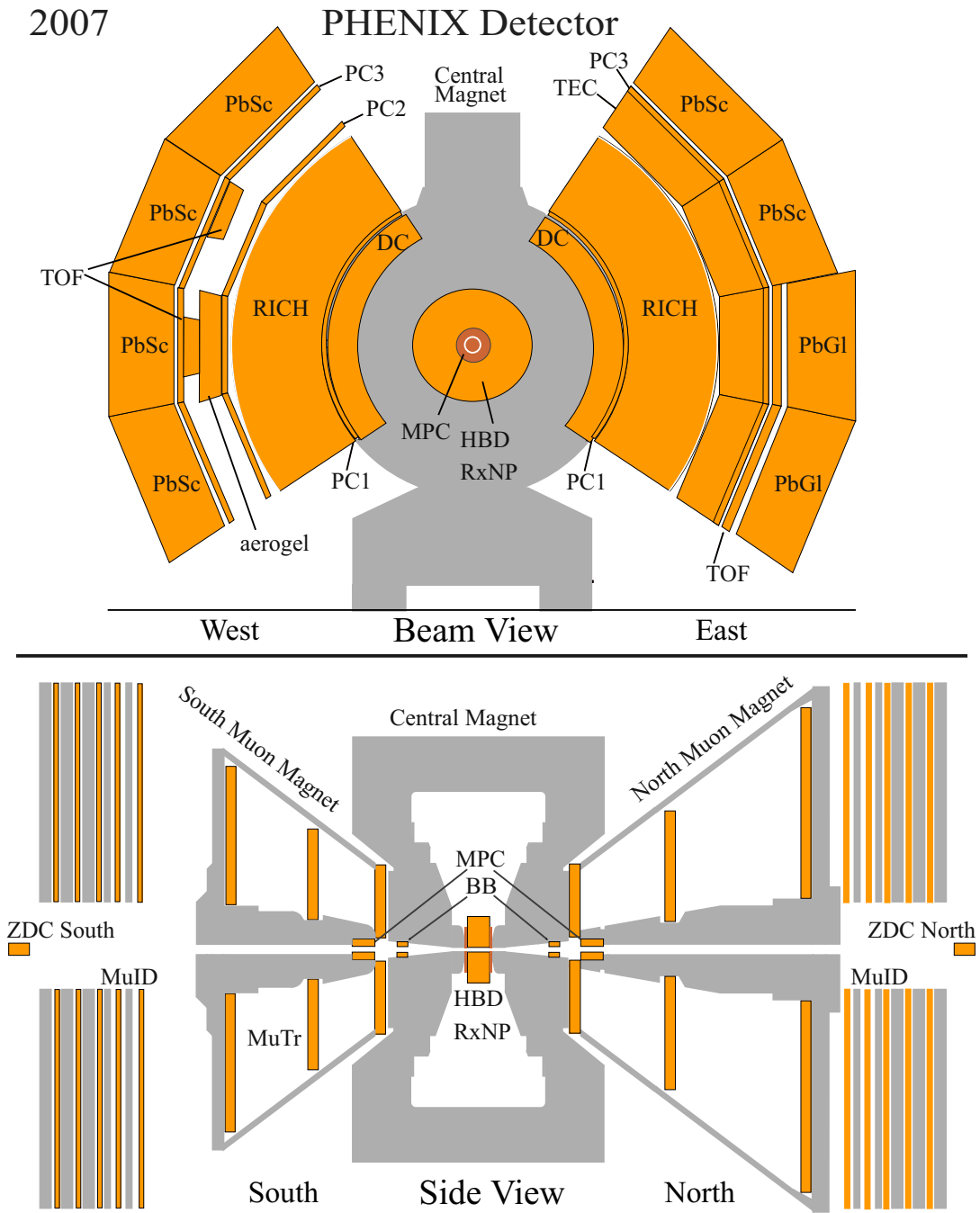


Figure 2.4: The PHENIX Detector configuration (2007).

2.2.1 The Inner Detectors

In order to characterize the collision event, the inner detectors [75] were installed. They consist of the Beam Beam Counters (BBCs), the Zero Degree Calorimeters (ZDCs) and the Multiplicity Vertex Detector (MVD).

The Beam Beam Counters (BBCs)

The Beam Beam Counters (BBCs) [75] have four major tasks: to measure the collision vertex, to produce a signal for the PHENIX trigger and to determine the centrality, the time of beam-beam collisions for the TOF (will be explained later) measurements and the reaction plane. The determination of the centrality and the reaction plane are discussed in the Section 3.2.

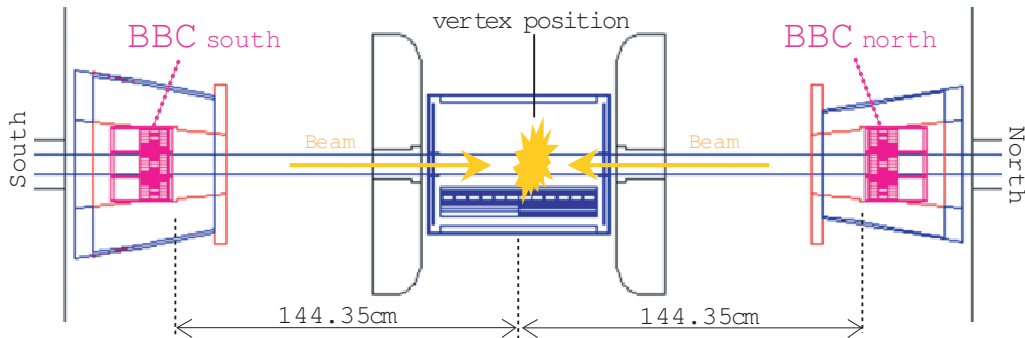


Figure 2.5: The position of BBC. The BBCs are placed 144 cm from the center of the interaction diamond and surround the beam pipe. Assume the arrival times of leading charged particles from beam collisions to each BBC south and north as T_S and T_N . So then the vertex position is $(T_S - T_N)/2 \times c$ and the vertex time is $(T_S - T_N - 144.35 \times 2/c)/2$.

The BBC consists of two identical sets of counters installed on both sides of the collision point along the beam axis, the one on the North side and the other on the South side of the PHENIX coordinate system. The Figure 2.5 shows the position of BBC and the way to measure the vertex position and the vertex time. The single BBC consisting of one-inch mesh dynode photomultiplier tubes mounted on a 3 cm quartz radiator. And it is comprising 64 BBC elements. The interaction position along the beam axis is calculated from individual time measurements of fast leading particles hitting BBC on the both sides of the interaction point. With an intrinsic timing resolution of 70 ps, BBC determines the interaction position with a precision of 0.6 cm.

The Zero Degree Calorimeters (ZDCs)

The Zero Degree Calorimeters (ZDC) [77] are hadron calorimeter standard to all four experiments at RHIC. The two ZDCs are located at 18 m north and south from the nominal collision point. Since both north and south ZDC sit at just the upstream of the last bending magnet on the RHIC ring, most of the charged particles are swept out from the acceptance. So then the ZDC measures the beam energy neutrons emitted in the breakup of the nuclear remnant that misses the interaction zone. The calorimeters are also the principle device to monitor the beam luminosity during the run and serves as an event trigger for all four RHIC experiments.

The Multiplicity Vertex Detector (MVD)

The Multiplicity Vertex Detector (MVD) [75] provides a more precise determination of event position and multiplicity and measures fluctuations of the charged particle distributions. It is composed of concentric barrels of silicon-strip detectors around the beam pipe and two disk-shaped end-caps of silicon pad detectors at $z \cong \pm 35$ cm, where z refers to the beam axis. The length of the active part of the silicon strip barrels is approximately 64 cm. The design criteria included large rapidity and good azimuthal coverage and granularity while also minimizing costs and material in the electron arm acceptance.

2.2.2 The Muon Arm Detectors

A pair of forward spectrometers were set for the purpose of measuring muons. Each muon spectrometer has a large geometric acceptance of about one steradian and excellent momentum resolution and muon identification.

The Muon Tracker

The Muon Tracker (MuTr) [78] consists of three stations of multi-plane drift chambers that provide precision tracking. Each of the three stations of cathode strip chambers presents unique design requirements. All are in the shape of octants built with a 3.175 mm half gap, 5 mm cathode strips and with alternate strips readout. The above design specifications led to the relative mass resolution, approximately given by $\sigma(M)/M = 6\%/\sqrt{M}$, where M is in GeV. This mass resolution enables a clear separation of the ρ/ω peak from the ϕ , J/ψ and ψ' , with an acceptable separation of Υ and Υ' .

The Muon Identifier

The Muon Identifier (MuID) [78] consists of alternating layers of steel absorbers and low resolution tracking layers of streamer tubes. There are six such panels per gap arranged around the square hole left for the beam pipe to pass through. The MuID design and the algorithms are used to reject the large hadron background from muon. The design goal of a pion rejection rate is about 2.0×10^{-4} and it is consistent with the result from a simulation [78].

2.2.3 The Central Arm Detectors

The central arm is equipped with detectors for electron, hadron and photon measurements. The separation of negative and positive tracks are done by applying a magnetic field from the Central Magnet. The tracking system uses three sets of the Pad Chamber to provide precise three-dimensional space points needed for pattern recognition. The precise projective tracking of the Drift Chamber is the basis of the excellent momentum resolution. The Time Expansion Chamber in the east arm provides additional tracking and particle identification. The Time-of-Flight and the Ring Imaging Čerenkov detectors also provide particle identification. The Aerogel Čerenkov Counter enhances

the particle identification capability. The Electro Magnetic Calorimeter described in the subsequent section is the outermost subsystem on the central arms and provides measurements of both photons and energetic electrons.

The Central Magnet

The Central Magnet [79] is energized by two pairs of concentric coils, which can be run separately, together or in opposition. The Figure 2.6 shows the field lines when both coils are turned on. It provides a field around the interaction vertex that is parallel to the beam. This allows momentum analysis of charged particles in the polar angle range from 70° to 110° .

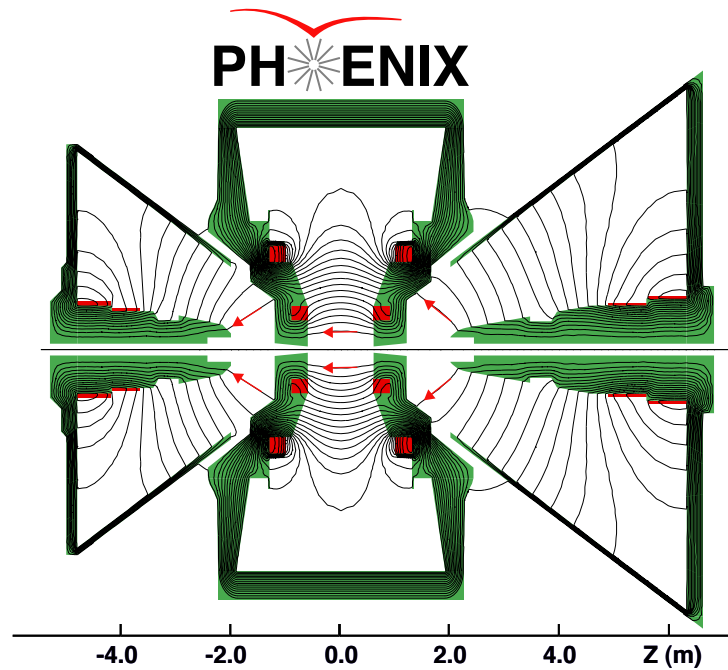
The Pad Chamber

The Pad Chambers (PC) [76] are multi-wire proportional chambers that form three separate layers of the PHENIX central tracking system. Each detector contains a single plane of wires inside a gas volume bounded by two cathode planes. One cathode is finely segmented into an array of pixels. The charge induced on a number of pixels when a charged particle starts an avalanche on an anode wire, is read out through specially designed readout electronics. There are three sets of Pad Chambers instrumented in the PHENIX, called PC1, PC2 and PC3. The PC1 is located immediately behind the Drift Chambers (DC). The PC2 in the west arm is behind the Ring Imaging Čerenkov (RICH) and the PC3 in both arms are in front of the Electromagnetic Calorimeter (EMCal). The Figure 2.3 shows the location.

The PCs are the only non-projective detectors in the central tracking system and thus are critical elements of the pattern recognition. Its information is also essential for particle identification, particularly for critical electron identification which has to have a hadron rejection factor of 10^4 . The DC and PC1 information gives direction vectors through the RICH, while PC2 and PC3 are needed to resolve ambiguities in the outer detectors where about 30% of the particle striking the EMCal are produced by either secondary interactions and particle decays outside the aperture of the DC.

The Drift Chamber

The Drift Chambers (DC) [76] are cylindrically shaped and located in the region from 2 to 2.4 m from the beam axis and 2 m along the beam direction shown in the Figure 2.3. Each DC measures charged particle trajectories to



Magnetic field lines for the two Central Magnet coils in combined (++) mode

Figure 2.6: PHENIX central magnet field lines.

determine p_T of each particle and ultimately, the invariant mass of particle pairs. The DC also participates in the pattern recognition at high particle track densities by providing position information that is used to link tracks through the various PHENIX detector sub-systems.

The Time Expansion Chamber

The Time Expansion Chamber (TEC) [76] is composed of a set of 24 large multi-wire tracking chambers and it resides in the East arm. The TEC measures all charged particles passing through its active area, providing direction vectors that are matched to additional track information from the DC's and PC's. It also enhances the momentum resolution at $p_T \geq 4$ GeV/c by combining with the DC to provide a long lever arm for improved track-angle resolution.

The Time-of-Flight

The Time-of-Flight (ToF) [80] system serves as a primary particle identification device for charged hadrons in the PHENIX. It is designed to have about 100 ps timing resolution in order to achieve clear particle separation in the high momentum region, i.e. π/K separation up to 2.4 GeV/ c and K/proton separation up to 4.0 GeV/ c . The ToF detector is placed at a distance of 5.1 m from the collision vertex, in between the PC3 and the EMCal in the East arm. It consists of 10 panels of ToF walls. One ToF wall consists of 96 segments, each equipped with a plastic scintillator slat and photomultiplier tubes which are read out at both ends.

The Ring Imaging Čerenkov

The Ring Imaging Čerenkov (RHIC) [80] is one of the primary devices for separation of electrons from the large numbers of the more copiously produced pions, that provides e/π discrimination below the π Čerenkov threshold which is set at about 4 GeV/ c . In combination with the EMCal in each arm and the TEC in one arm, the goal is to limit the false identification of hadrons as e^+ and e^- to less than 1 per 10^4 , for momenta below the Čerenkov threshold.

The RICH is located between the inner and outer tracking units. The location can be seen in the Figure 2.3. Each RICH detector has a volume of 40 m³ and contains 48 composite mirror panels forming two intersecting spherical surfaces, with a total reflecting area of 20 m². The spherical mirrors focus Čerenkov light onto two arrays of 1280 UV photomultiplier tubes.

The Aerogel Čerenkov Counter

The Aerogel Čerenkov Counter (AEROGEL) is the additional particle identification to cover gaps in the particle identification by TOF and RICH. The hadron particle identification can be achieved seamlessly up to $p_T \sim 8$ GeV/ c . Also, the AEROGEL system has excellent trigger capability for high p_T particles.

The detector is located between the PC2 and PC3 in the West arm (shown in the Figure 2.3). It consists of 160 boxes and each box has aerogel with a refractive index of $n = 1.0114$, the best index for a combination with RICH.

2.2.4 The Electro Magnetic Calorimeter

The Electro Magnetic Calorimeter (EMCal) [15] is used to measure the spatial position and energy of electrons and photons produced in heavy ion collisions. It covers the full central spectrometer acceptance of $70^\circ \leq \theta \leq 110^\circ$ with two walls, each subtending 90° in azimuth. The one wall comprises four sectors of a Lead Scintillator Calorimeter (PbSc) and the other has two sectors of the PbSc and two sectors of a Lead Glass Calorimeter (PbGl). The Figure 2.3 shows the location. Both detectors have very good energy, spatial and timing resolution; the PbSc excels in timing and the PbGl in energy measurements. We will describe them separately since their design and the properties are quite different. After that, the Cluster Algorithm which is used for precise particle identification will be explained.

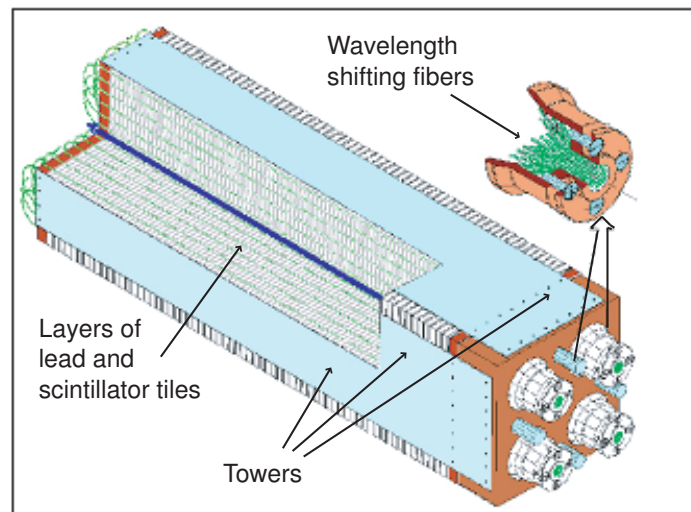


Figure 2.7: Interior view of PbSc module.

The Lead Scintillator Calorimeter (PbSc)

The Lead Scintillator Calorimeter (PbSc) is a shashlik type sampling calorimeter made of alternating tiles of Pb and scintillator consisting of 15552 individual towers and covering an area of approximately 48 m^2 . The basic building

block is a module consisting of four (optically isolated) towers which are read out individually. Four towers are mechanically grouped together into a single structural entity called a “module” as shown in the Figure 2.7. 36 modules are attached to a backbone and held together by welded stainless steel skins on the outside to form a rigid structure called a “supermodule”. 18 supermodules make a “sector”, a 2×4 m² plane with its own rigid steel frame.

The PbSc has a nominal energy resolution as,

$$\sigma_E/E = 2.1\% \oplus \frac{8.1\%}{\sqrt{E(\text{GeV})}},$$

where \oplus denotes a root of the quadratic sum, $\alpha \oplus \beta = \sqrt{\alpha^2 + \beta^2}$, and a position resolution as [81],

$$\sigma_x(E) = 1.4(\text{mm}) + \frac{5.9(\text{mm})}{\sqrt{E(\text{GeV})}}.$$

Intrinsic timing resolution is better than 200 ps for electromagnetic showers.

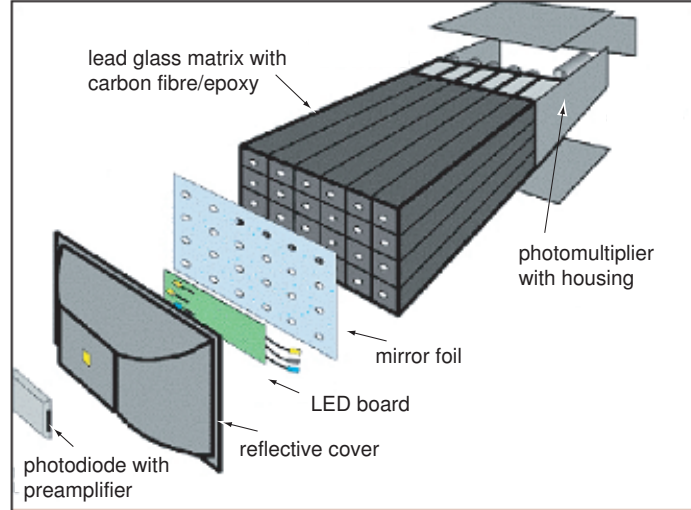


Figure 2.8: Exploded view of a PbGl supermodule(SM).

The Lead Glass Calorimeter (PbGl)

The Lead Glass Calorimeter (PbGl) is a Cherenkov type calorimeter, which occupies the two lower sectors of the East arm. Each PbGl sector comprises 192 supermodules (SM) in an array of 16 Lead Glass SM wide by 12 SM high as shown in the Figure 2.8. Each PbGl SM comprises 24 PbGl modules in a array of 6 PbGl modules wide by 4 modules high. Modules within the SM are individually wrapped with aluminized mylar foil and shrink tube and isolated optically. Steel sheets of 0.5mm thickness are used to house the entire towers and phototubes.

The PbGl has a nominal energy resolution as,

$$\sigma_E/E = [0.8 \pm 0.1]\% \oplus \frac{[5.9 \pm 0.1]\%}{\sqrt{E(\text{GeV})}}.$$

The measured position resolution is,

$$\sigma_x(E) = [0.2 \pm 0.1](\text{mm}) \oplus \frac{[8.4 \pm 0.3](\text{mm})}{\sqrt{E(\text{GeV})}}.$$

Intrinsic timing resolution is better than 300 ps for electromagnetic showers above the minimum ionizing peak energy.

The Cluster Algorithm

Since electromagnetic and hadronic particles produce quite different patterns of energy sharing between calorimeter towers, second moments of the measured showers are often used to differentiate between them. The first step in the calibration for the EMCal data is the conversion of the raw module information into energy and timing information, referred to as “calibrated towers”. Because an electromagnetic shower usually spreads over more than one module, this calibrated towers are passed the Cluster Algorithm, which summarizes associated areas of towers into the so-called “clusters”. The Cluster Algorithm can be divided into the following steps [21]:

- Find a cluster, which is a group of adjacent towers each with an energy above the noise threshold (see the Table 2.1).
- Find the local maxima of the cluster. A local maximum is a module above the peak threshold, given in the Table 2.1, with the maximum amplitude in the 3×3 region surrounding it.

- If more than one local maximum is found, split the cluster according to amplitude and positions of the maxima.
- Calculate the first and second moments of the clusters as the seed for the determination of the impact position.
- Compare the shape of the cluster with the expectation for an electromagnetic shower for particle identification (χ^2 method described next).
- Compute and correct the total energy for the cluster.

For each cluster the newly computed values such as corrected energy and position are stored in a list of clusters that can be used in the analysis.

	PbSc	PbGl
Minimum tower energy	10MeV	14MeV
Minimum cluster energy	15MeV	60MeV
Minimum peak energy	80MeV	80MeV

Table 2.1: The parameters of energy used by the Cluster Algorithm [21]

The one of the corrected energy, “ E_{core} ” are used for the photon analysis. Assume that there is a cluster from photon; it hits one tower, E5 and spreads out 3×3 towers from E1 to E9 but mainly deposited energy at E2, E4, E5, E6 and E8 shown as the Figure 2.2.4.

The E_{core} energy is defined as [81],

$$E_{core} = \sum_i^{core} E_i^{meas},$$

where E_i^{meas} is the measured energy in i -th tower. \sum_i^{core} is defined as summing of the towers belonging to the “core” towers. The “core” towers are defined in the following condition:

$$\frac{E_i^{pred}}{E_{all}^{meas}} > 0.02, \quad E_{all}^{meas} = \sum_i^{all} E_i^{meas},$$

where E_{all}^{meas} is the sum of measured energy in all towers belonging to the “peak area” cluster E_i^{pred} is the predicted energy (using the parametrization

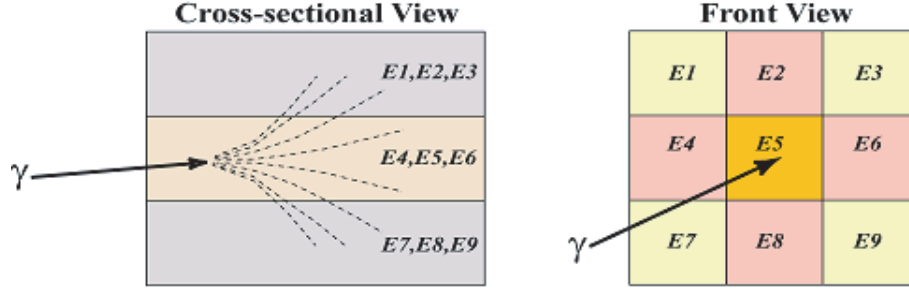


Figure 2.9: Cross-sectional and front view of cluster schematics.

and the actual measured impact point) for an electromagnetic particle of E_{all}^{meas} .

In above case, $E1+E2+\dots+E9$ corresponds to E_{all}^{meas} and if mainly deposited energy passed the “core” condition, E_{core} would be $E2 + E4 + E5 + E6 + E8$. So then E_{core} can chose the energy from highly identified as photon.

Not only for photons but also electrons to be identified, χ^2 method was introduced as:

$$\chi^2 = \sum_i \frac{(E_i^{pred} - E_i^{meas})^2}{\sigma_i^2}$$

where E_i^{meas} and E_i^{pred} are same value defined previously. The variance σ_i is given as,

$$\sigma_i^2 = q(E) + C \cdot E_i^{pred} \cdot \left(1 + a_1 \cdot \frac{E_i^{pred}}{E} + a_2 \cdot \left(\frac{E_i}{E} \right)^2 + f(E, \theta) \cdot \left(1 - \frac{E_i^{pred}}{E} \right) \right),$$

which provides the dependence of the fluctuations on the energy and angle of incidence, $f(E, \theta)$, and on losses to the total energy due to the thresholds used in the clustering, $q(E)$. This χ^2 value characterizes how “electromagnetic” a particular shower is and can be used to discriminate against hadrons. The important new feature of this model is that the fluctuations are also parameterized. Therefore, the resulting χ^2 distribution is close to the theoretical one and it is nearly independent of the energy or the impact angle of the electron. The χ^2 distributions for 2 GeV/c electrons and pions (with energy deposit above minimum ionization) are shown in the Figure 2.2.4. The arrow marks the χ^2 cut corresponding to 90% electron efficiency [15].

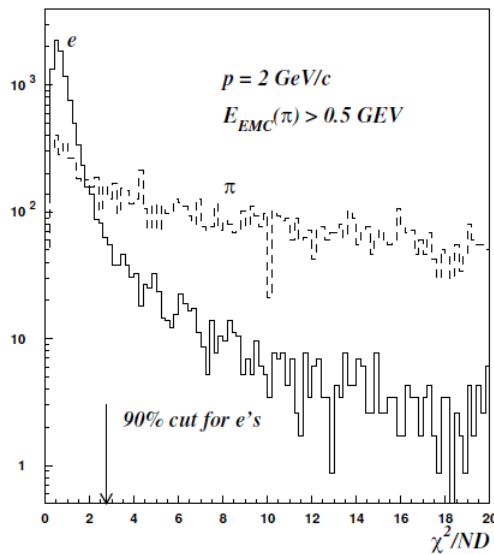


Figure 2.10: χ^2 distribution for showers induced by 2 GeV/ c electrons and pions in the PbSc calorimeter [15].

2.2.5 The Hadron Blind Detector

Between Run4 and Run7, four detectors were installed; the Reaction Plane Detector (RXNP), the Muon Piston Calorimeter (MPC)-North, the Time Of Flight (TOF)-West and the Hadron Blind Detector (HBD). Only the HBD detector is described in here since we included its influence in systematic errors, though we did not use it for analysis.

The Hadron Blind Detector

The HBD [82] is a Čerenkov detector. Its primary aim is to recognize and reject tracks originating from π^0 Dalitz decays and γ -conversions, thus allowing to measure low mass electron-positron pairs produced in central Au + Au collisions. The main idea is to exploit the fact that the opening angle of electron pairs from these sources is field-free region, where the pair opening angle is preserved. The field free region is created by the inner coil installed in the central arm of the PHENIX (the position can be seen in the overview section).

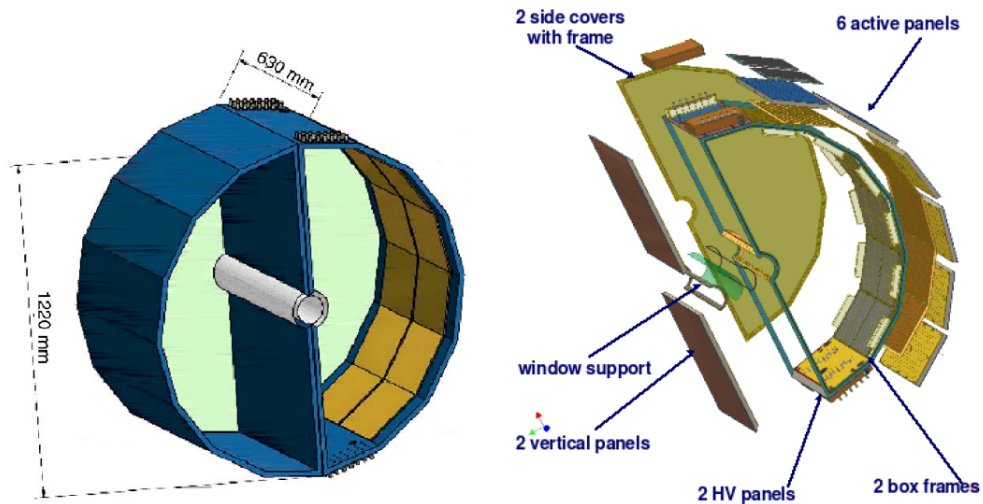


Figure 2.11: Design of the HBD [16]. Left: 3D view of the HBD final design. Right: an exploded view of one HBD vessel showing the main elements.

The HBD made backgrounds from γ -conversion to the photon analysis. The effect will be estimated in the analysis section.

2.3 Computing

In RHIC, collisions occur at about 10 kHz for Au + Au, while the beam crossing rate occurs at 9.6 MHz. These data need to be selected and archived in order to optimize the physics interest of the PHENIX. In this section, we are going to overview the system of the PHENIX On-Line System [83] which is designed to seamlessly accommodate improvements in the design luminosity. Furthermore, the PHENIX's general analysis system will be roughly described.

The On-Line system has two levels of triggering, denoted as Level-1 (LVL1) and Level-2 (LVL2). The LVL1 trigger operates in a synchronous pipelined mode, generates a decision every 106 ns and has an adjustable latency of some 40 beam crossings. It consists of two separate subsystems, the Local Level-1 (LL1) system which communicates directly with participating detector system such as BBC, MuID, ZDC, EMCAL and RICH and the Global Level-1 (GL1) which receives and combines these data to provide a trigger

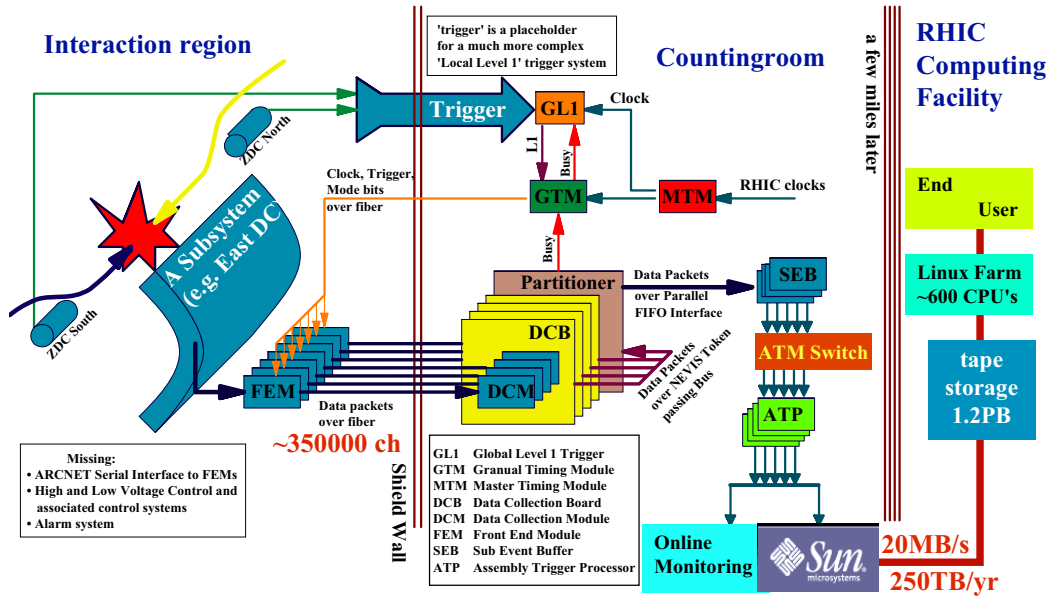


Figure 2.12: Schematic diagram of the PHENIX On-Line system.

decision. The LVL1 trigger and lower levels of the readout are clock-driven by bunch-crossing signals from the RHIC clock. The higher levels of readout and the LVL2 trigger are data-driven where the results of triggering and data processing propagate to the next higher level only after processing of a given event is completed.

The data collection and storage can be described in the Figure 2.3. Signals from the various PHENIX subsystems (e.g. the DC in the Figure 2.3) are processed by Front End Electronics (FEE) which are fed into Front End Modules (FEM) for each subsystems, that convert detector signals into digital event fragments. This involves analog signal processing with amplification and shaping to extract the optimum time and/or amplitude information, development of trigger input data and buffering to allow time for data processing by the LVL1 trigger and digitization. This is carried out for all detector elements at every beam crossing synchronously with the RHIC beam clock. The timing signal is a harmonic of the RHIC beam clock and is distributed to the FEM's by the PHENIX Master Timing System (MTS) which are fed

into the Master Timing Modules (MTM). The LVL1 trigger provides a fast filter for discarding empty beam crossings and uninteresting events before the data is fully digitized. If the LVL1 trigger accepts an event, a signal is transmitted to the Granule Timing Module (GTM) which generates an accept signal that is transmitted to the detector FEM's in the Interaction Region (IR).

Once an event is accepted, the data fragments from the FEM's and primitives from the LVL1 trigger move in parallel to the Data Collection Modules (DCM). The PHENIX architecture was designed so that all detector-specific electronics end with the FEM's, so that there is a single set of DCM's that communicate with the rest of the DAQ system. The only connection between the Interaction Region (IR) where the FEM's are located and the Counting House (CH) where the DCM's are located is by fiber-optic cable. The DCM's perform zero suppression, error checking and data reformation. Many parallel data streams from the DCM's are sent to the Event Builder (EvB). The EvB assembles a full event from the individual fragments of data from the DCM's. When the event is fully assembled and passed the LVL2 trigger, it is temporarily stored on a local disk. A fraction of the events are made available to processes on a farm of computer's running Linux for On-Line monitoring purposes. Long-term storage is provided by a High Performance Storage System (HPSS) type robot system operated by the RHIC Computing Facility (RCF). The average rate of transfer of data to HPSS is 20 Mbytes/s but for short time intervals rates as high as 60 Mbytes/s have been obtained.

Chapter 3

Analysis

3.1 Overview

In this chapter, we will describe analysis details in the following seven sections. Section 3.2 shows the data set used for this analysis. Section 3.3 describes the simulation study. In Section 3.4 we discuss the main source of the backgrounds in this analysis, then we explain the method of yield extraction in Section 3.5. Section 3.6 shows the reconstructed mass spectra. Section 3.7 describes the mathematical formula and corrections applied to the raw data. At last, in Section 3.8, we describe the systematic uncertainties in the measurement.

3.2 Event and Signal Selection

The data of Au + Au collisions at C.M.S. collision energy per nucleon pairs of 200 GeV is taken twice in the PHENIX, 2004 and 2007, each period is called “Run4 (sometimes denoted as ‘Year 4’)” and “Run7 (Year 7)”, respectively. The Figure 3.1 and 3.2 show the integrated luminosity taken in the PHENIX during Run4 and Run7. The total luminosity taken in Run4 is $241 \mu\text{b}^{-1}$ in minimum bias. Three years later, $813 \mu\text{b}^{-1}$ was accumulated in Run7 which corresponds to about 3.4 times larger statistics than Run4.

The trigger configuration and general event cuts are described in the subsection 3.2.1. Cuts for signal selection are described in the subsection 3.2.2. Cuts for π^0 candidates and parameterization of mean and width for π^0 are shown in the subsection 3.2.3. Lastly, kinematical cuts which is optimized

for reconstructing $\pi^0\gamma$ are shown in the subsection 3.2.4.

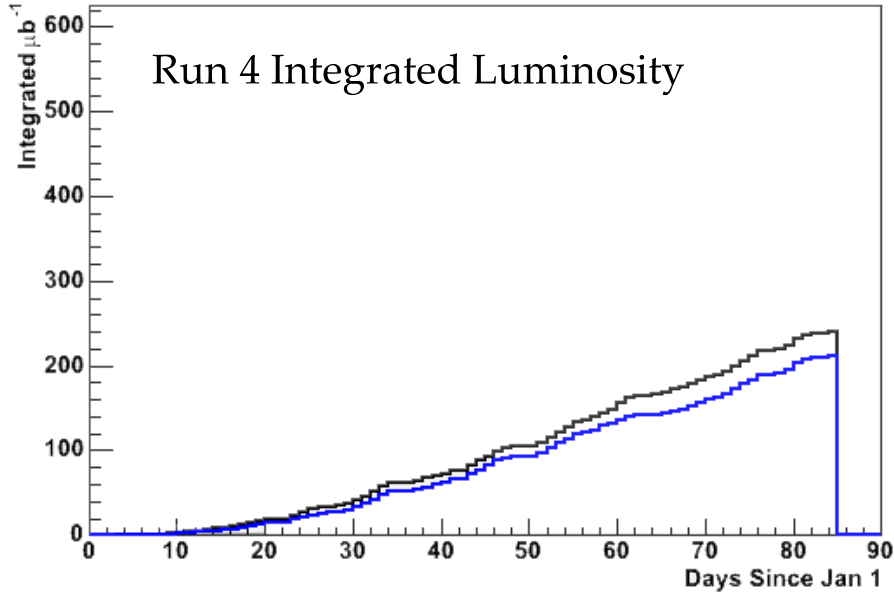


Figure 3.1: The Integrated Luminosity vs Weeks into the Run in Run4 [17]. The black line is the recorded minimum bias and the blue line is the recorded with Muon active.

3.2.1 Trigger

Minimum Bias Trigger

The condition for accepting an inelastic Au + Au reaction is given by the BBC and the ZDC. The collision has to trigger at least two photomultipliers at a time in both BBCs and cause a signal in both ZDCs. In Run4 dataset, the minimum bias trigger is defined as the logical AND(&&) of a coincidence between the north and south BBC, as well as the north and south ZDC while Run7 dataset only requires a coincidence between the north and south BBC. This trigger accepts 92% of the geometrical cross section for Au + Au collisions.

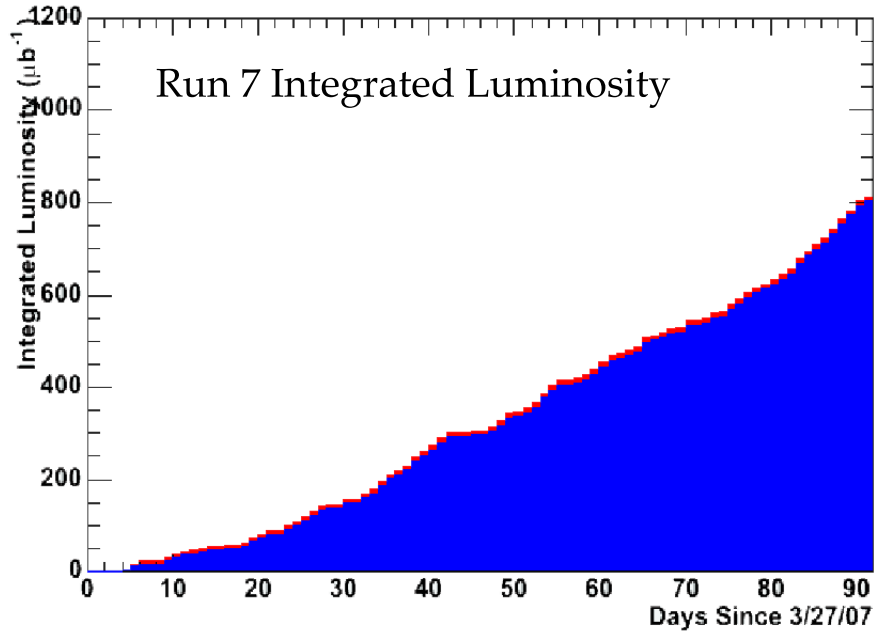


Figure 3.2: The Integrated Luminosity vs Weeks into the Run in Run7 [18]. The total Integrated luminosity (blue filled region) is $813 \mu\text{b}^{-1}$ corresponds to 5.12 Billion minimum bias events, which is about 3.4 times bigger than Run4 integrated luminosity.

BBC Vertex Cuts

We require that the z vertex (determined by BBC) of a given event lies within the range as,

$$\sqrt{|z|} < 30 \text{ cm},$$

in order to exclude regions that are shadowed by the pole tips of the central magnet and to minimize the background of scattered particles.

Event Centrality

The centrality is the value to characterize the heavy ion collisions. In Run4, it is determined via the correlation between the energy deposit in the ZDC

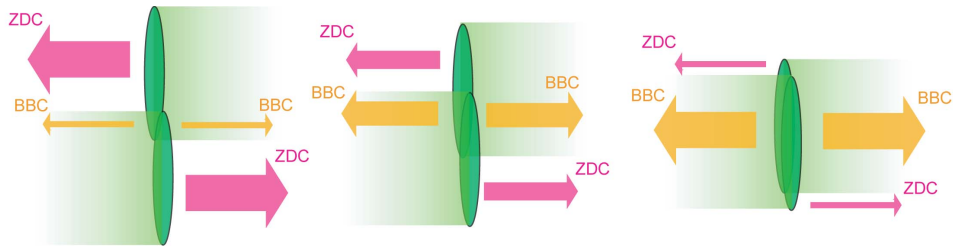


Figure 3.3: The schematic view of nuclear collisions. The left is the most peripheral and the right is the most central collision. The more the collisions is central, the more BBC collects the participants of the collisions and the less ZDC collects the spectators.

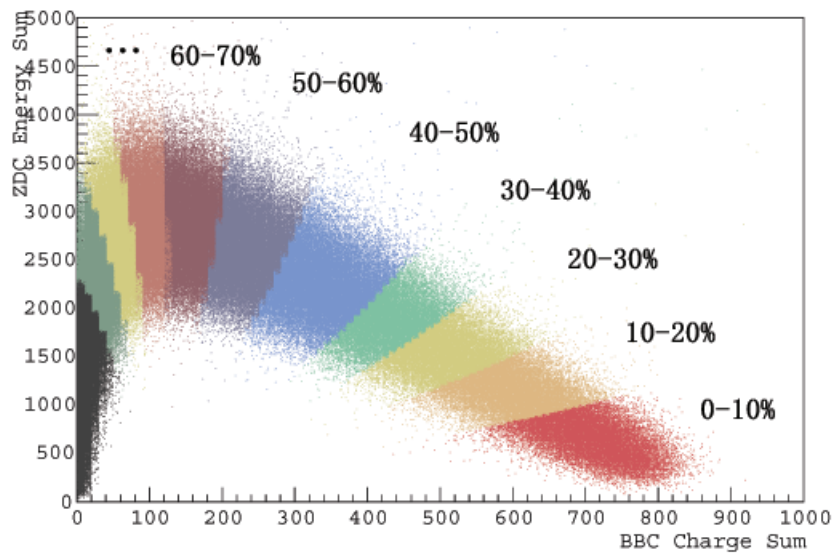


Figure 3.4: The correlation plot of the energy deposit in the ZDC and the charge deposit in the BBC.

and the charge deposit in the BBC (see the Figure 3.4). The schematic view of the relativistic heavy-ion collisions and their centrality are shown in the Figure 3.3. As explained in the Section 1.2, the collisions can be characterized by participants and spectators. The BBC collects participants while the ZDC collects spectators: e.g. if the impact parameter is larger, the BBC collects less participants and the ZDC collects more spectators. This behavior is illustrated in the Figure 3.4 for the minimum bias sample. The distribution is divided into the different centralities by an angle ϕ_{cent} in the BBC-ZDC plane defined as:

$$\phi_{cent} = \arctan \left(\frac{(Q_{BBC} - Q_0)/Q_{max}}{E_{ZDC}/E_{max}} \right),$$

where E_{max} and Q_{max} are the maximum ZDC energy deposit and the maximum BBC charge deposit, respectively. The value of Q_0 and the angular cuts shown in the Figure 3.4 is based on a simple simulation of the BBC and

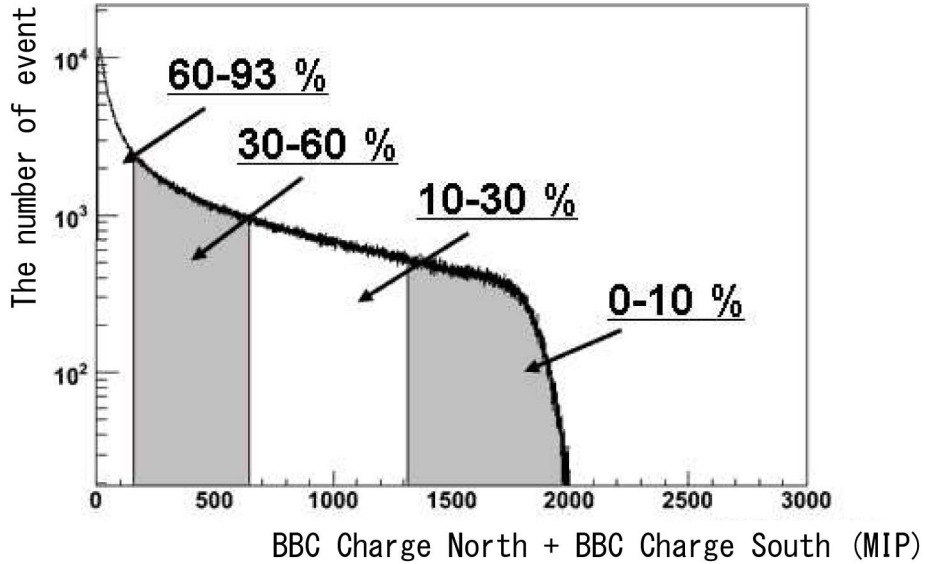


Figure 3.5: Example of cut region of the BBC charge sum. Charge sum was divided at 1% step segmentation.

ZDC signal together with a Glauber model in Au + Au collisions, which is described in [84].

The centrality determination via BBC/ZDC correlation was taken the place of using only the BBC charge measurement in Run7 after the study showing advantages of a precise centrality bin determination and a decrease of systematic errors on Monte Carlo Glauber model parameters. The Figure 3.5 shows the distribution of the total charge of the BBCs (sums of the north BBC and the south BBC). Since the particle multiplicity has a negative correlation with the total charge of the BBCs, the centrality class is defined by dividing 1% step segmentation. For this analysis, we consider 3 parts of centrality, 0-20% cent 60-92% and MinBias.

3.2.2 Photon Identification

Excluded Modules

We use both PbSc and PbGl for measuring photons. Quality criteria to the clusters were applied to extract some bad modules in the EMCal that distort the energy measurement of a hit. Modules without any energy signal mostly due to faulty photomultipliers are denoted as “dead”. It is also critical to exclude modules that only sporadically contribute in a wrong way to the signal. Those are denoted as “warn” determined by suspicious energy spectra. Additionally, the edge modules of the detector were cut considering to have a dead neighbor to exclude clusters that suffer from leakage at the calorimeter edge.

✓ *deadmap* and *warnmap* cut

A map of the excluded area in each detector is shown in the Figure 3.6. White area considered as dead and warn is all excluded during this analysis.

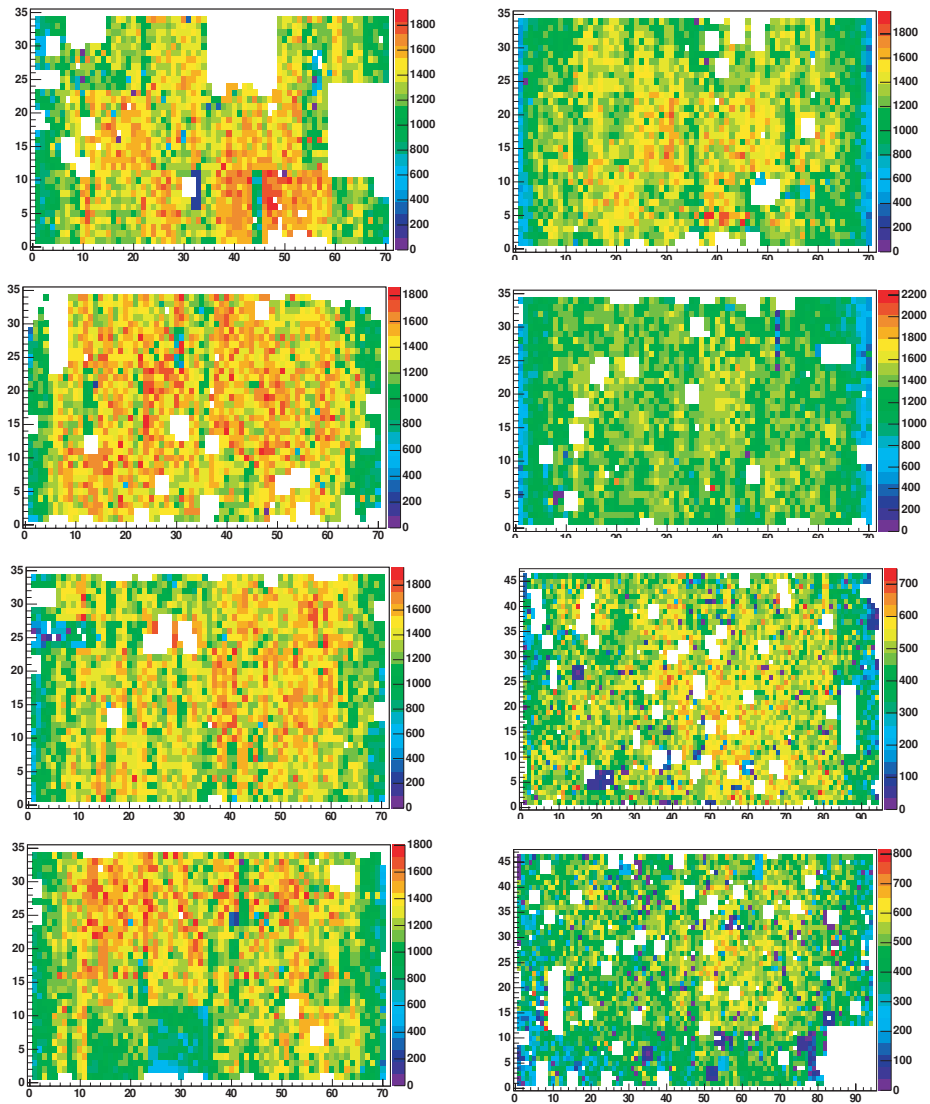


Figure 3.6: Excluded modules in the EMCAL. Maps on the left side are in the west arm and maps on the right side are in the east arm. Lower two maps on the right side are PbGl and the others are PbSc.

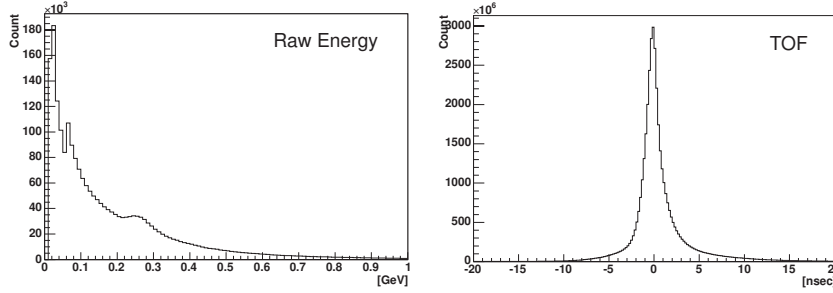


Figure 3.7: The distributions of energy (left) and a Time-Of-Flight (right). A plateau seen in the energy distribution is generated by Minimum Ionizing Particles.

Corrected Energy

To facilitate the measurement of photons in the EMCal, certain valuables for their identification are introduced. First of all, we put raw energy cut as,

$$\sqrt{E} > 0.2 \text{ (GeV)}$$

to exclude background from hadrons in low energy region. A cut on the shower shape is more effective to subtract hadrons because an hadronic shower usually spreads over more modules than an electromagnetic shower. We select the corrected energy and apply χ^2 as,

$$\sqrt{E_{core}} (prob > 0.02), \chi^2 < 3$$

Definitions of E_{core} and χ^2 are described in the Section 2.2.4.

TOF Cut

In addition to the energy cut, a Time-Of-Flight cut can also reject hadrons since hadrons have heavier mass. We put following cut from the width of the TOF distribution (see the Figure 3.7),

$$\sqrt{|TOF - bbct0|} < 2.0 \text{ (ns)}$$

, where $bbct0$ denotes time of collisions measured by the BBC.

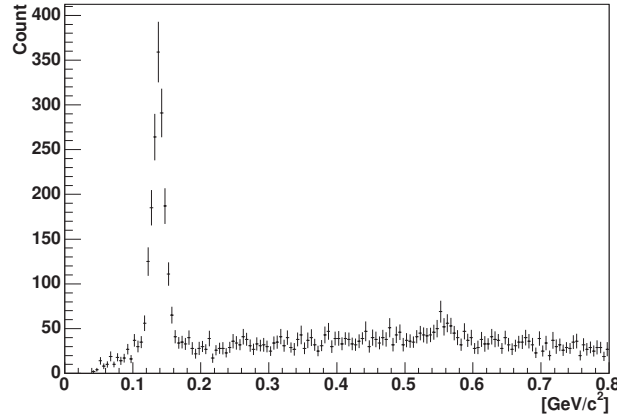


Figure 3.8: Example of invariant mass reconstructed from 2 photons.

3.2.3 Distribution of π^0 Invariant Mass

To reconstruct ω mesons, π^0 going to 2γ is needed to be first reconstructed. We put following selections for choosing π^0 .

π^0 Legs Selection

- ✓ Both photons in the same EMCal sector
- ✓ Energy asymmetry cut: $|E_1 - E_2|/|E_1 + E_2| < 0.8$

We require above conditions to cut some asymmetric pairs. The number is the optimized value from the study via the asymmetry distribution vs the measured asymmetry for photon candidate pairs in real Au + Au collisions from [50].

As shown in the Figure 3.8, an example spectrum, π^0 around 0.135 GeV/c² can be clearly identified (also, η can be seen around 0.56 GeV/c²).

Dependence on $\pi^0 p_T$

The position of π^0 mass and the width have a dependence on $\pi^0 p_T$ as seen in the Figure 3.9 and 3.10. Observed position shift upward due to the effect of photon conversion before arriving to EMCal and due to the p_T smearing

caused from the steep $\pi^0 p_T$ distribution of π^0 . Also, the multiplicity affects those value. We consider this shift parameter according to the $\pi^0 p_T$ and the centrality when reconstructing the ω .

3.2.4 Optimized Cuts for Reconstructing ω

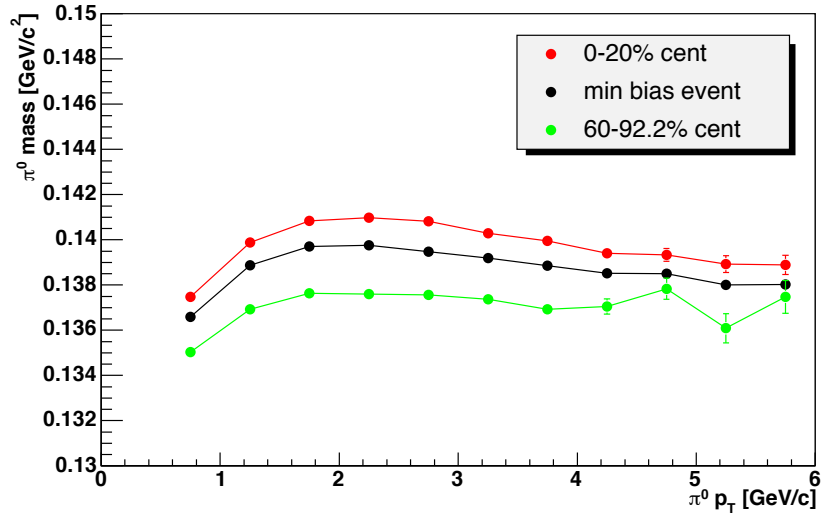
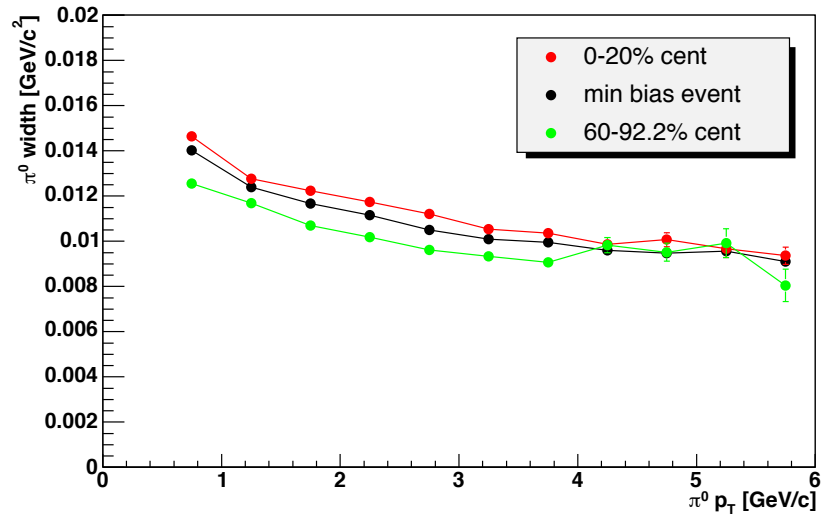
In Run4, we consider following values and apply the kinematical cuts tabulated in the Table 3.2.4 by the study of cut optimization.

- ✓ Transverse momentum cut of π^0
- ✓ Photon energy cut except π^0 candidate
- ✓ Width of π^0 invariant mass

Another possibility to reduce the combinatorial background is to make use of the phase-space distribution, such as minimum opening angle of π^0 and γ . In Run7, we add the angle cut of π^0 and γ as follows by [85], which shows an improvement of significance.

$$\checkmark |\cos \theta^*| < 0.8,$$

where θ^* is the relativistic angle of π^0 and γ . The effect of this cut is naturally included in the above kinematical cuts since the opening angle has linear correlation to the measured energy asymmetry ($|E_\pi - E_\gamma|/|E_\pi + E_\gamma| = \beta |\cos \theta^*|$, where $\beta = p/E \sim 1$).

Figure 3.9: Position of π^0 peak as a function of $\pi^0 p_T$.Figure 3.10: Width of π^0 mass as a function of $\pi^0 p_T$.

	$\pi^0 p_T$ Cut	γ energy Cut	π^0 mass width
$0.5 < p_T(\omega) < 1.5$	no cut	no cut	1.25σ
$1.5 < p_T(\omega) < 2.5$	no cut	no cut	1.25σ
$2.5 < p_T(\omega) < 3.5$	$1.25<$	$0.75<$	1.25σ
$3.5 < p_T(\omega) < 4.5$	$1.5<$	$0.75<$	1.25σ
$4.5 < p_T(\omega) < 5.5$	$2.0<$	$1.0<$	1.25σ
$5.5 < p_T(\omega) < 6.5$	$2.25<$	$1.25<$	1.5σ
$6.5 < p_T(\omega) < 7.5$	$2.75<$	$1.5<$	1.5σ
$7.5 < p_T(\omega) < 8.5$	$3.0<$	$1.5<$	1.5σ
$8.5 < p_T(\omega) < 9.5$	$3.0<$	$1.5<$	1.5σ
$9.5 < p_T(\omega) < 10.5$	$3.0<$	$1.5<$	1.5σ

Table 3.1: The kinematical cut table.

3.3 Simulation

In order to extract the reconstructed efficiency and to estimate the feasibility of the ω measurement, the simulation study was done ahead to the data analysis. In this section, we describe the simulation technics and estimated reconstructed efficiency in the former part, then discuss the significance and background of this analysis in the latter part.

3.3.1 Event Generator

A collision event is fully specified by the position coordinate of the interaction point called the “vertex”, or more specifically the “primary vertex”. For purposes of the simulation program, an event is viewed as a list of the particles with their type, energies, momenta, the point of production and the time of production which can be conveniently chosen to be the zero of the time. Naturally, the characteristics of the real events will be known only after the actual experiments begin taking data. Until then we must rely on various event generators which attempt to simulate the experimental events by making certain model assumptions. We used the one of such event generators called as “EXODUS”, the package of the Monte Carlo based code created in 1998 [86].

We generated 1.5 million events, one ω meson per event for following status:

- $1.0 < p_T < 14.0$ [GeV/c] generated as flat at first, then weighted after reconstruction. The weight function was taken from π^0 spectra as shown in the figure.
- $-0.5 < y < 0.5$,
- $0.0 < \phi < 2\pi$,

where those parameters are defined in the Appendix A *Kinematics*.

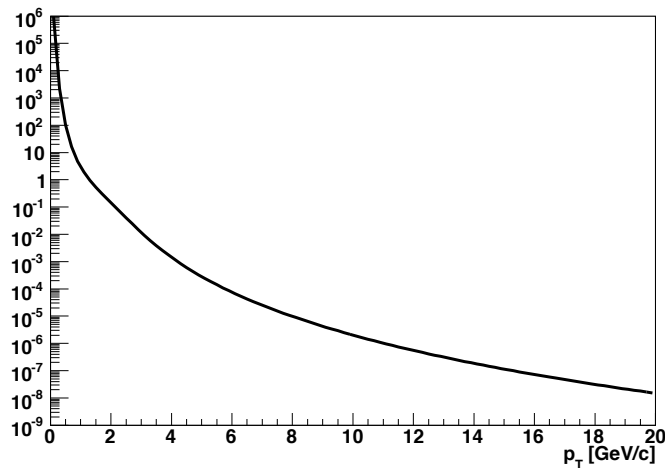


Figure 3.11: The p_T spectra of generated ω mesons in the simulation.

3.3.2 Detector Simulation

The PHENIX detector is very complex in character with a large variety of detector types and materials inside it. To simulate such PHENIX detector, “PISA”, PHENIX Integrates Simulation Application [87] was introduced. The PISA code is based heavily on the CERN software libraries [88]. Specifically, PISA is the PHENIX implementation of the GEANT geometry and event particle tracking software system. Using PISA, the PHENIX simulator can pick which (or all) aspects of the whole PHENIX detector geometry to introduce into an event simulation.

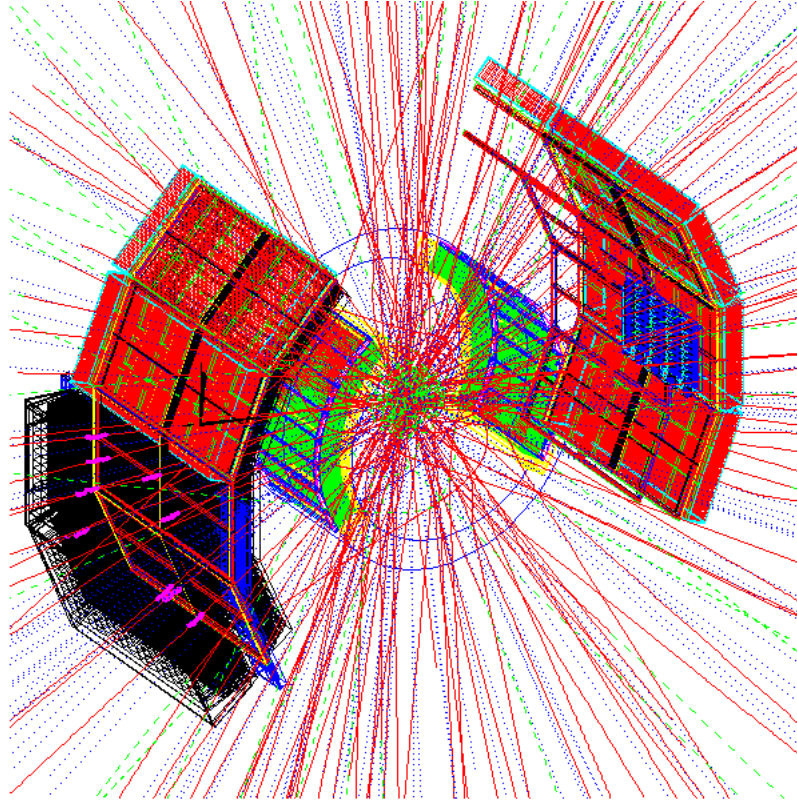


Figure 3.12: Demonstration of simulated 100 ω mesons' tracks (red lines denote electron and positron, blue dotted lines denote photons and green dotted lines denote muons). EMCAL, PC1/PC2/PC3, and DC are drawn (see the Chapter 2).

If we input information of particles that generated by the event generator, PISA will make them decay according to their branching ratio and lifetimes. The Figure 3.12 shows a demonstration of 100 ω going to various decay modes and hitting to (or straying from) the EMCal. We reconstruct ω mesons by calculating the Formula 3.3 after inputting about 7.5 million ω into PISA. The Figure 3.13 is an example plot of reconstructed invariant mass of the ω . There is a slight tail at lower region than the ω mass (782 MeV/c²) since some photons convert to electrons due to detectors located in front of EMCal depositing lower energies.

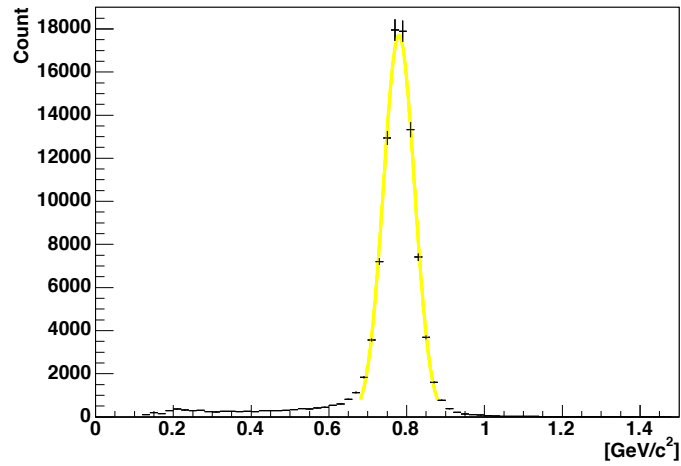


Figure 3.13: Invariant mass spectrum of the single ω event for all p_T .

The geometrical acceptance can be measured from this simulation by looking at,

$$\epsilon_{geo} = \frac{dN_{\omega}/dp_T|_{reconstructed}}{dN_{\omega}/dp_T|_{input}}, \quad (3.1)$$

where $dN_{\omega}/dp_T|_{reconstructed}$ and $dN_{\omega}/dp_T|_{input}$ denote the number of reconstructed ω mesons and input ω mesons for each p_T within the 2σ of ω mass, respectively. The calculated acceptance is shown in the Figure 3.17 together with efficiencies of Multiple Dependence Correction (explained in the next section).

3.3.3 Multiplicity Dependence

In the previous section, we calculate the acceptance using the single event simulation which is so-called “single function (SPC)” representing the correction due to geometrical acceptance, decay in flight, reconstruction efficiency and momentum resolution. In addition to this correction function, we have to take it into account the multiplicity dependence as long as dealing with multiple collisions such as Au+Au collisions for this analysis. In most central Au + Au events, the EMCal typically detects more than 300 clusters corresponding to a detector occupancy of $\sim 10\%$. This is the so called “multiplicity dependence correction function (MDC)”. Since ω mesons are reconstructed by γ s, we discuss MDC only in the EMCals. Multiple collisions generate huge backgrounds to the EMCal and those backgrounds interfere cluster algorithm. We consider two effects, the one is “cluster merging” and the other is “cluster splitting”. As shown those schematics in the Figure 3.14, backgrounds attached to the true clusters coming from ω cause to merge a cluster or split a cluster. The “cluster merging” overestimates the measurement values since multiple clusters are merged and identified as one cluster while “cluster splitting” underestimates the measurement values since single cluster is split and identified as multiple clusters.

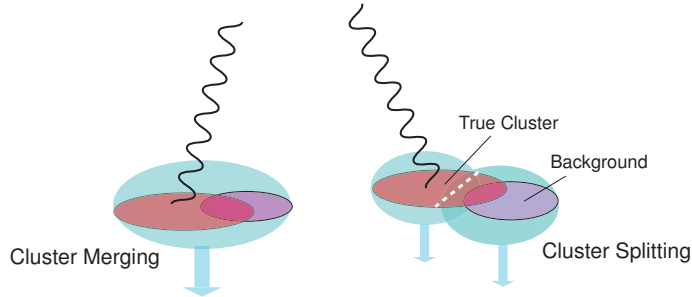


Figure 3.14: The effect of multiplicity on the Cluster Algorithm.

To evaluate the MDC, we use the technique called “embedding” [87]; embedding of the simulated particles into a real event. A DST (See the Chapter 2 2.3) containing real event is read in together with simulated DST that generated in previous. For each selected real event, the tower information is extracted from the DST and merged with the tower data from on simulated event. The list of merged towers is now the basis for a new clustering. Due to

the added information from the simulated event, the resulting list of merged clusters is different from the list of clusters from the real event. A comparison yields the modified or new clusters in the merged event and the lost clusters from the real event. We input about 1 million single ω to 1.2 million events of real data, and reconstruct the invariant mass using the Formula 3.3 (the Figure 3.15 is an example). It shows that ω mesons merging to the backgrounds.

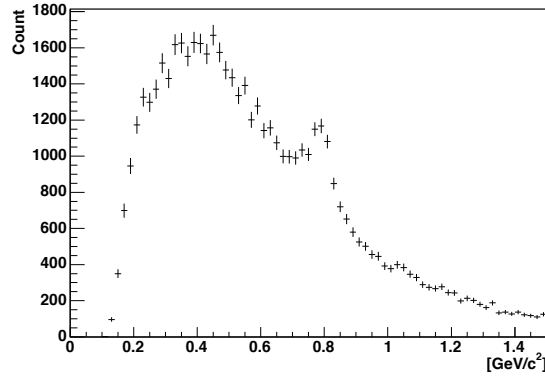


Figure 3.15: Invariant mass spectrum of simulated ω embedding to the real data.

To extract the clear peak position and width of the ω mass from the results, we choose only true clusters that are from the simulated DST and subtract the background (note that it is possible because we know the input data of simulation). After fitting the gaussian, we get the ω mass peak and width (see the Figure 3.16).

A measured raw yield then needs to be corrected for the total efficiency $\epsilon \times \epsilon_{emb}$, depending on the collision, centrality, and trigger involved, where ϵ corresponds to SPC and ϵ_{emb} corresponds to MDC. The merging effect results in $\sim 40\%$ loss of reconstruction efficiency in 0-20% central Au+Au and is almost negligible in peripheral collisions. The reconstruction efficiencies derived for Au + Au collisions at different centralities are shown in Figure 3.17.

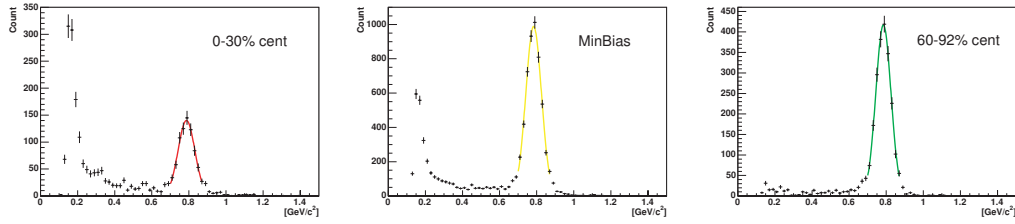


Figure 3.16: Invariant mass spectrum reconstructed by the true clusters. A peak around 0.1-0.2 (GeV/c^2) is due to the cluster splitting causing the measured energy lower than true energy.

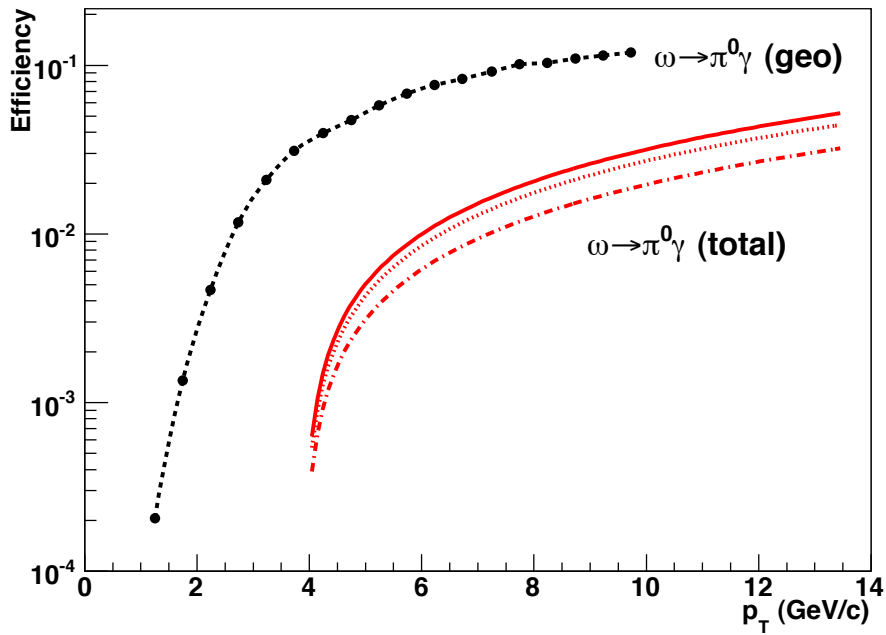


Figure 3.17: Typical geometrical acceptance (geo) and total reconstruction efficiencies for the $\omega \rightarrow \pi^0 \gamma$. The total efficiencies include the embedding efficiency and analysis cuts: solid lines are for 60-92% centrality, dotted lines are for 20-60% centrality and dot-dashed lines are for 0-20% centrality in Au + Au.

3.4 Background Consideration

3.4.1 Combinatorial Background

The most challenging issue for this analysis is to cope with the combinatorial background, which is created by three particle reconstruction, $\omega \rightarrow \pi^0 \gamma \rightarrow 3\gamma$. The Figure 3.18 shows the schematic of 3γ combinations creating foreground and background. We first reconstruct 2 γ s and set as “ π^0 candidate” by selecting the invariant mass within 1.25σ or 1.5σ (see the table 3.2.4), however there is a probability that the uncorrelated 2 γ s satisfies the criteria of π^0 candidate. Those include γ from π^0 or η inside of three combination (Background 1 and 2 in the Figure 3.18) and independent three γ s combination (Background 3).

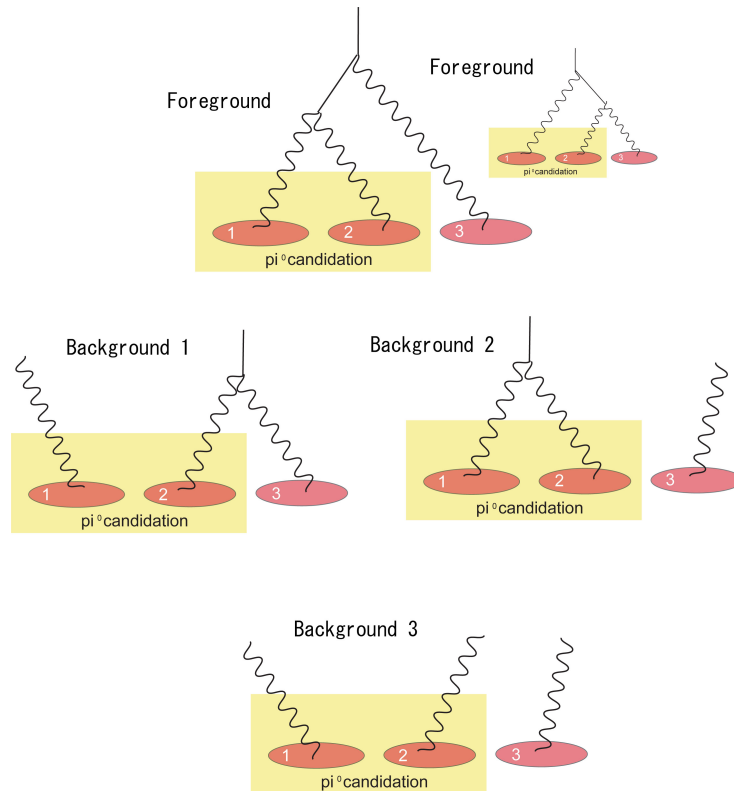


Figure 3.18: Conceivable combinations during 3γ reconstruction. Suppose γ_1 and γ_2 are the π^0 candidate (selected as π^0 mass) that we reconstruct first.

To produce combinatorial background shape, we introduce two event mixing methods described in the following subsections. In addition to the mixed event, we consider K_s^0 contribution and estimate its shape by requiring K_s^0 mass range.

Mixed Events Trail

The event mixing method is a widely used technique to determine the combinatorial background. The basic idea is to compare the result obtained by combining particles within one event to the result for particle combinations from different events, which are a priori not correlated. It is usually used for two pair reconstruction, such as π^0 and η .

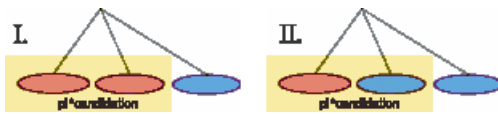


Figure 3.19: A schematic of Event mixing. Oval shapes indicate γ clusters and color differences (red or blue) indicate different collision events.

For this analysis dealing with three body decay mode, we consider two types of combinations as shown in the Figure 3.19: I. π^0 candidate is selected from the same event (having a correlation) and chose a different event for third photon and II. π^0 candidate is selected from different events (having no correlation)

and chose third photon as the same event with one of the candidate. We suppose I. is “uncorrelated” combination and II. is “correlated” combination. As seen in the Figure 3.20, the mixed event I. invariant mass shows “uncorrelated” shape on the left and the mixed event II. invariant mass shows “correlated” shape on the right.

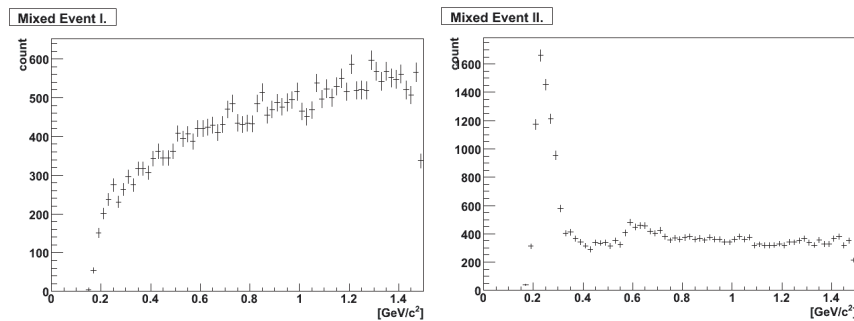


Figure 3.20: Invariant mass spectra shape of two different event mixing

3.4.2 K_s^0 Contribution

Considering the number of K_s/π^0 ratio (~ 0.438 [21]), and their high Branching Ratio of $K_s^0 \rightarrow 2\pi^0$ (31.05% [20]), K_s^0 is expected to be produced much more than the ω from the collision. Although the efficiency for catching 4 γ s is about the factor of 10 lower than catching 3 γ s the background from the K_s^0 contributes to the order of 7-8% of measured photons and it is not ignorable [21].

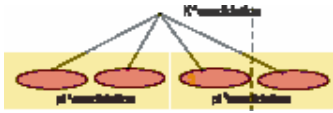


Figure 3.21: A schematic of K_s^0 reconstruction

To extract the background shape, we reconstruct 3 γ s from 4 γ s reconstruction after requiring K_s^0 mass (the Figure 3.21 shows the schematic). The Figure 3.22 shows an example shape of reconstructed mass spectra. The contributed area is estimated around 0.25 to 0.5 GeV/c^2 , where is lower than ω mass region.

Due to the relatively long lifetime of the K_s^0 (0.9×10^{-10} s [20]), the photon pairs does not correspond to the π^0 decay vertex and it makes the invariant mass shape asymmetrical and having a tail in low mass side.

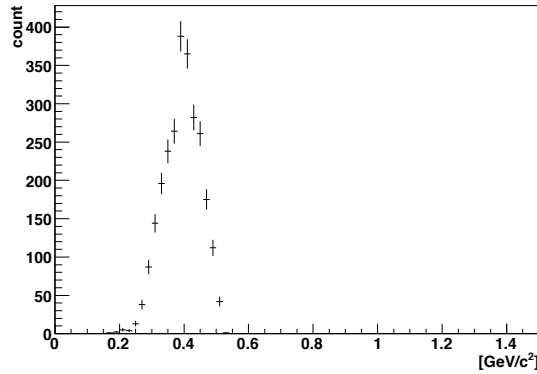


Figure 3.22: Reconstructed 3 gammas requiring K_s^0 mass range

3.4.3 Other Components

As described in the Section 2.2.5, an additional detector, Hadron Blind Detector (HBD) installed in Run7 causes the conversion of γ and makes backgrounds. We include this effect in the systematic error and will be discuss in the Section 3.8.6.

3.4.4 Cocktail Simulation Study

We study *cocktail simulation* to systematically check the integrated background shape as discussed in the previous subsections. The procedure of cocktail simulation study is; 1) generate multiple particles which have photon decay channel, 2) apply cuts that exactly used for real data analysis, and 3) reconstruct 3γ s and examine the mass shape.

Figure 3.23 shows the p_T spectra which was used for an input of generated particles; $\pi^0 \rightarrow \gamma\gamma$, $\eta \rightarrow \gamma\gamma$, $\eta' \rightarrow \gamma\gamma$, $K_s^0 \rightarrow \pi^0\pi^0$ ($\pi^0 \rightarrow \gamma\gamma$) and $\omega \rightarrow \pi^0\gamma$. The function of p_T is empirically determined from the π^+ , π^- and π^0 invariant

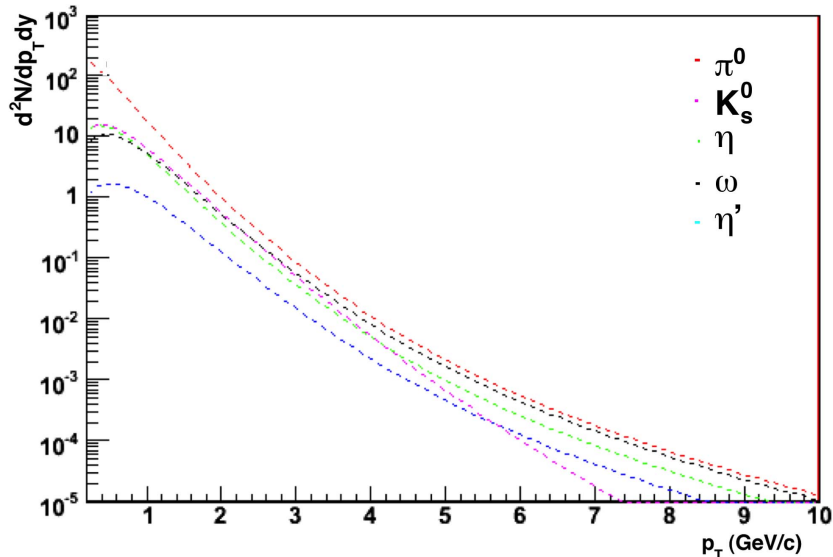


Figure 3.23: p_T spectra of generated particles used for cocktail simulation.

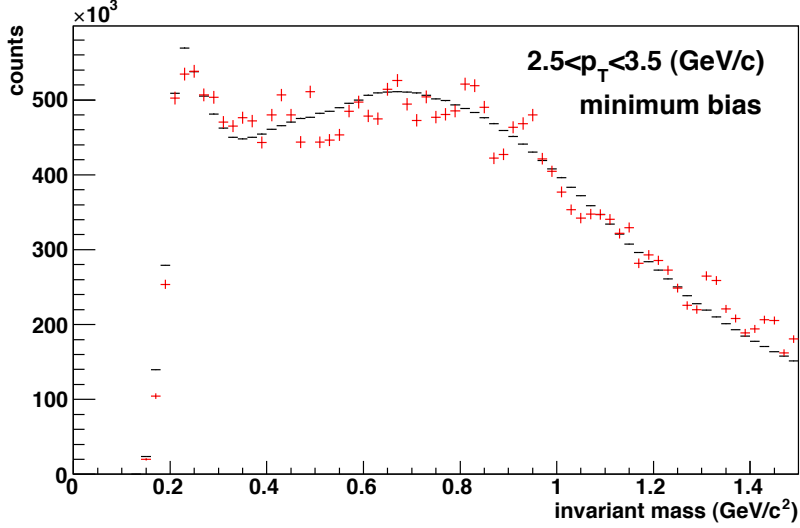


Figure 3.24: Example output of reconstructed invariant mass of cocktail simulation in minimum bias at $2.5 < p_T < 3.5$ GeV/c. Black points are real data and red points are simulation output.

yield in Au + Au [50], which is defined as:

$$f(p_T) = \frac{A_0}{p_T^{n_0}} \times \left(1 + \exp\left(\frac{p_T - 3.75}{0.1}\right)\right)^{-1} + \frac{A_1}{1 + \frac{\sqrt{p_T^2 - m_\pi^2 + m_{hadron}^2}}{p_1}} \times \left(1 - \left(1 + \exp\left(\frac{p_T - 3.75}{0.1}\right)\right)^{-1}\right),$$

where the χ^2 of this fitting function is 0.22 in the minimum bias π invariant yield in Au+Au collisions. To scale the p_T to other hadrons, we multiply above spectra by R_{h/π^0} where 0.45 (the average of empirical value [55]) for η and 1.0 for others.

Figure 3.24 is one of outputs of reconstructed mass spectra in minimum bias at $2.5 < p_T < 3.5$ (GeV/c). Comparing real data output and simulation output, that simulation results can represent the shape of background and we confirm that the background shape is mostly from the hadron contribution.

3.4.5 Cut Optimization

An improvement of peak significance, S/\sqrt{B} has a vital importance for this analysis since the combinatorial backgrounds are the main issue for the reconstruction of ω as described in the previous section. Here, we consider following parameters which have a great influence on the peak significance.

- Transverse momentum (p_T) cut of π^0
- Photon energy cut (except photons from π^0 candidate)
- Width of π^0 invariant mass

We investigate those cuts by calculating S/\sqrt{B} according to transverse momentum (p_T) of ω . The Figure 3.25 shows a roughly method. The single ω simulation data is used for calculating the number of signals (numerator) and partial real data are used for calculating backgrounds (denominator), including very few signals but ignorable.

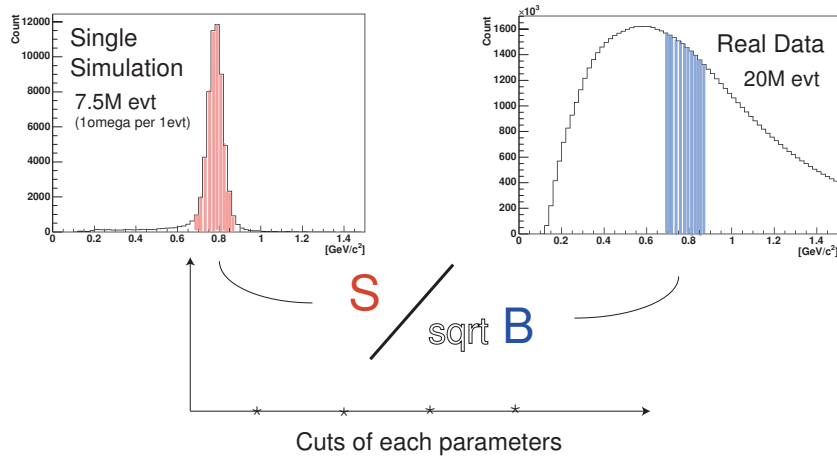


Figure 3.25: Schematic view of cut optimization method. We calculate S/\sqrt{B} where the single ω simulation is used for a numerator and real data is used for a denominator.

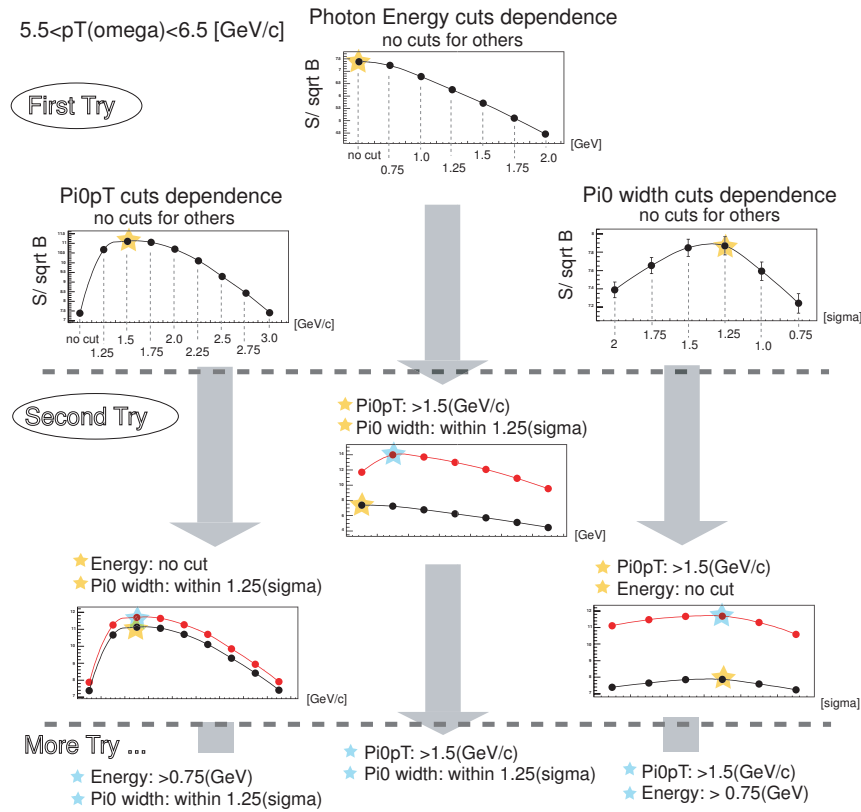


Figure 3.26: Flow chart of the cut optimization (see the text).

The goal is to find parameters that maximize the significance, S/\sqrt{B} maximum, however, the best cut can not be determined by one trial since those cuts, mostly p_T cut and energy cut, are correlative. The Figure 3.26 shows a flow chart of this study (e.g. $5.5 < p_T(\omega) < 6.5$ GeV/c). First, we calculate S/\sqrt{B} with no cuts for each value and find the point that makes the peak (yellow stars in the Figure 3.26). Next, we again calculate S/\sqrt{B} after applying cuts that make the peak before. The trial is iterated until cuts get unchanged. The results are shown in the Figure 3.27. The significance has been improved 4 times better in maximum if we set optimized kinematical cuts. The final cuts are summarized in the table 3.2.4.

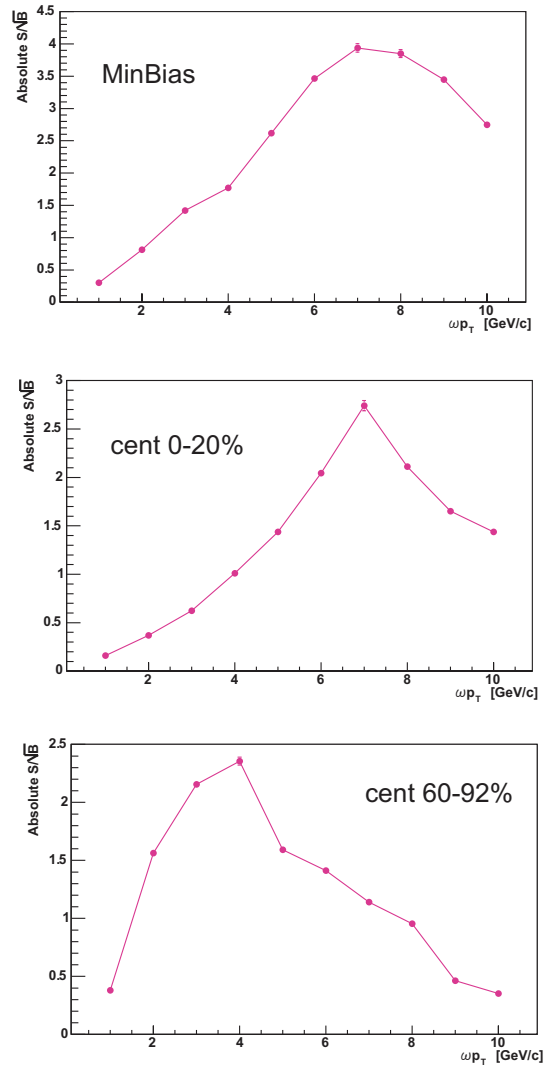


Figure 3.27: Absolute S/\sqrt{B} using the optimized cuts for MinBias, 0-20% and 60-92% centrality.

3.5 Yield Extraction

In this section, we describe the method used to extract the raw ω yield. The way of yield extraction is different in Run4 analysis and Run7 analysis. We first describe a general analysis method in Section 3.5.1 and Section 3.5.2, then separately explain two ways of yield extraction in Section 3.5.3 and Section 3.5.4.

3.5.1 Reconstruction of the ω

In $\omega \rightarrow \pi^0\gamma$ channels, the first analysis step is to reconstruct π^0 candidates by combining photon pairs.

The invariant mass of π^0 is,

$$M_{\pi^0}^2 = 2E_1E_2(1 - \cos\theta_{\gamma\gamma}), \quad (3.2)$$

where E_1 and E_2 are the measured energy of 2γ (suppose γ_1 and γ_2 arbitrarily) and $\theta_{\gamma\gamma}$ is the opening angle between 2γ calculated from the hit positions.

Next, candidates (which include combinatorial background) are combined with a third photon for $\omega \rightarrow \pi^0\gamma$ as,

$$M_{\pi^0\gamma}^2 = E_1^2 + E_2^2 + E_3^2 - p_x^2 - p_y^2 - p_z^2, \quad (3.3)$$

where,

$$\begin{aligned} p_x &= E_1 \cdot \frac{x_1}{\sqrt{x_1^2 + y_1^2 + z_1^2}} + E_2 \cdot \frac{x_2}{\sqrt{x_2^2 + y_1^2 + z_1^2}} + E_3 \cdot \frac{x_3}{\sqrt{x_3^2 + y_1^2 + z_1^2}}, \\ p_y &= E_1 \cdot \frac{y_1}{\sqrt{x_1^2 + y_1^2 + z_1^2}} + E_2 \cdot \frac{y_2}{\sqrt{x_2^2 + y_1^2 + z_1^2}} + E_3 \cdot \frac{y_3}{\sqrt{x_3^2 + y_1^2 + z_1^2}}, \\ p_z &= E_1 \cdot \frac{z_1}{\sqrt{x_1^2 + y_1^2 + z_1^2}} + E_2 \cdot \frac{z_2}{\sqrt{x_2^2 + y_1^2 + z_1^2}} + E_3 \cdot \frac{z_3}{\sqrt{x_3^2 + y_1^2 + z_1^2}}, \end{aligned}$$

(the coordinates of x, y and z are defined in the *Appendix*).

3.5.2 Event Mixing

The event mixing method is a widely used technique to determine the combinatorial background. The Figure 3.28 shows a schematic of the event mixing. The basic idea is to compare the result obtained by combining particles within one event to the result for particle combinations from different events, which are a priori not correlated. It is usually used for two pair reconstruction, such as π^0 and η . The Figure 3.29 shows the invariant mass spectra of π^0 for each p_T of π^0 . The foreground (reconstructed with same event) and the background (reconstructed with mixed event) are drawn together on the left side for each p_T . Right side of the plot is the spectra after subtraction of the background. Obviously, π^0 stands out after subtraction of the event mixing. Although it is not simple in the case of multiple decay mode, we consider this method for this analysis since a significance of the ω is scarce due to combinatorics.

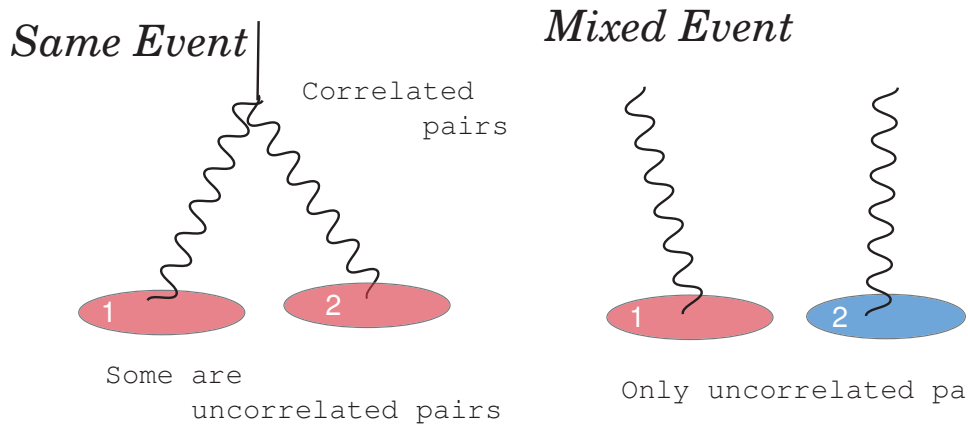


Figure 3.28: A schematic of Event mixing. Oval shapes indicate γ clusters and color differences (red or blue) indicate different collision events.

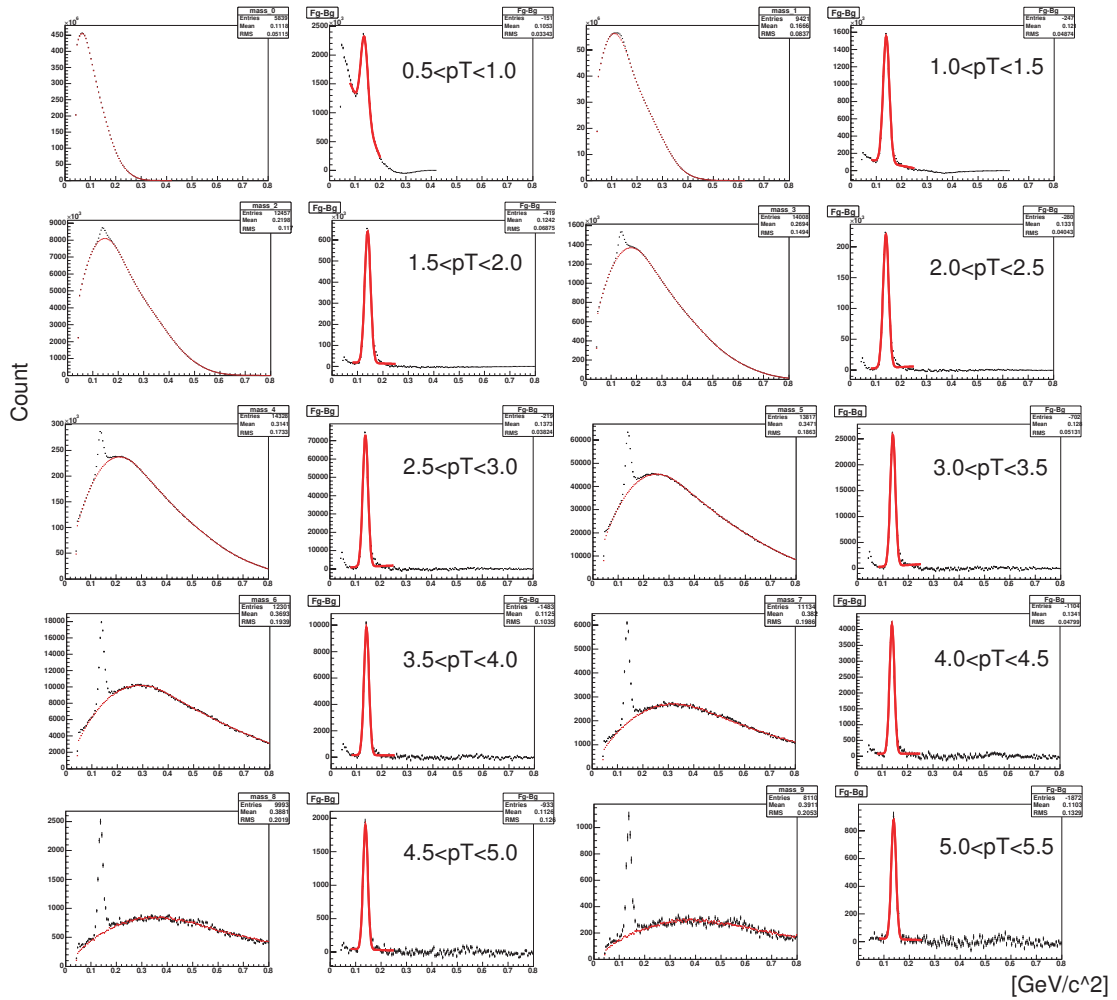


Figure 3.29: Invariant mass spectra of π^0 .

3.5.3 BG Trial Method (Run4)

Due to high multiplicity and low S/B associated with it, cut optimization was performed as described in the Section 3.4.5. In Run4, the background subtraction is executed by estimating three background sources: correlated background (for example, $\pi^0\gamma$ pairs from one of the photons from true π^0 or η making a fake π^0 candidate), uncorrelated background which comes from the combination of independent 3γ s, and K_s^0 contribution ($K_s^0 \rightarrow \pi^0\pi^0 \rightarrow 4\gamma$ s), then each amount of background is determined by free parameterized fitting. The Figure 3.30 shows the invariant mass distribution in Au + Au analysis with(a) and without(b) combinatorial background. Combinatorial backgrounds are estimated by a mixed event technique which is explained previously.

We scale three estimated background by free parameters defined as,

$$\sum_{bin} \frac{(FG - S1 \cdot BG1 - S2 \cdot BG2 - S3 \cdot BG3 - S4 \cdot SG)^2}{(\Delta FG)^2 + (S1 \cdot \Delta BG1)^2 + (S2 \cdot \Delta BG2)^2 + (S3 \cdot \Delta BG3)^2}, \quad (3.4)$$

where FG denotes foreground bin value, $BG1$ denotes background from the mixed event I., $BG2$ denotes background from the mixed event II. and SG denotes the gaussian function supposed as omega signal peak (mean and

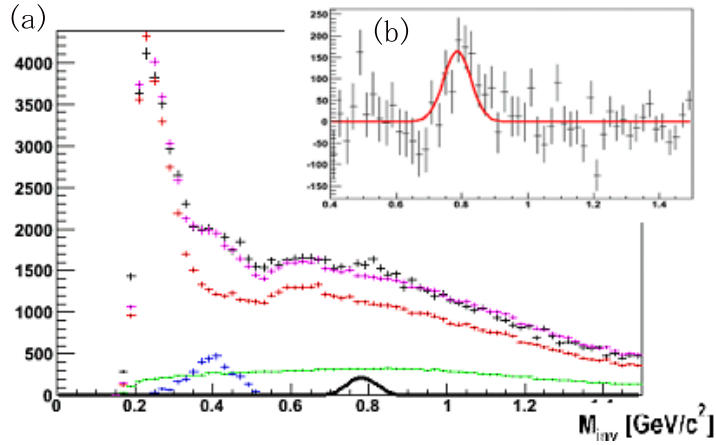


Figure 3.30: (a) Foreground and scaled background histograms in one of the p_T bins in Au + Au. (b) Foreground histogram after subtraction of scaled background.

width are fixed value extracted by the embedding simulation). $S1, S2, S3$ and $S4$ are the scaling free parameters.

3.5.4 Fitting Method (Run7)

In Run7, we performed the event mixing for only the combination of BG1 since BG2 did not match to the foreground. Those are considered due to the installed HBD creating radiative backgrounds.

We partially subtract uncorrelated combinatorial background by reconstructing third photon from different events while selecting π^0 candidate from same event. For every p_T bin background histogram was normalized to the foreground in a range of invariant masses, $1.75 < M_{inv} < 4.0 \text{ GeV}/c^2$ in which we expect no much correlated background and subtracted from the foreground histograms. Example of foreground and scaled background histograms is shown in (a) panel of Figure. Foreground histogram after subtraction of scaled background histogram is shown in (b) panel. Resulting histogram contains residual background coming from correlated particles, for example from $K_s \rightarrow \pi^0\pi^0$ decays or $\pi^0\gamma$ ($\eta\gamma$) pairs where one of the photons from true π^0 (η) $\rightarrow \gamma\gamma$ decay is used to build a fake π^0 (η) candidate for $\omega \rightarrow \pi^0\gamma$ decay. The peak corresponding to $\omega \rightarrow \pi^0\gamma$ decay is better seen after the background subtraction.

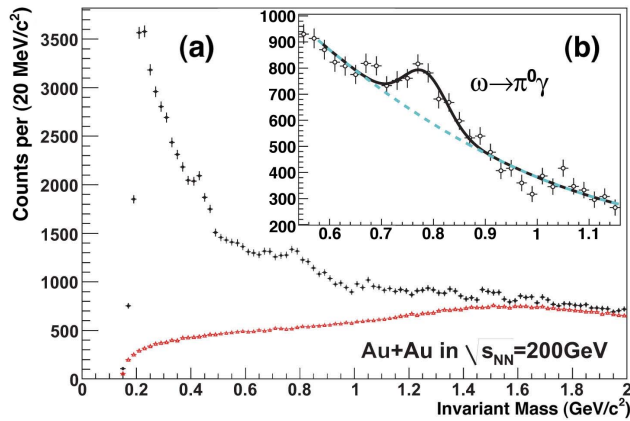


Figure 3.31: (a) Foreground and scaled background histograms in one of the p_T bins in Au + Au. (b) Foreground histogram after subtraction of scaled background.

Finally, raw yields are extracted by the fitting function which is a combination Gaussian and second order polynomial. In the fits to the data we limit the width of Gaussian to the value extracted from simulation within $\pm 1 MeV/c^2$ window. The ω yield is calculated as an integral of the Gaussian.

3.6 Invariant Mass Spectra

In this section, reconstructed invariant mass spectra in 4 centrality bin (0-20%, 20-60%, 60-92% and Minimum Bias) taken in two data set (Run4 and Run7) are shown. Those spectra are split by p_T bins in 1 GeV/ c bin and merged at high p_T . Counted number of ω mesons by fitting function and error associated to the fitting are shown in the Tables in each section for Run4 and Run7.

3.6.1 Run 4

- 0-20% centrality ($N_{evt} = 2.27 \times 10^8$).

p_T	6.0	7.0	8.0 - 10.0
Fit FG (Gaussian)	740	191	243
Error from FitFG	31.3%	39.2%	17.0%

- 20-60% centrality ($N_{evt} = 5.68 \times 10^8$).

p_T	5.0	6.0	7.0	8.0	9.0	10.0
Fit FG (Gaussian)	1847	689	236	180	136	62
Error from FitFG	18.7%	16.1%	17.6%	14.0%	13.1%	20.5%

- 60-92% centrality ($N_{evt} = 3.75 \times 10^8$).

p_T	3.0	4.0	5.0	6.0 - 10.0
Fit FG (Gaussian)	1361	852	276	110
Error from FitFG	22.4%	16.0%	19.4%	37.6%

- 0-92% centrality ($N_{evt} = 1.06 \times 10^9$).

p_T	6.0	7.0	8.0	9.0	10.0
Fit FG (Gaussian)	1633	528	315	206	94
Error from FitFG	14.9%	15.3%	12.9%	12.9%	20.5%

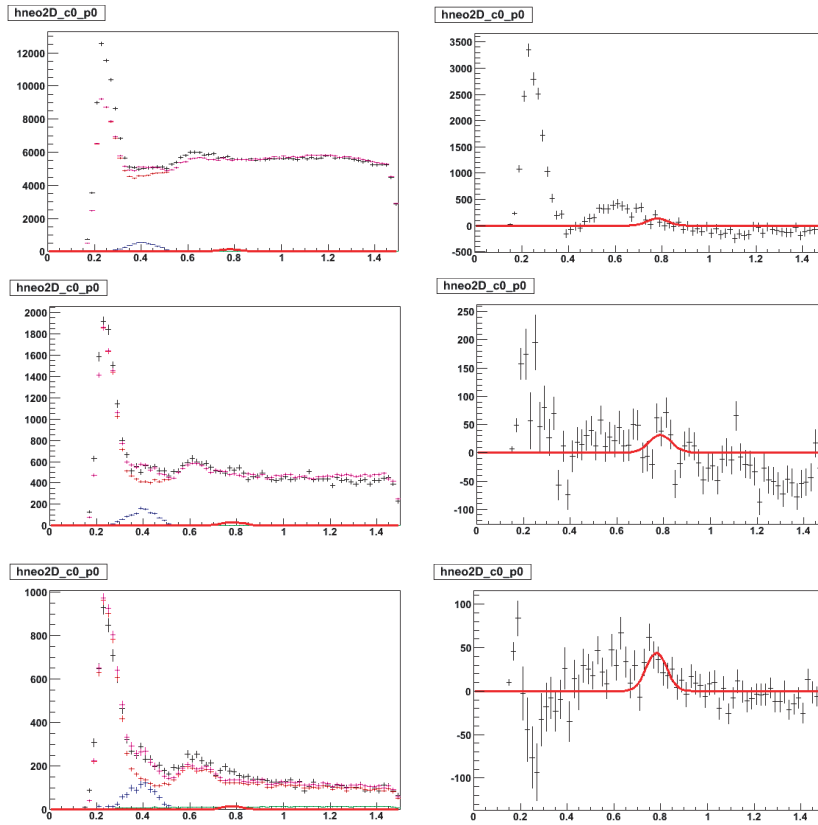


Figure 3.32: Invariant Mass Spectra (0-20% cent, $p_T=6.0$, $p_T=7.0$ and $p_T=8.0-10.0$ GeV/ c). Left Side: Black points denote Foreground, Green points denote BG1, Red points denote BG2, Blue points denote BG3 and Magenta points denote BG1+BG2+BG3. Red solid lines denote SG (mean and width are fixed value extracted by the embedding simulation).

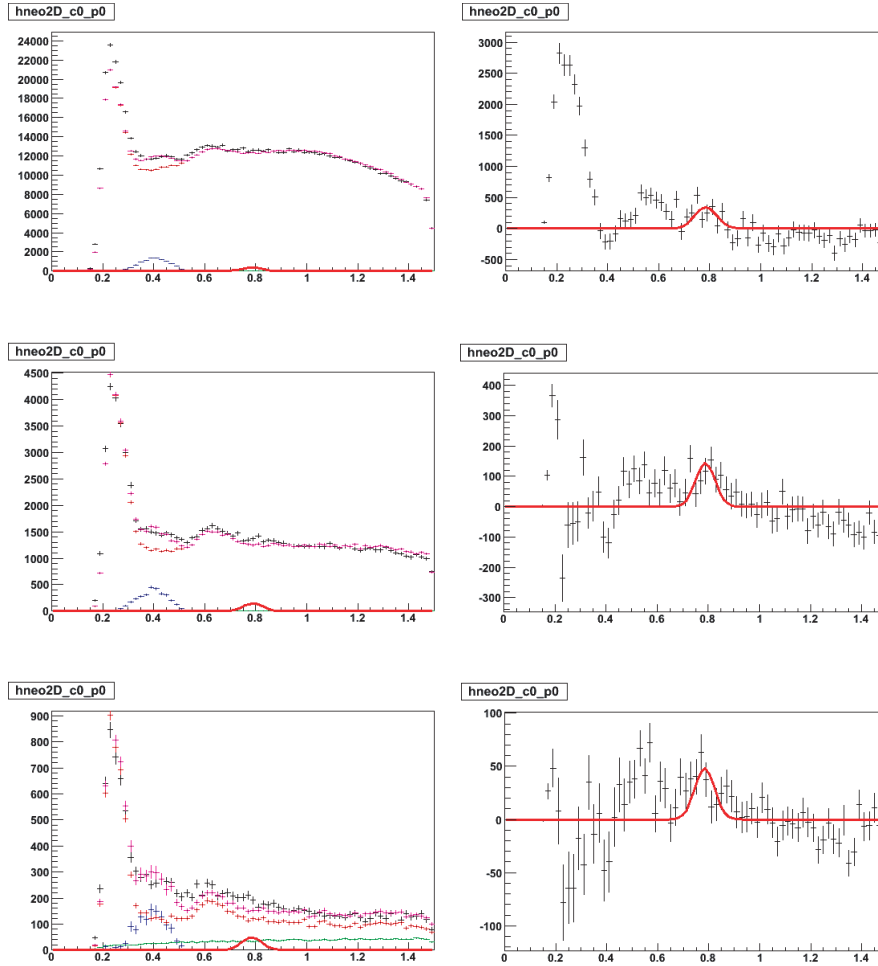


Figure 3.33: Invariant Mass Spectra (20-60% cent, $p_T=5.0$, $p_T=6.0$ and $p_T=7.0$ GeV/c).

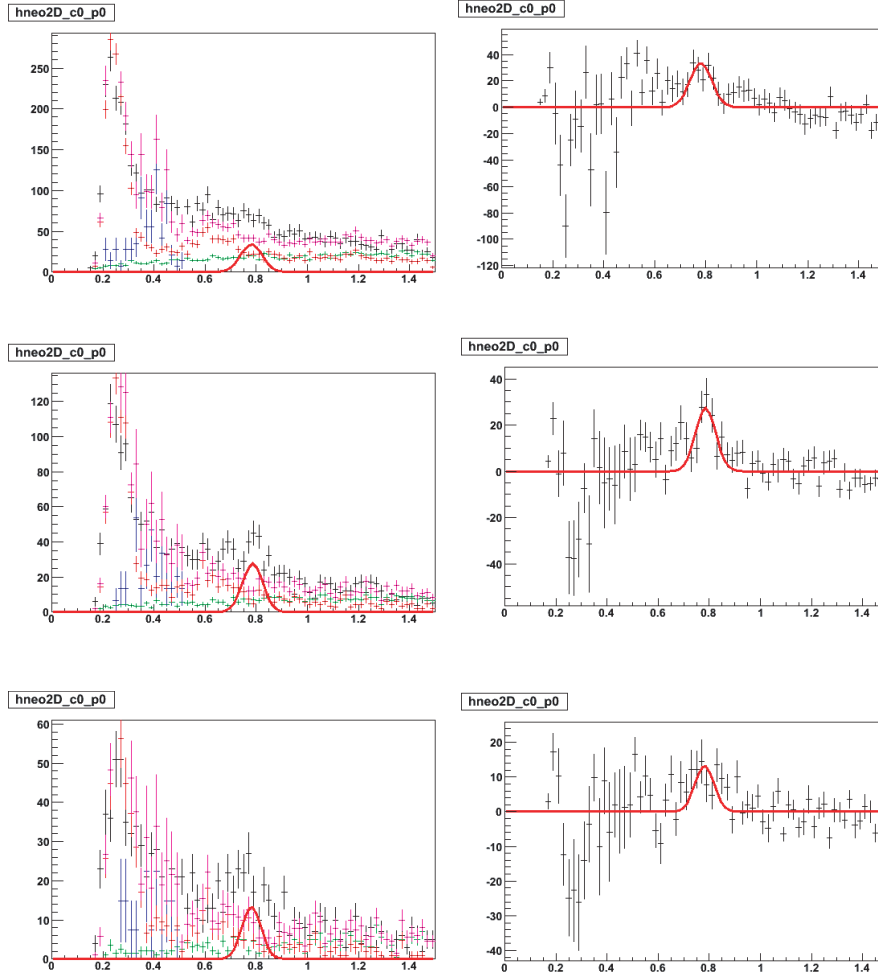


Figure 3.34: Invariant Mass Spectra (20-60% cent, $p_T=8.0$, $p_T=9.0$ and $p_T=10.0$ GeV/ c). Left Side: Black points denote Foreground, Green points denote BG1, Red points denote BG2, Blue points denote BG3 and Magenta points denote BG1+BG2+BG3. Red solid lines denote SG (mean and width are fixed value extracted by the embedding simulation).

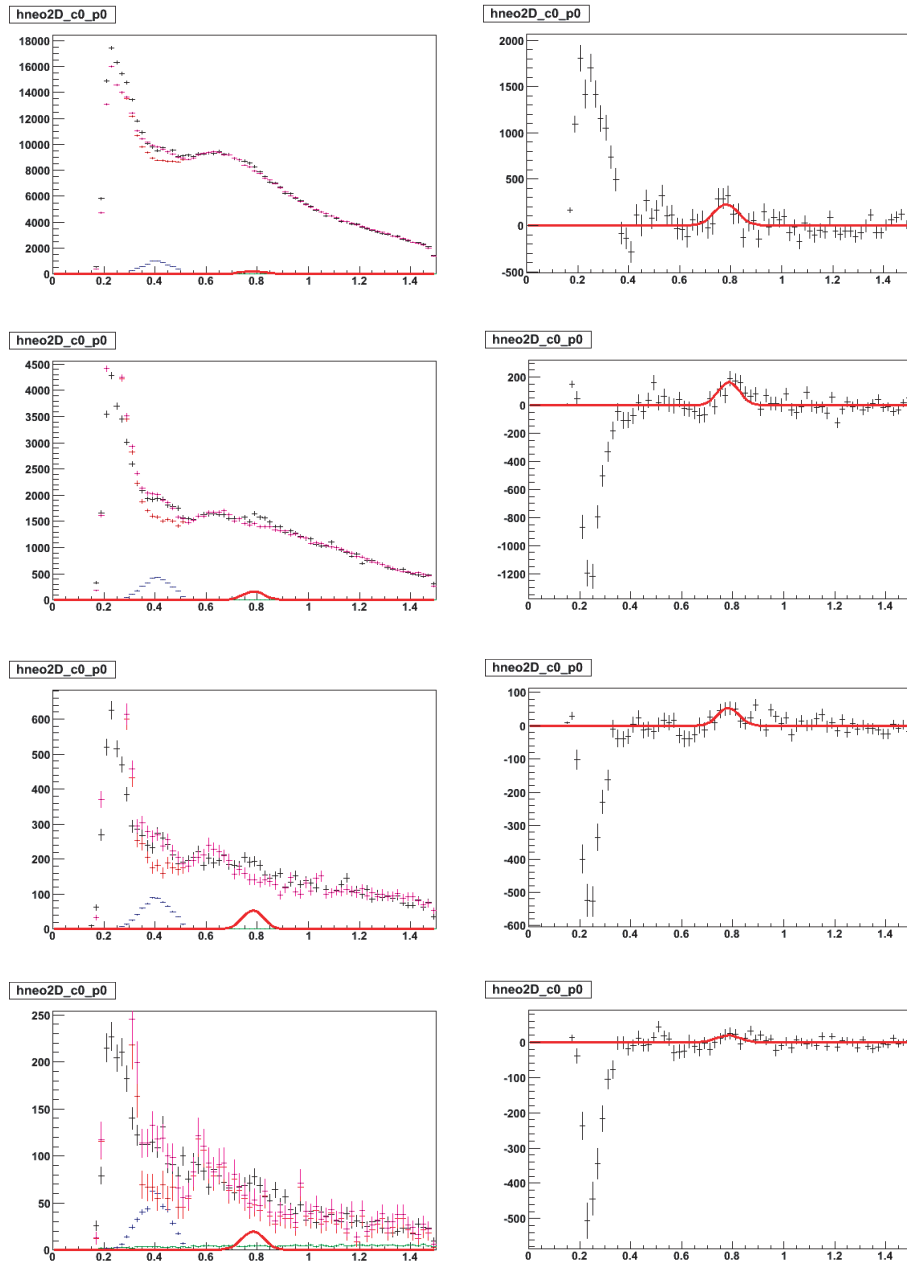


Figure 3.35: Invariant Mass Spectra (60-92% cent, $p_T=3.0$, $p_T=4.0$, $p_T=5.0$ and $p_T=6.0-10.0$ GeV/ c).

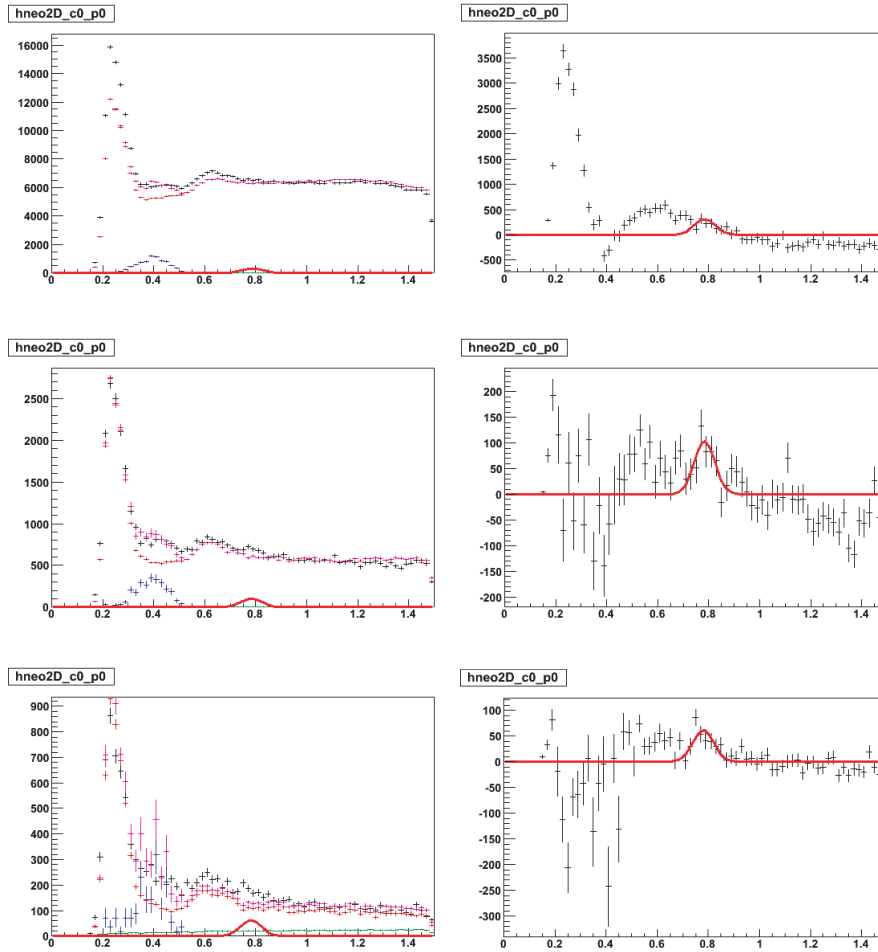


Figure 3.36: Invariant Mass Spectra (0-92% cent, $p_T=6.0$, $p_T=7.0$, $p_T=8.0$ GeV/ c). Left Side: Black points denote Foreground, Green points denote BG1, Red points denote BG2, Blue points denote BG3 and Magenta points denote BG1+BG2+BG3. Red solid lines denote SG (mean and width are fixed value extracted by the embedding simulation).

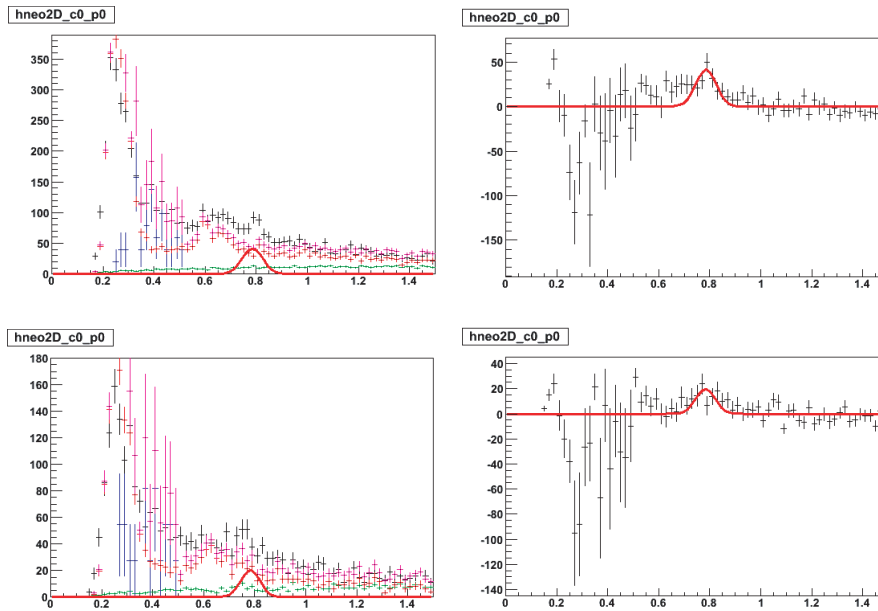


Figure 3.37: Invariant Mass Spectra (0-92% cent, $p_T=9.0$ and $p_T=10.0$ GeV/ c). Left Side: Black points denote Foreground, Green points denote BG1, Red points denote BG2, Blue points denote BG3 and Magenta points denote BG1+BG2+BG3. Red solid lines denote SG (mean and width are fixed value extracted by the embedding simulation).

3.6.2 Run 7

- 0-20% centrality ($N_{evt} = 8.8 \times 10^8$).

p_T	7.5	9.0	11.0
Fit FG (Gaussian)	134	203	87
Error from FitFG	23.1%	29.6%	33.3%

- 20-60% centrality ($N_{evt} = 2.41 \times 10^9$).

p_T	5.5	6.5	7.5	9.0	11.0
Fit FG (Gaussian)	861	337	192	204	87
Error from FitFG	47.8%	30.0%	31.2%	25.0%	31.0%

- 60-92% centrality ($N_{evt} = 1.45 \times 10^9$).

p_T	6.5	7.5	9.0
Fit FG (Gaussian)	101	34	64
Error from FitFG	21.8%	47.1%	25.0%

- 0-92% centrality ($N_{evt} = 4.09 \times 10^9$).

p_T	5.5	6.5	7.5	9.0	11.0
Fit FG (Gaussian)	1160	455	348	425	159
Error from FitFG	32.0%	40.0%	28.7%	18.6%	25.8%

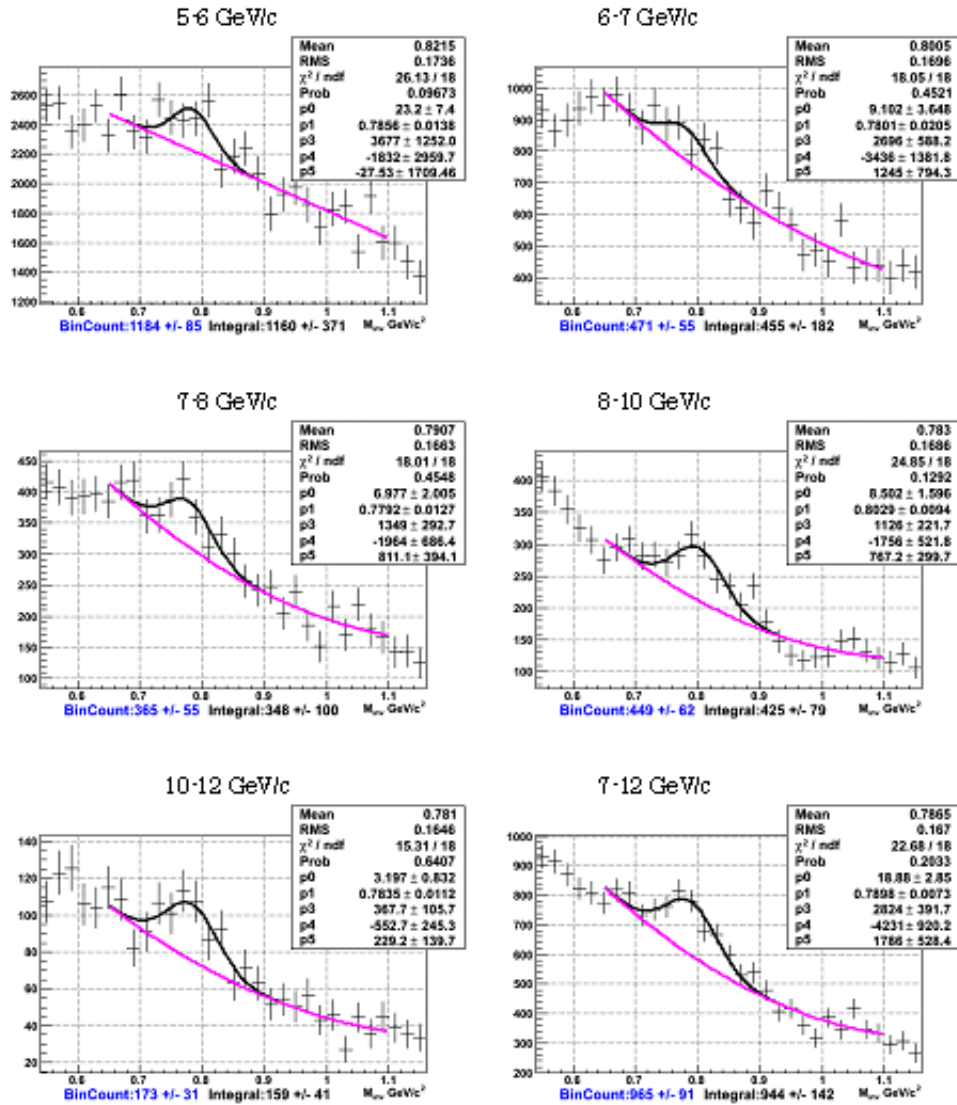


Figure 3.38: Invariant mass spectra at 0-92% centrality.

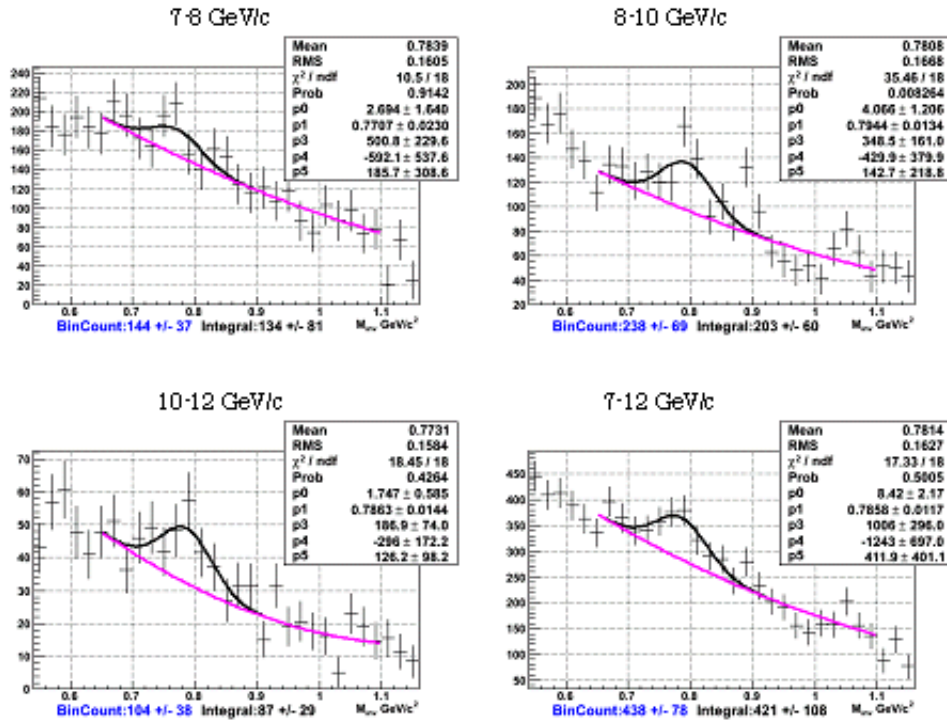


Figure 3.39: Invariant mass spectra at 0-20% centrality.

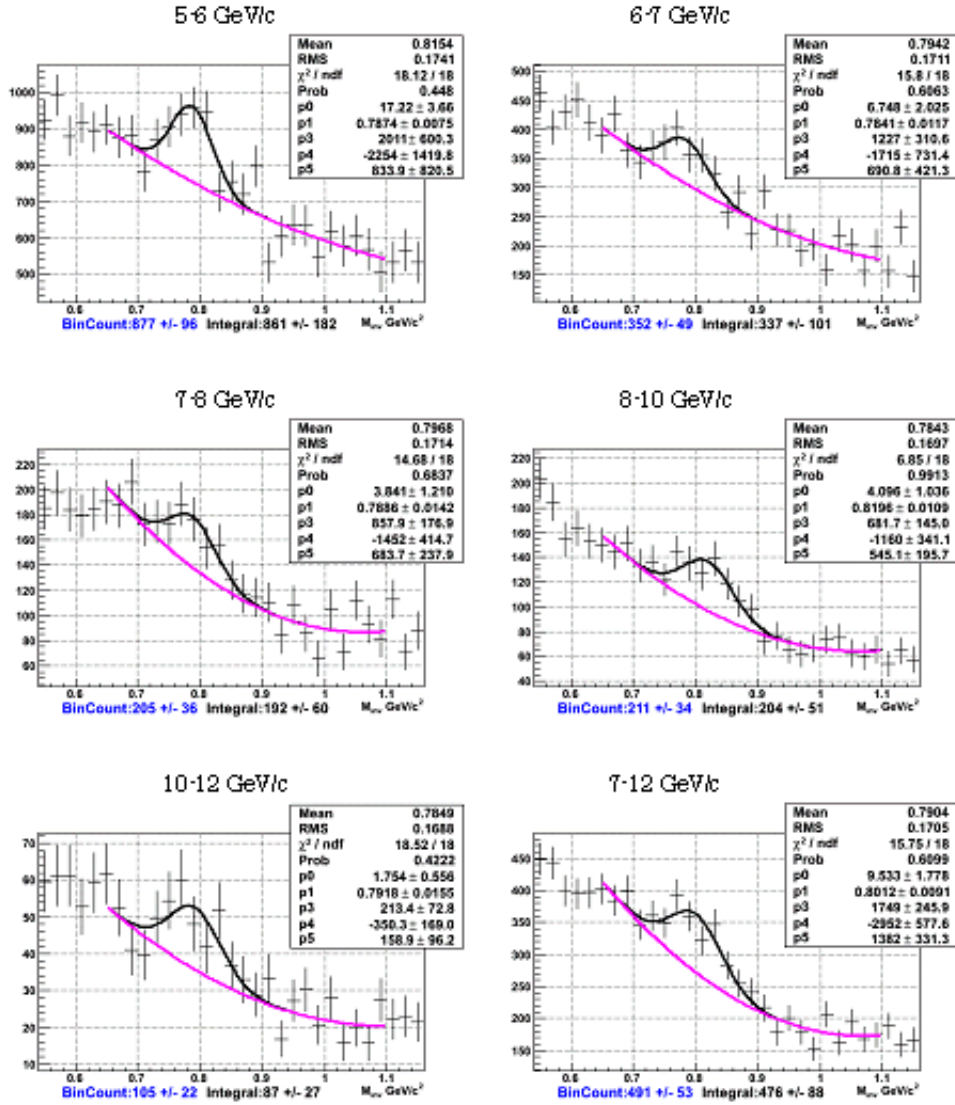


Figure 3.40: Invariant mass spectra at 20-60% centrality.

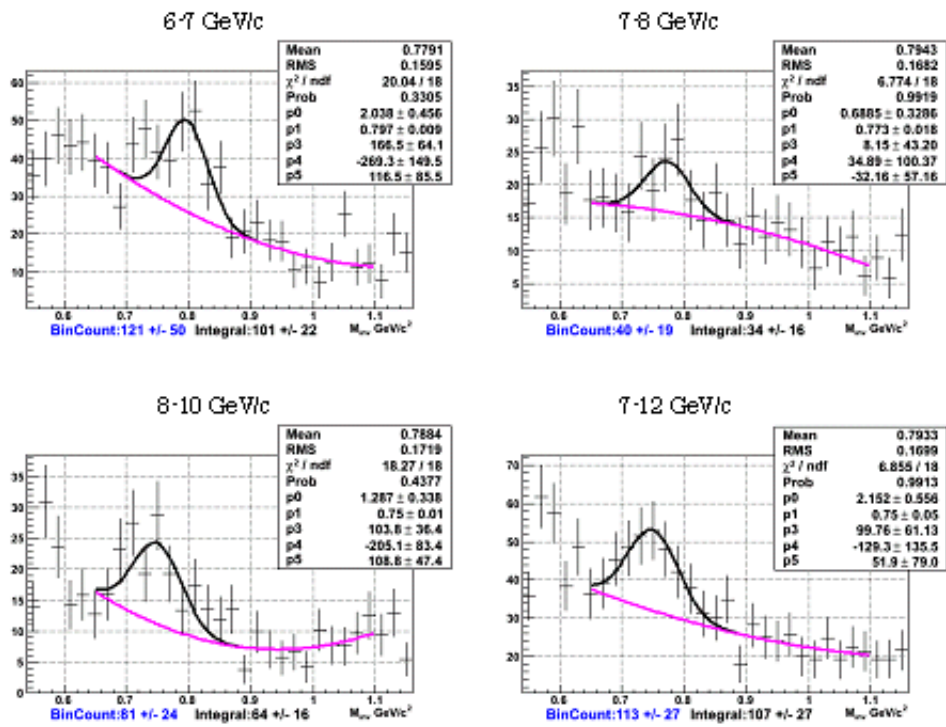


Figure 3.41: Invariant mass spectra at 60-92% centrality.

3.7 Calculation of Invariant Yield

The differential cross section is calculated from the invariant yield as,

$$E \frac{d^3\sigma}{dp^3} = \frac{1}{L} \times \frac{1}{2\pi p_T} \frac{d^2N}{dp_T dy}, \quad (3.5)$$

where L is the luminosity of the collisions.

For a given centrality bin, the invariant yields as a function of p_T in Au + Au are determined from:

$$\frac{1}{2\pi p_T} \frac{d^2N_{cent}}{dp_T dy} \equiv \frac{1}{2\pi p_T N_{cent}^{evt}} \frac{1}{BR} \frac{1}{\epsilon(p_T) \epsilon_{emb}(p_T, cent) \epsilon_{trig}(p_T)} \frac{N(\Delta p_T, cent)}{\Delta p_T \Delta y}, \quad (3.6)$$

where N_{cent}^{evt} is the number of event for each centrality, $N(\Delta p_T, cent)$ is counted number of ω for each p_T and centrality bin, $\epsilon(p_T)$, $\epsilon_{emb}(p_T, cent)$ and $\epsilon_{trig}(p_T)$ are geometrical acceptance, reconstruction efficiency and trigger efficiency, respectively. BR is $8.90 \pm 0.27\%$ is the known $\omega \rightarrow \pi^0 \gamma$ decay branching ratio [20].

3.7.1 Bin Shift Correction

The deviations of the data points from the true spectrum due to the finite bin size can be corrected by moving the points along the y-axis. We put the bin-shift correction for the y-axis as following method.

1. Fit the p_T spectrum with the following Hagedorn function [61]

$$f(p_T) = c \left(\frac{p_0}{p_0 + p_T} \right)^n. \quad (3.7)$$

Here, we use the different function to extract the systematic error described later.

2. Calculate following yield variable, m ,

$$m = \frac{1}{p_T^{max} - p_T^{min}} \cdot \int_{p_T^{min}}^{p_T^{max}} f(p_T) dp_T, \quad (3.8)$$

then calculate the ratio of the value m and the value $f(p_T^{cen})$ of the spectrum at the bin center p_T^{cen} ,

$$r = m / f(p_T^c), \quad (3.9)$$

so then the corrected yield can be obtained as,

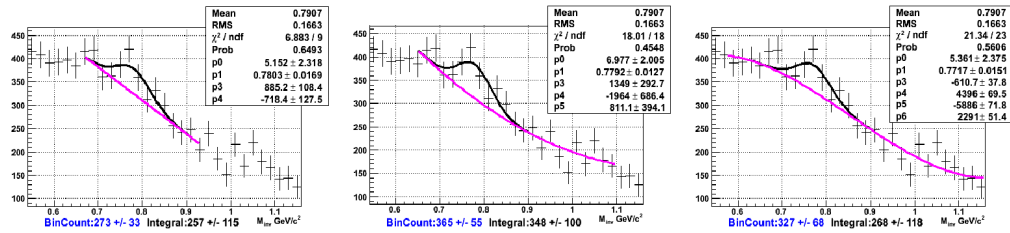
$$Y^{corr} = Y^{uncorr} / r. \quad (3.10)$$

3. Repeat above two steps (iteration).

3.8 Systematic uncertainties

3.8.1 Peak Extraction Uncertainties

Main systematic uncertainties in Au + Au analysis are coming from peak extraction due to the high multiplicity creating large combinatorial backgrounds. To evaluate systematic uncertainties related to raw yields extraction, we use three different fitting function: the first (pol1), the second (pol2), and the third polynomial (pol3) and three different fitting range for each function: Fitting Range A, B, C in the Figure 3.42. The basic fitting function and fitting range are the second polynomial and “Range B” respectively and the variance (RMS/Mean) is added to the peak extraction uncertainty. We then extract the variance (RMS/Mean for different counting method, cuts, fit function, width) as a function of the transverse momentum by constant fitting. Figure 3.43 shows the distribution of the variance in Run7. The estimated value is 25.0% for 0-20% centrality, 19.6% for 20-60% centrality, 33.4% for 60-92% centrality and 23.4% for 0-92% centrality.



(a) Fitting Function (pol1),(b) Fitting Function (pol2),(c) Fitting Function (pol3),
 Fitting Range A (0.67-0.93) Fitting Range B (0.65-1.1) Fitting Range C (0.575-1.18)

Figure 3.42: Examples of fits used for evaluation of raw yield extraction systematic uncertainties.

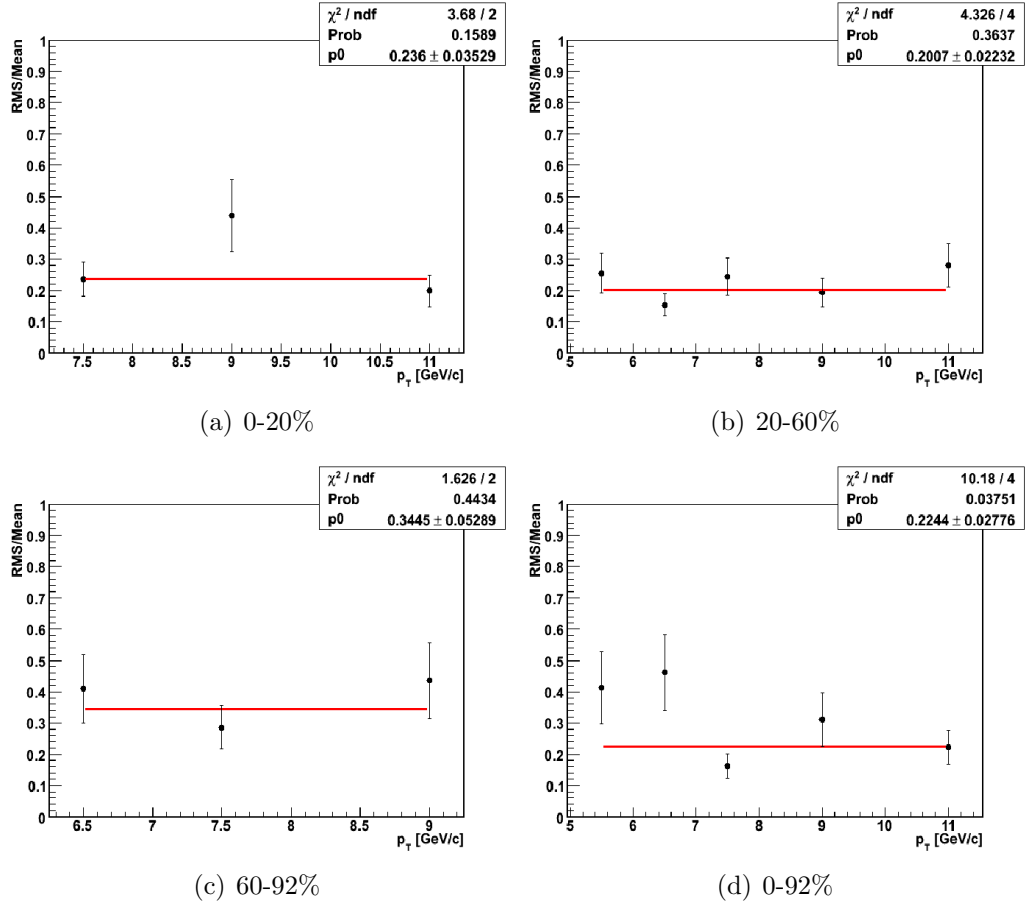


Figure 3.43: Systematic uncertainties for peak extraction in four centrality bins. The values were extracted by constant fitting (solid red line).

3.8.2 Other Errors for Background Scaling (Run4)

Since we did the background scaling for Run4 analysis, we added the systematical uncertainties of scaling by changing the factor of Background Scaling for 6 types ($S1 \pm \Delta S1$, $S2 \pm \Delta S2$, $S3 \pm \Delta S3$), and chose the RMS.

p_T	3.0	4.0	5.0	6.0	7.0	8.0	9.0	10.0
0-20% cent					9.4%		4.1 %	
20-60% cent			7.6%	11.0%	8.1%	1.4%	1.4%	3.4%
60-92% cent	8.5%	23%	11%		17.0%			
0-92% cent					2.5%	1.3%	1.2%	4.1 %

3.8.3 Uncertainties of Bin Shift Correction

We assume different fitting function for the Bin Shift Correction to evaluate the systematic errors.

Fit0 (Basic): Hagedorn function,
 Fit1: $C_1(1 + (p_T/C_2)^{-6})$ function,
 Fit2: Exponential function.

p_T	3.0	4.0	5.0	6.0	7.0	8.0	9.0	10.0
0-20% cent					0.3%	1.3 %		
20-60% cent			0.03%	0.2%	0.3%	0.3%	0.2%	0.1%
60-92% cent	0.9%	0.2%	0.1%	2.9%				
0-92% cent					0.1%	0.2%	0.1%	0.08%

3.8.4 EMC Uncertainties

The results of EMC energy resolution uncertainty and energy scale uncertainty are used from [55]. It shows slight p_T dependence on the level of 1%.

p_T	3.0	4.0	5.0	6.0	7.0	8.0	9.0	10.0
EMC geom.acceptance	18%							
EMC energy resolution		2%	2%	2%	2%	3%	3%	3%
EMC energy scale	3%	3%	4%	5%	6%	7%	11%	17%
Conversion	4.5%							

3.8.5 Acceptance Correction

Uncertainty of calculated acceptance and embedding corrections is dominated by statistical errors in peak extraction in Monte-Carlo and was estimated to be 3-6 % (used from [55]).

3.8.6 Conversion Correction Uncertainty

We used results from [6] where the photon conversion was estimated for π^0 and η mesons decaying into two photons. The uncertainties quoted there are below 3% then we multiplied the results by 3/2. Since HBD configuration is changed during the run (HBD west was taken off in 707M events out of 4.1B), we applied the correction to the total yield by using the estimated values of photon conversion for π^0 and η in HBD [6]. We multiplied the lost factor of π^0 (8%) by 3/2 and estimated the correction factor to the total

yield as 1.04. For a systematic uncertainty of this correction, we scaled 30% (a fraction value of yield from [6]) to the lost factor and the evaluated error is 1.2%.

3.8.7 Branching Ratio Uncertainties

PDG branching ratios [20] uncertainty for the $\omega \rightarrow \pi^0\gamma$ decay is 3.4%.

3.8.8 N_{part} and N_{coll} Uncertainty

A Glauber Monte Carlo [31] with the BBC and ZDC responses was used to estimate the number of binary nucleon-nucleon collisions (N_{coll}) and the number of participating collisions (N_{part}) for each centrality bin [89]. The following Table shows N_{part} and N_{coll} values and systematic error used for this analysis.

Table 3.2: The number of participating collisions ($\langle N_{part} \rangle$) and the number of binary nucleon-nucleon collisions ($\langle N_{coll} \rangle$).

System	$\langle N_{part} \rangle$	$\langle N_{coll} \rangle$
Au+Au MinBias	109.1±4.1	257.8±25.4
Au+Au 0-20%	280.5±4.6	783.2±77.5
Au+Au 20-60%	101.6±5.4	197.5±20.8
Au+Au 60-92%	11.8±2.1	11.5±2.5
Cu+Cu MinBias	34.6±1.2	51.8±5.6
Cu+Cu 0-20%	85.9±2.3	151.8±17.1
Cu+Cu 20-60%	33.2±1.6	41.9±4.8
Cu+Cu 60-94%	6.5±0.6	5.1±0.7

3.8.9 Summary

A summary of assigned systematic uncertainties is listed in Table 3.3 for $\omega \rightarrow \pi^0\gamma$ in Au + Au. Those are classified into three types: Type A is p_T -uncorrelated, Type B is p_T -correlated and Type C is the overall normalization uncertainty.

Table 3.3: Summary of assigned systematic errors in Au + Au analysis.

Source	Au+Au(Run4)	Au+Au(Run7)
peak extraction	21-40%	20.1-34.5% (A)
conversion (HBD loss)	N/A	1.2% (B)
energy scale		4-7% (B)
energy resolution		2-3% (B)
acceptance correction		3-6% (B)
conversion (other)		4.5% (C)
branching ratio		3.4% (C)

Chapter 4

Results and Discussion

4.1 Invariant Yields

Invariant transverse momentum spectra measured for the ω meson in Au+Au collisions at $\sqrt{s_{NN}}=200$ GeV are shown in Figure 4.1. Results are presented for three centrality bins: 0-20%, 20-60%, 60-92% and minimum bias collisions. The dashed lines represent N_{coll} scaled fits to $p+p$ results, where N_{coll} values were shown in Section 3.8. The results show that in peripheral heavy ion collisions the ω production generally follows binary scaling (points are along the dashed line or slightly above it), while in mid-central and central collisions the ω is suppressed at high p_T (points are significantly below than the dashed line). Such behavior is similar to one previously observed for other light mesons [5, 90] and can be attributed to medium induced effects.

Comparison with other collision systems

Figure 4.2 shows a comparison with the spectra measured in Cu+Cu collisions for three centrality bins: 0-20%, 20-60%, 60-94% and minimum bias collisions [7]. The results of Cu+Cu also show the same suppression pattern as Au+Au, though the suppression is less obvious. This is considered to be due to less multiplicity of Cu+Cu than Au+Au : N_{coll} is 51.8 ± 5.6 for Cu+Cu collisions (minimum bias) and N_{coll} is 257.8 ± 25.4 for Au + Au collisions (minimum bias). This centrality dependence will be discussed in the later section by introducing the nuclear modification factor.

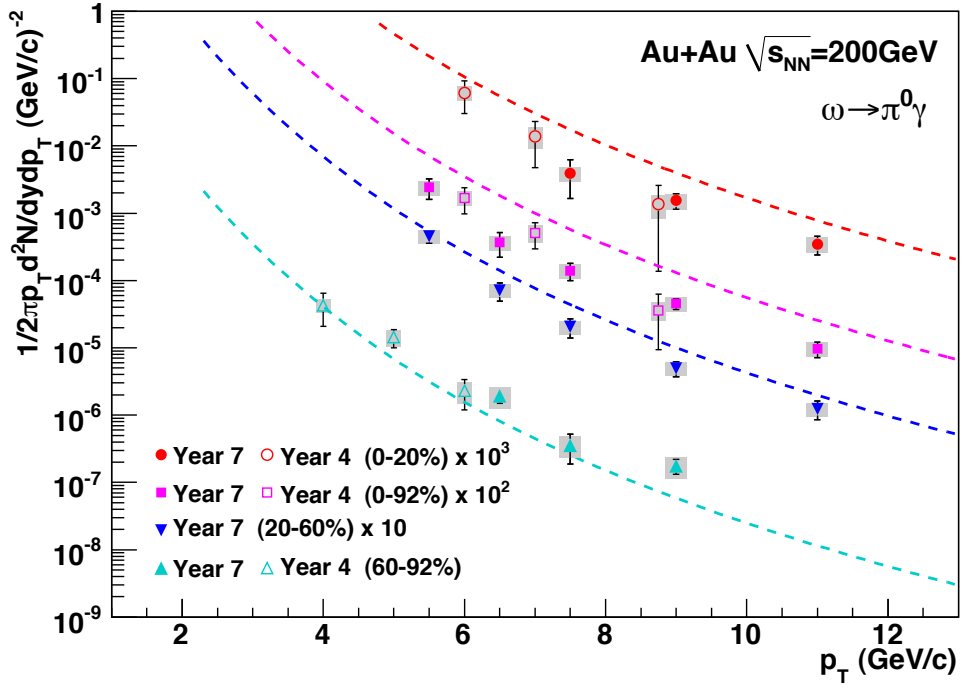


Figure 4.1: Invariant transverse momentum spectra of the ω in Au + Au from the $\omega \rightarrow \pi^0 \gamma$ decay channel for three centrality bins and minimum bias. The dashed lines are the $p + p$ results scaled by the corresponding number of binary collisions: N_{coll} values used for the scaling were shown in Section 3.8.

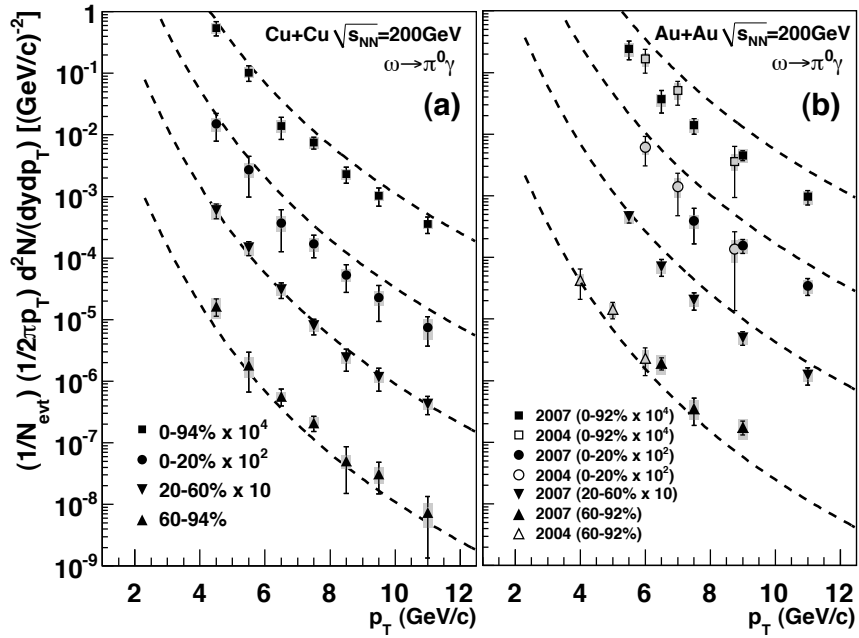


Figure 4.2: Invariant transverse momentum spectra of the ω production in (a) Cu + Cu and (b) Au + Au collisions from the $\omega \rightarrow \pi^0 \gamma$ decay channel for three centrality bins and minimum bias (this work). The dashed lines are the $p+p$ results scaled by the corresponding number of binary collisions: N_{coll} values used for the scaling were shown in Section 3.8. The (a) Cu + Cu data were recorded in 2005 and the (b) Au + Au data were recorded in 2004 (Year 4) and 2007 (Year 7).

4.2 The ω/π Ratio

In calculating the ω/π ratio the same methodology from [42, 5, 19] for the π^+/π^- and π^0 was used. The charged pion results, $(\pi^+ + \pi^-)/2$, were used to extend neutral pion measurements at the lower limit of the p_T domain from 1 to 0.2 GeV/ c . Inclusion of the charged pion spectrum in the fit has a small effect in the 1-2 GeV/ c overlap region, and is smaller than 5%, compared to the fit result with neutral pions alone.

The ω/π ratios measured in Au + Au (0-92, 0-20, 60-92%) collisions at $\sqrt{s_{NN}}=200$ GeV are presented in Figure 4.3. As in the case of $p + p$ and d + Au collisions described in Section 1.4.2, there is no indication that the ratios depend on transverse momentum for $p_T > 2$ GeV/ c . The dashed lines show a fit of constant value at $p_T > 2$ GeV/ c : $0.83 \pm 0.09(\text{stat}) \pm 0.06(\text{sys})$ in minimum bias Au + Au. The centrality dependence is not clearly seen due to the large statistical errors (shown as bars) and systematic errors (shown as boxes): the constant value is $1.34 \pm 0.23(\text{stat}) \pm 0.1(\text{sys})$ in 0-20% and $1.51 \pm 0.21(\text{stat}) \pm 0.37(\text{sys})$ in 60-92%. The same procedure as for $\langle \pi \rangle$ references [42, 5, 19] is used for extracting systematic error.

Comparison with other collision systems

As a comparison, the results of Cu + Cu are together shown in Figure 4.4, where the constant fit values are $0.71 \pm 0.07(\text{stat}) \pm 0.07(\text{sys})$ in minimum bias ($0.64 \pm 0.10(\text{stat}) \pm 0.08(\text{sys})$ in 0-20% and $1.32 \pm 0.24(\text{stat}) \pm 0.29(\text{sys})$ in 60-94%). The dashed lines and boxes are a fit of constant value to data points at $p_T > 2$ GeV/ c in $p + p$ from [7] (fit result: $0.81 \pm 0.02(\text{stat}) \pm 0.09(\text{sys})$). Both Cu + Cu and Au + Au results are consistent with the constant value in $p + p$ within statistical and systematic errors.

To see more clearly, we plot those constant values as a function of centrality (N_{part}) with statistical and systematic combined errors in Figure 4.5. In addition to $p + p$ and Cu + Cu, d + Au results are added from [7]. The dashed line shows a fit of constant value for all points, resulting 0.79 ± 0.04 with $\chi^2/\text{ndf} = 12.11/7$ and probability $\sim 10\%$. Within the uncertainties the ω/π ratios measured in different collision systems for $p_T > 2$ GeV/ c are in agreement. This agrees with previous measurements in $p + p$ and d + Au [10] within the uncertainties. Therefore, the ratios in various collision systems assume similar suppression factors and p_T dependences within the uncertainties for the ω and π production in nucleus-nucleus collisions at high p_T .

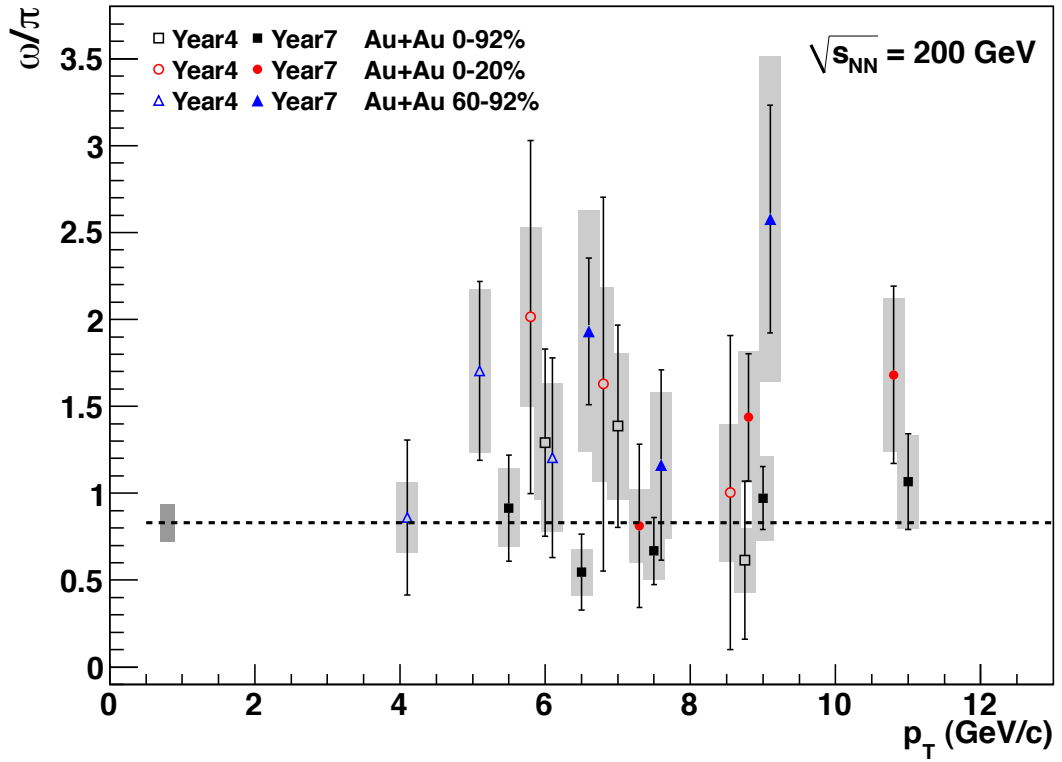


Figure 4.3: The ω/π ratio versus transverse momentum in Au + Au (0-92, 0-20, 60-92%) for the $\omega \rightarrow \pi^0\gamma$. The dashed lines and boxes are fitted of constant values and overall errors in minimum bias (fit results: $0.83 \pm 0.09(\text{stat}) \pm 0.06(\text{sys})$).

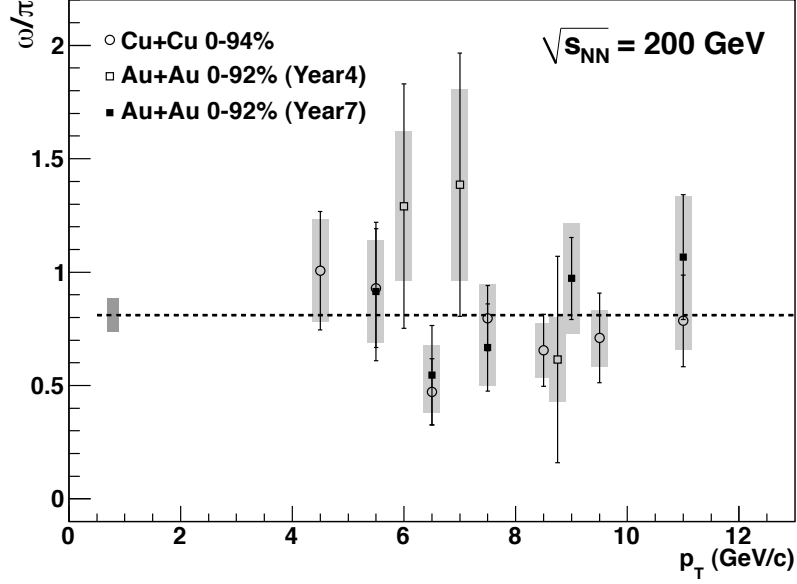


Figure 4.4: The ω/π ratio versus transverse momentum in Cu + Cu (0-94%) for the $\omega \rightarrow \pi^0\gamma$ and in Au + Au (0-92%) for the $\omega \rightarrow \pi^0\gamma$. The dashed lines and boxes are a fit of constant value to data points at $p_T > 2$ GeV/c in $p + p$ [7] (fit result: $0.81 \pm 0.02(\text{stat}) \pm 0.09(\text{sys})$).

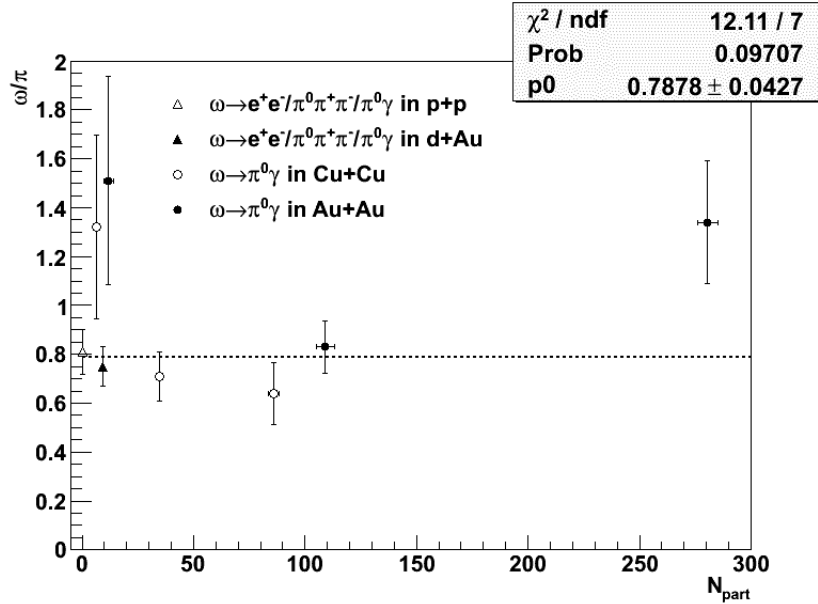


Figure 4.5: Constant fitting values of the ω/π at $p_T > 2$ GeV/c as a function of centrality (N_{part}): $0.75 \pm 0.01(\text{stat}) \pm 0.08(\text{sys})$ in d+Au, $0.71 \pm 0.07(\text{stat}) \pm 0.07(\text{sys})$ in MB Cu + Cu ($0.64 \pm 0.10(\text{stat}) \pm 0.08(\text{sys})$ in 0-20% and $1.32 \pm 0.24(\text{stat}) \pm 0.29(\text{sys})$ in 60-94%), and $0.83 \pm 0.09(\text{stat}) \pm 0.06(\text{sys})$ in MB Au + Au ($1.34 \pm 0.23(\text{stat}) \pm 0.1(\text{sys})$ in 0-20% and $1.51 \pm 0.21(\text{stat}) \pm 0.37(\text{sys})$ in 60-92%). Error bars are combined statistical and systematic values. The dashed line shows a fit of constant value to this plot (0.79 ± 0.04).

4.3 The Nuclear Modification Factor

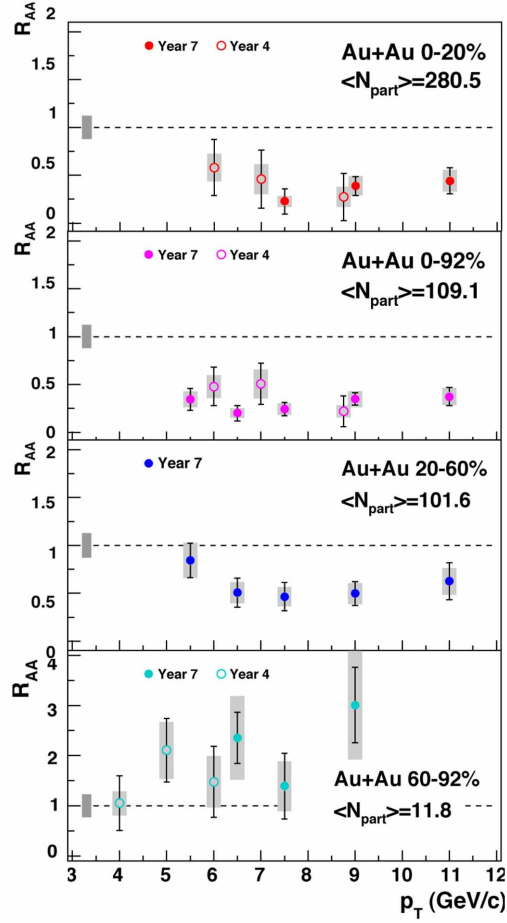


Figure 4.6: R_{AA} of the ω in Au + Au for the $\omega \rightarrow \pi^0 \gamma$ decay channel for three centrality bins and minimum bias. The uncertainty in the determination of $p + p$ scaling is shown as a box on the left in each plot.

As described in Section 1.3.1, a suppression pattern of the ω production due to the medium-induced effects can be quantified by the nuclear modifi-

cation factor,

$$R_{AA}(p_T) = \frac{d^2 N_{AA}/dydp_T}{(\langle N_{coll} \rangle / \sigma_{pp}^{inel}) \times d^2 \sigma_{pp}/dydp_T}.$$

We divide our results of the invariant yield of the ω by the $p+p$ results scaled by the number of binary collisions for each centrality. Figure 4.6 shows the nuclear modification factor, R_{AA} of the ω as a function of p_T in the three centrality bins and minimum bias in Au + Au. The multiplicity increases from the bottom ($\langle N_{part} \rangle = 11.8$) to the top ($\langle N_{part} \rangle = 280.5$). It shows that R_{AA} is generally suppressed below 1 if the centrality ($\langle N_{part} \rangle$) goes higher.

Comparison with other collision systems

As a comparison, the nuclear modification factor measured in Cu + Cu and Au + Au collisions at $\sqrt{s_{NN}}=200$ GeV as a function of p_T are together shown in Figure 4.7. Results are presented for minimum bias, most central (0-20%), mid-central (20-60%) and peripheral (60-94% in Cu + Cu; 60-92% in Au + Au) collisions. The nuclear modification factors do not depend on p_T for $p_T > 6$ GeV/c at all centralities. For $N_{part} > 34$ suppression of the ω production begins to be observed (between 0-20% and 20-60% in Cu + Cu), with suppression increasing as N_{part} increases. The nuclear modification factors for π^0 in Cu + Cu [19] and Au + Au [5] are shown as a comparison (depicted as rhombuses in Figure 4.7). The ω results are consistent with the π^0 within the uncertainties.

To see the universal p_T dependence of R_{AA} for the π^0 , the η and the ω in all collision systems, we plot integrated R_{AA} values for $p_T > 7$ GeV/c as a function the number of participants shown as Figure 4.8. Our results are $0.25 \pm 0.06(\text{stat}) \pm 0.06(\text{sys})$ for Au + Au 0-20% ($N_{part} = 280.5$), $0.43 \pm 0.08(\text{stat}) \pm 0.09(\text{sys})$ for Au + Au 20-60% ($N_{part} = 101.6$), and $1.76 \pm 0.45(\text{stat}) \pm 0.63(\text{sys})$ for Au + Au 60-92% ($N_{part} = 11.8$). In addition to our results, we present four centrality bins in d + Au, three centrality bins in Cu + Cu for the ω mesons. For comparison the average values of R_{AA} for π^0 [5] and η mesons [6] for $p_T > 7$ GeV/c are plotted. To see whether the ω follows the suppression pattern of π^0 and η , integrated R_{AA} of the N_{part} dependence is fit to a fractional energy loss function $R_{AA} = (1 - S_0 N_{part}^a)^{n-2}$ [5, 27]. The parameter n is an exponent of the power law fit to the ω p_T spectrum measured in $p+p$ for $p_T > 5$ GeV/c [54], fixed to 8. The fitting gives χ^2/ndf less than three and parameters $S_0 = (9.9 \pm 0.7) \times 10^{-3}$ and $a = 0.55 \pm 0.01$.

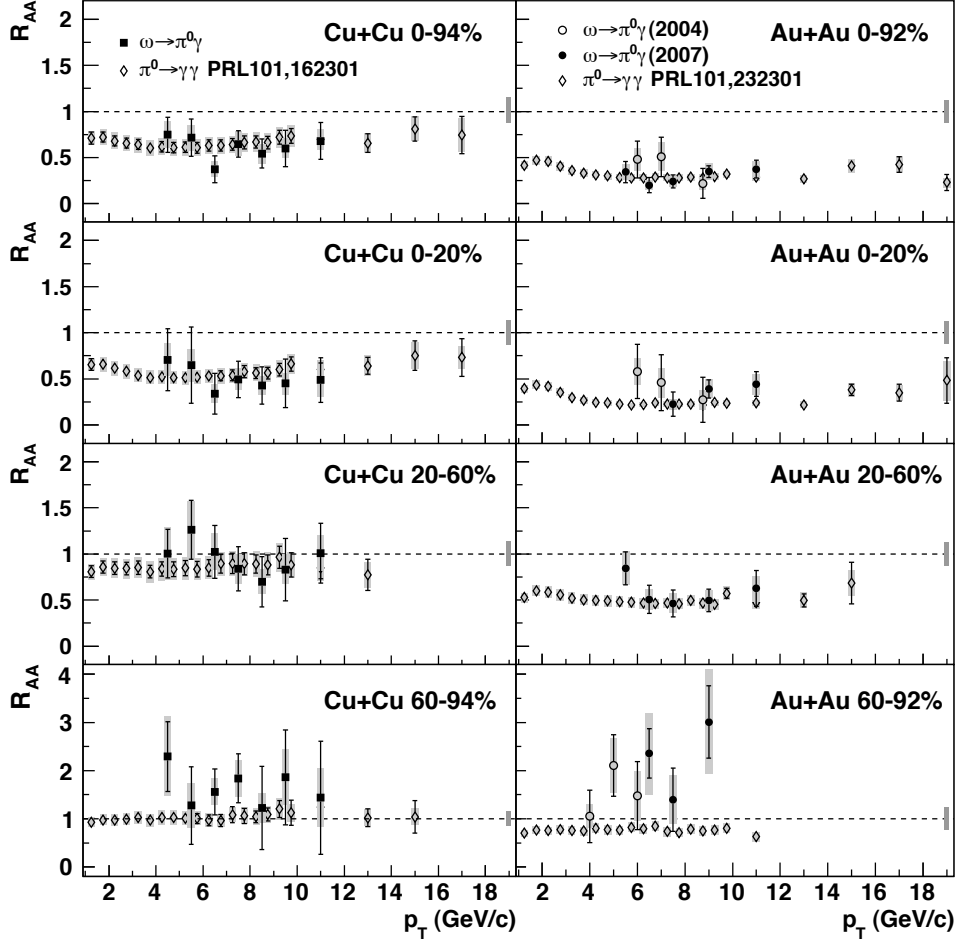


Figure 4.7: R_{AA} of the ω in Cu+Cu (left) and Au+Au (right) from $\omega \rightarrow \pi^0\gamma$ decay channel for three centrality bins and minimum bias. The uncertainty in the determination of $p+p$ scaling is shown as a box on the left in each plot. Rhombuses in each plot are R_{AA} of the π^0 in Cu+Cu [19] and Au+Au [5] shown as a comparison.

As in [5] we find parameter a consistent with predictions of the GLV and PQM models ($a \sim 2/3$, see the Section 1.3.2). Therefore, we can conclude that the ω production has similar suppression pattern as π^0 and η which supports the scenario that the energy loss takes place at the parton level in the hot and dense medium formed in the collisions. The consistency of the

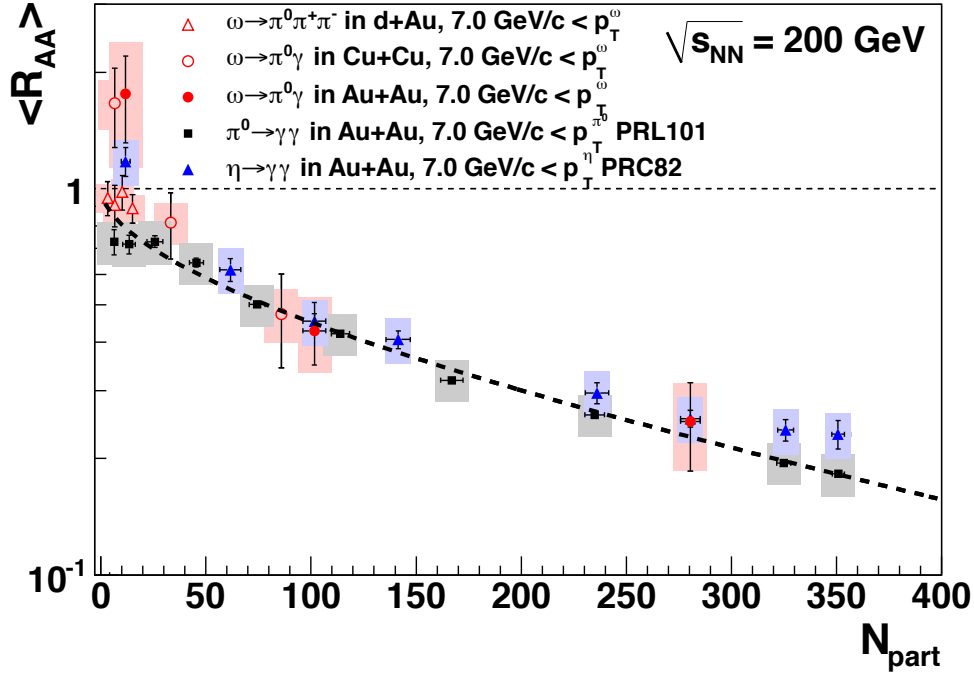


Figure 4.8: R_{AA} for the ω meson integrated over the range $p_T > 7$ GeV/c as a function of the number participating nucleons (N_{part}). Results for π^0 's and η 's R_{AA} are shown for comparison. Squares correspond to $\pi^0 \rightarrow \gamma\gamma$ where $p_T(\pi^0) > 7$ GeV/c [5], triangles correspond to $\eta \rightarrow \gamma\gamma$ where $p_T(\eta) > 7$ GeV/c [6] and other points (closed circle, opened circle and opened triangle) correspond to our results. The dashed line shows fitted fractional energy loss function, $R_{AA} = (1 - S_0 N_{part}^a)^{n-2}$.

model and the results suggests that particle production in central collisions is 'surface' dominated.

Chapter 5

Summary and Conclusion

In summary, we measured the ω meson production via the hadronic decay mode ($\pi^0\gamma$) in Au + Au collisions at C.M.S. collision energy per nucleon pairs of 200 GeV taken at the PHENIX experiment.

The invariant yields show that the ω production has a suppression pattern at high transverse momentum, which is similar to that of π^0 and η in central and mid-central collisions, but no suppression is observed in peripheral collisions. As the previous conclusions for the π^0 and η , this results suggest the hot and dense medium formed in central and mid-central Au + Au collisions could affect the ω production, since there is no such effect observed in an absence of the hot and dense medium in peripheral collisions.

The ω/π ratio has no indication of a dependence on transverse momentum and the constant fit shows $0.83 \pm 0.09(\text{stat}) \pm 0.06(\text{sys})$ in Au + Au minimum bias. This value is consistent with other collision systems: $p + p$, $d + \text{Au}$, and $\text{Cu} + \text{Cu}$ within the uncertainties.

The nuclear modification factor R_{AA} shows below 1 in central and mid-central collisions and those values are consistent with $\text{Cu} + \text{Cu}$ collisions at similar numbers of participant nucleons. Finally, integrated R_{AA} of the ω of $p_T > 7 \text{ GeV}/c$ in Au + Au is shown as a function of the number of participants (N_{part}) together with the results in $d + \text{Au}$ and $\text{Cu} + \text{Cu}$ for the ω , also with the π^0 and the η in Au + Au. The results clearly show that all R_{AA} have systematically same suppression pattern in a dependence of the number of participants: fit results of a fractional energy loss function $R_{AA} = (1 - S_0 N_{\text{part}}^a)^{n-2}$ give χ^2/ndf less than three and parameters $S_0 = (9.9 \pm 0.7) \times 10^{-3}$ and $a = 0.55 \pm 0.01$. This supports the scenario that the energy loss takes place at the parton level in the hot and dense medium formed in

the collisions.

This thesis provides systematical results that indicates the hot and dense matter, the QGP is created in central Au + Au collisions at RHIC. Not only for π and η , but also ω mesons showing the same suppression pattern will give a light to clear understanding of the phase transition and the particle production mechanism in the relativistic heavy-ion collisions. This measurement, for the first time, permits the study of ω suppression at high p_T in the PHENIX experiment.

Acknowledgements

First of all, I would like to express my gratitude to my supervisor, Prof. K. Shigaki who supported my long journey. The original idea of the ω measurement via $\pi^0\gamma$ in the PHENIX belongs to him.

I greatly thank Prof. T. Sugitate for his continuous guidance in the Hiroshima group. Among the group, I would like to appreciate Dr. K. Homma for his insightful suggestions to the analysis. I would like to thank Dr. H. Torii, Dr. T. Horaguchi, Dr. T. Hachiya, Dr. T. Nakamura and Mr. Y. Tsuchimoto who taught me much knowledge and many technical skills of the analysis. Also, I would like to express my appreciation to whom I worked together in the group in 2004-2010: Dr. H. Harada, Mr. K. Haruna, Mr. Y. Nakamiya, Mr. D. Watanabe, Mr. K. Yamaura, Dr. K. M. Kijima, Mr. M. Nihashi and Mr. Y. Iwanaga.

I must acknowledge Dr. H. En'yo and Dr. K. Ozawa for the financial support during JRA at RIKEN and all my stays at BNL. Without their agreements of my travel to BNL, this work would not have been completed.

I have greatly benefited from many mentors at BNL, including Dr. Y. Akiba, Dr. T. Sakaguchi, Dr. D. Gabor, Dr. S. Bathe, Dr. T. Isobe, and Dr. A. Milov. Either in the physics working group meetings or in the private discussions, those people provided me fruitful suggestions that improved my analysis.

I would like to express my sincere gratitude from the bottom of my heart to the member of the Paper Preparation Group 118. First and foremost, Dr. V. Riabov provided vital contributions to the paper. It was wonderful that we could collaborate and made the paper final together. I also need to acknowledge Dr. D. Jouan, Dr. D. Sharma, Dr. D. Ivanishev and Dr. D. Winter for many iterated discussions, needless to say Mr. Y. Nakamiya, Dr. K. M. Kijima and Prof. K. Shigaki from the same group. Many thanks to Dr. W. Craig, Dr. D.H. Eric, and Dr. B. V. Jacak for the proof reading



Figure 5.1: The PHENIX collaboration (taken on May 2008).

of the paper. Of course, I and PPG118 greatly thank Dr. B. Johnson for finalizing the submission of the paper.

I would like to acknowledge the staff of the Collider-Accelerator and Physics Departments at BNL and the staff of the other PHENIX participating institutions for their vital contributions. I am more than happy to have been able to experience one of the cutting edge physics research with many wonderful people.

Lastly, I would like to thank my father and mother, Nobuyuki and Chizuko for watching over my activities, as always.

Appendix A

Kinematics

Here, we describe the coordinate and the kinematic variables that are commonly used in the PHENIX experiment.

Coordinate

The coordinate system of the PHENIX experiment is shown in the Figure A.1. The axis of collision (beam axis) is defined as the z axis. Components along the beam axis are called as the longitudinal components, while components lying on the x - y plane are called as the transverse components. ϕ is the polar angle measured from the z axis and θ is the azimuthal angle measured clockwise from the x axis.

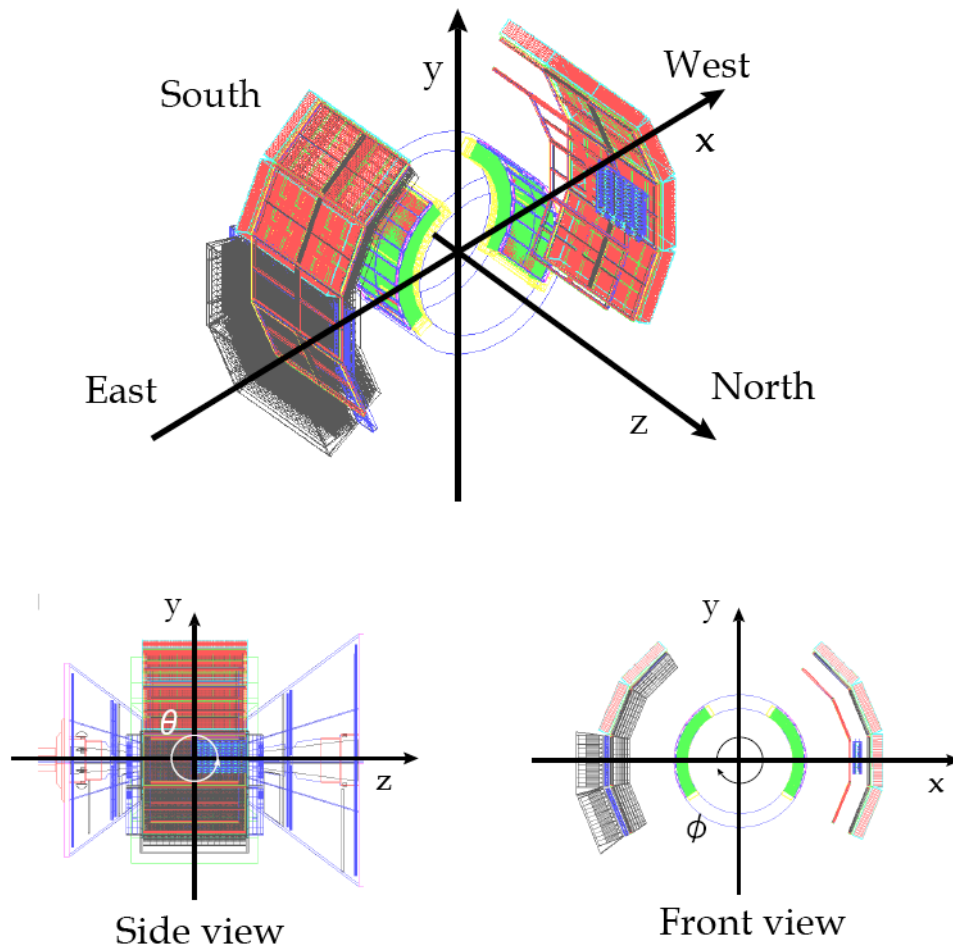


Figure A.1: Coordinates of the PHENIX experiment.

Energy and Momentum

The relativistic energy allows to use the natural units, $c = \hbar = 1$. So then the energy of the particle is written as,

$$E = \sqrt{\mathbf{p}^2 + m},$$

and the momentum composed of 4-vectors is written as,

$$p = (E, \mathbf{p}),$$

The component along the beam-axis, the longitudinal momentum is defined as,

$$p_z = p \cos \theta,$$

where p is the magnitude of particle's momentum. While the transverse momentum, which is a Lorentz invariant is given as,

$$p_T = \sqrt{p_x^2 + p_y^2} = p \sin \theta.$$

Rapidity and Pseudorapidity

The longitudinal variable, the rapidity y , is commonly used. It is defined as,

$$y = \frac{1}{2} \ln \left(\frac{E + p_z}{E - p_z} \right) = \frac{1}{2} \ln \left(\frac{1 + \beta \cos \theta}{1 - \beta \cos \theta} \right)$$

If we go to higher energy that the momentum relatively much higher than the mass, i.e. $E \simeq p$, the rapidity is translated as the pseudorapidity defined as,

$$\eta = -\frac{1}{2} \ln \left(\tan \frac{\theta}{2} \right).$$

Appendix B

Data Table

- Table B.1 : The invariant yield of the $\omega \rightarrow \pi^0\gamma$ in Au + Au (Run4).
- Table B.2 : The Invariant yield of the $\omega \rightarrow \pi^0\gamma$ in Au + Au (Run7).
- Table B.3 : The ω/π of the $\omega \rightarrow \pi^0\gamma$ in Au + Au in 0-20% , 60-92% and minimum bias in Run4.
- Table B.4 : The ω/π of the $\omega \rightarrow \pi^0\gamma$ in Au + Au in 0-20% , 60-92% and minimum bias in Run7.
- Table B.5 : R_{AA} of the $\omega \rightarrow \pi^0\gamma$ in Au + Au (Run4).
- Table B.6 : R_{AA} of the $\omega \rightarrow \pi^0\gamma$ in Au + Au (Run7).

Table B.1: The invariant yield of the $\omega \rightarrow \pi^0\gamma$ in Au + Au (Run4).

MB				0-20%		
p_T	Inv.Yield	Sta.error	Sys.error	Inv.yield	Sta.error	Sys.error
6.0	0.167594	0.0700198	0.0418985	0.00615277	0.0031003	0.00153819
7.0	0.0508239	0.021302	0.0152472	0.00139437	0.000921993	0.000474086
8.75	0.00361534	0.00267718	0.0010846	0.000136339	0.000122705	5.31722e-05
60-92%						
p_T	Inv.Yield	Sta.error	Sys.error			
4.0	4.29123e-05	2.21782e-05	9.86983e-06			
5.0	1.43776e-05	4.33705e-06	3.88195e-06			
6.0	2.30315e-06	1.09843e-06	8.06102e-07			

Table B.2: The invariant yield of the $\omega \rightarrow \pi^0\gamma$ in Au + Au (Run7).

MB				0-20%		
p_T	Inv.Yield	Sta.error	Sys.error	Inv.yield	Sta.error	Sys.error
5.5	2.4245e-05	8.0893e-06	5.83901e-06	-	-	-
6.5	3.67722e-06	1.4738e-06	8.85599e-07	-	-	-
7.5	1.39051e-06	3.99605e-07	3.37469e-07	3.93791e-06	2.27783e-06	9.99493e-07
9.0	4.54189e-07	8.44257e-08	1.11439e-07	1.54742e-06	3.93335e-07	3.96699e-07
11.0	9.61529e-08	2.47941e-08	2.3592e-08	3.45858e-07	1.0491e-07	8.86645e-08
20-60%				60-92%		
p_T	Inv.yield	Sta.error	Sys.error	Inv.yield	Sta.error	Sys.error
5.5	4.56919e-05	9.69812e-06	1.00341e-05	-	-	-
6.5	7.08452e-06	2.12564e-06	1.55579e-06	1.91824e-06	4.17834e-07	6.83201e-07
7.5	2.03551e-06	6.4135e-07	4.51159e-07	3.55683e-07	1.6738e-07	1.27129e-07
9.0	4.96882e-07	1.2422e-07	1.11578e-07	1.75408e-07	4.38521e-08	6.30128e-08
11.0	1.23215e-07	3.82391e-08	2.76688e-08	-	-	-

Table B.3: The ω/π results for the $\omega \rightarrow \pi^0\gamma$ in Au + Au in 0-20% , 60-92% and minimum bias in Run4.

MB				0-20%		
p_T	Ratio	Sta.error	Sys.error	Ratio	Sta.error	Sys.error
6.00	1.29089	0.53935	0.329644	2.01388	1.01488	0.515475
7.00	1.38568	0.580824	0.421856	1.62799	1.07658	0.560893
8.75	0.614334	0.454938	0.187076	1.00323	0.902995	0.395495
60-92%						
p_T	Ratio	Sta.error	Sys.error			
4.00	0.861383	0.44526	0.203877			
5.00	1.70408	0.514599	0.469238			
6.00	1.20334	0.574275	0.426017			

Table B.4: The ω/π results for the $\omega \rightarrow \pi^0\gamma$ in Au + Au in 0-20% , 60-92% and minimum bias in Run7.

MB				0-20%		
p_T	Ratio	Sta.error	Sys.error	Ratio	Sta.error	Sys.error
5.5	0.914926	0.305279	0.0826085	-	-	-
6.5	0.546008	0.218848	0.0485048	-	-	-
7.5	0.667523	0.191868	0.0589324	0.812337	0.469961	0.0574526
9.0	0.972332	0.180873	0.0852604	1.43656	0.365636	0.0999036
11.0	1.06702	0.275312	0.0917559	1.68113	0.510661	0.113509
60-92%						
p_T	Ratio	Sta.error	Sys.error			
5.5	-	-	-			
6.5	1.93194	0.422601	0.838843			
7.5	1.16257	0.548148	0.497678			
9.0	2.57743	0.655359	1.08075			
11.0	-	-	-			

Table B.5: R_{AA} of the $\omega \rightarrow \pi^0\gamma$ in Au + Au (Run4).

MB				0-20%		
p_T	R_{AA}	Sta.error	Sys.error	R_{AA}	Sta.error	Sys.error
6.00	0.479883	0.200492	0.119971	0.579907	0.292207	0.144976
7.00	0.50746	0.212693	0.152238	0.45827	0.30302	0.155812
8.75	0.220153	0.163025	0.0660459	0.273279	0.245951	0.106579
60-92%						
p_T	R_{AA}	Sta.error	Sys.error			
4.00	1.05236	0.543885	0.242042			
5.00	2.10656	0.63545	0.568771			
6.00	1.47837	0.705074	0.517431			

Table B.6: R_{AA} of the $\omega \rightarrow \pi^0\gamma$ in Au + Au (Run7).

MB				0-20%		
p_T	R_{AA}	Sta.error	Sys.error	R_{AA}	Sta.error	Sys.error
5.5	0.34301	0.11444	0.0826085	-	-	-
6.5	0.201404	0.0807212	0.0485048	-	-	-
7.5	0.242825	0.0697831	0.0589324	0.226358	0.130933	0.0574526
9.0	0.347493	0.0645928	0.0852604	0.389699	0.0990564	0.0999036
11.0	0.373966	0.0964315	0.0917559	0.44277	0.134307	0.113509
20-60%				60-92%		
p_T	R_{AA}	Sta.error	Sys.error	R_{AA}	Sta.error	Sys.error
5.5	0.843802	0.179097	0.185303	-	-	-
6.5	0.506494	0.151969	0.111228	2.35524	0.513023	0.838843
7.5	0.463991	0.146194	0.102841	1.39241	0.655253	0.497678
9.0	0.496225	0.124056	0.111431	3.00846	0.752116	1.08075
11.0	0.625531	0.19413	0.140468	-	-	-

Bibliography

- [1] RHICwebsite. <http://www.bnl.gov/rhic>.
- [2] F. Abe *et al.*, “Transverse-Momentum Distributions of Charged Particles Produced in pp Interactions at $\sqrt{s}=630$ and 1800 GeV,” *Phys. Rev. Lett.*, vol. 61, p. 1819, 1988.
- [3] S. Adler *et al.*, “Inclusive cross section and double helicity asymmetry for π^0 production in p+p collisions at $\sqrt{s_{NN}}=200$ GeV,” *Phys. Rev. D*, vol. 76, p. 051106, 2007.
- [4] S. Adler *et al.*, “Absence of suppression in particle production at large transverse momentum in $\sqrt{s_{NN}}=200$ GeV d+Au collisions,” *Phys. Rev. Lett.*
- [5] A. Adare *et al.*, “Suppression pattern of neutral pions at high transverse momentum in Au+Au collisions at $\sqrt{s_{NN}}=200$ GeV and constraints on medium transport coefficients,” *Phys. Rev. Lett*, vol. 101, p. 232301, 2008.
- [6] A. Adare *et al.*, “Transverse momentum dependence of η meson suppression in Au+Au collisions at $\sqrt{s_{NN}}=200$ GeV,” *Phys. Rev. C*, vol. 82, p. 011902, 2010.
- [7] A. Adare *et al.*, “Production of ω mesons in p+p, d+Au, Cu+Cu, and Au+Au collisions at $\sqrt{s_{NN}}=200$ GeV,” *Phys. Rev. C*, vol. 84, p. 044902, 2011.
- [8] C. Tsallis, “Possible generalization of Boltzmann-Gibbs statistics,” *J. Statist. Phys.*, vol. 52, pp. 479–487, 1988.
- [9] T. Sjostrand *et al.*, “PYTHIA 6.2: Physics and manual,” 2001.

- [10] S. Adler *et al.*, “Production of ω meson at Large Transverse Momenta in $p+p$ and $d+Au$ Collisions at $\sqrt{s_{NN}}=200$ GeV,” *Phys. Rev. C*, vol. 75, p. 051902, 2007.
- [11] L. Apanasevich *et al.*, “Inclusive production of ω mesons at large transverse momenta in π^- Be interaction at 515 GeV/c,” 2000.
- [12] M. Diakonou *et al.*, “Inclusive high P(T) omega**0 and eta’ Production at the ISR,” *Phys. Lett. B*, vol. 89, pp. 432–436, 1980.
- [13] S. S. Adler *et al.*, “Centrality dependence of pi0 and eta production at large transverse momentum in $\sqrt{s(NN)} = 200$ GeV d + Au collisions,” *Phys. Rev. Lett.*, vol. 98, p. 172302, 2007.
- [14] D. Trnka *et al.*, “First observation of in-medium modifications of the omega meson,” *Phys. Rev. Lett.*, vol. 94, p. 192303, 2005.
- [15] L. Aphecetche *et al.*, “PHENIX calorimeter,” *Nucl. Instrum. Meth.*, vol. A499, pp. 521–536, 2003.
- [16] D. Sharma, *Omega and phi meson production in p+p and d+Au collisions at RHIC energies, using the PHENIX Detector*. PhD thesis, 2010.
- [17] PHENIXwebsite. <http://www.phenix.gov/>.
- [18] M. Leitch, “PHENIX Collaboration Meeting at U.Colorado in Boulder,” 2007.
- [19] A. Adare *et al.*, “Onset of pi-zero suppression studied in Cu+Cu collisions at $\sqrt{s_{NN}}=22.4, 62.4, \text{ and } 200$ GeV,” *Phys. Rev. Lett*, vol. 101, p. 162301, 2008.
- [20] K. Nakamura *et al.*, “Particle Data Book,” *Journal of Physics*, vol. G37, p. 075021, 2010.
- [21] C. Klein-Bösing, *Production of Neutral Pions and Direct Photons in Ultra-Relativistic Au+Au Collisions*. PhD thesis, 2004.
- [22] F. A. Wilczek, *QCD Made Simple*. Physics Today, 2000.
- [23] J. Bjorken, “Energy loss of energetic partons in Quark-Gluon Plasma: Possible extinction of high p(t) Jets in hadon-hadron collisions,” *FERMILAB-PUB*, vol. 82, p. 059, 1982.

- [24] M. A. Stephanov *Int. J. Mod. Phys.*, vol. A20, pp. 4387–4392, 2005.
- [25] P. Braun-Munzinger and J. Stachel, “The quest for the quark-gluon plasma,” *Nature*, vol. 448, 2007.
- [26] K. P. Braun-Munzinger and J. Stachel, “Particle production in heavy ion collisions,” *Quark gluon plasma*, pp. 491–599, 2003.
- [27] K. Adcox *et al.*, “Formation of dense partonic matter in relativistic nucleus-nucleus collisions at RHIC: Experimental evaluation by the PHENIX collaboration,” *Nucl. Phys. A*, vol. 757, pp. 184–283, 2005.
- [28] J. Adams *et al.*, “Experimental and theoretical challenges in the search for the quark gluon plasma: The STAR Collaboration’s critical assessment of the evidence from RHIC collisions,” *Nucl. Phys.*, vol. A757, pp. 102–183, 2005.
- [29] B. Back *et al.*, “The PHOBOS perspective on discoveries at RHIC,” *Nucl. Phys.*, vol. A757, pp. 28–101, 2005.
- [30] I. Arsene *et al.*, “Quark gluon plasma and color glass condensate at RHIC? The Perspective from the BRAHMS experiment.,” *Nucl. Phys.*, vol. A757, pp. 1–27, 2005.
- [31] R. Glauber and G. Matthiae, “High-energy scattering of protons by nuclei,” *Nucl. Phys.*, vol. B21, pp. 135–157, 1970.
- [32] B. Mohanty, “Exploring the quantum chromodynamics landscape with high-energy nuclear collisions,” *New J. Phys.*, vol. 13, p. 065031, 2011.
- [33] M. J. Tannenbaum, “Hard-scattering and Jets from RHIC to LHC: A Critical review,” *PoS LHC*, vol. 07, p. 004, 2007.
- [34] C. A. Salgado and U. A. Wiedemann, “Calculating Quenching Weights,” *Phys. Rev.*, vol. D68, p. 014008, 2003.
- [35] C. Loizides, “High transverse momentum suppression and surface effects in Cu+Cu and Au+Au collisions within the PQM model,” *Eur. Phys. J. C*, vol. 49, pp. 339–345, 2007.

- [36] C. L. Andrea Dainese and G. Paić, “Leading-particle suppression and surface emission in nucleus-nucleus collisions,” *Acta Phys.Hung.*, vol. A27, pp. 245–249, 2006.
- [37] M. Gyulassy, P. Levai, and I. Vitev, “Non-Abelian Energy Loss at Finite Opacity,” *Phys. Rev. Lett.*, vol. 85, pp. 5535–5538, 2000.
- [38] I. Vitev, “Testing the theory of QGP-induced energy loss at RHIC and the LHC,” *Phys. Lett.*, vol. B639, pp. 38–45, 2006.
- [39] J. W. Cronin *et al.*, “Production of Hadrons with Large Transverse Momentum at 200-GeV, 300-GeV, and 400-GeV,” *Phys. Rev.*, vol. D11, p. 3105, 1975.
- [40] P. Straub *et al.*, “Nuclear dependence of high $x(t)$ hadron and high tau hadron pair production in p A interactions at $\sqrt{s} = 38.8$ -GeV.,” *Phys. Rev.Lett.*, vol. 68, pp. 452–455, 1992.
- [41] D. Antreasyan *et al.*, “Production of hadrons at large transverse momentum in 200-GeV, 300-GeV and 400-GeV p p and p n collisions.,” *Phys. Rev. D.*, vol. 19, pp. 764–778, 1979.
- [42] S. S. Adler *et al.*, “Nuclear Effects on Hadron Production in d +Au and p + p Collisions at $\sqrt{s_{NN}}=200$ GeV,” *Phys. Rev. C*, vol. 74, p. 024904, 2006.
- [43] M. Lev and B. Petersson, “Nuclear effects at large transverse momentum in a QCD parton model,” *Z. Phys. C*, vol. 21, p. 155, 1983.
- [44] J. Aubert *et al.*, “The ratio of the nucleon structure functions,” *Phys. Lett.*, vol. B123, p. 275, 1983.
- [45] J. wei Qiu and I. Vitev, “Resummed QCD power corrections to nuclear shadowing,” *Phys. Rev. Lett.*, vol. 93, p. 262301, 2004.
- [46] J. Adams *et al.*, “Evidence from d +Au measurements for final state suppression of high $p(T)$ hadrons in Au+Au collisions at RHIC.,” *Phys. Rev. Lett.*
- [47] B. Back *et al.*, “Centrality dependence of charged hadron transverse momentum spectra in d +Au collisions at $\sqrt{s_{NN}}=200$ GeV.,” *Phys. Rev. Lett.*

- [48] I. Arsene *et al.*, “Transverse momentum spectra in Au+Au and d+Au collisions at $\sqrt{s_{\text{NN}}}=200$ GeV and the pseudorapidity dependence of high $p(\text{T})$ suppression.,” *Phys. Rev. Lett.*
- [49] A. Adare *et al.*, “Nuclear modification factors of phi mesons in d+Au, Cu+Cu and Au+Au collisions at $\sqrt{s_{\text{NN}}}=200$ GeV,” 2010.
- [50] S. Adler *et al.*, “Detailed study of high- p_{T} neutral pion suppression and azimuthal anisotropy in Au+Au collisions at $\sqrt{s_{\text{NN}}}=200$ GeV,” *Phys. Rev. C*, vol. 76, p. 034904, 2007.
- [51] J.G.Messchendorp *et al.*, “Studying the omega mass in-medium in $\gamma + A \rightarrow \pi^0(\gamma) + X$ reactions,” *Eur. Phys. J.*, vol. A11, pp. 95–103, 2001.
- [52] T. P. Muhlich and U.Mosel, “Inclusive omega photoproduction of nuclei,” *Eur. Phys. J.*, vol. A20, pp. 499–508, 2004.
- [53] A.Sibirtsev *et al.*, “Studying the omega properties in pA collisions via the $\omega \rightarrow \pi^0\gamma$ decay,” *Phys. Lett.*, vol. B483, pp. 405–409, 2000.
- [54] A. Adare *et al.*, “Measurement of neutral mesons in $p+p$ collisions at $\sqrt{s_{\text{NN}}}=200$ GeV and scaling properties of hadron production,” *Phys. Rev. D*, vol. 83, p. 052004, 2011.
- [55] S. Adler *et al.*, “High transverse momentum η meson production in $p+p$, d+Au and Au+Au collisions at $\sqrt{s_{\text{NN}}}=200$ GeV,” *Phys. Rev. C*, vol. 75, p. 024909, 2007.
- [56] A. Adare *et al.*, “ J/Ψ production versus transverse momentum and rapidity in p+p collisions at $\sqrt{s}=200$ GeV,” *Phys. Rev. Lett.*, vol. 98, p. 232002, 2007.
- [57] A. Adare *et al.*, “Transverse momentum dependence of J/Ψ polarization at midrapidity in p+p collisions at $\sqrt{s}=200$ GeV,” *Phys. Rev. D*, vol. 82, p. 012001, 2010.
- [58] A. Adare *et al.*, “Identified charged hadron production in p+p collisions at $\sqrt{s}=200$ and 62.4 GeV,” *Phys. Rev. C*, vol. 83, p. 064903, 2011.

- [59] K. M. Kijima, *First measurement of ω and ϕ mesons via di-electron decay channels in proton+proton collisions at $\sqrt{s} = 200$ GeV.* PhD thesis, 2012.
- [60] A. Adare *et al.*, “Detailed measurement of the e^+e^- pair continuum in p+p and Au+Au collisions at $\sqrt{s_{NN}}=200$ GeV and implications for direct photon production,” *Phys. Rev. C*, vol. 81, p. 034911, 2010.
- [61] R. Hagedorn, “Multiplicities, p_T distributions and the expected hadron \rightarrow quark-gluon phase transition,” *Riv. Nuovo Cimento Soc. Ital. Fis.*, vol. 6N10, p. 1, 1984.
- [62] G. Arnison *et al.*, “Transverse momentum spectra for charged particles at the CERN proton anti-proton collider,” *Phys. Lett. B*, vol. 118, p. 167, 1982.
- [63] M. Biyajima *et al.*, “Modified Hagedorn formula including temperature fluctuation - Estimation of temperatures at RHIC experiments -,” *Eur. Phys. J. C*, vol. 48, pp. 597–603, 2006.
- [64] A. Adare *et al.*, “Quantitative constraints on the transport properties of hot partonic matter from semi-inclusive single high transverse momentum pion suppression in Au+Au collisions at $\sqrt{s_{NN}}=200$ GeV,” *Phys. Rev. C*, vol. 77, p. 064907, 2008.
- [65] R. Fries *et al.*, “Hadron production in heavy ion collisions: Fragmentation and recombination from a dense parton phase,” *Phys. Rev. C*, vol. 68, p. 044902, 2003.
- [66] R. C. Hwa and C. Yang, “Recombination of shower partons at high p_T in heavy ion collisions,” *Phys. Rev. C*, vol. 70, p. 024905, 2004.
- [67] M. Naruki *et al.*, “Experimental signature of the medium modification for rho and omega mesons in 12-GeV p+A reactions,” *Phys. Rev. Lett.*, vol. 96, p. 092301, 2006.
- [68] C. Djalai *et al.*, “Medium modifications of light vector mesons in photoproduction reactions at JLab,” *J. Phys. G*, vol. 35, p. 104035, 2008.
- [69] D. Adamova *et al.*, “Modification of the rho-meson detected by low-mass electron-positron pairs in central Pb-Au collisions at 158-A-GeV/c,” *Phys. Lett. B*, vol. 666, pp. 425–429, 2008.

- [70] R. Arnaldi *et al.*, “First measurement of the rho spectral function in high-energy nuclear collisions,” *Phys. Rev. Lett.*, vol. 96, p. 162302, 2006.
- [71] K. Ackermann *et al.*, “STAR detector overview,” *Nucl. Instrum. Meth.*, vol. A499, pp. 624–632, 2003.
- [72] K. Adcox *et al.*, “PHENIX detector overview,” *Nucl. Instrum. Meth.*, vol. A499, pp. 469–479, 2003.
- [73] B. Back *et al.*, “The PHOBOS detector at RHIC,” *Nucl. Instrum. Meth.*, vol. A499, pp. 603–623, 2003.
- [74] M. Adamczyk *et al.*, “The BRAHMS experiment at RHIC,” *Nucl. Instrum. Meth.*, vol. A499, pp. 437–468, 2003.
- [75] M. Allen *et al.*, “PHENIX inner detectors,” *Nucl. Instrum. Meth.*, vol. A499, pp. 549–559, 2003.
- [76] K. Adcox *et al.*, “PHENIX central arm tracking detectors,” *Nucl. Instrum. Meth.*, vol. A499, pp. 489–507, 2003.
- [77] S. S. Adler *et al.*, “The RHIC zero-degree calorimeters,” *Nucl. Instrum. Meth.*, vol. A499, pp. 433–436, 2003.
- [78] H. Akikawa *et al.*, “PHENIX muon arms,” *Nucl. Instrum. Meth.*, vol. A499, pp. 537–548, 2003.
- [79] S. H. Aronson *et al.*, “PHENIX magnet system,” *Nucl. Instrum. Meth.*, vol. A499, pp. 480–488, 2003.
- [80] M. Aizawa *et al.*, “PHENIX central arm particle ID detectors,” *Nucl. Instrum. Meth.*, vol. A499, pp. 508–520, 2003.
- [81] H. Torii, *Midrapidity Neutral-Pion Production in Proton-Proton Collisions at $\sqrt{s_{NN}}=200$ GeV*. PhD thesis, 2004.
- [82] W. Anderson *et al.*, “Design, Construction, Operation and Performance of a Hadron Blind Detector for the PHENIX Experiment,”
- [83] S. Adler *et al.*, “PHENIX on-line systems,” *Nucl. Instrum. Meth.*, vol. A499, pp. 560–592, 2003.

- [84] J. N. S. Kelly, D. Morrison *et al.*, “Calculation of the number of participating nucleons for centrality classes defined with the ZDC and BBC,” *PHENIX Internal Analysis Note*, vol. 33, 2000.
- [85] L. de Barbaro, *Omega Meson Production at High Transverse Momentum by Negative 515 GeV/c Pions Incident on Beryllium and Copper Targets*. PhD thesis, 1995.
- [86] R. Aeverbeck. PHENIX CVS Repository offline/analysis/exodus.
- [87] PISAwebsite. <https://www.phenix.bnl.gov/WWW/simulation/primer4/>.
- [88] CERNwebsite. <http://www.cern.ch>.
- [89] S. Adler *et al.*, “Identified Charged Particle Spectra and Yields in Au+Au Collisions at $\sqrt{s_{NN}}=200$ GeV,” *Phys. Rev. C*, vol. 69, p. 034909, 2004.
- [90] S. Adler *et al.*, “Measurement of Transverse Single-Spin Asymmetries for Midrapidity Production of Neutral Pions and Charged Hadrons in Polarized $p+p$ Collisions at $\sqrt{s_{NN}}=200$ GeV,” *Phys. Rev. Lett*, vol. 95, p. 202001, 2005.

公表論文

(1) Production of ω mesons in p + p, d + Au, Cu + Cu, and Au + Au collisions
at $\sqrt{s_{NN}}=200$ GeV

A. Adler *et al.* (PHENIX Collaboration)

.....Physical Review C 84, 044902 (2011).



Barbara Jacak,
Distinguished Professor of Physics,
Spokesperson for PHENIX
Stony Brook University
Department of Physics and Astronomy
Stony Brook, New York 11794-3800
Phone: (631) 632-6041
FAX (631) 632-8573

Letter of Acceptance

We approve that Ms. Misaki Ouchida preferentially applies following article as the main part of her doctoral dissertation at Hiroshima University.

Article: Physical Review C 84, 044902 (2011)

Title: Production of ω mesons in $p + p$, $d + Au$, $Cu + Cu$ and $Au + Au$ collisions at $\sqrt{s_{NN}} = 200$ GeV

Spokesperson of the PHENIX Collaboration:
Barbara V. Jacak
Professor of Physics and Astronomy at SUNY Stony Brook University

Date: November 8, 2011

Signature: _____

A handwritten signature in black ink, appearing to read "Barbara V. Jacak", written over a horizontal line.

Production of ω mesons in $p + p$, $d + Au$, $Cu + Cu$, and $Au + Au$ collisions at $\sqrt{s_{NN}} = 200$ GeV

A. Adare,¹¹ S. Afanasiev,²⁷ C. Aidala,^{12,41} N. N. Ajitanand,⁵⁸ Y. Akiba,^{52,53} H. Al-Bataineh,⁴⁷ A. Al-Jamel,⁴⁷ J. Alexander,⁵⁸ A. Angerami,¹² K. Aoki,^{34,52} N. Apadula,⁵⁹ L. Aphecetche,⁶⁰ Y. Aramaki,¹⁰ R. Armendariz,⁴⁷ S. H. Aronson,⁵ J. Asai,⁵³ E. T. Atomssa,³⁵ R. Averbeck,⁵⁹ T. C. Awes,⁴⁸ B. Azmoun,⁵ V. Babintsev,²² M. Bai,⁴ G. Baksay,¹⁸ L. Baksay,¹⁸ A. Baldisseri,¹⁴ K. N. Barish,⁶ P. D. Barnes,^{37,*} B. Bassalleck,⁴⁶ A. T. Basye,¹ S. Bathe,^{6,53} S. Batsouli,^{12,48} V. Baublis,⁵¹ F. Bauer,⁶ C. Baumann,⁴² A. Bazilevsky,⁵ S. Belikov,^{5,26,*} R. Belmont,⁶⁴ R. Bennett,⁵⁹ A. Berdnikov,⁵⁵ Y. Berdnikov,⁵⁵ J. H. Bhom,⁶⁷ A. A. Bickley,¹¹ M. T. Bjorndal,¹² D. S. Blau,³³ J. G. Boissevain,³⁷ J. S. Bok,⁶⁷ H. Borel,¹⁴ K. Boyle,⁵⁹ M. L. Brooks,³⁷ D. S. Brown,⁴⁷ D. Bucher,⁴² H. Buesching,⁵ V. Bumazhnov,²² G. Bunce,^{5,53} J. M. Burward-Hoy,³⁷ S. Butsyk,^{37,59} C. M. Camacho,³⁷ S. Campbell,⁵⁹ A. Caringi,⁴³ J.-S. Chai,²⁹ B. S. Chang,⁶⁷ J.-L. Charvet,¹⁴ C.-H. Chen,⁵⁹ S. Chernichenko,²² C. Y. Chi,¹² J. Chiba,³⁰ M. Chiu,^{5,12,23} I. J. Choi,⁶⁷ J. B. Choi,⁸ R. K. Choudhury,³ P. Christiansen,³⁹ T. Chujo,^{63,64} P. Chung,⁵⁸ A. Churnin,²² O. Chvala,⁶ V. Cianciolo,⁴⁸ Z. Citron,⁵⁹ C. R. Cleven,²⁰ Y. Cobigo,¹⁴ B. A. Cole,¹² M. P. Comets,⁴⁹ Z. Conesa del Valle,³⁵ M. Connors,⁵⁹ P. Constantin,^{26,37} M. Csanád,¹⁶ T. Csörgő,³¹ T. Dahms,⁵⁹ S. Dairaku,^{34,52} I. Danchev,⁶⁴ K. Das,¹⁹ A. Datta,⁴¹ G. David,⁵ M. K. Dayananda,²⁰ M. B. Deaton,¹ K. Dehmelt,¹⁸ H. Delagrange,⁶⁰ A. Denisov,²² D. d'Enterria,¹² A. Deshpande,^{53,59} E. J. Desmond,⁵ K. V. Dharmawardane,⁴⁷ O. Dietzsch,⁵⁶ A. Dion,^{26,59} M. Donadelli,⁵⁶ J. L. Drachenberg,¹ O. Drapier,³⁵ A. Drees,⁵⁹ K. A. Drees,⁴ A. K. Dubey,⁶⁶ J. M. Durham,⁵⁹ A. Durum,²² D. Dutta,³ V. Dzordzhadze,^{6,61} L. D'Orazio,⁴⁰ S. Edwards,¹⁹ Y. V. Efremenko,⁴⁸ J. Egdemir,⁵⁹ F. Ellinghaus,¹¹ W. S. Emam,⁶ T. Engelmore,¹² A. Enokizono,^{21,36,48} H. En'yo,^{52,53} B. Espagnon,⁴⁹ S. Esumi,⁶³ K. O. Eyser,⁶ B. Fadem,⁴³ D. E. Fields,^{46,53} M. Finger,^{7,27} M. Finger Jr.,^{7,27} F. Fleuret,³⁵ S. L. Fokin,³³ B. Forestier,³⁸ Z. Fraenkel,^{66,*} J. E. Frantz,^{12,59} A. Franz,⁵ A. D. Frawley,¹⁹ K. Fujiwara,⁵² Y. Fukao,^{34,52} S.-Y. Fung,⁶ T. Fusayasu,⁴⁵ S. Gadrat,³⁸ I. Garishvili,⁶¹ F. Gastineau,⁶⁰ M. Germain,⁶⁰ A. Glenn,^{11,36,61} H. Gong,⁵⁹ M. Gonin,³⁵ J. Gosset,¹⁴ Y. Goto,^{52,53} R. Granier de Cassagnac,³⁵ N. Grau,^{12,26} S. V. Greene,⁶⁴ G. Grim,³⁷ M. Grosse Perdekamp,^{23,53} T. Gunji,¹⁰ H.-Å. Gustafsson,^{39,*} T. Hachiya,^{21,52} A. Hadj Henni,⁶⁰ C. Haegemann,⁴⁶ J. S. Haggerty,⁵ M. N. Hagiwara,¹ K. I. Hahn,¹⁷ H. Hamagaki,¹⁰ J. Hamblen,⁶¹ R. Han,⁵⁰ J. Hanks,¹² H. Harada,²¹ E. P. Hartouni,³⁶ K. Haruna,²¹ M. Harvey,⁵ E. Haslum,³⁹ K. Hasuko,⁵² R. Hayano,¹⁰ X. He,²⁰ M. Heffner,³⁶ T. K. Hemmick,⁵⁹ T. Hester,⁶ J. M. Heuser,⁵² H. Hiejima,²³ J. C. Hill,²⁶ R. Hobbs,⁴⁶ M. Hohlmann,¹⁸ M. Holmes,⁶⁴ W. Holzmann,^{12,58} K. Homma,²¹ B. Hong,³² T. Horaguchi,^{21,52,62} D. Hornback,⁶¹ S. Huang,⁶⁴ M. G. Hur,²⁹ T. Ichihara,^{52,53} R. Ichimiya,⁵² J. Ide,⁴³ H. Iinuma,^{34,52} Y. Ikeda,⁶³ K. Imai,^{34,52} M. Inaba,⁶³ Y. Inoue,^{52,54} D. Isenhower,¹ L. Isenhower,¹ M. Ishihara,⁵² T. Isobe,¹⁰ M. Issah,^{58,64} A. Isupov,²⁷ D. Ivanischew,⁵¹ Y. Iwanaga,²¹ B. V. Jacak,^{59,†} J. Jia,^{5,12,58} X. Jiang,³⁷ J. Jin,¹² O. Jinnouchi,⁵³ B. M. Johnson,⁵ T. Jones,¹ K. S. Joo,⁴⁴ D. Jouan,⁴⁹ D. S. Jumper,¹ F. Kajihara,^{10,52} S. Kametani,^{10,52,65} N. Kamihara,^{52,53,62} J. Kamin,⁵⁹ M. Kaneta,⁵³ J. H. Kang,⁶⁷ H. Kanou,^{52,62} J. Kapustinsky,³⁷ K. Karatsu,³⁴ M. Kasai,^{52,54} T. Kawagishi,⁶³ D. Kawall,^{41,53} M. Kawashima,^{54,52} A. V. Kazantsev,³³ S. Kelly,¹¹ T. Kempel,²⁶ A. Khanzadeev,⁵¹ K. M. Kijima,²¹ J. Kikuchi,⁶⁵ A. Kim,¹⁷ B. I. Kim,³² D. H. Kim,⁴⁴ D. J. Kim,^{28,67} E. Kim,⁵⁷ E. J. Kim,⁸ S. H. Kim,⁶⁷ Y.-J. Kim,²³ Y.-S. Kim,²⁹ Y. J. Kim,²³ E. Kinney,¹¹ K. Kiriluk,¹¹ Á. Kiss,¹⁶ E. Kistenev,⁵ A. Kiyomichi,⁵² J. Klay,³⁶ C. Klein-Boesing,⁴² L. Kochenda,⁵¹ V. Kochetkov,²² B. Komkov,⁵¹ M. Konno,⁶³ J. Koster,²³ D. Kotchetkov,^{6,46} A. Kozlov,⁶⁶ A. Král,¹³ A. Kravitz,¹² P. J. Kroon,⁵ J. Kubart,^{7,25} G. J. Kunde,³⁷ N. Kurihara,¹⁰ K. Kurita,^{52,54} M. Kurosawa,⁵² M. J. Kweon,³² Y. Kwon,^{61,67} G. S. Kyle,⁴⁷ R. Lacey,⁵⁸ Y. S. Lai,¹² J. G. Lajoie,²⁶ A. Lebedev,²⁶ Y. Le Bornec,⁴⁹ S. Leckey,⁵⁹ D. M. Lee,³⁷ J. Lee,¹⁷ K. Lee,⁵⁷ K. B. Lee,³² K. S. Lee,³² M. K. Lee,⁶⁷ T. Lee,⁵⁷ M. J. Leitch,³⁷ M. A. L. Leite,⁵⁶ E. Leitner,⁶⁴ B. Lenzi,⁵⁶ X. Li,⁹ X. H. Li,⁶ P. Lichtenwalner,⁴³ P. Liebing,⁵³ H. Lim,⁵⁷ L. A. Linden Levy,¹¹ T. Liška,¹³ A. Litvinenko,²⁷ H. Liu,^{37,47} M. X. Liu,³⁷ B. Love,⁶⁴ R. Luechtenborg,⁴² D. Lynch,⁵ C. F. Maguire,⁶⁴ Y. I. Makdisi,^{4,5} A. Malakhov,²⁷ M. D. Malik,⁴⁶ V. I. Manko,³³ E. Mannel,¹² Y. Mao,^{50,52} L. Mašek,^{7,25} H. Masui,⁶³ F. Matathias,^{12,59} M. C. McCain,²³ M. McCumber,⁵⁹ P. L. McGaughey,³⁷ N. Means,⁵⁹ B. Meredith,²³ Y. Miake,⁶³ T. Mibe,³⁰ A. C. Mignerey,⁴⁰ P. Mikeš,^{7,25} K. Miki,^{52,63} T. E. Miller,⁶⁴ A. Milov,^{5,59} S. Mioduszewski,⁵ G. C. Mishra,²⁰ M. Mishra,² J. T. Mitchell,⁵ M. Mitrovski,⁵⁸ A. K. Mohanty,³ H. J. Moon,⁴⁴ Y. Morino,¹⁰ A. Morreale,⁶ D. P. Morrison,⁵ J. M. Moss,³⁷ T. V. Moukhanova,³³ D. Mukhopadhyay,⁶⁴ T. Murakami,³⁴ J. Murata,^{52,54} S. Nagamiya,³⁰ Y. Nagata,⁶³ J. L. Nagle,¹¹ M. Naglis,⁶⁶ M. I. Nagy,^{16,31} I. Nakagawa,^{52,53} Y. Nakamiya,²¹ K. R. Nakamura,³⁴ T. Nakamura,^{21,30,52} K. Nakano,^{52,62} S. Nam,¹⁷ J. Newby,³⁶ M. Nguyen,⁵⁹ M. Nihashi,²¹ B. E. Norman,³⁷ R. Nouicer,⁵ A. S. Nyanin,³³ J. Nystrand,³⁹ C. Oakley,²⁰ E. O'Brien,⁵ S. X. Oda,¹⁰ C. A. Ogilvie,²⁶ H. Ohnishi,⁵² I. D. Ojha,⁶⁴ M. Oka,⁶³ K. Okada,⁵³ O. O. Omiwade,¹ Y. Onuki,⁵² A. Oskarsson,³⁹ I. Otterlund,³⁹ M. Ouchida,^{21,52} K. Ozawa,¹⁰ R. Pak,⁵ D. Pal,⁶⁴ A. P. T. Palounek,³⁷ V. Pantuev,^{24,59} V. Papavassiliou,⁴⁷ I. H. Park,¹⁷ J. Park,⁵⁷ S. K. Park,³² W. J. Park,³² S. F. Pate,⁴⁷ H. Pei,²⁶ J.-C. Peng,²³ H. Pereira,¹⁴ V. Peresedov,²⁷ D. Yu. Peressouko,³³ R. Petti,⁵⁹ C. Pinkenburg,⁵ R. P. Pisani,⁵ M. Proissl,⁵⁹ M. L. Purschke,⁵ A. K. Purwar,^{37,59} H. Qu,²⁰ J. Rak,^{26,28,46} A. Rakotozafindrabe,³⁵ I. Ravinovich,⁶⁶ K. F. Read,^{48,61} S. Rembeczki,¹⁸ M. Reuter,⁵⁹ K. Reygers,⁴² V. Riabov,⁵¹ Y. Riabov,⁵¹ E. Richardson,⁴⁰ D. Roach,⁶⁴ G. Roche,³⁸ S. D. Rolnick,⁶ A. Romana,^{35,*} M. Rosati,²⁶ C. A. Rosen,¹¹ S. S. E. Rosendahl,³⁹ P. Rosnet,³⁸ P. Rukoyatkin,²⁷ P. Ružička,²⁵ V. L. Rykov,⁵² S. S. Ryu,⁶⁷ B. Sahlmueller,⁴² N. Saito,^{30,34,52,53} T. Sakaguchi,^{5,10,65} S. Sakai,⁶³ K. Sakashita,^{52,62} H. Sakata,²¹ V. Samsonov,⁵¹ S. Sano,^{10,65} H. D. Sato,^{34,52} S. Sato,^{5,30,63} T. Sato,⁶³ S. Sawada,³⁰ K. Sedgwick,⁶ J. Seele,¹¹ R. Seidl,^{23,53} A. Yu. Semenov,²⁶ V. Semenov,²² R. Seto,⁶ D. Sharma,⁶⁶ T. K. Shea,⁵ I. Shein,²² A. Shevel,^{51,58} T.-A. Shibata,^{52,62} K. Shigaki,²¹ M. Shimomura,⁶³ T. Shohjoh,⁶³ K. Shoji,^{34,52} P. Shukla,³ A. Sickles,^{5,59} C. L. Silva,^{26,56} D. Silvermyr,⁴⁸ C. Silvestre,¹⁴ K. S. Sim,³² B. K. Singh,² C. P. Singh,² V. Singh,² S. Skutnik,²⁶ M. Slunečka,^{7,27} W. C. Smith,¹ A. Soldatov,²² R. A. Soltz,³⁶ W. E. Sondheim,³⁷ S. P. Sorensen,⁶¹ I. V. Sourikova,⁵ N. A. Sparks,¹ F. Staley,¹⁴ P. W. Stankus,⁴⁸ E. Stenlund,³⁹ M. Stepanov,⁴⁷ A. Ster,³¹ S. P. Stoll,⁵ T. Sugitate,²¹

C. Suire,⁴⁹ A. Sukhanov,⁵ J. P. Sullivan,³⁷ J. Sziklai,³¹ T. Tabaru,⁵³ S. Takagi,⁶³ E. M. Takagui,⁵⁶ A. Taketani,^{52,53} R. Tanabe,⁶³ K. H. Tanaka,³⁰ Y. Tanaka,⁴⁵ S. Taneja,⁵⁹ K. Tanida,^{34,52,53,57} M. J. Tannenbaum,⁵ S. Tarafdar,² A. Taranenko,⁵⁸ P. Tarján,¹⁵ H. Themann,⁵⁹ D. Thomas,¹ T. L. Thomas,⁴⁶ M. Togawa,^{34,52,53} A. Toia,⁵⁹ J. Tojo,⁵² L. Tomásek,²⁵ H. Torii,^{21,52} R. S. Towell,¹ V-N. Tram,³⁵ I. Tserruya,⁶⁶ Y. Tsuchimoto,^{21,52} S. K. Tuli,^{2,*} H. Tydesjö,³⁹ N. Tyurin,²² C. Vale,^{5,26} H. Valle,⁶⁴ H. W. van Hecke,³⁷ E. Vazquez-Zambrano,¹² A. Veicht,²³ J. Velkovska,⁶⁴ R. Vértesi,^{15,31} A. A. Vinogradov,³³ M. Virius,¹³ V. Vrba,²⁵ E. Vznuzdaev,⁵¹ M. Wagner,^{34,52} D. Walker,⁵⁹ X. R. Wang,⁴⁷ D. Watanabe,²¹ K. Watanabe,⁶³ Y. Watanabe,^{52,53} F. Wei,²⁶ R. Wei,⁵⁸ J. Wessels,⁴² S. N. White,⁵ N. Willis,⁴⁹ D. Winter,¹² J. P. Wood,¹ C. L. Woody,⁵ R. M. Wright,¹ M. Wysocki,¹¹ W. Xie,^{6,53} Y. L. Yamaguchi,^{10,65} K. Yamaura,²¹ R. Yang,²³ A. Yanovich,²² Z. Yasin,⁶ J. Ying,²⁰ S. Yokkaichi,^{52,53} Z. You,⁵⁰ G. R. Young,⁴⁸ I. Younus,⁴⁶ I. E. Yushmanov,³³ W. A. Zajc,¹² O. Zaudtke,⁴² C. Zhang,^{12,48} S. Zhou,⁹ J. Zimányi,^{31,*} and L. Zolin²⁷

(PHENIX Collaboration)

¹Abilene Christian University, Abilene, Texas 79699, USA

²Department of Physics, Banaras Hindu University, Varanasi 221005, India

³Bhabha Atomic Research Centre, Bombay 400 085, India

⁴Collider Accelerator Department, Brookhaven National Laboratory, Upton, New York 11973-5000, USA

⁵Physics Department, Brookhaven National Laboratory, Upton, New York 11973-5000, USA

⁶University of California-Riverside, Riverside, California 92521, USA

⁷Charles University, Ovocný trh 5, Praha 1, 116 36, Prague, Czech Republic

⁸Chonbuk National University, Jeonju, 561-756, Korea

⁹Science and Technology on Nuclear Data Laboratory, China Institute of Atomic Energy, Beijing 102413, P. R. China

¹⁰Center for Nuclear Study, Graduate School of Science, University of Tokyo, 7-3-1 Hongo, Bunkyo, Tokyo 113-0033, Japan

¹¹University of Colorado, Boulder, Colorado 80309, USA

¹²Columbia University, New York, New York 10027 and Nevis Laboratories, Irvington, New York 10533, USA

¹³Czech Technical University, Zikova 4, 166 36 Prague 6, Czech Republic

¹⁴Dapnia, CEA Saclay, F-91191, Gif-sur-Yvette, France

¹⁵Debrecen University, H-4010 Debrecen, Egyetem tér 1, Hungary

¹⁶ELTE, Eötvös Loránd University, H-1117 Budapest, Pázmány P. s. 1/A, Hungary

¹⁷Ewha Womans University, Seoul 120-750, Korea

¹⁸Florida Institute of Technology, Melbourne, Florida 32901, USA

¹⁹Florida State University, Tallahassee, Florida 32306, USA

²⁰Georgia State University, Atlanta, Georgia 30303, USA

²¹Hiroshima University, Kagamiyama, Higashi-Hiroshima 739-8526, Japan

²²IHEP Protvino, State Research Center of Russian Federation, Institute for High Energy Physics, Protvino, 142281, Russia

²³University of Illinois at Urbana-Champaign, Urbana, Illinois 61801, USA

²⁴Institute for Nuclear Research of the Russian Academy of Sciences, prospekt 60-letiya Oktyabrya 7a, Moscow 117312, Russia

²⁵Institute of Physics, Academy of Sciences of the Czech Republic, Na Slovance 2, 182 21 Prague 8, Czech Republic

²⁶Iowa State University, Ames, Iowa 50011, USA

²⁷Joint Institute for Nuclear Research, 141980 Dubna, Moscow Region, Russia

²⁸Helsinki Institute of Physics and University of Jyväskylä, P.O.Box 35, FI-40014 Jyväskylä, Finland

²⁹KAERI, Cyclotron Application Laboratory, Seoul, Korea

³⁰KEK, High Energy Accelerator Research Organization, Tsukuba, Ibaraki 305-0801, Japan

³¹KFKI Research Institute for Particle and Nuclear Physics of the Hungarian Academy of Sciences (MTA KFKI RMKI), H-1525 Budapest 114, POBox 49, Budapest, Hungary

³²Korea University, Seoul, 136-701, Korea

³³Russian Research Center "Kurchatov Institute," Moscow, 123098 Russia

³⁴Kyoto University, Kyoto 606-8502, Japan

³⁵Laboratoire Leprince-Ringuet, Ecole Polytechnique, CNRS-IN2P3, Route de Saclay, F-91128, Palaiseau, France

³⁶Lawrence Livermore National Laboratory, Livermore, California 94550, USA

³⁷Los Alamos National Laboratory, Los Alamos, New Mexico 87545, USA

³⁸LPC, Université Blaise Pascal, CNRS-IN2P3, Clermont-Fd, 63177 Aubiere Cedex, France

³⁹Department of Physics, Lund University, Box 118, SE-221 00 Lund, Sweden

⁴⁰University of Maryland, College Park, Maryland 20742, USA

⁴¹Department of Physics, University of Massachusetts, Amherst, Massachusetts 01003-9337, USA

⁴²Institut für Kernphysik, University of Muenster, D-48149 Muenster, Germany

⁴³Muhlenberg College, Allentown, Pennsylvania 18104-5586, USA

⁴⁴Myongji University, Yongin, Kyonggido 449-728, Korea

⁴⁵Nagasaki Institute of Applied Science, Nagasaki-shi, Nagasaki 851-0193, Japan

⁴⁶University of New Mexico, Albuquerque, New Mexico 87131, USA

⁴⁷New Mexico State University, Las Cruces, New Mexico 88003, USA⁴⁸Oak Ridge National Laboratory, Oak Ridge, Tennessee 37831, USA⁴⁹IPN-Orsay, Universite Paris Sud, CNRS-IN2P3, BPI, F-91406, Orsay, France⁵⁰Peking University, Beijing 100871, P. R. China⁵¹PNPI, Petersburg Nuclear Physics Institute, Gatchina, Leningrad region, 188300, Russia⁵²RIKEN Nishina Center for Accelerator-Based Science, Wako, Saitama 351-0198, Japan⁵³RIKEN BNL Research Center, Brookhaven National Laboratory, Upton, New York 11973-5000, USA⁵⁴Physics Department, Rikkyo University, 3-34-1 Nishi-Ikebukuro, Toshima, Tokyo 171-8501, Japan⁵⁵Saint Petersburg State Polytechnic University, St. Petersburg, 195251 Russia⁵⁶Universidade de São Paulo, Instituto de Física, Caixa Postal 66318, São Paulo CEP05315-970, Brazil⁵⁷Seoul National University, Seoul, Korea⁵⁸Chemistry Department, Stony Brook University, SUNY, Stony Brook, New York 11794-3400, USA⁵⁹Department of Physics and Astronomy, Stony Brook University, SUNY, Stony Brook, New York 11794-3400, USA⁶⁰SUBATECH (Ecole des Mines de Nantes, CNRS-IN2P3, Université de Nantes) BP 20722-44307, Nantes, France⁶¹University of Tennessee, Knoxville, Tennessee 37996, USA⁶²Department of Physics, Tokyo Institute of Technology, Oh-okayama, Meguro, Tokyo 152-8551, Japan⁶³Institute of Physics, University of Tsukuba, Tsukuba, Ibaraki 305, Japan⁶⁴Vanderbilt University, Nashville, Tennessee 37235, USA⁶⁵Waseda University, Advanced Research Institute for Science and Engineering, 17 Kikui-cho, Shinjuku-ku, Tokyo 162-0044, Japan⁶⁶Weizmann Institute, Rehovot 76100, Israel⁶⁷Yonsei University, IPAP, Seoul 120-749, Korea

(Received 17 May 2011; published 7 October 2011)

The PHENIX experiment at the Relativistic Heavy Ion Collider has measured ω meson production via leptonic and hadronic decay channels in $p + p$, $d + \text{Au}$, $\text{Cu} + \text{Cu}$, and $\text{Au} + \text{Au}$ collisions at $\sqrt{s_{NN}} = 200$ GeV. The invariant transverse momentum spectra measured in different decay modes give consistent results. Measurements in the hadronic decay channel in $\text{Cu} + \text{Cu}$ and $\text{Au} + \text{Au}$ collisions show that ω production has a suppression pattern at high transverse momentum, similar to that of π^0 and η in central collisions, but no suppression is observed in peripheral collisions. The nuclear modification factors, R_{AA} , are consistent in $\text{Cu} + \text{Cu}$ and $\text{Au} + \text{Au}$ collisions at similar numbers of participant nucleons.

DOI: [10.1103/PhysRevC.84.044902](https://doi.org/10.1103/PhysRevC.84.044902)

PACS number(s): 25.75.Dw, 25.40.Ve

I. INTRODUCTION

The measurement of hadrons produced in relativistic heavy-ion collisions is a well established tool in the study of the hot and dense matter created in the collisions. The PHENIX experiment at the Relativistic Heavy Ion Collider has carried out systematic measurement of hadrons in $p + p$, $d + \text{Au}$, $\text{Cu} + \text{Cu}$, and $\text{Au} + \text{Au}$ collisions at $\sqrt{s_{NN}} = 200$ GeV. When compared to existing measurements in $p + p$ and $d + \text{Au}$, measurements in heavy-ion collisions suggest that particle production at high p_T is affected by jet quenching, which is considered to be an effect of extremely dense matter created by the collisions [1]. High p_T suppression of π^0 and η was measured in $\text{Cu} + \text{Cu}$ and $\text{Au} + \text{Au}$ [2–5] and the nuclear modification factors (R_{AA}) of these mesons were found to be consistent with each other in p_T and centrality. A comparison with theoretical models was first done for π^0 suppression in [4], with the result that the suppression increases proportional to the number of participating nucleons as $N_{\text{part}}^{2/3}$. This result is consistent with existing energy loss models such as the Parton Quenching Model (PQM) [6].

The ω meson comprises light valence quarks similar to the π^0 and η but has a larger mass (782 MeV) and a spin [1]. These

differences make the omega measurement an additional probe to a systematic study to understand mechanisms of parton energy loss and hadron production in the collisions. The p_T dependence of the particle production ratio (ω/π) and the nuclear modification factors (R_{AA}) should add information about the parton energy loss mechanism. Furthermore, using multiple decay channels: a leptonic channel $\omega \rightarrow e^+e^-$ (with branching ratio $\text{BR} = 7.18 \pm 0.12 \times 10^{-5}$) and two hadronic decay channels $\omega \rightarrow \pi^+\pi^-\pi^0$ ($\text{BR} = (89.1 \pm 0.7) \times 10^{-2}$) and $\omega \rightarrow \pi^0\gamma$ ($\text{BR} = (8.90 + 0.27 - 0.23) \times 10^{-2}$) [9] extends the p_T range by using the hadronic channels at high p_T and the leptonic channel at low p_T .

Baseline measurements of the ω have been performed for $p + p$ via the leptonic channel [7] and for the $p + p$ and $d + \text{Au}$ in the hadronic channel [8,10]. The ω/π^0 ratio was found to be independent of transverse momentum and equal to $0.85 \pm 0.05^{\text{stat}} \pm 0.09^{\text{syst}}$ in $p + p$ and $0.94 \pm 0.08^{\text{stat}} \pm 0.12^{\text{syst}}$ in $d + \text{Au}$ collisions for $p_T > 2$ GeV/c [8].

This article presents the first measurements of ω meson production in $\text{Cu} + \text{Cu}$ and $\text{Au} + \text{Au}$ collisions at PHENIX via the $\pi^0\gamma$ channel. These measurements permit the study of ω suppression at high p_T . This paper also presents measurements of the ω meson in $d + \text{Au}$ collisions with significantly reduced uncertainties in the hadronic channel and a first measurement in the dielectronic channel.

*Deceased.

†PHENIX Spokesperson: jacak@skipper.physics.sunysb.edu

II. EXPERIMENTAL SETUP

The PHENIX experiment is designed specifically to measure electromagnetic probes such as electrons, muons, and photons [11]. The detectors of the PHENIX experiment can be grouped into three categories: inner detectors close to the beam pipe, two central arms with pseudorapidity coverage of ± 0.35 , each covering 90 degrees in azimuthal angle, and two muon detectors, which have 2π azimuthal and pseudorapidity coverage of $+(1.2-2.2)$ for the south muon arm and $-(1.2-2.4)$ for the north muon arm. The central arms are used to measure the ω mesons at midrapidity.

The inner detectors are used for triggering, measurement of the z coordinate of the collision vertex, and centrality of the interactions with beam-beam counters (BBC) and zero-degree calorimeters (ZDC). The central arms are capable of measuring a variety of particles by using drift chambers and pad chambers for tracking and momentum measurement of charged particles, ring imaging Čerenkov detectors (RICH) for the separation of electrons up to the π Čerenkov threshold at 4 GeV/ c , and an electromagnetic calorimeter (EMCal) for the measurement of spatial positions and energies of photons and electrons. The EMCal comprises six sectors of lead-scintillator calorimeter and two sectors of lead-glass calorimeter. Additional details of the PHENIX experimental setup and performance of the detector subsystems can be found elsewhere [7,12].

We used data samples collected in 2004, 2005, 2007, and 2008 as summarized in Table I. The data were taken using a minimum bias trigger (MB) and the EMCal-RICH-trigger (ERT), which is described below. The 2003 $d + Au$ data were published in Ref. [8] and are included here for comparison. The 2005 $p + p$ data were published in Ref. [7] and are used as the baseline for R_{AA} in $d + Au$, $Cu + Cu$, and $Au + Au$. Two $Au + Au$ data samples were taken in 2004 and 2007. The MB trigger required a coincidence between the north and south BBC [13]. In the $Au + Au$ data sample taken in 2004, additional coincidence between the ZDC and BBC was required. To enhance the statistics at high p_T , the ERT trigger was used for $p + p$, $d + Au$, and $Cu + Cu$ data taking, which required the event to satisfy the MB trigger conditions and that there be at least one high- p_T electron or photon candidate

in the event. For electron candidates the ERT trigger required a minimum energy deposit of 0.4 (0.6 and 0.8) GeV/ c in a tile of 2×2 EMCal towers matched to a hit in the RICH in $p + p$ ($d + Au$) collisions. For the photon candidates, the ERT trigger required a minimum energy deposit of 1.4, 2.4, and 3.4 GeV/ c in a tile of 4×4 EMCal towers in $p + p$, $d + Au$, and $Cu + Cu$ collisions, respectively. In the $d + Au$ and the $Cu + Cu$ analysis, the MB data set was used to measure ω production up to 4 GeV/ c in $d + Au$ and 6 GeV/ c in $Cu + Cu$; the ERT sample was used at higher p_T . The ERT trigger efficiencies measured for single photons and electrons and calculated for ω mesons is described in Sec. III D.

III. DATA ANALYSIS

In this section, we describe the event selection and data analysis for reconstructing the leptonic ($\omega \rightarrow e^+e^-$) and hadronic ($\omega \rightarrow \pi^+\pi^-\pi^0$ and $\omega \rightarrow \pi^0\gamma$) decay channels of the ω . Corrections applied to the raw data to calculate the ω meson invariant yields and systematic uncertainties related to the measurements are also presented.

A. Event selection and basic analysis cut

For data taken in 2004, the correlation of the charge deposited in the BBCs with energy deposited in the ZDCs provides a determination of the centrality of the collisions. For data taken in 2005, 2007, and 2008, the centralities were only determined by using BBC. A Glauber Monte Carlo [14] with the BBC and ZDC responses was used to estimate the number of binary nucleon-nucleon collisions (N_{coll}) and the number of participating collisions (N_{part}) for each centrality bin [15].

Events are selected with a reconstructed z vertex within 30 cm of the center of the interaction region. Charged tracks were required to have momenta in the range of $0.2 < p_T < 5.0$ (7.0) GeV/ c for the $\omega \rightarrow e^+e^-$ analysis in $p + p$ ($d + Au$) [7] and $0.3 < p_T < 8.0$ GeV/ c for the $\omega \rightarrow \pi^+\pi^-\pi^0$ decay channel [8]. Charged particles with $p_T < 0.2$ GeV/ c have a large bending angle in the axial magnetic field of the PHENIX central magnet [16] and most of them do not pass

TABLE I. Summary of the analyzed data samples and ω meson decay channels. Values for previously published PHENIX data (PRD83) [7] and (PRC75) [8] are given for comparison. Threshold refers to the thresholds for electron or photon candidates, which is discussed in text.

Data set	Trigger	Sampled events	$\int Ldt$	Threshold	Decay channel	Reference
2003 $d + Au$	ERT	5.5B	2.74 nb $^{-1}$	2.4 GeV	$\omega \rightarrow \pi^+\pi^-\pi^0$	PRC75 [8]
				2.4 GeV	$\omega \rightarrow \pi^0\gamma$	PRC75 [8]
2004 $Au + Au$	MB	1.5B	241 μb^{-1}	N/A	$\omega \rightarrow \pi^0\gamma$	This work
2005 $p + p$	ERT	85B	3.78 pb $^{-1}$	0.4 GeV	$\omega \rightarrow e^+e^-$	PRD83 [7]
				1.4 GeV	$\omega \rightarrow \pi^+\pi^-\pi^0$	PRD83 [7]
				1.4 GeV	$\omega \rightarrow \pi^0\gamma$	PRD83 [7]
2005 $Cu + Cu$	MB	8.6B	3.06 pb $^{-1}$	N/A	$\omega \rightarrow \pi^0\gamma$	This work
	ERT			3.4 GeV	$\omega \rightarrow \pi^0\gamma$	This work
2007 $Au + Au$	MB	5.1B	813 μb^{-1}	N/A	$\omega \rightarrow \pi^0\gamma$	This work
2008 $d + Au$	ERT	160B	80 nb $^{-1}$	0.6/0.8 GeV	$\omega \rightarrow e^+e^-$	This work
				2.4 GeV	$\omega \rightarrow \pi^+\pi^-\pi^0$	This work
				2.4 GeV	$\omega \rightarrow \pi^0\gamma$	This work

through the entire tracking system. Electrons and positrons are identified mainly by the Čerenkov photons emitted in the RICH by requiring at least two photomultipliers hit in the RICH cells matched to the track [17]. Also, matching of the energy measured for the charged track in the EMCal with the momentum measured in the tracking system, $|E/p - 1| < 0.5$, helps to further improve e/π separation. Together the RICH and EMCal provide an e/π rejection factor of about $1:10^4$. Photon identification is performed by the shower shape criteria in the EMCal [18], and the energy of the selected γ clusters is above 0.2 GeV.

B. Leptonic analysis

The leptonic analysis is done only in $p + p$ and $d + Au$. In case of $\omega \rightarrow e^+e^-$, all electrons and positrons reconstructed in each event are combined into pairs, resulting in signal peaks that sit on top of a combinatorial background in the invariant mass distribution. The uncorrelated part of the background is estimated with an event-mixing technique, which combines tracks from different events with similar event centrality and z coordinate of the collision vertex. Details of the event mixing procedure are presented in Ref. [19].

Figure 1 shows invariant mass spectra of e^+e^- pairs in $p + p$ and $d + Au$ collisions at $\sqrt{s_{NN}} = 200$ GeV after subtraction of combinatorial background as described above. The solid lines show the global fits which include: (1) contributions from ω , ρ , and ϕ mesons approximated with Breit-Wigner functions convolved with Gaussian distributions to account for the detector mass resolution; masses and widths of the ω , ρ , and ϕ are fixed to the PDG values; the ρ component is calculated assuming that ω and ρ have the same yield and vacuum branching ratios; (2) other correlated residual background, which is dominated by a contribution from jets, is approximated by a second-order polynomial function. The detector resolution, which is determined from simulations, is found to be dependent on mass and momentum and varies from 6 to 18 MeV/ c^2 .

The ω yield is determined by counting bin contents in a 3σ width (derived from the fitting) and subtracting the polynomial background. An associated systematic uncertainty from the raw yield extraction is calculated by varying the background normalization, fitting functions, range, and counting methods. The estimated value is 4–15% in $p + p$ [7] and 8–15% in $d + Au$ collisions.

C. Hadronic analysis

In the $\omega \rightarrow \pi^+\pi^-\pi^0$ and $\omega \rightarrow \pi^0\gamma$ channels, the first analysis step is to reconstruct π^0 mesons by combining pairs of photons reconstructed in an event. Then the mass and width of the π^0 peak in the invariant mass distribution of photon pairs are parametrized as a function of transverse momentum. The 1σ width of the π^0 peak varies from 13 to 9 MeV/ c^2 as p_T increases from 1 to 4 GeV/ c and is determined by the EMCal energy resolution. A pair of photons is selected as a π^0 candidate if its invariant mass is within 2σ of the reconstructed π^0 mass. In Cu + Cu and Au + Au, an additional asymmetry cut for π^0 candidates is used to reduce combinatorial background,

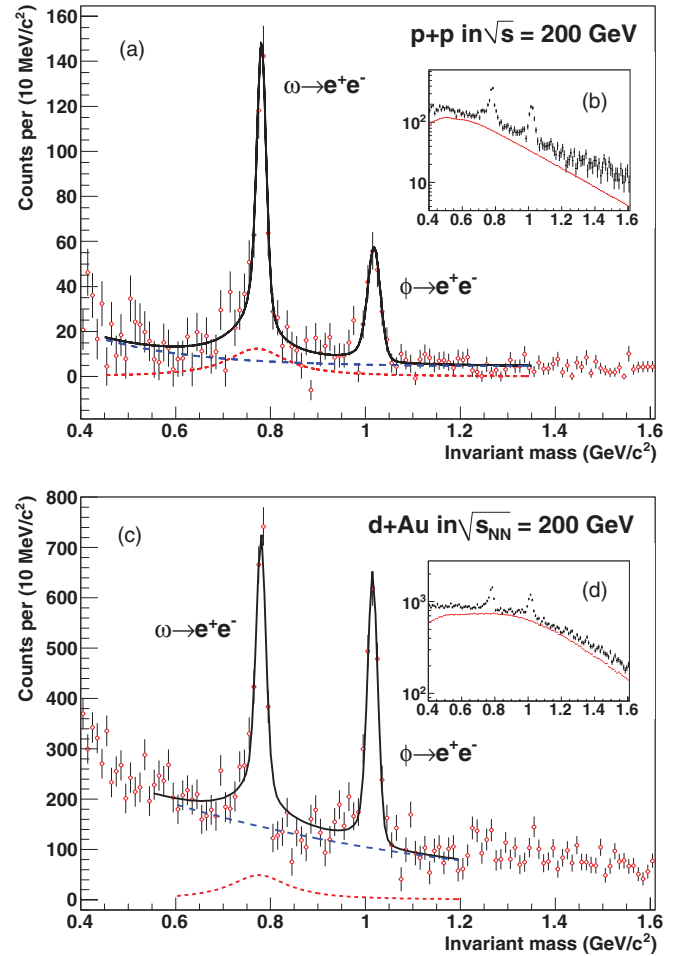


FIG. 1. (Color online) Invariant mass of e^+e^- pairs detected by the PHENIX central arms with uncorrelated combinatorial background subtracted (see text) for (a) $p + p$ collisions and (c) minimum-bias $d + Au$ collisions at $\sqrt{s_{NN}} = 200$ GeV and integrated over p_T . Inserts (b) and (d) show the raw spectra before subtraction. The spectrum is fit to the ω and ϕ resonances where the masses and widths are set to the PDG values; the Breit-Wigner resonance shape is convolved with a Gaussian to account for detector mass resolution estimated from simulation and then corrected for the radiative tail. The ρ contribution is shown as the dotted (red) line with an assumption that the yield is the same as that of the ω . The residual continuum component is estimated by a polynomial fit as shown by the dashed (blue) line.

$\alpha = |E_{\gamma_1} - E_{\gamma_2}| / |E_{\gamma_1} + E_{\gamma_2}| < 0.8$. Selected π^0 candidates, which include true π^0 s and combinatorial background are combined either with the third photon with energy $E_\gamma > 1.0$ GeV/ c for the $\omega \rightarrow \pi^0\gamma$ or with a pair of opposite-sign charged tracks for the $\omega \rightarrow \pi^+\pi^-\pi^0$ decay.

In the $p + p$ and $d + Au$ analysis, the ω meson raw yields are extracted by fitting the p_T slices of the invariant mass distribution with a combination of a Gaussian for the signal and a second order polynomial for the background. The width and mass of the reconstructed ω mesons were found to be in good agreement with values expected from simulation. Details of these analyses are described in Ref. [10].

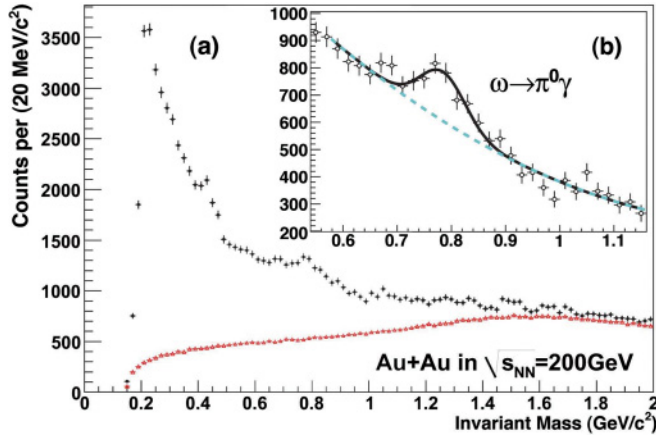


FIG. 2. (Color online) (a) Invariant mass and scaled mixed background distributions for $\pi^0\gamma$ decay at $7 < p_T < 12$ GeV/c in Au + Au collisions. (b) Invariant mass distribution after subtraction of scaled background.

In the Cu + Cu and Au + Au analysis, only the $\omega \rightarrow \pi^0\gamma$ channel was analyzed due to high combinatorial background in the $\omega \rightarrow \pi^+\pi^-\pi^0$ channel. The uncorrelated combinatorial background was estimated using an event mixing technique where the third photon in the $\pi^0\gamma$ decay was taken from the different events with a similar centrality and z vertex. For every p_T bin, before subtraction, the calculated background was normalized to match the integral of the foreground at an invariant mass $1.75 < M_{\text{inv}} < 4.0$ GeV/c², over which we expect the contribution from correlated background to be small. An example of the invariant mass distribution and normalized background distributions is shown in Fig. 2(a) and the invariant mass distribution after subtraction shown in Fig. 2(b). The resulting invariant mass distribution contains residual background from correlated particles: the background contributions are from $K_s \rightarrow \pi^0\pi^0$ decays, and π^0 and η , where one of the photons from $\pi^0(\eta) \rightarrow \gamma\gamma$ decay creates a fake π^0 candidate for the $\omega \rightarrow \pi^0\gamma$ reconstruction. The $\omega \rightarrow \pi^0\gamma$ peak is further enhanced by a mixed background subtraction. Finally, raw yields of ω are extracted by fitting the spectra with a combination of a Gaussian and a polynomial. The width of the Gaussian used in the fit to the data is limited to ± 1 MeV/c² around the value determined from simulation. The ω yield is calculated as an integral of the Gaussian.

Systematic uncertainties associated with the raw yield extraction are evaluated using different fitting functions and ranges, different counting methods and kinematic cuts, varying the EMCAL resolution in simulation, and applying different limits for the width of ω peaks in fits to data. The estimated value is 13–35% in Cu + Cu and 20–35% in Au + Au collisions.

D. Reconstruction efficiencies

The reconstruction efficiency of the ω is determined using a GEANT simulation of the PHENIX detector tuned to reproduce the performance of the detector subsystems. The ω mesons are generated and decayed into corresponding decay channels

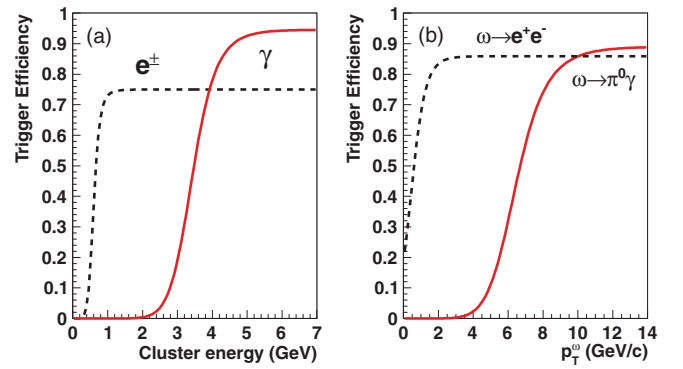


FIG. 3. (Color online) Typical ERT trigger efficiencies for (a) single electrons (0.6 GeV threshold) and photons (3.4 GeV threshold) and (b) $\omega \rightarrow e^+e^-$ and $\omega \rightarrow \pi^0\gamma$ using corresponding triggered electrons/photons.

and reconstructed with the same analysis chain as the real data. The generated ω spectra were weighted to match the measured particle spectra. It was verified that the simulated positions and widths of the reconstructed particle peaks are consistent with the values measured in real data.

The reconstruction efficiency is divided into three components: ϵ , ϵ_{trig} , and ϵ_{emb} . The efficiency ϵ is the reconstruction efficiency for minimum bias events in a low-occupancy environment, like in $p + p$ and $d + \text{Au}$ collisions. This efficiency accounts for the limited geometrical acceptance, resolution, and efficiencies of the detector subsystems as well as for analysis cuts. When a selective ERT trigger is used, an additional trigger efficiency factor, ϵ_{trig} , is applied. This factor measures the efficiency of the ERT trigger logic. For higher multiplicity collisions, one needs to account for the loss of efficiency from increased detector occupancy: this is measured through the embedding efficiency ϵ_{emb} . A measured raw yield then needs to be corrected for the total efficiency $\epsilon \times \epsilon_{\text{emb}} \times \epsilon_{\text{trig}}$, depending on the collision, centrality, and trigger involved.

The ERT data sample was used to measure dielectron and hadronic decay channels of the ω at high p_T in $p + p$, $d + \text{Au}$, and Cu + Cu. The threshold settings for ERT are described in Sec. II. The single particle ERT efficiency was measured by dividing the energy spectra of gamma clusters or electrons that fired the ERT trigger by the energy spectra of all clusters or electrons in the minimum bias data sample. Figure 3(a) shows a typical example of the ERT trigger efficiencies for single electrons and single photons as a function of cluster energy. The level of saturation of trigger efficiency curves is below 100% because of inactive areas of the ERT and the RICH detectors.

The ERT efficiencies for the ω meson in both the leptonic and hadronic decay modes were evaluated with the help of a Monte-Carlo simulation. For all fully reconstructed ω mesons, the calculated single photon or electron ERT efficiency curves were used to calculate the probability that one of the particles in the final state fires the ERT trigger. Figure 3(b) shows the corresponding trigger efficiencies for $\omega \rightarrow e^+e^-$ and $\omega \rightarrow \pi^0\gamma$. More detailed descriptions are presented in Refs. [7,10].

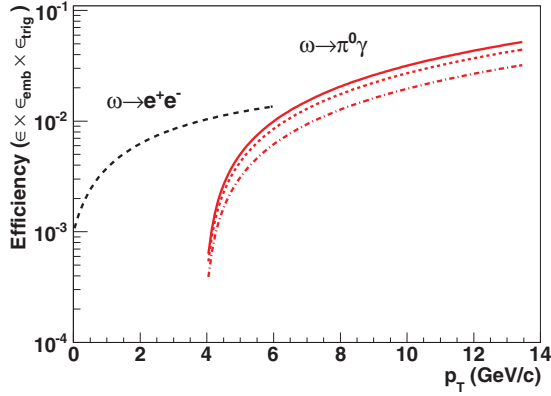


FIG. 4. (Color online) Typical reconstruction efficiencies for $\omega \rightarrow e^+e^-$ and $\omega \rightarrow \pi^0\gamma$. The curves for $\omega \rightarrow \pi^0\gamma$ include the embedding efficiency in Au + Au collisions: solid, dotted, and dot-dashed lines (red) are for 60–92%, 20–60%, and 0–20% centrality, respectively.

Figure 4 shows typical reconstruction efficiencies ϵ for $\omega \rightarrow e^+e^-$ and $\omega \rightarrow \pi^0\gamma$. In the case of Cu + Cu and Au + Au collisions, an additional efficiency correction ϵ_{emb} due to cluster overlap in high multiplicity environment must be applied. In most central Au + Au events, the EMCal typically detects more than 300 clusters corresponding to a detector occupancy of $\sim 10\%$. To estimate the corresponding loss in efficiency, the simulated ω decays are embedded into real A + A events and analyzed. The merging effect results in $\sim 40\%$ loss of reconstruction efficiency in 0–20% central Au + Au collisions, $\sim 15\%$ loss in 0–20% central Cu + Cu collisions, and is almost negligible in peripheral collisions. Figure 4 shows the reconstruction efficiencies derived for Au + Au collisions at different centralities. Finally, in each bin we apply also a correction factor [7] to replace the average value of the yield in the analyzed p_T bin by the value of the yield in the middle of the bin.

E. Calculation of invariant yields

In $p + p$ and minimum bias $d + \text{Au}$ collisions, the invariant yield is related to the invariant cross section as:

$$E \frac{d^3\sigma}{dp^3} = \sigma_{pp}^{\text{inel}}(\sigma_{d\text{Au}}^{\text{inel}}) \times \frac{1}{2\pi p_T N_{\text{evt}}} \frac{d^2N}{dp_T dy}, \quad (1)$$

where $\sigma_{pp}^{\text{inel}}$ and $\sigma_{d\text{Au}}^{\text{inel}}$ are the total inelastic cross section, 42.2 and 2260 mb, respectively.

For a given centrality bin, the invariant yields as a function of p_T (invariant transverse momentum) are determined from:

$$\frac{1}{2\pi p_T} \frac{d^2N_{\text{cent}}}{dp_T dy} \equiv \frac{1}{2\pi p_T N_{\text{cent}}^{\text{evt}}} \frac{1}{BR} \frac{1}{\epsilon(p_T)\epsilon_{\text{emb}}(p_T, \text{cent})\epsilon_{\text{trig}}(p_T)} \times \frac{N(\Delta p_T, \text{cent})}{\Delta p_T \Delta y}, \quad (2)$$

where $N_{\text{cent}}^{\text{evt}}$ is the number of events for a given centrality bin, $N(\Delta p_T, \text{cent})$ is the raw yield of ω for each p_T and centrality bin, $\epsilon(p_T)$, $\epsilon_{\text{emb}}(p_T, \text{cent})$ and $\epsilon_{\text{trig}}(p_T)$ are, as previously defined, reconstruction efficiency, embedding efficiency, and trigger efficiency, respectively. The trigger efficiency is applied

TABLE II. Summary of assigned systematic uncertainties of $\omega \rightarrow e^+e^-$ in $p + p$ and $d + \text{Au}$ analysis. (A), (B), and (C) refer to the uncertainty type, which is explained in text.

Source	$p + p$	$d + \text{Au}$
Peak extraction	4–15%(A)	8.4–24.1%(A)
ERT efficiency	1–3%(B)	1–7%(B)
BBC cross section	9.7%(C)	7.9%(C)
Momentum scale	2–11%(B)	1.2–5.3%(B)
Acceptance correction	5%(B)	7%(B)
Electron ID		10%(B)
Branching ratio		1.7%(C)

only for the analyses using the ERT data set. BR is the decay branching ratio from Ref. [9], $(89.2 \pm 0.7 \times 10^{-2})$ for $\omega \rightarrow \pi^+\pi^-\pi^0$, $(8.90 \pm 0.27 \times 10^{-2})$ for $\omega \rightarrow \pi^0\gamma$, and $(7.16 \pm 0.12 \times 10^{-5})$ for $\omega \rightarrow e^+e^-$.

F. Systematic uncertainties

In addition to uncertainties related to the raw yield extraction described in the corresponding analysis sections, other sources of the uncertainties should also be taken into account. Uncertainties of the ERT trigger efficiency and acceptance corrections were estimated by varying the analysis cuts, energy, and momentum scales of the EMCal and drift chamber by $\sim 1\%$ [7]. Uncertainties of detector response (mainly from the RICH for electron analysis and from the EMCal for hadronic analysis) are estimated by changing particle identification criteria in the analysis. A summary of assigned systematic uncertainties is listed in Table II for $\omega \rightarrow e^+e^-$ in $p + p$ and $d + \text{Au}$ and in Table III for $\omega \rightarrow \pi^0\gamma$ in Cu + Cu and Au + Au. Those are classified into three types: Type A is p_T -uncorrelated, Type B is p_T -correlated, and Type C is the overall normalization uncertainty. Total uncertainties for $\omega \rightarrow e^+e^-$ are 16–24% in $p + p$ [7] and 19–26% in $d + \text{Au}$. The total uncertainties for $\omega \rightarrow \pi^0\gamma$ are 15–37% in Cu + Cu and 21–37% in Au + Au. Uncertainties for $\omega \rightarrow \pi^0\pi^+\pi^0$ analysis are 7–20% in $p + p$ and 10–15% in $d + \text{Au}$, as described in Ref. [8].

TABLE III. Summary of assigned systematic uncertainties of $\omega \rightarrow \pi^0\gamma$ in Cu + Cu and Au + Au analysis. (A), (B), and (C) refer to the uncertainty type, which is explained in text.

Source	Cu + Cu	Au + Au
Peak extraction	13–35%(A)	20.1–34.5%(A)
ERT efficiency	3–4%(B)	N/A
Energy scale		4–7%(B)
Energy resolution		2–3%(B)
Acceptance correction		3–6%(B)
Conversion		4.5%(C)
Branching ratio		3.4%(C)

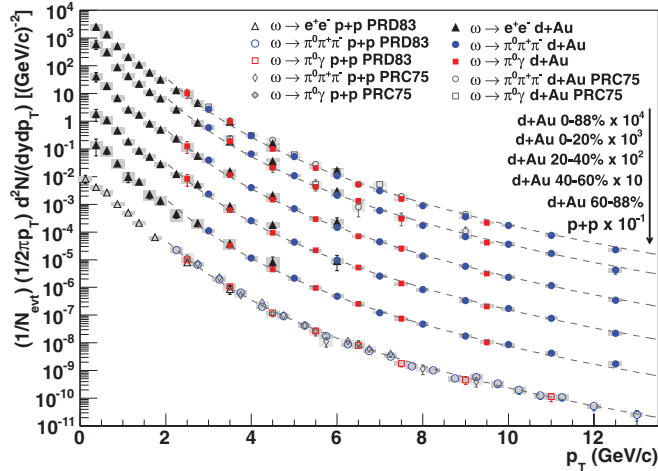


FIG. 5. (Color online) Invariant transverse momentum spectra of ω production in $p + p$ and $d + Au$ collisions at $\sqrt{s} = 200$ GeV. The dashed lines represent fits to $p + p$ results by a Tsallis distribution [20] scaled by the corresponding number of binary collisions for $d + Au$. The previously published PHENIX data (PRD83) [7] and π^0 (PRC75) [8] are shown for comparison.

IV. RESULTS

A. Invariant transverse momentum spectra

Figure 5 presents the invariant transverse momentum spectra measured for the ω meson in $p + p$ and $d + Au$ at $\sqrt{s} = 200$ GeV. Previously published results are shown with open markers [8]. Results for different decay channels and data samples agree within uncertainties in the overlap region. The dashed curves in Fig. 5 are fixed on $p + p$ results at $p_T > 2$ GeV/c using a Tsallis distribution [20] and then scaled by the number of binary nucleon-nucleon collisions (N_{coll}) estimated using Glauber Monte-Carlo simulation [14] for $d + Au$ results.

Figure 6 shows the invariant transverse momentum spectra measured for the ω meson in Cu + Cu and Au + Au collisions at $\sqrt{s_{NN}} = 200$ GeV. Measurements were performed only in the $\omega \rightarrow \pi^0 \gamma$ channel. Results are presented for three centrality bins: 0–20%, 20–60%, 60–92% (60–94% in Cu + Cu) and minimum bias collisions. The dashed lines represent N_{coll} scaled fits to $p + p$ results, where N_{coll} values were taken from [15] summarized in Table IV. The results show that in peripheral heavy ion collisions ω production generally follows binary scaling, while in midcentral and central collisions, production of ω mesons is suppressed at high p_T . Such behavior is similar to one previously observed for other light mesons [4,21] and can be attributed to medium-induced effects.

B. ω/π ratio

Measurement of ω production can be used to study the relative production of vector and pseudoscalar mesons consisting of the same valence quarks, i.e., ω/π ratio as a function of transverse momentum. In calculating the ω/π ratio,

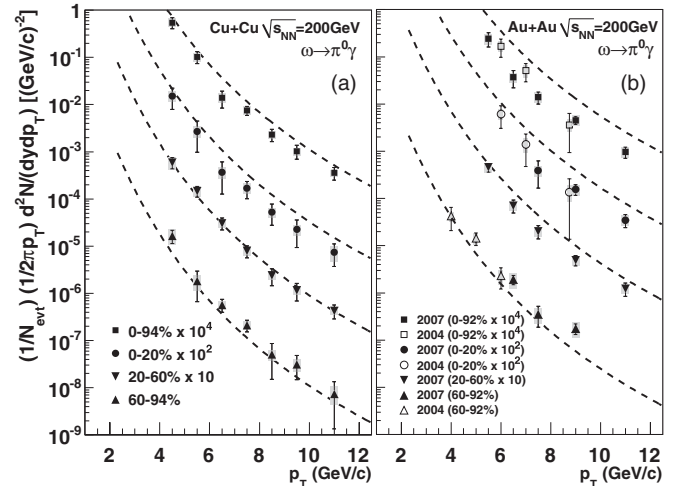


FIG. 6. Invariant transverse momentum spectra of ω production in (a) Cu + Cu and (b) Au + Au collisions from the $\omega \rightarrow \pi^0 \gamma$ decay channel for three centrality bins and minimum bias. The dashed lines are the $p + p$ results scaled by the corresponding number of binary collisions. The (a) Cu + Cu data were recorded in 2005 and the (b) Au + Au data were recorded in 2004 and 2007, as indicated.

the same methodology from [4,22,23] for the π^+/π^- and π^0 was used. The charged pion results, $(\pi^+ + \pi^-)/2$, were used to extend neutral pion measurements at the lower limit of the p_T range from 1 to 0.2 GeV/c. To produce the average pion spectrum in $p + p$ [22] and $d + Au$ collisions [24], we simultaneously fit $(\pi^+ + \pi^-)/2$ and π^0 spectra with the modified Hagedorn function [19]. Inclusion of the charged pion spectrum in the fit has a small effect in the 1–2 GeV/c overlap region, smaller than 5% compared to fitting neutral pions alone. The resulting fitted pion distributions are used to calculate ω/π ratios for $p + p$ and $d + Au$. Uncertainties for the fit values are evaluated by taking into account statistical and systematic uncertainties of the experimental points as described in [7,25].

Figure 7 presents the ω/π ratio measured in $p + p$ collisions at $\sqrt{s} = 200$ GeV as a function of transverse momentum. Open markers show our previous measurements of the ω/π ratio [8]. One can see good agreement between previous results and this measurement. For completeness, we also present similar measurements performed in lower-energy

TABLE IV. The number of participating collisions ($\langle N_{\text{part}} \rangle$) and the number of binary nucleon-nucleon collisions ($\langle N_{\text{coll}} \rangle$).

System	$\langle N_{\text{part}} \rangle$	$\langle N_{\text{coll}} \rangle$
Au + Au MinBias	109.1 ± 4.1	257.8 ± 25.4
Au + Au 0-20%	280.5 ± 4.6	783.2 ± 77.5
Au + Au 20-60%	101.6 ± 5.4	197.5 ± 20.8
Au + Au 60-92%	11.8 ± 2.1	11.5 ± 2.5
Cu + Cu MinBias	34.6 ± 1.2	51.8 ± 5.6
Cu + Cu 0-20%	85.9 ± 2.3	151.8 ± 17.1
Cu + Cu 20-60%	33.2 ± 1.6	41.9 ± 4.8
Cu + Cu 60-94%	6.5 ± 0.6	5.1 ± 0.7

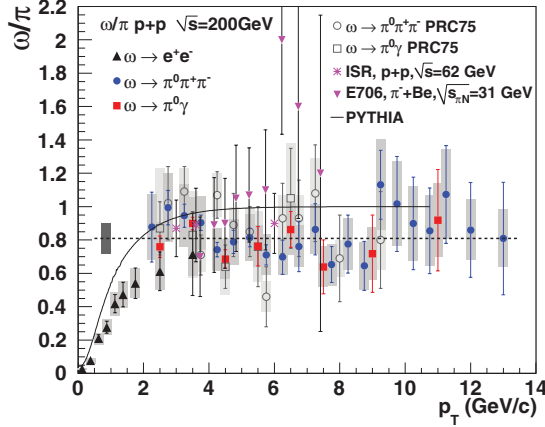


FIG. 7. (Color online) Measured ω/π ratio as a function of p_T in $p + p$ collisions at $\sqrt{s} = 200$ GeV. (Dashed line) Fit of a constant value to data points at $p_T > 2$ GeV/c. The fit result is $0.81 \pm 0.02^{\text{stat}} \pm 0.09^{\text{syst}}$. (Gray box) The overall error of the fitting. (Solid line) The PYTHIA prediction [28] for $p + p$ at $\sqrt{s} = 200$ GeV. Shown for comparison are previously published results from PHENIX (PRC75) [8] and lower collision energies at $\sqrt{s_{NN}} = 31$ GeV (E706) [26] and $\sqrt{s} = 62$ GeV (ISR) [27].

experiments: $\pi + \text{Be}$ at $\sqrt{s_{NN}} = 31$ GeV (E706 [26]), $p + p$ at $\sqrt{s} = 62$ GeV (ISR [27]). Please note that the branching ratio for the $\omega \rightarrow \pi^0 \gamma$ decay was set equal to $(8.8 \pm 0.5)\%$, which is 6% different from the latest PDG value of $(8.28 \pm 0.28)\%$.

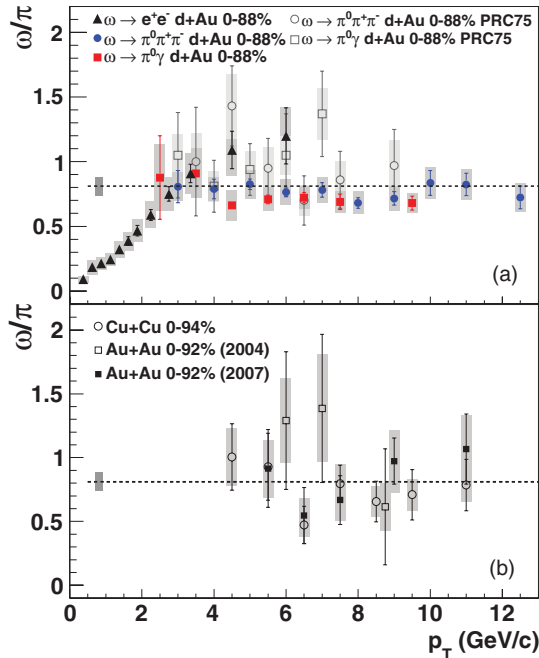


FIG. 8. (Color online) The ω/π ratios versus transverse momentum at $\sqrt{s_{NN}} = 200$ GeV in (a) $d + \text{Au}$ collisions (0–88% centrality) for $\omega \rightarrow e^+ e^-$, $\pi^0 \pi^+ \pi^-$, and $\pi^0 \gamma$ and (b) $\text{Cu} + \text{Cu}$ collisions (0–94% centrality) and $\text{Au} + \text{Au}$ collisions (0–92% centrality) for $\omega \rightarrow \pi^0 \gamma$. The dashed lines and boxes are a fit of a constant value to the data points at $p_T > 2$ GeV/c in $p + p$ (Fit result: $0.81 \pm 0.02^{\text{stat}} \pm 0.09^{\text{syst}}$). The previously published data (PRC75) [8] are shown for comparison.

Within measurement uncertainties, the ω/π ratio in hadronic interactions is energy independent at high p_T .

A linear fit to the ratio at $p_T > 2$ GeV/c gives a value of the linear coefficient consistent with zero within less than one standard deviation ($-0.013 \pm 0.009^{\text{stat}} \pm 0.014^{\text{syst}}$), indicating no significant p_T dependence of the ratio at $p_T > 2$ GeV/c. A fit to a constant gives a value of the ratio equal to $0.81 \pm 0.02^{\text{stat}} \pm 0.09^{\text{syst}}$ consistent with our previous measurement of $0.85 \pm 0.05^{\text{stat}} \pm 0.09^{\text{syst}}$ [8]. The PYTHIA prediction of the ω/π ratio, shown in Fig. 7 with a solid line, lies above the measured ratio.

The ω/π ratios measured in minimum bias $d + \text{Au}$, $\text{Cu} + \text{Cu}$, and $\text{Au} + \text{Au}$ collisions at $\sqrt{s_{NN}} = 200$ GeV are presented in Fig. 8. As in the case of $p + p$ collisions, there is no indication that the ratios depend on transverse momentum for $p_T > 2$ GeV/c. Fits to a constant for $p_T > 2$ GeV/c give the following values of the ω/π ratio: $0.75 \pm 0.01^{\text{stat}} \pm 0.08^{\text{syst}}$ in $d + \text{Au}$, $0.71 \pm 0.07^{\text{stat}} \pm 0.07^{\text{syst}}$ in $\text{Cu} + \text{Cu}$, and $0.83 \pm 0.09^{\text{stat}} \pm 0.06^{\text{syst}}$ in MB $\text{Au} + \text{Au}$ collisions. Within the uncertainties, the ω/π ratios measured in different collision systems for $p_T > 2$ GeV/c are in agreement. This agrees with previous measurements in $d + \text{Au}$ [8] within the uncertainties. The ratios in various collision systems imply similar suppression factors and p_T dependencies within the uncertainties for the ω and π production in nucleus-nucleus collisions at high p_T .

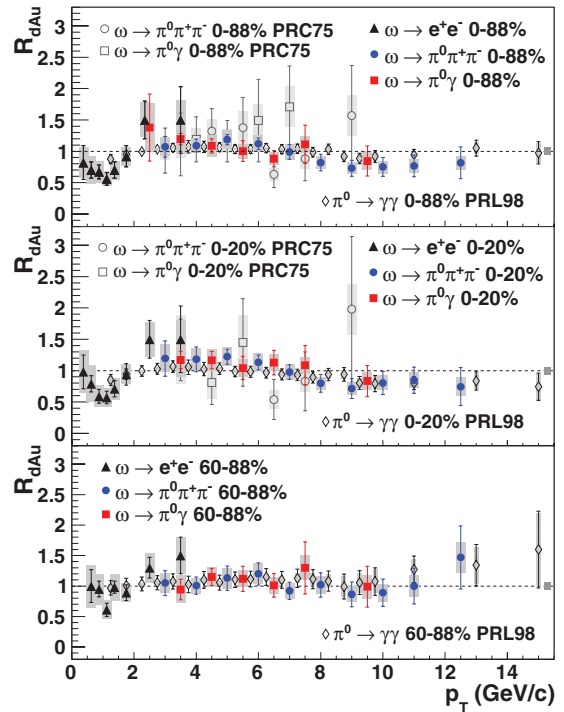


FIG. 9. (Color online) Nuclear modification factor, $R_{d\text{Au}}$, measured for the ω in 0–88, 0–20, and 60–88% centrality bins in $d + \text{Au}$ collisions at $\sqrt{s} = 200$ GeV. The gray box at the rightmost end of the constant fit line shows the uncertainty of the fit. The previously published data for ω (PRC75) [8] and π^0 (PRL98) [24] are shown for comparison.

C. Nuclear modification factors

To quantify medium-induced effects on high p_T particle production, the nuclear modification factor is defined as

$$R_{AB}(p_T) = \frac{d^2 N_{AB}/dydp_T}{(\langle N_{\text{coll}} \rangle / \sigma_{pp}^{\text{inel}}) \times d^2 \sigma_{pp}/dydp_T}, \quad (3)$$

where $d^2 N_{AB}/dydp_T$ is the differential yield per event in nucleus-nucleus collisions, $\langle N_{\text{coll}} \rangle$ is the number of binary nucleon-nucleon collisions averaged over the impact parameter range of the corresponding centrality bin calculated by Glauber Monte-Carlo simulation [14], and $\sigma_{pp}^{\text{inel}}$ and $d^2 \sigma_{pp}/dydp_T$ are the total and differential cross sections for inelastic $p + p$ collisions, respectively. In the absence of medium-induced effects, the yield of high- p_T particles is expected to scale with $\langle N_{\text{coll}} \rangle$, resulting in $R_{AB} = 1$ at high- p_T .

Figure 9 presents R_{dAu} measured for the ω in minimum bias, most central and peripheral $d + Au$ collisions at $\sqrt{s_{NN}} = 200$ GeV. Good agreement is observed between different decay modes and between new and previously published PHENIX ω results [8] shown with open markers. For comparison we also present π^0 results published in Ref. [24]. In peripheral collisions, the measured values of R_{dAu} are consistent with unity over the whole p_T range of measurements. In most central collisions, a modest Cronin-like enhancement is observed in a range of p_T from 2 to 6 GeV/c and suppression of ω production at $p_T > 8$ GeV/c. A similar enhancement at 2–6 GeV/c was previously observed for neutral and charged pions [22,24] and ϕ mesons [29]. Suppression of ω production at higher p_T is in agreement with π^0 results [24]. Similarity of

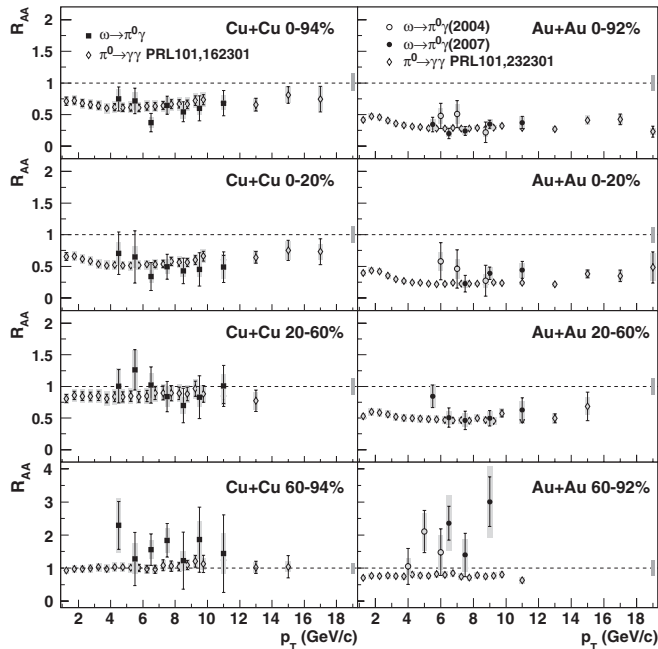


FIG. 10. R_{AA} of the ω in Cu + Cu and Au + Au collisions from the $\omega \rightarrow \pi^0 \gamma$ decay channel for three centrality bins and minimum bias. The uncertainty in the determinations of $p + p$ scaling are indicated in gray boxes near the rightmost end of the $R_{AA} = 1$ dashed lines. Rhombuses in each plot are R_{AA} of π^0 in Cu + Cu [23] and Au + Au [4] shown as a comparison.

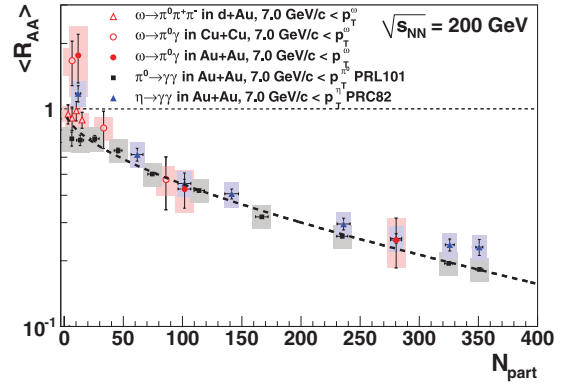


FIG. 11. (Color online) R_{AA} for the ω meson integrated over the range $p_T > 7$ GeV/c as a function of the number participating nucleons (N_{part}). Results for π^0 (PRL101) [4] and η (PRC82) [5] are shown for comparison. The dashed line shows the fitted fractional energy loss function, $R_{AA} = (1 - S_0 N_{\text{part}}^a)^{n-2}$.

the observed effects for the mesons with very different masses suggests that the collective nuclear effects occur at the partonic level [30–32].

Figure 10 shows the nuclear modification factors measured in Cu + Cu and Au + Au collisions at $\sqrt{s_{NN}} = 200$ GeV as a function of p_T . Results are presented for minimum bias, most central (0–20%), midcentral (20–60%) and peripheral (60–94% in Cu + Cu; 60–92% in Au + Au) collisions. The nuclear modification factors do not depend on p_T for $p_T > 6$ GeV/c at all centralities. For $N_{\text{part}} > 34$ suppression of ω production begins to be observed, with suppression increasing as N_{part} increases.

Figure 11 shows R_{AA} values integrated for $p_T > 7$ GeV/c as a function the number of participants. For ω mesons we present four centrality bins in $d + Au$, and three centrality bins in Cu + Cu and Au + Au. For comparison the average values of R_{AA} for π^0 [4] and η mesons [5] mesons for $p_T > 7$ GeV/c are also plotted. To see whether the ω follows the suppression pattern of π^0 and η , the integrated R_{AA} vs N_{part} dependence is fit to a fractional energy loss function $R_{AA} = (1 - S_0 N_{\text{part}}^a)^{n-2}$ [4,33]. The parameter n , which is an exponent of the power law fit to the ω p_T spectrum measured in $p + p$ for $p_T > 5$ GeV/c [7], was fixed to 8. The fitting gives χ^2/ndf less than three and parameters $S_0 = (9.9 \pm 0.7) \times 10^{-3}$ and $a = 0.55 \pm 0.01$. As in Ref. [4], we find the parameter a consistent with predictions of the GLV [34] and PQM [6] models ($a \sim 2/3$). Therefore, we can conclude that ω production has a similar suppression pattern as π^0 and η , which supports the scenario that the energy loss takes place at the parton level in the hot and dense medium formed in the collisions.

V. SUMMARY

We measured production of the ω meson via both leptonic and hadronic decay channels in $p + p$, $d + Au$, Cu + Cu, and Au + Au at $\sqrt{s_{NN}} = 200$ GeV. The invariant transverse momentum spectra show good agreement in different decay channels in $p + p$ and $d + Au$. The R_{dAu} shows a moderate Cronin-like enhancement at intermediate p_T 2–6 GeV/c

and suppression for $p_T > 8$ GeV/ c in most central $d + Au$ collisions. The measurement of the nuclear modification factor for the ω meson in Cu + Cu and Au + Au collisions show that ω production has a similar suppression pattern as the π^0 and η within model agreement, thus supporting the scenario that the energy loss takes place at the partonic level in the hot and dense medium formed in the collisions.

ACKNOWLEDGMENTS

We thank the staff of the Collider-Accelerator and Physics Departments at Brookhaven National Laboratory and the staff of the other PHENIX participating institutions for their vital contributions. We acknowledge support from the Office of Nuclear Physics in the Office of Science of the Department of Energy, the National Science Foundation, Abilene Christian University Research Council, Research Foundation of SUNY, and Dean of the College of Arts and Sciences, Vanderbilt University (USA), Ministry of Education, Culture, Sports, Science, and Technology and the Japan Society for the Promotion of Science (Japan), Conselho Nacional de

Desenvolvimento Científico e Tecnológico and Fundação de Amparo à Pesquisa do Estado de São Paulo (Brazil), Natural Science Foundation of China (P.R. China), Ministry of Education, Youth and Sports (Czech Republic), Centre National de la Recherche Scientifique, Commissariat à l'Énergie Atomique, and Institut National de Physique Nucléaire et de Physique des Particules (France), Ministry of Industry, Science and Technologies, Bundesministerium für Bildung und Forschung, Deutscher Akademischer Austausch Dienst, and Alexander von Humboldt Stiftung (Germany), Hungarian National Science Fund, OTKA (Hungary), Department of Atomic Energy and Department of Science and Technology (India), Israel Science Foundation (Israel), National Research Foundation and WCU program of the Ministry Education Science and Technology (Korea), Ministry of Education and Science, Russian Academy of Sciences, Federal Agency of Atomic Energy (Russia), VR and the Wallenberg Foundation (Sweden), the US Civilian Research and Development Foundation for the Independent States of the Former Soviet Union, the US-Hungarian Fulbright Foundation for Educational Exchange, and the US-Israel Binational Science Foundation.

-
- [1] X. N. Wang, *Phys. Lett. B* **579**, 299 (2004).
 [2] S. Adler *et al.* (PHENIX Collaboration), *Phys. Rev. Lett.* **96**, 202301 (2006).
 [3] B. Abelev *et al.* (STAR Collaboration), *Phys. Rev. C* **80**, 44905 (2009).
 [4] A. Adare *et al.* (PHENIX Collaboration), *Phys. Rev. Lett.* **101**, 232301 (2008).
 [5] A. Adare *et al.* (PHENIX Collaboration), *Phys. Rev. C* **82**, 011902 (2010).
 [6] C. Loizides (PQM Collaboration), *Eur. Phys. J. C* **49**, 339 (2007).
 [7] A. Adare *et al.* (PHENIX Collaboration), *Phys. Rev. D* **83**, 052004 (2011).
 [8] S. Adler *et al.* (PHENIX Collaboration), *Phys. Rev. C* **75**, 051902 (2007).
 [9] K. Nakamura *et al.* (Particle Data Group Collaboration), *J. Phys. G* **37**, 075021 (2010).
 [10] S. Adler *et al.* (PHENIX Collaboration), *Phys. Rev. C* **75**, 024909 (2007).
 [11] K. Adcox *et al.* (PHENIX Collaboration), *Nucl. Instrum. Methods A* **499**, 469 (2003).
 [12] K. Adcox *et al.* (PHENIX Collaboration), *Nucl. Instrum. Methods A* **499**, 469 (2003).
 [13] M. Allen *et al.* (PHENIX Collaboration), *Nucl. Instrum. Methods A* **499**, 549 (2003).
 [14] R. J. Glauber and G. Matthiae, *Nucl. Phys. B* **21**, 135 (1970).
 [15] M. L. Miller, K. Reygers, S. J. Sanders, and P. Steinberg, *Annu. Rev. Nucl. Part. Sci.* **57**, 205 (2007).
 [16] M. Aizawa *et al.* (PHENIX Collaboration), *Nucl. Instrum. Methods A* **499**, 508 (2003).
 [17] K. Adcox *et al.* (PHENIX Collaboration), *Nucl. Instrum. Methods A* **499**, 489 (2003).
 [18] L. Aphecetche *et al.* (PHENIX Collaboration), *Nucl. Instrum. Methods A* **499**, 521 (2003).
 [19] A. Adare *et al.* (PHENIX Collaboration), *Phys. Rev. C* **81**, 034911 (2010).
 [20] C. Tsallis, *J. Stat. Phys.* **52**, 479 (1988).
 [21] S. Adler *et al.* (PHENIX Collaboration), *Phys. Rev. Lett.* **95**, 202001 (2005).
 [22] S. S. Adler *et al.* (PHENIX Collaboration), *Phys. Rev. C* **74**, 024904 (2006).
 [23] A. Adare *et al.* (PHENIX Collaboration), *Phys. Rev. Lett.* **101**, 162301 (2008).
 [24] S. S. Adler *et al.* (PHENIX Collaboration), *Phys. Rev. Lett.* **98**, 172302 (2007).
 [25] A. Adare *et al.* (PHENIX Collaboration), *Phys. Rev. C* **77**, 064907 (2008).
 [26] L. Apanasevich *et al.* (E706 Collaboration), *arXiv:hep-ex/0004012* (2000).
 [27] M. Diakonou *et al.* (ISR Collaboration), *Phys. Lett. B* **89**, 432 (1980).
 [28] T. Sjostrand, L. Lonnblad, and S. Mrenna *arXiv:hep-ph/0108264* (2001).
 [29] A. Adare *et al.* (PHENIX Collaboration), *Phys. Rev. C* **83**, 024909 (2011).
 [30] R. J. Fries, B. Muller, C. Nonaka, and S. A. Bass, *Phys. Rev. C* **68**, 044902 (2003).
 [31] R. C. Hwa and C. B. Yang, *Phys. Rev. C* **70**, 024905 (2004).
 [32] J. W. Cronin *et al.*, *Phys. Rev. D* **11**, 3105 (1975).
 [33] K. Adcox *et al.* (PHENIX Collaboration), *Nucl. Phys. A* **757**, 184 (2005).
 [34] M. Gyulassy, P. Levai, and I. Vitev (GLV Collaboration), *Phys. Rev. Lett.* **85**, 5535 (2000).

参考論文

(1) Transverse momentum dependence of η meson suppression in Au+Au collisions at $\sqrt{s_{NN}}=200$ GeV

A. Adler *et al.* (PHENIX Collaboration)

..... Physical Review C 82, 011902 (2010).

(2) Suppression Pattern of Neutral Pions at High Transverse Momentum in Au+Au Collisions at $\sqrt{s_{NN}}=200$ GeV and Constraints on Medium

A. Adler *et al.* (PHENIX Collaboration)

..... Physical Review Letter 101, 232301 (2008).

Transverse momentum dependence of η meson suppression in Au + Au collisions at $\sqrt{s_{NN}} = 200$ GeV

A. Adare,¹² S. Afanasiev,²⁷ C. Aidala,⁴⁰ N. N. Ajitanand,⁵⁷ Y. Akiba,^{51,52} H. Al-Bataineh,⁴⁶ J. Alexander,⁵⁷ K. Aoki,^{33,51} L. Aphecetche,⁵⁹ Y. Aramaki,¹¹ J. Asai,⁵¹ E. T. Atomssa,³⁴ R. Averbeck,⁵⁸ T. C. Awes,⁴⁷ B. Azmoun,⁶ V. Babintsev,²³ M. Bai,⁵ G. Baksay,¹⁹ L. Baksay,¹⁹ A. Baldissieri,¹⁵ K. N. Barish,⁷ P. D. Barnes,³⁶ B. Bassalleck,⁴⁵ A. T. Basye,¹ S. Bathe,⁷ S. Batsouli,⁴⁷ V. Baublis,⁵⁰ C. Baumann,⁴¹ A. Bazilevsky,⁶ S. Belikov,^{6,*} R. Belmont,⁶³ R. Bennett,⁵⁸ A. Berdnikov,⁵⁴ Y. Berdnikov,⁵⁴ A. A. Bickley,¹² J. G. Boissevain,³⁶ J. S. Bok,⁶⁶ H. Borel,¹⁵ K. Boyle,⁵⁸ M. L. Brooks,³⁶ H. Buesching,⁶ V. Bumazhnov,²³ G. Bunce,^{6,52} S. Butsyk,³⁶ C. M. Camacho,³⁶ S. Campbell,⁵⁸ B. S. Chang,⁶⁶ W. C. Chang,² J.-L. Charvet,¹⁵ C.-H. Chen,⁵⁸ S. Chernichenko,²³ C. Y. Chi,¹³ M. Chiu,^{6,24} I. J. Choi,⁶⁶ R. K. Choudhury,⁴ P. Christiansen,³⁸ T. Chujo,⁶² P. Chung,⁵⁷ A. Churny,²³ O. Chvala,⁷ V. Cianciolo,⁴⁷ Z. Citron,⁵⁸ B. A. Cole,¹³ M. A. Connors,⁵⁸ P. Constantin,³⁶ M. Csanád,¹⁷ T. Csörgő,³⁰ T. Dahms,⁵⁸ S. Dairaku,^{33,51} I. Danchev,⁶³ K. Das,²⁰ A. Datta,⁴⁰ G. David,⁶ A. Denisov,²³ D. d'Enterria,³⁴ A. Deshpande,^{52,58} E. J. Desmond,⁶ O. Dietzsch,⁵⁵ A. Dion,⁵⁸ M. Donadelli,⁵⁵ O. Drapier,³⁴ A. Drees,⁵⁸ K. A. Drees,⁵ A. K. Dubey,⁶⁵ J. M. Durham,⁵⁸ A. Durum,²³ D. Dutta,⁴ V. Dzhordzhadze,⁷ S. Edwards,²⁰ Y. V. Efremenko,⁴⁷ F. Ellinghaus,¹² T. Engelmöre,¹³ A. Enokizono,³⁵ H. En'yo,^{51,52} S. Esumi,⁶² K. O. Eyster,⁷ B. Fadem,⁴² D. E. Fields,^{45,52} M. Finger Jr.,⁸ M. Finger,⁸ F. Fleuret,³⁴ S. L. Fokin,³² Z. Fraenkel,^{65,*} J. E. Frantz,⁵⁸ A. Franz,⁶ A. D. Frawley,²⁰ K. Fujiwara,⁵¹ Y. Fukao,^{33,51} T. Fusayasu,⁴⁴ I. Garishvili,⁶⁰ A. Glenn,¹² H. Gong,⁵⁸ M. Gonin,³⁴ J. Gosset,¹⁵ Y. Goto,^{51,52} R. Granier de Cassagnac,³⁴ N. Grau,¹³ S. V. Greene,⁶³ M. Grosse Perdekamp,^{24,52} T. Gunji,¹¹ H.-Å. Gustafsson,^{38,*} A. Hadj Henni,⁵⁹ J. S. Haggerty,⁶ K. I. Hahn,¹⁸ H. Hamagaki,¹¹ J. Hamblen,⁶⁰ J. Hanks,¹³ R. Han,⁴⁹ E. P. Hartouni,³⁵ K. Haruna,²² E. Haslum,³⁸ R. Hayano,¹¹ M. Heffner,³⁵ S. Hegyi,³⁰ T. K. Hemmick,⁵⁸ T. Hester,⁷ X. He,²¹ J. C. Hill,²⁶ M. Hohmann,¹⁹ W. Holzmann,^{13,57} K. Homma,²² B. Hong,³¹ T. Horaguchi,^{11,22,51,61} D. Hornback,⁶⁰ S. Huang,⁶³ T. Ichihara,^{51,52} R. Ichimiya,⁵¹ J. Ide,⁴² H. Iinuma,^{33,51} Y. Ikeda,⁶² K. Imai,^{33,51} J. Imrek,¹⁶ M. Inaba,⁶² D. Isenhower,¹ M. Ishihara,⁵¹ T. Isobe,¹¹ M. Issah,^{57,63} A. Isupov,²⁷ D. Ivanischev,⁵⁰ B. V. Jacak,^{58,†} J. Jia,^{6,13,57} J. Jin,¹³ B. M. Johnson,⁶ K. S. Joo,⁴³ D. Jouan,⁴⁸ D. S. Jumper,¹ F. Kajihara,¹¹ S. Kametani,⁵¹ N. Kamihara,⁵² J. Kamin,⁵⁸ J. H. Kang,⁶⁶ J. Kapustinsky,³⁶ K. Karatsu,³³ D. Kawall,^{40,52} M. Kawashima,^{51,53} A. V. Kazantsev,³² T. Kempel,²⁶ A. Khanzadeev,⁵⁰ K. M. Kijima,²² J. Kikuchi,⁶⁴ B. I. Kim,³¹ D. H. Kim,⁴³ D. J. Kim,^{28,66} E. J. Kim,⁹ E. Kim,⁵⁶ S. H. Kim,⁶⁶ Y. J. Kim,²⁴ E. Kinney,¹² K. Kiriluk,¹² Á. Kiss,¹⁷ E. Kistenev,⁶ J. Klay,³⁵ C. Klein-Boesing,⁴¹ L. Kochenda,⁵⁰ B. Komkov,⁵⁰ M. Konno,⁶² J. Koster,²⁴ D. Kotchetkov,⁴⁵ A. Kozlov,⁶⁵ A. Král,¹⁴ A. Kravitz,¹³ G. J. Kunde,³⁶ K. Kurita,^{51,53} M. Kurosawa,⁵¹ M. J. Kweon,³¹ Y. Kwon,^{60,66} G. S. Kyle,⁴⁶ R. Lacey,⁵⁷ Y. S. Lai,¹³ J. G. Lajoie,²⁶ D. Layton,²⁴ A. Lebedev,²⁶ D. M. Lee,³⁶ J. Lee,¹⁸ K. B. Lee,³¹ K. Lee,⁵⁶ K. S. Lee,³¹ T. Lee,⁵⁶ M. J. Leitch,³⁶ M. A. L. Leite,⁵⁵ E. Leitner,⁶³ B. Lenzi,⁵⁵ P. Liebing,⁵² L. A. Linden Levy,¹² T. Liška,¹⁴ A. Litvinenko,²⁷ H. Liu,^{36,46} M. X. Liu,³⁶ X. Li,¹⁰ B. Love,⁶³ R. Luechtenborg,⁴¹ D. Lynch,⁶ C. F. Maguire,⁶³ Y. I. Makdisi,⁵ A. Malakhov,²⁷ M. D. Malik,⁴⁵ V. I. Manko,³² E. Mannel,¹³ Y. Mao,^{49,51} L. Mašek,^{8,25} H. Masui,⁶² F. Matathias,¹³ M. McCumber,⁵⁸ P. L. McGaughey,³⁶ N. Means,⁵⁸ B. Meredith,²⁴ Y. Miake,⁶² A. C. Mignerey,³⁹ P. Mikeš,^{8,25} K. Miki,⁶² A. Milov,⁶ M. Mishra,³ J. T. Mitchell,⁶ A. K. Mohanty,⁴ Y. Morino,¹¹ A. Morreale,⁷ D. P. Morrison,⁶ T. V. Moukhanova,³² D. Mukhopadhyay,⁶³ J. Murata,^{51,53} S. Nagamiya,²⁹ J. L. Nagle,¹² M. Naglis,⁶⁵ M. I. Nagy,¹⁷ I. Nakagawa,^{51,52} Y. Nakamiya,²² T. Nakamura,^{22,29} K. Nakano,^{51,61} J. Newby,³⁵ M. Nguyen,⁵⁸ T. Niita,⁶² R. Nouicer,⁶ A. S. Nyanin,³² E. O'Brien,⁶ S. X. Oda,¹¹ C. A. Ogilvie,²⁶ K. Okada,⁵² M. Oka,⁶² Y. Onuki,⁵¹ A. Oskarsson,³⁸ M. Ouchida,²² K. Ozawa,¹¹ R. Pak,⁶ A. P. T. Palounek,³⁶ V. Pantuev,⁵⁸ V. Papavassiliou,⁴⁶ I. H. Park,¹⁸ J. Park,⁵⁶ S. K. Park,³¹ W. J. Park,³¹ S. F. Pate,⁴⁶ H. Pei,²⁶ J.-C. Peng,²⁴ H. Pereira,¹⁵ V. Peresedov,²⁷ D. Yu. Peressounko,³² C. Pinkenburg,⁶ R. P. Pisani,⁶ M. Proissl,⁵⁸ M. L. Purschke,⁶ A. K. Purwar,³⁶ H. Qu,²¹ J. Rak,^{28,45} A. Rakotozafindrabe,³⁴ I. Ravinovich,⁶⁵ K. F. Read,^{47,60} S. Rembeczki,¹⁹ K. Reygers,⁴¹ V. Riabov,⁵⁰ Y. Riabov,⁵⁰ E. Richardson,³⁹ D. Roach,⁶³ G. Roche,³⁷ S. D. Rolnick,⁷ M. Rosati,²⁶ C. A. Rosen,¹² S. S. E. Rosendahl,³⁸ P. Rosnet,³⁷ P. Rukoyatkin,²⁷ P. Ružička,²⁵ V. L. Rykov,⁵¹ B. Sahlmueller,⁴¹ N. Saito,^{29,33,51,52} T. Sakaguchi,⁶ S. Sakai,⁶² K. Sakashita,^{51,61} V. Samsonov,⁵⁰ S. Sano,^{11,64} T. Sato,⁶² S. Sawada,²⁹ K. Sedgwick,⁷ J. Seele,¹² R. Seidl,²⁴ A. Yu. Semenov,²⁶ V. Semenov,²³ R. Seto,⁷ D. Sharma,⁶⁵ I. Shein,²³ T.-A. Shibata,^{51,61} K. Shigaki,²² M. Shimomura,⁶² K. Shoji,^{33,51} P. Shukla,⁴ A. Sickles,⁶ C. L. Silva,⁵⁵ D. Silvermyr,⁴⁷ C. Silvestre,¹⁵ K. S. Sim,³¹ B. K. Singh,³ C. P. Singh,³ V. Singh,³ M. Slunečka,⁸ A. Soldatov,²³ R. A. Soltz,³⁵ W. E. Sondheim,³⁶ S. P. Sorensen,⁶⁰ I. V. Sourikova,⁶ N. A. Sparks,¹ F. Staley,¹⁵ P. W. Stankus,⁴⁷ E. Stenlund,³⁸ M. Stepanov,⁴⁶ A. Ster,³⁰ S. P. Stoll,⁶ T. Sugitate,²² C. Suires,⁴⁸ A. Sukhanov,⁶ J. Sziklai,³⁰ E. M. Takagui,⁵⁵ A. Taketani,^{51,52} R. Tanabe,⁶² Y. Tanaka,⁴⁴ K. Tanida,^{33,51,52,56} M. J. Tannenbaum,⁶ S. Tarafdar,³ A. Taranenko,⁵⁷ P. Tarján,¹⁶ H. Themann,⁵⁸ T. L. Thomas,⁴⁵ M. Togawa,^{33,51} A. Toia,⁵⁸ L. Tomášek,²⁵ Y. Tomita,⁶² H. Torii,^{22,51} R. S. Towell,¹ V.-N. Tram,³⁴ I. Tserruya,⁶⁵ Y. Tsuchimoto,²² C. Vale,^{6,26} H. Valle,⁶³ H. W. van Hecke,³⁶ E. Vazquez-Zambrano,¹³ A. Veicht,²⁴ J. Velkovska,⁶³ R. Vértési,^{16,30} A. A. Vinogradov,³² M. Virius,¹⁴ V. Vrba,²⁵ E. Vznuzdaev,⁵⁰ X. R. Wang,⁴⁶ D. Watanabe,²² K. Watanabe,⁶² Y. Watanabe,^{51,52} F. Wei,²⁶ R. Wei,⁵⁷ J. Wessels,⁴¹ S. N. White,⁶ D. Winter,¹³ J. P. Wood,¹ C. L. Woody,⁶ R. M. Wright,¹ M. Wysocki,¹² W. Xie,⁵² Y. L. Yamaguchi,^{11,64} K. Yamaura,²² R. Yang,²⁴ A. Yanovich,²³ J. Ying,²¹ S. Yokkaichi,^{51,52} G. R. Young,⁴⁷ I. Younus,⁴⁵ Z. You,⁴⁹ I. E. Yushmanov,³² W. A. Zajc,¹³ O. Zaudtke,⁴¹ C. Zhang,⁴⁷ S. Zhou,¹⁰ and L. Zolin²⁷

(PHENIX Collaboration)

¹Abilene Christian University, Abilene, Texas 79699, USA²Institute of Physics, Academia Sinica, Taipei 11529, Taiwan³Department of Physics, Banaras Hindu University, Varanasi 221005, India

- ⁴*Bhabha Atomic Research Centre, Bombay 400 085, India*
- ⁵*Collider-Accelerator Department, Brookhaven National Laboratory, Upton, New York 11973-5000, USA*
- ⁶*Physics Department, Brookhaven National Laboratory, Upton, New York 11973-5000, USA*
- ⁷*University of California–Riverside, Riverside, California 92521, USA*
- ⁸*Charles University, Ovocný trh 5, Praha 1, 116 36, Prague, Czech Republic*
- ⁹*Chonbuk National University, Jeonju 561-756, Korea*
- ¹⁰*China Institute of Atomic Energy (CIAE), Beijing, People’s Republic of China*
- ¹¹*Center for Nuclear Study, Graduate School of Science, University of Tokyo, 7-3-1 Hongo, Bunkyo, Tokyo 113-0033, Japan*
- ¹²*University of Colorado, Boulder, Colorado 80309, USA*
- ¹³*Columbia University, New York, New York 10027 and Nevis Laboratories, Irvington, New York 10533, USA*
- ¹⁴*Czech Technical University, Zikova 4, 166 36 Prague 6, Czech Republic*
- ¹⁵*Dapnia, CEA Saclay, F-91191, Gif-sur-Yvette, France*
- ¹⁶*Debrecen University, H-4010 Debrecen, Egyetem tér 1, Hungary*
- ¹⁷*ELTE, Eötvös Loránd University, H-1117 Budapest, Pázmány P. s. 1/A, Hungary*
- ¹⁸*Ewha Womans University, Seoul 120-750, Korea*
- ¹⁹*Florida Institute of Technology, Melbourne, Florida 32901, USA*
- ²⁰*Florida State University, Tallahassee, Florida 32306, USA*
- ²¹*Georgia State University, Atlanta, Georgia 30303, USA*
- ²²*Hiroshima University, Kagamiyama, Higashi-Hiroshima 739-8526, Japan*
- ²³*IHEP Protvino, State Research Center of Russian Federation, Institute for High Energy Physics, Protvino, 142281, Russia*
- ²⁴*University of Illinois at Urbana-Champaign, Urbana, Illinois 61801, USA*
- ²⁵*Institute of Physics, Academy of Sciences of the Czech Republic, Na Slovance 2, 182 21 Prague 8, Czech Republic*
- ²⁶*Iowa State University, Ames, Iowa 50011, USA*
- ²⁷*Joint Institute for Nuclear Research, 141980 Dubna, Moscow Region, Russia*
- ²⁸*Helsinki Institute of Physics and University of Jyväskylä, P.O. Box 35, FI-40014 Jyväskylä, Finland*
- ²⁹*KEK, High Energy Accelerator Research Organization, Tsukuba, Ibaraki 305-0801, Japan*
- ³⁰*KFKI Research Institute for Particle and Nuclear Physics of the Hungarian Academy of Sciences (MTA KFKI RMKI), H-1525 Budapest 114, P.O. Box 49, Budapest, Hungary*
- ³¹*Korea University, Seoul 136-701, Korea*
- ³²*Russian Research Center “Kurchatov Institute”, Moscow, Russia*
- ³³*Kyoto University, Kyoto 606-8502, Japan*
- ³⁴*Laboratoire Leprince-Ringuet, Ecole Polytechnique, CNRS-IN2P3, Route de Saclay, F-91128, Palaiseau, France*
- ³⁵*Lawrence Livermore National Laboratory, Livermore, California 94550, USA*
- ³⁶*Los Alamos National Laboratory, Los Alamos, New Mexico 87545, USA*
- ³⁷*LPC, Université Blaise Pascal, CNRS-IN2P3, Clermont-Fd, 63177 Aubiere Cedex, France*
- ³⁸*Department of Physics, Lund University, Box 118, SE-221 00 Lund, Sweden*
- ³⁹*University of Maryland, College Park, Maryland 20742, USA*
- ⁴⁰*Department of Physics, University of Massachusetts, Amherst, Massachusetts 01003-9337, USA*
- ⁴¹*Institut für Kernphysik, University of Muenster, D-48149 Muenster, Germany*
- ⁴²*Muhlenberg College, Allentown, Pennsylvania 18104-5586, USA*
- ⁴³*Myongji University, Yongin, Kyonggido 449-728, Korea*
- ⁴⁴*Nagasaki Institute of Applied Science, Nagasaki-shi, Nagasaki 851-0193, Japan*
- ⁴⁵*University of New Mexico, Albuquerque, New Mexico 87131, USA*
- ⁴⁶*New Mexico State University, Las Cruces, New Mexico 88003, USA*
- ⁴⁷*Oak Ridge National Laboratory, Oak Ridge, Tennessee 37831, USA*
- ⁴⁸*IPN-Orsay, Université Paris Sud, CNRS-IN2P3, BPI, F-91406, Orsay, France*
- ⁴⁹*Peking University, Beijing, People’s Republic of China*
- ⁵⁰*PNPI, Petersburg Nuclear Physics Institute, Gatchina, Leningrad region, 188300, Russia*
- ⁵¹*RIKEN Nishina Center for Accelerator-Based Science, Wako, Saitama 351-0198, Japan*
- ⁵²*RIKEN BNL Research Center, Brookhaven National Laboratory, Upton, New York 11973-5000, USA*
- ⁵³*Physics Department, Rikkyo University, 3-34-1 Nishi-Ikebukuro, Toshima, Tokyo 171-8501, Japan*
- ⁵⁴*Saint Petersburg State Polytechnic University, St. Petersburg, Russia*
- ⁵⁵*Universidade de São Paulo, Instituto de Física, Caixa Postal 66318, São Paulo CEP 05315-970, Brazil*
- ⁵⁶*Seoul National University, Seoul 151-742, Korea*
- ⁵⁷*Chemistry Department, Stony Brook University, SUNY, Stony Brook, New York 11794-3400, USA*
- ⁵⁸*Department of Physics and Astronomy, Stony Brook University, SUNY, Stony Brook, New York 11794, USA*
- ⁵⁹*SUBATECH (Ecole des Mines de Nantes, CNRS-IN2P3, Université de Nantes) Boîte Postale 20722-44307, Nantes, France*
- ⁶⁰*University of Tennessee, Knoxville, Tennessee 37996, USA*
- ⁶¹*Department of Physics, Tokyo Institute of Technology, Oh-okayama, Meguro, Tokyo 152-8551, Japan*
- ⁶²*Institute of Physics, University of Tsukuba, Tsukuba, Ibaraki 305, Japan*

⁶³Vanderbilt University, Nashville, Tennessee 37235, USA⁶⁴Waseda University, Advanced Research Institute for Science and Engineering, 17 Kikui-cho, Shinjuku-ku, Tokyo 162-0044, Japan⁶⁵Weizmann Institute, Rehovot 76100, Israel⁶⁶Yonsei University, IPAP, Seoul 120-749, Korea

(Received 26 May 2010; published 27 July 2010)

New measurements by the PHENIX experiment at the Relativistic Heavy Ion Collider for η production at midrapidity as a function of transverse momentum (p_T) and collision centrality in $\sqrt{s_{NN}} = 200$ GeV Au + Au and $p + p$ collisions are presented. They indicate nuclear modification factors (R_{AA}) which are similar in both magnitude and trend to those found in earlier π^0 measurements. Linear fits to R_{AA} as a function of p_T in 5–20 GeV/ c show that the slope is consistent with zero within two standard deviations at all centralities, although a slow rise cannot be excluded. Having different statistical and systematic uncertainties, the π^0 and η measurements are complementary at high p_T ; thus, along with the extended p_T range of these data they can provide additional constraints for theoretical modeling and the extraction of transport properties.

DOI: [10.1103/PhysRevC.82.011902](https://doi.org/10.1103/PhysRevC.82.011902)

PACS number(s): 25.75.Dw, 13.85.Qk, 13.20.Fc, 13.20.He

Suppression of high- p_T hadron production in Au + Au collisions at the Relativistic Heavy Ion Collider (RHIC) [1,2] and its absence in $d + Au$ collisions [3] provided the first direct evidence that an extremely dense medium is formed in heavy ion collisions at RHIC energies. This suppression relative to the yield expected from the convolution of independent nucleon-nucleon scatterings, measured by the nuclear modification factor R_{AA} , is now confirmed up to 20 GeV/ c with identified π^0 and attributed to the energy loss of the hard scattered partons in the dense medium. Several models with very different assumptions describe the magnitude of the observed π^0 suppression, but predict slightly different evolution with increasing p_T . Calculations based on perturbative quantum chromodynamics (pQCD) and static plasma predict that the fractional parton energy loss decreases with p_T as $\log(p_T)/p_T$, leading to a slow rise of the R_{AA} with p_T (for a recent review see [4]). In contrast, some anti-de Sitter Conformal Field Theory (CFT) calculations find that the fractional energy loss is proportional to p_T . Therefore, R_{AA} decreases with increasing transverse momentum [5–8]. The universal upper bound model [9] predicts that R_{AA} remains almost independent of the energy of the original gluon or quark. Other effects (modified nuclear parton distribution functions, Cronin effect, modified fragmentation functions, and the quark/gluon ratio) at given x_T ($2p_T/\sqrt{s}$) can also change the p_T dependence of R_{AA} . A precise measurement of the evolution of R_{AA} with p_T would help in confirming or rejecting classes of theories and putting tight constraints on the free parameters of the remaining ones. The first rigorous attempt to confront the observed π^0 suppression with various pQCD-based parton energy loss calculations and to put quantitative constraints on the transport properties of the medium was made in [10] using PHENIX π^0 data. One intriguing result was that a linear fit with a slope consistent with zero described the evolution of R_{AA} with p_T slightly better than any of the pQCD models predicting a slow rise. However, the large statistical and

systematic uncertainties of the high- p_T π^0 points prevented a clear distinction between constant or slowly rising R_{AA} .

One reason the π^0 data [2] allow such ambiguous interpretations is that the experimental uncertainties rise rapidly as we move to higher p_T (>12 – 14 GeV/ c), because of “shower merging,” as explained below. In the case of the η this problem is absent for p_T up to 50 GeV/ c , significantly beyond the p_T range expected to be accessible at RHIC. While the yield of the actually reconstructed η mesons is smaller except at the highest p_T , the improvement in systematic uncertainties can help provide better constraints in comparisons to theory at high p_T and thus complement the π^0 results. Of course, some caution in interpreting the results is warranted: while both π^0 and η consist of light quarks, η does have a hidden strangeness ($s\bar{s}$) content so it is not *a priori* obvious that the π^0 and η results are interchangeable. Earlier measurements [11] have shown that, at least up to 12 GeV/ c , the π^0 and η nuclear modification factors in Au + Au agree within uncertainties and the η/π^0 ratio is constant for $p_T \geq 4$ GeV/ c in $p + p$ [11]. Using recent, more precise measurements in PHENIX, we will reexamine whether π^0 and η production at midrapidity is indeed similar and study the asymptotic behavior of R_{AA} .

This analysis used 3.25B minimum bias (MB) $\sqrt{s_{NN}} = 200$ GeV Au + Au events, corresponding to 0.511 nb^{-1} recorded in 2007 as well as 429M minimum bias (18.7 nb^{-1}) and 2.06B triggered (6.90 pb^{-1}) $\sqrt{s} = 200$ GeV $p + p$ events recorded in 2006 in the PHENIX experiment at RHIC. Both the Au + Au and $p + p$ data sets were analyzed using the same analysis chain and cuts; thus, some of the systematic uncertainties cancel when we calculate the nuclear modification factor R_{AA} for Au + Au. Collision centrality in Au + Au has been established by the beam-beam counters (BBCs, $3.0 < |\eta| < 3.9$) [12]. A Glauber-model Monte Carlo [13] along with a simulation of the BBC response was used to estimate the average number of participating nucleons (N_{part}) and binary nucleon-nucleon collisions (N_{coll}) for each centrality bin.

The η mesons were measured via their $\eta \rightarrow \gamma\gamma$ decay channel. The photons were reconstructed in the lead-scintillator (PbSc) sectors of the PHENIX electromagnetic calorimeter (EMCal) [14] covering $3/8$ of the full azimuth and $-0.35 < \eta < 0.35$ in pseudorapidity, and the η yield was extracted from

*Deceased.

[†]PHENIX spokesperson; jacak@skipper.physics.sunysb.edu

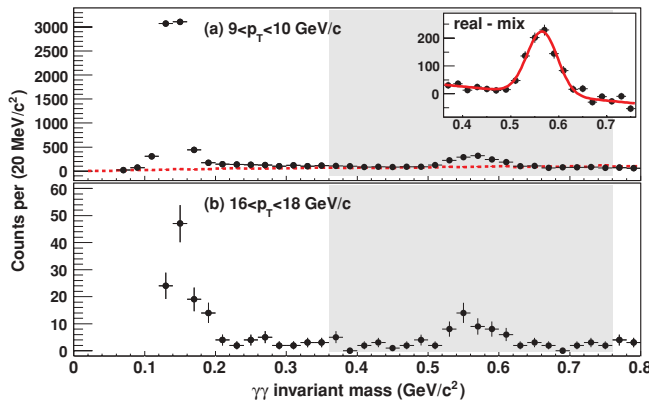


FIG. 1. (Color online) $\gamma\gamma$ invariant mass distribution for two different bins in p_T of the $\gamma\gamma$ pair (minimum bias data). (a) $9 < p_T < 10$ GeV/c, both foreground (real, points) and normalized combinatorial background (mix, dashed lines) are shown. Note the large difference between π^0 and η raw yields. Inset: the magnified η region after background subtraction. (b) $16 < p_T < 18$ GeV/c region, where mixed event subtraction is no longer necessary. Also, here a cut on the γ -pair energy asymmetry, $\alpha < 0.6$, has been applied, which greatly improves the signal-to-background ratio at the η peak but cuts into the lower part of the π^0 peak owing to cluster merging.

two-photon invariant mass distributions. There are important differences between π^0 and η measurements. In the case of π^0 , starting around $p_T = 12$ GeV/c the minimum opening angle of the two decay photons is small enough for the photon showers to merge and become indistinguishable. As p_T increases, this effect leads to an increasing loss of observed π^0 , resulting in large corrections and corresponding systematic uncertainties (which are in fact the dominant systematic uncertainties at high p_T). Since the mass of the η is about four times larger than the π^0 , this is not a problem for the η measurement up to $p_T \sim 50$ GeV/c. However, the observable η rates are much lower at low and medium p_T , as seen in the invariant mass distributions in Fig. 1, because of the smaller branching ratio into two photons (39%) and the small $\eta/\pi^0 \approx 0.5$ production ratio. The raw yields become comparable only around 20 GeV/c. Therefore we applied an $\alpha < 0.6$ photon pair energy asymmetry cut (as opposed to $\alpha < 0.8$ for π^0) in order to improve the signal-to-background ratio in the η region. The other part of the η analysis is the same as the one described in [11,15].

The raw η yield is always counted by integrating the histogram bin content in the η mass window (typically ± 30 MeV/c²), but the way we treat the underlying combinatorial background varies as a function of p_T . In Au + Au up to 10 GeV/c, mixed event subtraction is used. The η region is then fitted with a polynomial and Gaussian (see inset in Fig. 1) to estimate the residual background. When the signal-to-background ratio reaches 1.0, already in the 7–10 GeV/c range, depending on centrality, mixed event subtraction is no longer needed; a polynomial and Gaussian fit is used on the original invariant mass distribution to estimate the background. At even higher p_T (12–16 GeV/c) we estimate the residual background under the peak simply

TABLE I. Typical systematic uncertainties on η spectra and R_{AA} . See text for explanation of error types.

Source	Type	Au + Au	$p + p$	R_{AA}
Raw yield	B	7%	3%	6.3%
Acceptance variations	B	1.5%	1.5%	2.1%
Photon PID	B	3%	3%	3%
Acceptance \times efficiency	A	3%	3%	4.2%
Energy scale	B	8%	8%	11.3%
Conversion (HBD)	C	1.3%	N/A	1.3%
Conversion (other)	C	5%	5%	N/A
BBC cross section	C	N/A	9.7%	9.7%
BBC efficiency	C	N/A	3.8%	3.8%
ERT norm.	C	N/A	6.2%	6.2%

from the average bin content of the sidebands (the regions above and below the peak).

Systematic uncertainties are classified into three types: Type A is p_T uncorrelated (“point-by-point”) and, for the purposes of fitting and plotting, is added in quadrature to the statistical errors. Type C is the overall normalization uncertainty allowing all points to move by the same fraction up or down. Type B is all other p_T -correlated uncertainties (including the cases where the shape of the correlation function is not known). Table I lists typical uncertainties on the spectra and R_{AA} . “Conversion (HBD)” stands for loss due to photon conversion in the Hadron Blind Detector, which was present in one of the two central arms during the 2007 (Au + Au) data taking. “ERT norm.” stands for the normalization uncertainty of the EMCAL-Ring-Imaging-Čerenkov trigger, selecting high- p_T photons and electrons. “Acceptance variations” are small day-by-day changes of dead areas in the detector and thus are independent for the $p + p$ and Au + Au runs. The systematic uncertainties on raw yield, photon particle identification (PID), and conversion (other) are common in $p + p$ and Au + Au, and hence were partially canceled out in the R_{AA} calculation.

Cross sections for $p + p \rightarrow \eta + X$ and invariant yield of inclusive η production in Au + Au collisions for different centralities are shown in Fig. 2. They cover the $5 < p_T < 22$ GeV/c range and five orders of magnitude in cross section

TABLE II. Parameters of the power-law fits A/p_T^n for Au + Au and $p + p$. The errors used for fit are the statistical and p_T -uncorrelated (type A) systematic uncertainties added in quadrature. The p_T range of the fits is 5–22 GeV/c.

System/Centrality	A	n	χ^2 /NDF
Au + Au 0–5%	27.2 ± 11.9	7.90 ± 0.22	3.1/7
Au + Au 0–10%	17.6 ± 5.5	7.77 ± 0.15	10.6/8
Au + Au 10–20%	19.1 ± 5.9	7.89 ± 0.16	10.2/9
Au + Au 0–20%	18.5 ± 4.3	7.84 ± 0.12	10.5/7
Au + Au 20–40%	17.3 ± 4.2	8.01 ± 0.12	17.2/8
Au + Au 40–60%	9.53 ± 2.65	8.05 ± 0.15	5.5/8
Au + Au 20–60%	14.5 ± 2.5	8.07 ± 0.08	11.2/9
Au + Au 60–92%	1.13 ± 0.40	7.78 ± 0.18	2.98/6
Au + Au MinBias	10.4 ± 1.4	8.04 ± 0.08	9.41/9
$p + p$	8.84 ± 0.99	8.21 ± 0.05	8.33/9

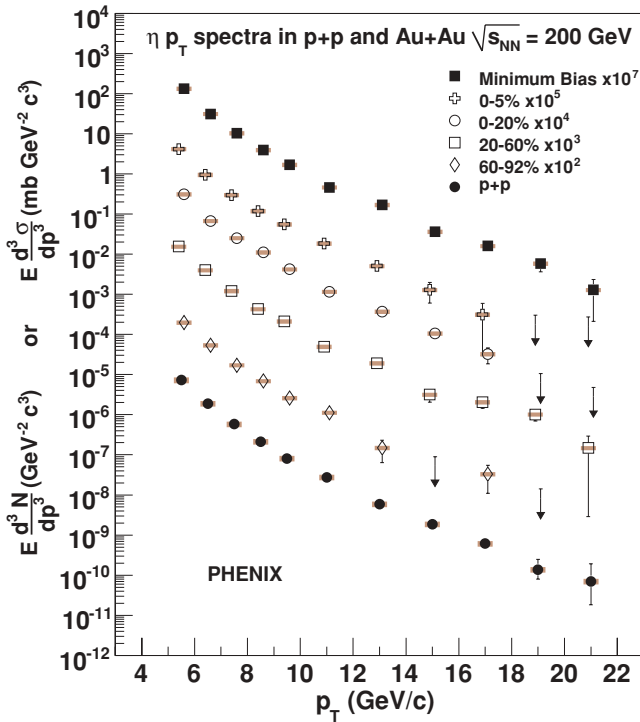


FIG. 2. (Color online) Cross section of $p + p \rightarrow \eta + X$ from the 2006 $p + p$ data set (solid circles) and η invariant yield in Au + Au collisions of various centralities (open symbols) and minimum bias (solid squares) from the 2007 data set. $p + p$ is shown at the true p_T value; all other spectra are shifted alternately by ± 0.1 GeV/c for better visibility of the error bars and upper limits.

(invariant yield). The overall normalization uncertainties (type C) are 13% for $p + p$ and 5% for Au + Au. Parameters of simple power-law fits (A/p_T^n) to various, partially overlapping centrality selections, including ones not shown in Fig. 2, are given in Table II. Fits include all available points in the $5 < p_T < 22$ GeV/c range but exclude upper limits. Only statistical and p_T -uncorrelated uncertainties were used in the fits. Note that for π^0 in Au + Au collisions the power n was consistent within uncertainties at all centralities [2] ranging from 8.00 ± 0.12 in 0–5% to 8.06 ± 0.08 in 80–92%, and for π^0 in $p + p$ the power n was 8.22 ± 0.09 . In this measurement we find that for η production $p + p \rightarrow \eta + X$ the power n is the same as it was for π^0 . The powers obtained for η in

TABLE III. Parameters from linear function fit to ηR_{AA} .

Centrality	N_{part}	Slope	χ^2/NDF
0–5%	351	0.008 ± 0.008	2.77/7
0–10%	326	0.011 ± 0.007	9.79/7
10–20%	236	$0.010^{+0.009}_{-0.008}$	11.7/8
0–20%	280	$0.010^{+0.007}_{-0.006}$	10.8/7
20–40%	142	0.004 ± 0.010	15.7/8
40–60%	61.6	$0.010^{+0.018}_{-0.017}$	4.64/7
20–60%	102	0.005 ± 0.011	11.7/8
60–92%	11.8	$0.056^{+0.043}_{-0.038}$	1.52/6
MinBias	109	0.006 ± 0.007	10.1/8

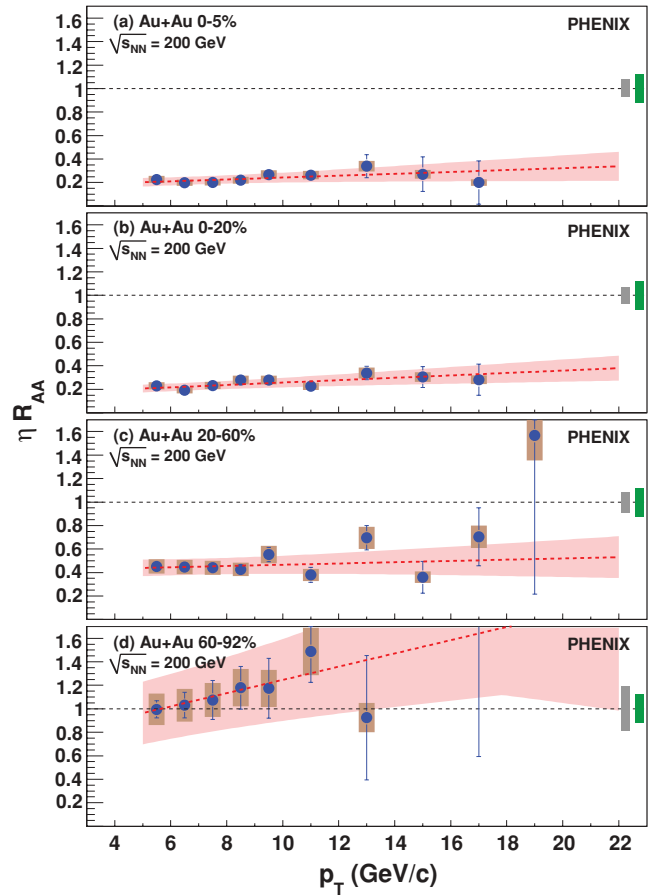


FIG. 3. (Color online) Nuclear modification factor for η at various centralities, calculated using the measured $p + p$ points. Dark (green) band around 1 indicates the absolute normalization error from $p + p$, light (gray) band is the (centrality-dependent) absolute normalization error from Au + Au. Error bars include statistical and p_T -uncorrelated systematic errors. Also shown: linear fits to the data with 1σ error bands.

Au + Au are also consistent with those from π^0 within two standard deviations.

The nuclear modification factor R_{AA} is defined as

$$R_{AA} = \frac{1/N_{\text{evt}} dN/dy dp_T}{\langle T_{AB} \rangle d\sigma_{pp}/dy dp_T},$$

where σ_{pp} is the production cross section of the particle in $p + p$ collisions, and $\langle T_{AB} \rangle$ is the nuclear thickness function averaged over a range of impact parameters for the given centrality, calculated within a Glauber model [13]. When calculating R_{AA} , the measured $p + p$ points are used. R_{AA} for η production is shown in Fig. 3 for four centralities, along with linear fits to R_{AA} which properly take both systematic and statistical uncertainties into account. Fit parameters are listed in Table III. In the measured p_T range we observe strong suppression in all but the most peripheral collisions. As shown in Fig. 4, for the minimum bias case the suppression is quite comparable to the one observed for π^0 , and above 13 GeV/c the (relative) systematic errors are smaller.

Based upon the most central (0–5%) collisions in [10], we found that the $\pi^0 R_{AA}$ is consistent with a completely flat p_T

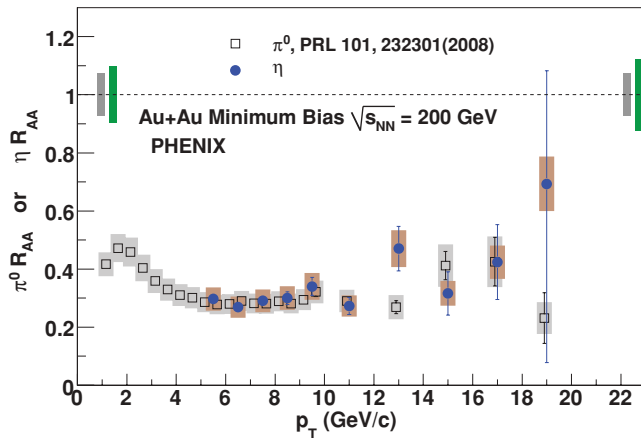


FIG. 4. (Color online) Nuclear modification factor R_{AA} for π^0 (open squares, points shifted for clarity, data from [2]) and η (solid circles, this analysis) in MB Au + Au collisions. Error bars include statistical and p_T -uncorrelated systematic errors, bands show p_T -correlated systematic errors. The pair of bands at $R_{AA} = 1$ are the absolute normalization error for $p + p$ (larger, dark) and Au + Au (lighter) for π^0 (left) and η (right).

dependence when fitted in the $5 < p_T < 18$ GeV/ c region, namely, the slope of a linear fit was $m = 0.0017^{+0.0035}_{-0.0039}$ c/GeV. Fitting the current η R_{AA} data with straight lines gives the slopes and uncertainties listed in Table III and shown in Fig. 5, where centrality is expressed in terms of participating nucleons N_{part} . All slopes are consistent with zero; the largest deviation is less than 2σ (for the 0–20% centrality bin). One and two

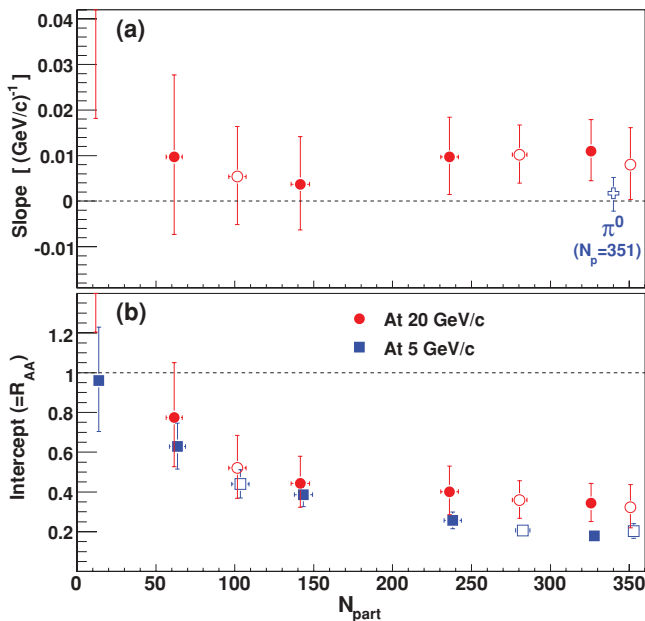


FIG. 5. (Color online) (a) Slopes of the linear fits (like the ones shown in Fig. 3) along with the fitting errors. Centrality is shown in terms of participating nucleons N_{part} . Open symbols are overlapping, solid symbols are non-overlapping centrality bins (0–10%, 10–20%, 20–40%, 40–60%, and 60–92%). Also shown: slope of the linear fit to 0–5% π^0 data [10], shifted for better visibility. (b) Value of R_{AA} calculated from the fit at 5 GeV/ c (blue) and 20 GeV/ c (red).

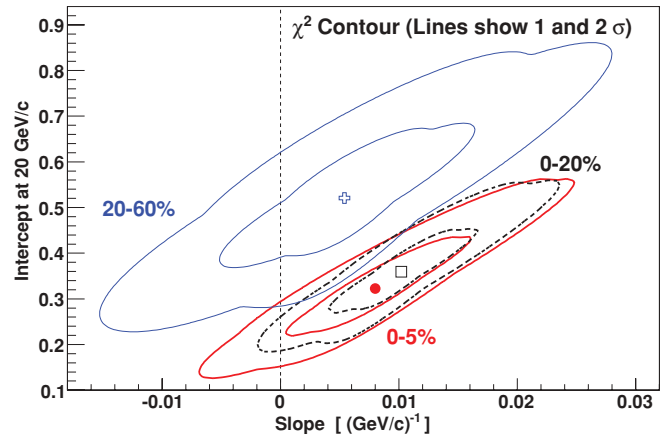


FIG. 6. (Color online) One and two standard deviation χ^2 contours of the linear fits to R_{AA} in Au + Au collisions for 0–5%, 0–20%, and 20–60% centralities.

standard deviation χ^2 contours for selected centrality bins are shown in Fig. 6. For 0–5% centrality we repeated the linear fits using only the first 3, 4, \dots , $(n - 1)$ points and found that the slope already stabilizes around its final value with the first few points; data above 10 GeV/ c improve the significance but barely change the central value itself. The same is true for other centralities.

While the above result indicates that R_{AA} for η is consistent with a p_T -independent, constant value, and disfavors a decreasing R_{AA} , a slow rise ($\sim 0.01c/GeV$) of R_{AA} with increasing p_T cannot be excluded. In fact, a detailed statistical analysis, comparing to various theories, like the study done for π^0 in [10], is necessary once theoretical calculations of η production are available. However, assuming the linear dependence, we can calculate the R_{AA} values at 5 GeV/ c (where the suppression is already at its maximum) and 20 GeV/ c ; the results are shown in the bottom panel of Fig. 5.

In summary, we measured invariant yields of η in $\sqrt{s_{NN}} = 200$ GeV Au + Au collisions at various centralities, as well as the η production cross section in $\sqrt{s} = 200$ GeV $p + p$ collisions in the $5 < p_T < 22$ GeV/ c transverse momentum range using the PbSc calorimeter of the PHENIX experiment at RHIC. The nuclear modification factor for η in minimum bias collisions is consistent with earlier π^0 results. In conclusion, linear fits to R_{AA} as a function of p_T indicate that R_{AA} is consistent with a constant at all centralities, although a slow rise cannot be excluded.

We thank the staff of the Collider-Accelerator and Physics Departments at BNL for their vital contributions. We acknowledge support from the Office of Nuclear Physics in DOE Office of Science, NSF, and a sponsored research grant from Renaissance Technologies (United States), MEXT and JSPS (Japan), CNPq and FAPESP (Brazil), NSFC (China), MSMT (Czech Republic), IN2P3/CNRS and CEA (France), BMBF, DAAD, and AvH (Germany), OTKA (Hungary), DAE and DST (India), ISF (Israel), NRF (Korea), MES, RAS, and FAE (Russia), VR and KAW (Sweden), US CRDF for the FSU, US-Hungary Fulbright, and US-Israel BSF.

- [1] K. Adcox *et al.*, *Phys. Rev. Lett.* **88**, 022301 (2001).
- [2] A. Adare *et al.*, *Phys. Rev. Lett.* **101**, 232301 (2008).
- [3] S. S. Adler *et al.*, *Phys. Rev. Lett.* **91**, 072303 (2003).
- [4] S. A. Bass, C. Gale, A. Majumder, C. Nonaka, G.-Y. Qin, T. Renk, and J. Ruppert, *Phys. Rev. C* **79**, 024901 (2009).
- [5] H. Liu, K. Rajagopal, and U. A. Wiedemann, *Phys. Rev. Lett.* **97**, 182301 (2006).
- [6] W. A. Horowitz and M. Gyulassy, *Phys. Lett. B* **666**, 320 (2008).
- [7] P. M. Chesler, K. Jensen, A. Karch, and L. G. Yaffe, *Phys. Rev. D* **79**, 125015 (2009).
- [8] S. S. Gubser, D. R. Gulotta, S. S. Pufu, and F. D. Rocha, *J. High Energy Phys.* **10** (2008) 052.
- [9] D. E. Kharzeev, [arXiv:0806.0358](https://arxiv.org/abs/0806.0358) [nucl-th].
- [10] A. Adare *et al.*, *Phys. Rev. C* **77**, 064907 (2008).
- [11] S. S. Adler *et al.*, *Phys. Rev. C* **75**, 024909 (2007).
- [12] M. Allen *et al.*, *Nucl. Instrum. Methods Phys. Res. A* **499**, 549 (2003).
- [13] M. L. Miller, K. Reygers, S. J. Sanders, and P. Steinberg, *Annu. Rev. Nucl. Part. Sci.* **57**, 205 (2007).
- [14] L. Aphecetche *et al.*, *Nucl. Instrum. Methods Phys. Res. A* **499**, 521 (2003).
- [15] S. S. Adler *et al.*, *Phys. Rev. C* **76**, 034904 (2007).

Suppression Pattern of Neutral Pions at High Transverse Momentum in Au + Au Collisions at $\sqrt{s_{NN}} = 200$ GeV and Constraints on Medium Transport Coefficients

A. Adare,⁸ S. Afanasiev,²² C. Aidala,⁹ N. N. Ajitanand,⁴⁹ Y. Akiba,^{43,44} H. Al-Bataineh,³⁸ J. Alexander,⁴⁹ A. Al-Jamel,³⁸ K. Aoki,^{28,43} L. Aphecetche,⁵¹ R. Armendariz,³⁸ S. H. Aronson,³ J. Asai,⁴⁴ E. T. Atomssa,²⁹ R. Averbeck,⁵⁰ T. C. Awes,³⁹ B. Azmoun,³ V. Babintsev,¹⁸ G. Baksay,¹⁴ L. Baksay,¹⁴ A. Baldissari,¹¹ K. N. Barish,⁴ P. D. Barnes,³¹ B. Bassalleck,³⁷ S. Bathe,⁴ S. Batsouli,^{9,39} V. Baublis,⁴² F. Bauer,⁴ A. Bazilevsky,³ S. Belikov,^{3,21,*} R. Bennett,⁵⁰ Y. Berdnikov,⁴⁶ A. A. Bickley,⁸ M. T. Bjornrdal,⁹ J. G. Boissevain,³¹ H. Borel,¹¹ K. Boyle,⁵⁰ M. L. Brooks,³¹ D. S. Brown,³⁸ D. Bucher,³⁴ H. Buesching,³ V. Bumazhnov,¹⁸ G. Bunce,^{3,44} J. M. Burward-Hoy,³¹ S. Butsyk,^{31,50} S. Campbell,⁵⁰ J.-S. Chai,²³ B. S. Chang,⁵⁸ J.-L. Charvet,¹¹ S. Chernichenko,¹⁸ J. Chiba,²⁴ C. Y. Chi,⁹ M. Chiu,^{9,19} I. J. Choi,⁵⁸ T. Chujo,⁵⁵ P. Chung,⁴⁹ A. Churny,¹⁸ V. Ciencialo,³⁹ C. R. Clevén,¹⁶ Y. Cobigo,¹¹ B. A. Cole,⁹ M. P. Comets,⁴⁰ P. Constantin,^{21,31} M. Csanád,¹³ T. Csörgő,²⁵ T. Dahms,⁵⁰ K. Das,¹⁵ G. David,³ M. B. Deaton,¹ K. Dehmelt,¹⁴ H. Delagrangé,⁵¹ A. Denisov,¹⁸ D. d'Enterria,⁹ A. Deshpande,^{44,50} E. J. Desmond,³ O. Dietzsch,⁴⁷ A. Dion,⁵⁰ M. Donadelli,⁴⁷ J. L. Drachenberg,¹ O. Drapier,²⁹ A. Drees,⁵⁰ A. K. Dubey,⁵⁷ A. Durum,¹⁸ V. Dzhordzhadze,^{4,52} Y. V. Efremenko,³⁹ J. Egdemir,⁵⁰ F. Ellinghaus,⁸ W. S. Emam,⁴ A. Enokizono,^{17,30} H. En'yo,^{43,44} B. Espagnon,⁴⁰ S. Esumi,⁵⁴ K. O. Eyser,⁴ D. E. Fields,^{37,44} M. Finger,^{5,22} M. Finger, Jr.,^{5,22} F. Fleuret,²⁹ S. L. Fokin,²⁷ B. Forestier,³² Z. Fraenkel,^{57,*} J. E. Frantz,^{9,50} A. Franz,³ A. D. Frawley,¹⁵ K. Fujiwara,⁴³ Y. Fukao,^{28,43} S.-Y. Fung,⁴ T. Fusayasu,³⁶ S. Gadrat,³² I. Garishvili,⁵² F. Gastineau,⁵¹ M. Germain,⁵¹ A. Glenn,^{8,52} H. Gong,⁵⁰ M. Gonin,²⁹ J. Gosset,¹¹ Y. Goto,^{43,44} R. Granier de Cassagnac,²⁹ N. Grau,²¹ S. V. Greene,⁵⁵ M. Grosse Perdekamp,^{19,44} T. Gunji,⁷ H.-Å. Gustafsson,³³ T. Hachiya,^{17,43} A. Hadj Henni,⁵¹ C. Haegemann,³⁷ J. S. Haggerty,³ M. N. Hagiwara,¹ H. Hamagaki,⁷ R. Han,⁴¹ H. Harada,¹⁷ E. P. Hartouni,³⁰ K. Haruna,¹⁷ M. Harvey,³ E. Haslum,³³ K. Hasuko,⁴³ R. Hayano,⁷ M. Heffner,³⁰ T. K. Hemmick,⁵⁰ T. Hester,⁴ J. M. Heuser,⁴³ X. He,¹⁶ H. Hiejima,¹⁹ J. C. Hill,²¹ R. Hobbs,³⁷ M. Hohlmann,¹⁴ M. Holmes,⁵⁵ W. Holzmann,⁴⁹ K. Homma,¹⁷ B. Hong,²⁶ T. Horaguchi,^{43,53} D. Hornback,⁵² M. G. Hur,²³ T. Ichihara,^{43,44} K. Imai,^{28,43} J. Imrek,¹² M. Inaba,⁵⁴ Y. Inoue,^{45,43} D. Isenhower,¹ L. Isenhower,¹ M. Ishihara,⁴³ T. Isobe,⁷ M. Issah,⁴⁹ A. Isupov,²² B. V. Jacak,^{50,+} J. Jia,⁹ J. Jin,⁹ O. Jinnouchi,⁴⁴ B. M. Johnson,³ K. S. Joo,³⁵ D. Jouan,⁴⁰ F. Kajihara,^{7,43} S. Kametani,^{7,56} N. Kamihara,^{43,53} J. Kamin,⁵⁰ M. Kaneta,⁴⁴ J. H. Kang,⁵⁸ H. Kanou,^{43,53} T. Kawagishi,⁵⁴ D. Kawall,⁴⁴ A. V. Kazantsev,²⁷ S. Kelly,⁸ A. Khanzadeev,⁴² J. Kikuchi,⁵⁶ D. H. Kim,³⁵ D. J. Kim,⁵⁸ E. Kim,⁴⁸ Y.-S. Kim,²³ E. Kinney,⁸ A. Kiss,¹³ E. Kistenev,³ A. Kiyomichi,⁴³ J. Klay,³⁰ C. Klein-Boesing,³⁴ L. Kochenda,⁴² V. Kochetkov,¹⁸ B. Komkov,⁴² M. Konno,⁵⁴ D. Kotchetkov,⁴ A. Kozlov,⁵⁷ A. Král,¹⁰ A. Kravitz,⁹ P. J. Kroon,³ J. Kubart,^{5,20} G. J. Kunde,³¹ N. Kurihara,⁷ K. Kurita,^{45,43} M. J. Kweon,²⁶ Y. Kwon,^{52,58} G. S. Kyle,³⁸ R. Lacey,⁴⁹ Y.-S. Lai,⁹ J. G. Lajoie,²¹ A. Lebedev,²¹ Y. Le Bornec,⁴⁰ S. Leckey,⁵⁰ D. M. Lee,³¹ M. K. Lee,⁵⁸ T. Lee,⁴⁸ M. J. Leitch,³¹ M. A. L. Leite,⁴⁷ B. Lenzi,⁴⁷ H. Lim,⁴⁸ T. Liška,¹⁰ A. Litvinenko,²² M. X. Liu,³¹ X. Li,⁶ X. H. Li,⁴ B. Love,⁵⁵ D. Lynch,³ C. F. Maguire,⁵⁵ Y. I. Makdisi,³ A. Malakhov,²² M. D. Malik,³⁷ V. I. Manko,²⁷ Y. Mao,^{41,43} L. Mašek,^{5,20} H. Masui,⁵⁴ F. Matathias,^{9,50} M. C. McCain,¹⁹ M. McCumber,⁵⁰ P. L. McGaughey,³¹ Y. Miake,⁵⁴ P. Mikeš,^{5,20} K. Miki,⁵⁴ T. E. Miller,⁵⁵ A. Milov,⁵⁰ S. Mioduszewski,³ G. C. Mishra,¹⁶ M. Mishra,² J. T. Mitchell,³ M. Mitrovski,⁴⁹ A. Morreale,⁴ D. P. Morrison,³ J. M. Moss,³¹ T. V. Moukhanova,²⁷ D. Mukhopadhyay,⁵⁵ J. Murata,^{45,43} S. Nagamiya,²⁴ Y. Nagata,⁵⁴ J. L. Nagle,⁸ M. Naglis,⁵⁷ I. Nakagawa,^{43,44} Y. Nakamiya,¹⁷ T. Nakamura,¹⁷ K. Nakano,^{43,53} J. Newby,³⁰ M. Nguyen,⁵⁰ B. E. Norman,³¹ A. S. Nyanin,²⁷ J. Nystrand,³³ E. O'Brien,³ S. X. Oda,⁷ C. A. Ogilvie,²¹ H. Ohnishi,⁴³ I. D. Ojha,⁵⁵ H. Okada,^{28,43} K. Okada,⁴⁴ M. Oka,⁵⁴ O. O. Omiwade,¹ A. Oskarsson,³³ I. Otterlund,³³ M. Ouchida,¹⁷ K. Ozawa,⁷ R. Pak,³ D. Pal,⁵⁵ A. P. T. Palounek,³¹ V. Pantuev,⁵⁰ V. Papavassiliou,³⁸ J. Park,⁴⁸ W. J. Park,²⁶ S. F. Pate,³⁸ H. Pei,²¹ J.-C. Peng,¹⁹ H. Pereira,¹¹ V. Peresedov,²² D. Yu. Peressounko,²⁷ C. Pinkenburg,³ R. P. Pisani,³ M. L. Purschke,³ A. K. Purwar,^{31,50} H. Qu,¹⁶ J. Rak,^{21,37} A. Rakotozafindrabe,²⁹ I. Ravinovich,⁵⁷ K. F. Read,^{39,52} S. Rembeczki,¹⁴ M. Reuter,⁵⁰ K. Reygers,³⁴ V. Riabov,⁴² Y. Riabov,⁴² G. Roche,³² A. Romana,^{29,*} M. Rosati,²¹ S. S. E. Rosendahl,³³ P. Rosnet,³² P. Rukoyatkin,²² V. L. Rykov,⁴³ S. S. Ryu,⁵⁸ B. Sahlmueller,³⁴ N. Saito,^{28,43,44} T. Sakaguchi,^{3,7,56} S. Sakai,⁵⁴ H. Sakata,¹⁷ V. Samsonov,⁴² H. D. Sato,^{28,43} S. Sato,^{3,24,54} S. Sawada,²⁴ J. Seele,⁸ R. Seidl,¹⁹ V. Semenov,¹⁸ R. Seto,⁴ D. Sharma,⁵⁷ T. K. Shea,³ I. Shein,¹⁸ A. Shevel,^{42,49} T.-A. Shibata,^{43,53} K. Shigaki,¹⁷ M. Shimomura,⁵⁴ T. Shohjoh,⁵⁴ K. Shoji,^{28,43} A. Sickles,⁵⁰ C. L. Silva,⁴⁷ D. Silvermyr,³⁹ C. Silvestre,¹¹ K. S. Sim,²⁶ C. P. Singh,² V. Singh,² S. Skutnik,²¹ M. Slunečka,^{5,22} W. C. Smith,¹ A. Soldatov,¹⁸ R. A. Soltz,³⁰ W. E. Sondheim,³¹ S. P. Sorensen,⁵² I. V. Sourikova,³ F. Staley,¹¹ P. W. Stankus,³⁹ E. Stenlund,³³ M. Stepanov,³⁸ A. Ster,²⁵ S. P. Stoll,³ T. Sugitate,¹⁷ C. Suire,⁴⁰ J. P. Sullivan,³¹ J. Sziklai,²⁵ T. Tabaru,⁴⁴ S. Takagi,⁵⁴ E. M. Takagui,⁴⁷ A. Taketani,^{43,44} K. H. Tanaka,²⁴ Y. Tanaka,³⁶ K. Tanida,^{43,44} M. J. Tannenbaum,³ A. Taranenko,⁴⁹ P. Tarján,¹² T. L. Thomas,³⁷

M. Togawa,^{28,43} A. Toia,⁵⁰ J. Tojo,⁴³ L. Tomášek,²⁰ H. Torii,⁴³ R. S. Towell,¹ V-N. Tram,²⁹ I. Tserruya,⁵⁷
 Y. Tsuchimoto,^{17,43} S. K. Tuli,² H. Tydesjö,³³ N. Tyurin,¹⁸ C. Vale,²¹ H. Valle,⁵⁵ H. W. van Hecke,³¹ J. Velkovska,⁵⁵
 R. Vertesi,¹² A. A. Vinogradov,²⁷ M. Virius,¹⁰ V. Vrba,²⁰ E. Vznuzdaev,⁴² M. Wagner,^{28,43} D. Walker,⁵⁰ X. R. Wang,³⁸
 Y. Watanabe,^{43,44} J. Wessels,³⁴ S. N. White,³ N. Willis,⁴⁰ D. Winter,⁹ C. L. Woody,³ M. Wysocki,⁸ W. Xie,^{4,44}
 Y. L. Yamaguchi,⁵⁶ A. Yanovich,¹⁸ Z. Yasin,⁴ J. Ying,¹⁶ S. Yokkaichi,^{43,44} G. R. Young,³⁹ I. Younus,³⁷ I. E. Yushmanov,²⁷
 W. A. Zajc,⁹ O. Zaudtke,³⁴ C. Zhang,^{9,39} S. Zhou,⁶ J. Zimányi,^{25,*} and L. Zolin²²

(PHENIX Collaboration)

- ¹Abilene Christian University, Abilene, Texas 79699, USA
²Department of Physics, Banaras Hindu University, Varanasi 221005, India
³Brookhaven National Laboratory, Upton, New York 11973-5000, USA
⁴University of California-Riverside, Riverside, California 92521, USA
⁵Charles University, Ovocný trh 5, Praha 1, 116 36, Prague, Czech Republic
⁶China Institute of Atomic Energy (CIAE), Beijing, People's Republic of China
⁷Center for Nuclear Study, Graduate School of Science, University of Tokyo, 7-3-1 Hongo, Bunkyo, Tokyo 113-0033, Japan
⁸University of Colorado, Boulder, Colorado 80309, USA
⁹Columbia University, New York, New York 10027 and Nevis Laboratories, Irvington, New York 10533, USA
¹⁰Czech Technical University, Zikova 4, 166 36 Prague 6, Czech Republic
¹¹Dapnia, CEA Saclay, F-91191, Gif-sur-Yvette, France
¹²Debrecen University, H-4010 Debrecen, Egyetem tér 1, Hungary
¹³ELTE, Eötvös Loránd University, H-1117 Budapest, Pázmány P. s. 1/A, Hungary
¹⁴Florida Institute of Technology, Melbourne, Florida 32901, USA
¹⁵Florida State University, Tallahassee, Florida 32306, USA
¹⁶Georgia State University, Atlanta, Georgia 30303, USA
¹⁷Hiroshima University, Kagamiyama, Higashi-Hiroshima 739-8526, Japan
¹⁸IHEP Protvino, State Research Center of Russian Federation, Institute for High Energy Physics, Protvino, 142281, Russia
¹⁹University of Illinois at Urbana-Champaign, Urbana, Illinois 61801, USA
²⁰Institute of Physics, Academy of Sciences of the Czech Republic, Na Slovance 2, 182 21 Prague 8, Czech Republic
²¹Iowa State University, Ames, Iowa 50011, USA
²²Joint Institute for Nuclear Research, 141980 Dubna, Moscow Region, Russia
²³KAERI, Cyclotron Application Laboratory, Seoul, Korea
²⁴KEK, High Energy Accelerator Research Organization, Tsukuba, Ibaraki 305-0801, Japan
²⁵KFKI Research Institute for Particle and Nuclear Physics of the Hungarian Academy of Sciences (MTA KFKI RMKI),
 H-1525 Budapest 114, POBox 49, Budapest, Hungary
²⁶Korea University, Seoul, 136-701, Korea
²⁷Russian Research Center "Kurchatov Institute", Moscow, Russia
²⁸Kyoto University, Kyoto 606-8502, Japan
²⁹Laboratoire Leprince-Ringuet, Ecole Polytechnique, CNRS-IN2P3, Route de Saclay, F-91128, Palaiseau, France
³⁰Lawrence Livermore National Laboratory, Livermore, California 94550, USA
³¹Los Alamos National Laboratory, Los Alamos, New Mexico 87545, USA
³²LPC, Université Blaise Pascal, CNRS-IN2P3, Clermont-Fd, 63177 Aubiere Cedex, France
³³Department of Physics, Lund University, Box 118, SE-221 00 Lund, Sweden
³⁴Institut für Kernphysik, University of Muenster, D-48149 Muenster, Germany
³⁵Myongji University, Yongin, Kyonggido 449-728, Korea
³⁶Nagasaki Institute of Applied Science, Nagasaki-shi, Nagasaki 851-0193, Japan
³⁷University of New Mexico, Albuquerque, New Mexico 87131, USA
³⁸New Mexico State University, Las Cruces, New Mexico 88003, USA
³⁹Oak Ridge National Laboratory, Oak Ridge, Tennessee 37831, USA
⁴⁰IPN-Orsay, Université Paris Sud, CNRS-IN2P3, BPI, F-91406, Orsay, France
⁴¹Peking University, Beijing, People's Republic of China
⁴²PNPI, Petersburg Nuclear Physics Institute, Gatchina, Leningrad region, 188300, Russia
⁴³RIKEN, The Institute of Physical and Chemical Research, Wako, Saitama 351-0198, Japan
⁴⁴RIKEN BNL Research Center, Brookhaven National Laboratory, Upton, New York 11973-5000, USA
⁴⁵Physics Department, Rikkyo University, 3-34-1 Nishi-Ikebukuro, Toshima, Tokyo 171-8501, Japan
⁴⁶Saint Petersburg State Polytechnic University, St. Petersburg, Russia
⁴⁷Universidade de São Paulo, Instituto de Física, Caixa Postal 66318, São Paulo CEP05315-970, Brazil
⁴⁸System Electronics Laboratory, Seoul National University, Seoul, Korea
⁴⁹Chemistry Department, Stony Brook University, SUNY, Stony Brook, New York 11794-3400, USA

⁵⁰*Department of Physics and Astronomy, Stony Brook University, SUNY, Stony Brook, New York 11794, USA*⁵¹*SUBATECH (Ecole des Mines de Nantes, CNRS-IN2P3, Université de Nantes) BP 20722-44307, Nantes, France*⁵²*University of Tennessee, Knoxville, Tennessee 37996, USA*⁵³*Department of Physics, Tokyo Institute of Technology, Oh-okayama, Meguro, Tokyo 152-8551, Japan*⁵⁴*Institute of Physics, University of Tsukuba, Tsukuba, Ibaraki 305, Japan*⁵⁵*Vanderbilt University, Nashville, Tennessee 37235, USA*⁵⁶*Waseda University, Advanced Research Institute for Science and Engineering, 17 Kikui-cho, Shinjuku-ku, Tokyo 162-0044, Japan*⁵⁷*Weizmann Institute, Rehovot 76100, Israel*⁵⁸*Yonsei University, IPAP, Seoul 120-749, Korea*

(Received 25 January 2008; published 3 December 2008)

For Au + Au collisions at 200 GeV, we measure neutral pion production with good statistics for transverse momentum, p_T , up to 20 GeV/ c . A fivefold suppression is found, which is essentially constant for $5 < p_T < 20$ GeV/ c . Experimental uncertainties are small enough to constrain any model-dependent parametrization for the transport coefficient of the medium, e.g., $\langle \hat{q} \rangle$ in the parton quenching model. The spectral shape is similar for all collision classes, and the suppression does not saturate in Au + Au collisions.

DOI: 10.1103/PhysRevLett.101.232301

PACS numbers: 25.75.Dw

Large transverse momentum (p_T) hadrons originate primarily from the fragmentation of hard scattered quarks or gluons. In high energy $p + p$ collisions, this is well described in the framework of perturbative QCD [1]. In ultrarelativistic heavy ion collisions, such hard scatterings occur in the early phase of the reaction, and the transiting partons serve as probes of the strongly interacting medium produced in the collisions. Lattice QCD predicts a phase transition to a plasma of deconfined quarks and gluons, which induces gluon radiation from the scattered parton and depletes hadron production at high p_T (“jet quenching”) [2,3]. The measurements in Au + Au collisions at Relativistic Heavy Ion Collider (RHIC) showed suppressed hadron yields in central collisions [4] as predicted [5,6], and motivated advanced theoretical studies of radiative energy loss.

All energy loss models must incorporate the space-time evolution of the medium, as it is not static, and the initial distribution of the partons throughout the medium. Models generally also include an input parameter for the medium density and/or the coupling. Different assumptions in the various models lead to similar descriptions of the π^0 suppression with different model-dependent parameters [7,8]. For instance, the Parton Quenching model (PQM) is a Monte Carlo program using the quenching weights from Baier-Dokshitzer-Mueller-Peigne-Schiff (BDMPS) [5] that combines the coupling strength with the color-charge density to create a single transport coefficient, often referred to as $\langle \hat{q} \rangle$ [9,10], which gives the $\langle p_T^2 \rangle$ transferred from the medium to the parton per mean free path.

Establishing the magnitude, p_T and centrality dependence of the suppression pattern up to the highest possible p_T is crucial to constrain the theoretical models and separate contributions of initial and final state effects from the energy loss mechanism. As neutral pions can be identified up to very high p_T , their suppression and its centrality (average pathlength) dependence puts important con-

straints on the energy loss. Whereas di-hadron suppression at high p_T may be somewhat more sensitive to medium opacity [11] than single hadron suppression, such improvement is contingent upon theoretical and experimental, statistical and systematic uncertainties.

This Letter reports on the measurement of π^0 s up to $p_T = 20$ GeV/ c in Au + Au collisions at $\sqrt{s_{NN}} = 200$ GeV at RHIC, using the high statistics data taken in 2004. The results are used to extract the $\langle \hat{q} \rangle$ parameter of the PQM model for the most central collisions.

The analysis used 1.03×10^9 minimum bias events taken by the PHENIX experiment [12]. Collision centrality was determined from the correlation between the number of charged particles detected in the Beam-Beam Counters (BBC, $3.0 < |\eta| < 3.9$) and the energy measured in the Zero Degree Calorimeters (ZDC). A Glauber model Monte Carlo program with a simulation of the BBC and ZDC responses was used to estimate the average number of participating nucleons ($\langle N_{\text{part}} \rangle$) and binary nucleon-nucleon collisions ($\langle N_{\text{coll}} \rangle$) for each centrality bin [13].

Neutral pions were measured in the $\pi^0 \rightarrow \gamma\gamma$ decay channel with the photons reconstructed in the Electromagnetic Calorimeter (EMCal) located in the two central arms of PHENIX ($|\eta| \leq 0.35$). The EMCal [14] consists of two subsystems: six sectors of lead-scintillator sandwich calorimeter (PbSc) and two sectors of lead-glass Čerenkov calorimeter (PbGl) at the radial distance of about 5 m. The fine segmentation of the EMCal ($\delta\phi \times \delta\eta \sim 0.01 \times 0.01$ for PbSc and $\sim 0.008 \times 0.008$ for PbGl) ensures that the two photons from a $\pi^0 \rightarrow \gamma\gamma$ decay are well resolved up to $p_T^{\pi^0} \approx 12$ (PbSc) and 16 (PbGl) GeV/ c . Data from the two subsystems were analyzed separately, and the fully corrected results were combined.

Details of the analysis including extraction of the raw π^0 yield, correction for acceptance, detector response, reconstruction efficiency have been described elsewhere [15,16]. In this analysis, the higher p_T range required an additional

TABLE I. Summary of the systematic uncertainties on the π^0 yield extracted independently with the PbSc (PbG) electromagnetic calorimeters. The last row is the total systematic uncertainty on the combined spectra.

p_T (GeV/c)	2	6	10	16
uncertainty source	PbSc (PbG)			
yield extraction (%)	3.0 (4.1)	3.0 (4.1)	3.0 (4.1)	3.0 (4.1)
PID efficiency (%)	3.5 (3.9)	3.5 (3.5)	3.5 (3.7)	3.5 (3.9)
Energy scale (%)	6.7 (9.0)	8.0 (9.2)	8.0 (8.2)	8.0 (12.3)
Acceptance (%)	1.5 (4.1)	1.5 (4.1)	1.5 (4.1)	1.5 (4.1)
π^0 merging (%)	... (...)	... (...)	4.4 (...)	28 (4.8)
Conversion (%)	3.0 (2.5)	3.0 (2.5)	3.0 (2.5)	3.0 (2.5)
off-vertex π^0 (%)	1.5 (1.5)	1.5 (1.5)	1.5 (1.5)	1.5 (1.5)
Total (%)	8.7 (12)	9.8 (11)	11 (11)	30 (15)
PbSc and PbG combined: Total (%)	7.0	7.5	7.6	14

correction for losses in the observed (raw) π^0 s due to “cluster merging.”

With increasing $p_T^{\pi^0}$, the minimum opening angle of the two photons decreases, and eventually they will be reconstructed as a single cluster. Such “merging” reaches 50% of the total raw yield at $p_T = 14$ GeV/c in the PbSc and at $p_T = 18$ GeV/c in the PbG. Merged clusters were rejected by various shower profile cuts, and the loss was determined by simulated π^0 s embedded into real events and analyzed with the same cuts. The systematic uncertainties were estimated by comparing π^0 yields in the PbSc extracted in bins of asymmetry $|E_{\gamma_1} - E_{\gamma_2}|/(E_{\gamma_1} + E_{\gamma_2})$ and also by comparing yields in the PbSc and PbG.

We considered two sources of π^0 s not coming from the vertex (off-vertex π^0): those produced by hadrons interacting with detector material (instrumental background) and feed-down products from weak decay of higher mass hadrons (physics background). Based upon simulations both types of background were found to be negligible ($< 1\%$ at $p_T > 2.0$ GeV/c) except for π^0 s from K_S^0 decay ($\approx 3\%$ of π^0 yield for $p_T > 1$ GeV/c), which has been subtracted from the data. Finally, the yields were corrected to the center of the p_T bins using the local slope.

The main sources of systematic uncertainties are yield extraction, efficiency corrections, energy scale, and merging, none of which exhibits a significant centrality dependence. The PbSc and PbG have quite different systematics with all but one of them (off-vertex π^0) uncorrelated. Therefore, when combining their results, the total error is reduced in the weighted average of the two independent measurements. The final systematic uncertainties (1 standard deviation) on the spectra are shown in Table I.

The top panel of Fig. 1 shows the π^0 invariant yield for all centralities and minimum bias, combined from the independent PbSc and PbG measurements which now extend to $p_T \sim 20$ GeV/c, 6 GeV/c higher than those published earlier [15]. In the overlap region, the results are consistent with the ones in [15] while the errors are reduced by a factor of 2 to 2.5. The bottom panel shows the

consistency of the PbSc and PbG results. The spectra are similar at all centralities: when fitting $p_T > 5$ GeV/c with a power-law function ($\propto p_T^{-n}$), the exponents vary from $n = 8.00 \pm 0.12$ in 0–5% to $n = 8.06 \pm 0.08$ in the 80–92% (most peripheral) bin. Note that $n = 8.22 \pm 0.09$ in $p + p$ collisions. The errors are combined statistical errors and systematic uncertainties.

To quantify the comparison of spectra in heavy ion and $p + p$ collisions, the nuclear modification factor

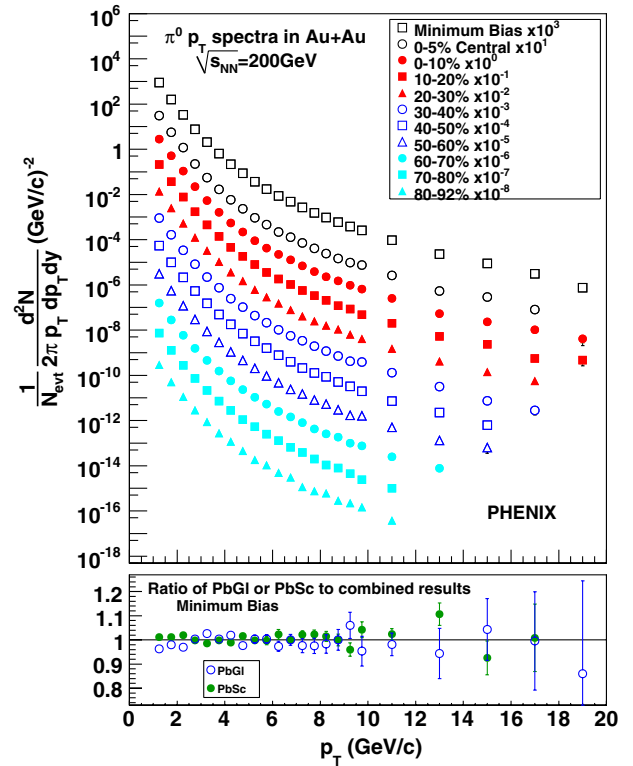


FIG. 1 (color online). Top: π^0 invariant yields for all centralities and minimum bias. Bottom: ratios of the (separately analyzed) PbSc and PbG yields to the combined minimum bias invariant yield, which is shown in the top panel.

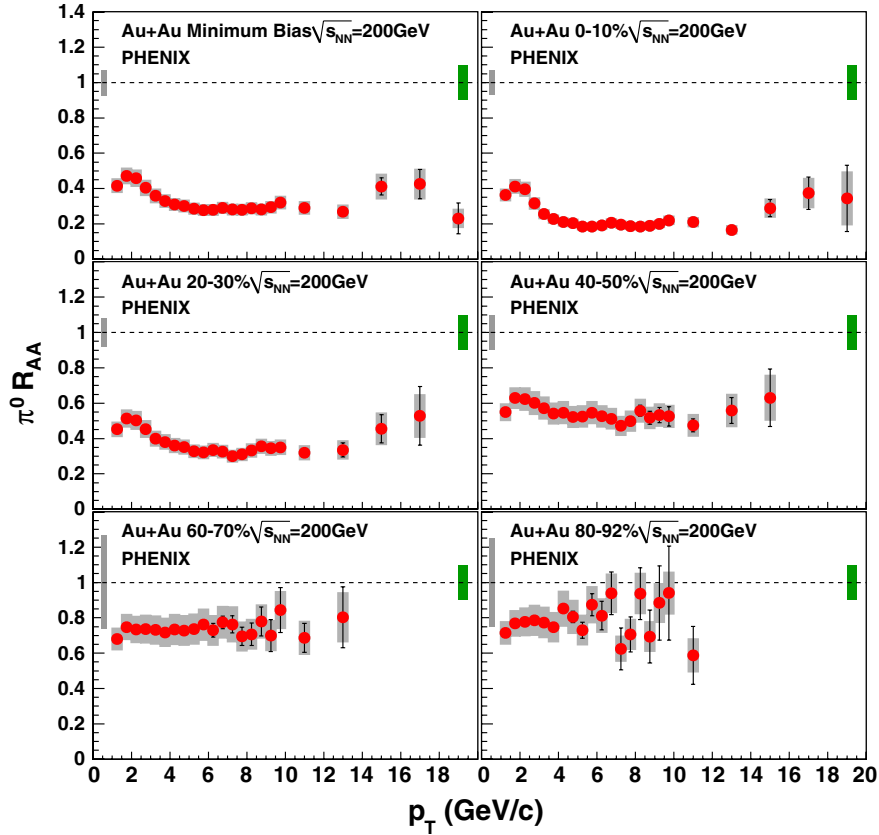


FIG. 2 (color online). Nuclear modification factor (R_{AA}) for π^0 s. Error bars are statistical and p_T -uncorrelated errors, boxes around the points indicate p_T -correlated errors. Single box around $R_{AA} = 1$ on the left is the error due to N_{coll} , whereas the single box on the right is the overall normalization error of the $p + p$ reference spectrum.

$$R_{AA} = \frac{1/N_{\text{evt}} d^2N/dydp_T}{\langle T_{AB} \rangle d^2\sigma_{pp}/dydp_T} \quad (1)$$

is used, where σ_{pp} is the production cross section of the particle in $p + p$ collisions, and $\langle T_{AB} \rangle$ is the nuclear thickness function averaged over a range of impact parameters for the given centrality, calculated within a Glauber model [13]. Figures 2 and 3 show R_{AA} for π^0 at different centralities. The reference $p + p$ yield was obtained from the 2005 (Run-5) RHIC $p + p$ measurement [17].

R_{AA} reaches ~ 0.2 in 0–10% centrality at $p_T > 5$ GeV/c with very little (if any) p_T dependence. This trend is compatible with most current energy loss models but not with a semiopaque medium assumption, where R_{AA} would decrease with increasing p_T [7]. While its magnitude changes, the suppression pattern itself is remarkably similar at all centralities suggesting that the bulk R_{AA} (integrated over azimuth) is sensitive only to the N_{part} but not to the specific geometry. Consequently, study of the p_T -integrated R_{AA} vs centrality is instructive.

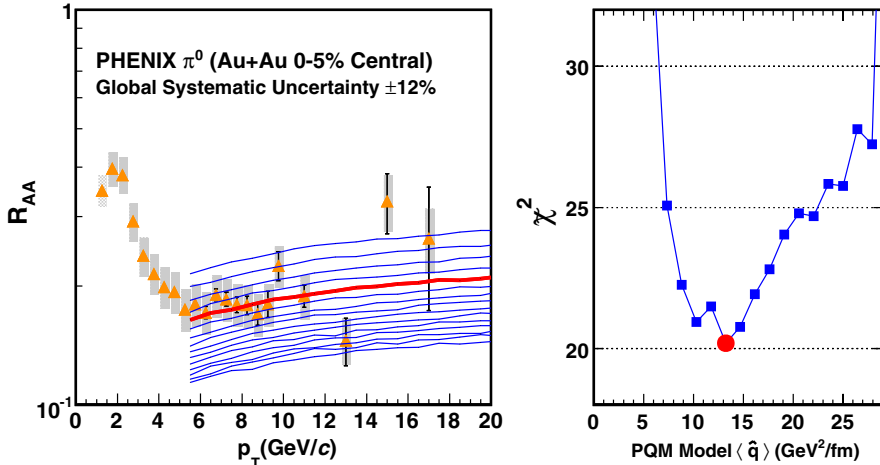


FIG. 3 (color online). Left: $\pi^0 R_{AA}$ for the most central (0–5%) Au + Au collisions and PQM model calculations for different values of $\langle \hat{q} \rangle$. Right: $\chi^2(\epsilon_b, \epsilon_c, p)$ distribution for the corresponding values of $\langle \hat{q} \rangle$. The bold (red) curve in the left panel and the round (red) point in the right panel are the best fit values.

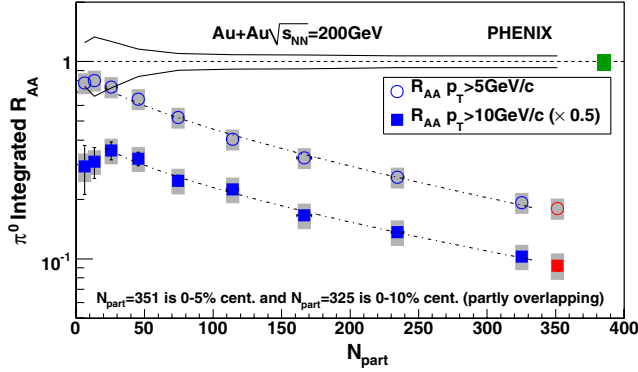


FIG. 4 (color online). Integrated nuclear modification factor (R_{AA}) for π^0 as a function of collision centrality expressed in terms of N_{part} . The error bars/bands are the same as in Fig. 2. The two lines at unity show the errors on $\langle N_{coll} \rangle$. The last two points correspond to partially overlapping centrality bins. The dashed lines show the fit explained in the text.

Figure 4 shows R_{AA} for π^0 s integrated above $p_T > 5$ GeV/c, and $p_T > 10$ GeV/c, as a function of centrality. The last two points indicate overlapping 0–10% and 0–5% bins. In both cases, the suppression increases monotonically with N_{part} without any sign of saturation, suggesting that larger colliding systems (such as $U + U$ planned at RHIC) should exhibit even more suppression.

The common power-law behavior ($\propto p_T^{-n}$) in $p + p$ and Au + Au allows the suppression to be reinterpreted as a fractional energy loss $S_{loss} = 1 - R_{AA}^{1/(n-2)}$ where n is the power-law exponent, and we found that $S_{loss} \propto N_{part}^a$ [15,18]. Fitting the integrated R_{AA} with a function $R_{AA} = (1 - S_0 N_{part}^a)^{n-2}$, where n is fixed as 8.1, gives $a = 0.57 \pm 0.13$ for $N_{part} > 20$ for $p_T > 5$ GeV/c, and $a = 0.55 \pm 0.14$ for $p_T > 10$ GeV/c. The fit does not take errors on $p + p$ luminosity into account. The Gyulassy-Levai-Vitev (GLV) [6] and PQM [10] models predict that $a \approx 2/3$, which is consistent with the data. The fitted values of S_0 are $(9.0 \pm 6.1) \times 10^{-3}$ and $(9.4 \pm 7.3) \times 10^{-3}$ for $p_T > 5$ GeV/c and $p_T > 10$ GeV/c, respectively. The fits are shown as dashed lines in Fig. 4.

We use the highest centrality (0–5%) R_{AA} data as shown in Fig. 3 to constrain the PQM model parameter $\langle \hat{q} \rangle$. This must be done with careful consideration of the various, partially coupled error sources, leading to necessary refinement beyond a naive least square analysis. We calculate

$$\tilde{\chi}^2(\epsilon_b, \epsilon_c, p) = \left(\sum_{i=1}^n \frac{[y_i + \epsilon_b \sigma_{b_i} + \epsilon_c y_i \sigma_c - \mu_i(p)]^2}{\tilde{\sigma}_i^2} \right) + \epsilon_b^2 + \epsilon_c^2, \quad (2)$$

using theory curves $\mu_i(p)$ with different values of the input parameter p , i.e., $\langle \hat{q} \rangle$ in the PQM model. p_T -uncorrelated, statistical \oplus systematic errors are σ_i , p_T -correlated errors are σ_{b_i} (boxes on Figs. 2 and 3), while uniform fractional

shifts of all points are given by σ_c . All the measured values y_i are allowed to shift by the same fraction, ϵ_b , of their systematic error σ_{b_i} from the nominal values. The ϵ_c is a similar correlated fraction of σ_c , and $\tilde{\sigma}_i = \sigma_i(y_i + \epsilon_b \sigma_{b_i} + \epsilon_c y_i \sigma_c)/y_i$ is the point-to-point random error scaled by the multiplicative shift, so that the fractional error is unchanged by the shift, which is true for the present measurement. The best fit, $\tilde{\chi}_{min}^2$, the minimum of $\tilde{\chi}^2(\epsilon_b, \epsilon_c, p)$ by variation of ϵ_b , ϵ_c , and p , is found by standard methods. Further details are given in [16]. The right panel of Fig. 3 shows the minima of $\tilde{\chi}^2(\epsilon_b, \epsilon_c, p)$ by varying ϵ_b and ϵ_c for a wide range of values of the PQM model transport coefficient, $\langle \hat{q} \rangle$. Our data constrain $\langle \hat{q} \rangle$ as $13.2_{-3.2}^{+2.1}$ and $_{-5.2}^{+6.3}$ GeV²/fm at the 1 and 2 standard deviation levels. These constraints include only the experimental uncertainties and do not account for the large model-dependent differences in the quenching scenario and description of the medium. Extracting fundamental model-independent properties of the medium from the present data requires resolution of ambiguities and open questions in the models themselves, which also will have to account simultaneously for the p_T and centrality (average path-length) dependence. This work demonstrates the power of data for pion production in constraining the energy loss of partons. The large $\langle \hat{q} \rangle$ suggests that the matter consists of strongly coupled partons.

The $R_{AA}(p_T)$ for 0–5% was fitted with a simple linear function in the entire $p_T > 5$ GeV/c range as well: the slope of the fit is $0.0017_{-0.0039}^{+0.0035}$ and $_{-0.0076}^{+0.0070}$ c/GeV at the 1 and 2 standard deviation levels [16]. The fact that R_{AA} as well as the power (n) for all spectra from $p + p$ to Au + Au are essentially constant proves that the dominant term in energy loss is proportional to p_T .

In summary, PHENIX has measured neutral pions in Au + Au collisions at $\sqrt{s_{NN}} = 200$ GeV at mid rapidity in the transverse momentum range of $1 < p_T < 20$ GeV/c, analyzing high statistics data taken in 2004. The shape of the spectra is similar for all centralities, as is the shape of $R_{AA}(p_T)$ at $p_T > 5$ GeV/c. In central collisions, the yield is suppressed by a factor of ~ 5 at 5 GeV/c compared to the binary scaled $p + p$ reference, and the suppression prevails with little or no change up to 20 GeV/c. The integrated R_{AA} vs centrality does not saturate at this nuclear size; also, the predicted $S_{loss} \propto N_{part}^{2/3}$ [6,10] is consistent with our data. In this picture, the energy loss increases with p_T . Using the 0–5% (most central) R_{AA} , we find that the transport coefficient $\langle \hat{q} \rangle$ of the PQM model is constrained to $13.2_{-3.2}^{+2.1}$ ($_{-5.2}^{+6.3}$) GeV²/fm at the one (two) σ level. The experimental evidence for a high transport coefficient, derived with remarkable accuracy due to high quality data and sophisticated new analysis, as presented here and in [16], reveals a totally nontrivial feature of the dense QCD medium created at RHIC. The shape of the spectra and the suppression pattern

indicate that the dominant term in energy loss is proportional to p_T .

We thank the staff of the Collider-Accelerator and Physics Departments at BNL for their vital contributions. We acknowledge support from the Office of Nuclear Physics in DOE Office of Science and NSF (USA), MEXT and JSPS (Japan), CNPq and FAPESP (Brazil), NSFC (China), MSMT (Czech Republic), IN2P3/CNRS, and CEA (France), BMBF, DAAD, and AvH (Germany), OTKA (Hungary), DAE (India), ISF (Israel), KRF and KOSEF (Korea), MES, RAS, and FAAE (Russia), VR and KAW (Sweden), U.S. CRDF for the FSU, US-Hungarian NSF-OTKA-MTA, and US-Israel BSF.

*Deceased

†PHENIX Spokesperson:

jacak@skipper.physics.sunysb.edu

- [1] D. de Florian and W. Vogelsang, Phys. Rev. D **71**, 114004 (2005).
- [2] M. Gyulassy and M. Plumer, Phys. Lett. B **243**, 432 (1990).
- [3] X.-N. Wang and M. Gyulassy, Phys. Rev. Lett. **68**, 1480 (1992).
- [4] K. Adcox *et al.*, Phys. Rev. Lett. **88**, 022301 (2001).
- [5] R. Baier, Y.L. Dokshitzer, A.H. Mueller, S. Peigne, and D. Schiff, Nucl. Phys. B **484**, 265 (1997).
- [6] M. Gyulassy, P. Levai, and I. Vitev, Phys. Rev. Lett. **85**, 5535 (2000).
- [7] T. Renk, Phys. Rev. C **74**, 034906 (2006).
- [8] R. Baier and D. Schiff, J. High Energy Phys. 09 (2006) 059.
- [9] A. Dainese, C. Loizides, and G. Paic, Eur. Phys. J. C **38**, 461 (2005).
- [10] C. Loizides, Eur. Phys. J. C **49**, 339 (2007).
- [11] H. Zhang, J.F. Owens, E. Wang, and X.-N. Wang, Phys. Rev. Lett. **98**, 212301 (2007).
- [12] K. Adcox *et al.*, Nucl. Instrum. Methods Phys. Res., Sect. A **499**, 469 (2003).
- [13] M.L. Miller, K. Reygers, S.J. Sanders, and P. Steinberg, Annu. Rev. Nucl. Part. Sci. **57**, 205 (2007).
- [14] L. Aphecetche *et al.*, Nucl. Instrum. Methods Phys. Res., Sect. A **499**, 521 (2003).
- [15] S.S. Adler *et al.*, Phys. Rev. C **76**, 034904 (2007).
- [16] A. Adare *et al.*, Phys. Rev. C **77**, 064907 (2008).
- [17] A. Adare, Phys. Rev. D **76**, 051106 (2007).
- [18] K. Adcox *et al.* (PHENIX), Nucl. Phys. A **757**, 184 (2005).